

UNIVERSITÉ DU QUÉBEC
INRS- ÉNERGIE, MATÉRIAUX ET TÉLÉCOMMUNICATIONS

Spectral Domain Interferometry for Terahertz Detection: Concept and Application

par
Akram Yousif Ibrahim

Thèse présentée
pour l'obtention
du grade de Philosophiæ Doctor (Ph.D)
en Sciences de l'Énergie et des Matériaux

Jury d'évaluation

Président du jury
et examinateur interne :

Dr. Luca Razzari,
(INRS-EMT),
Varenes, QC, Canada

Examineur externes :

Dr. Maksim Skorobogatiy,
École Polytechnique,
Montréal, QC, Canada.

Dr. Jean-Michel Ménard.
University of Ottawa,
Ottawa, ON, Canada.

Directeur de recherche :

Dr. Tsuneyuki Ozaki,
(INRS-EMT),
Varenes, QC, Canada.

Dedication

To:

The souls of my parents:

Alawia and Yousif.

&

To:

My sisters and brothers Safa, Taisser, Naser, and Ibrahim.

Abstract

The current golden standard for measuring terahertz (THz) temporal waveform is the electro-optic sampling (EOS) technique. However, EOS technique when exploited for measuring intense THz electric field has a limited dynamic range (DR) due to a phenomenon called over-rotation. This limited DR makes it very difficult to measure intense THz signals and weak signals at the same time. Routinely, THz filters (such as silicon) are used to ensure that the measurements are within the DR of the EOS technique and then calibrated against reference data. However, this not only distorts the THz waveform but when those filters are irradiated with intense THz radiation, recent researches have shown that there could be substantial changes in their transmission characteristics due to nonlinear THz effects. Therefore, a proper interpretation of the data obtained through the EOS technique in intense THz experiments could be complicated.

In the framework of this thesis, we describe a novel technique for measuring THz waveform that does not suffer from over-rotation limitation, possessing a tremendous DR of $\sim 7 \times 10^6$, while at the same time having high signal-to-noise ratio (SNR) that are comparable to that of the commonly used EOS techniques. In this new technique, we make use of spectral-domain interferometry (SDI) technique to develop different detection schemes, such as Michelson interferometer type based SDI (later we distinguish it as the standard SDI), Mach-Zehnder interferometer based SDI (MZI-SDI), and fiber-based SDI (later we distinguish it as cross-polarized SDI (CP-SDI)) schemes to measure intense THz electric fields.

We perform a comparison between the three SDI schemes for THz electric field measurement schemes. Based on our experimental findings, the temporal waveform of the THz electric field measured with the standard SDI technique exhibits reasonable DR and SNR. However, the temporal scanning window is limited due to the finite fixed thickness of the glass plate that is used to create the two interfering signals. This limitation in the temporal scanning window has been avoided in both MZI-SDI and CP-SDI for THz electric field measurement schemes. We find that the SNR of the THz electric field measurement obtained with MZI-SDI scheme is inferior to that obtained with the CP-SDI scheme. We attributed this inferior SNR in the former scheme to the fact that there are more optical components in the optical probe beam signal, compared to the latter scheme. Each of these optical components is susceptible to

vibrational noise in the setup, and thus contributes to the overall noise buildup in the measurement. On the other hand, in the case of the CP-SDI scheme, the situation is different, since both interfering signals are propagating along one common path (along the optical fiber). In this case, the noises associated with vibrations in the optical components, which in turn change the optical path difference (OPD) between two interfering signals, are mitigated since any change in OPD is common to both signals.

Owing to the excellent performance of the CP-SDI scheme, with an SNR ~ 48.97 dB and DR $\sim 7 \times 10^6$, we find this version the best among all SDI-THz detection technique versions and thus suitable for carrying out THz spectroscopic measurements.

Furthermore, as a second objective of this thesis, the new CP-SDI THz detection technique was validated successfully in measuring the THz response *-in transmission geometry-* of high-permittivity materials, which are encountering challenges in the THz frequency range. In this work, we chose Barium Strontium Titanate (BST), which notoriously has significant losses in the THz frequency region, thus affecting the SNR of the THz measurement. Furthermore, we hold a comparison between the dielectric response results obtained via CP-SDI THz detection technique and those obtained via conventional EOS THz detection technique for the same BST sample. We show that from the comparison, the CP-SDI technique enables obtaining more accurate results due to its ultra-high DR and good SNR.

Table of Contents

| | |
|--|-----|
| List of Figures | ix |
| List of Tables | xii |
| Chapter 1: Introduction and motivation | 1 |
| 1.1 Terahertz gap: Historical background | 1 |
| 1.2 Motivation of this thesis work | 2 |
| 1.2.1 The imperative need for intense THz sources and detectors..... | 2 |
| 1.3 The objectives and scope of this thesis work | 4 |
| Chapter 1 references..... | 5 |
| Chapter 2: Theoretical background | 8 |
| 2.1 Conventional femtosecond laser methods for generating few-cycle THz pulse | 8 |
| 2.1.1 Photoconductive switches (antennas)..... | 8 |
| 2.1.2 Difference frequency mixing or optical rectification in nonlinear media | 11 |
| 2.1.3 THz waves generation in plasma..... | 16 |
| 2.2 Intense THz pulse detection | 18 |
| 2.2.1 Conventional techniques for coherent THz detection..... | 18 |
| 2.2.1.1 PCA for THz electric field measurement..... | 18 |
| 2.2.1.2 Electro-optic sampling technique | 19 |
| 2.2.1.3 THz-air-biased coherent detection (THz-ABCD) | 22 |
| 2.3 Conventional THz detection techniques in measuring intense THz electric field: challenges and limitations | 24 |
| 2.4 Advanced technique for coherent THz detection based on spectral-domain interferometry (SDI) technique | 25 |
| 2.4.1 Concept of spectral-domain interferometry (SDI) technique | 26 |
| 2.5.2 Pursuing SDI technique for THz electric field measurement..... | 28 |
| 2.5 Applications of THz radiation | 29 |
| 2.5.1 THz spectroscopy..... | 29 |

| | | |
|---|---|-----------|
| 2.5.1.1 | Terahertz time-domain spectroscopy (THz-TDS) | 29 |
| 2.5.1.2 | Terahertz frequency -domain spectroscopy (THz-FDS)..... | 33 |
| 2.5.2 | Applications of intense field THz pulses | 34 |
| 2.5.2.1 | Nonlinear THz spectroscopy of condensed matter..... | 35 |
| 2.5.2.1.1 | Optical-pump / intense THz-probe and THz-pump/THz-probe experiments | 35 |
| 2.5.2.1.2 | Ponderomotive effect | 37 |
| Chapter 2 references..... | | 37 |
| Chapter 3: Innovative coherent THz detection techniques using SDI part | | |
| I: Michelson-type and Mach-Zehnder interferometer based SDI | | |
| techniques in THz electric field measurement..... | | |
| 46 | | |
| 3.1 | SDI in THz electric field measurement | 46 |
| 3.2 | Michelson-type interferometer based SDI in THz electric field measurement..... | 47 |
| 3.2.1 | Experimental realization of standard SDI technique for THz electric field measurement..... | 47 |
| 3.2.2 | Phase change data acquisition by SDI technique | 52 |
| 3.2.3 | Experimental results and discussion..... | 54 |
| 3.2.3.1 | THz electric field measurement obtained with the standard SDI technique | 54 |
| 3.2.4 | Challenges and limitation of the standard SDI technique for THz electric field measurement..... | 56 |
| 3.2.4.1 | Signal-to-noise ratio (SNR) | 57 |
| 3.2.4.2 | Limited temporal scan length..... | 58 |
| 3.3 | The idea of self-referencing in the standard SDI technique for THz electric field measurement..... | 58 |
| 3.4 | MZI based SDI technique for THz electric field measurement | 61 |
| 3.4.1 | Experimental realization of MZI-based-SDI technique for THz electric field measurement..... | 62 |
| 3.4.2 | Experimental results and discussion..... | 64 |
| 3.4.2.1 | THz electric field measurement obtained with MZI-based-SDI technique | 64 |
| 3.5 | Characterization of MZI-based-SDI technique for THz electric field measurement..... | 65 |

| | |
|--|-----------|
| 3.5.1 Temporal scan range..... | 65 |
| 3.5.2 SNR of MZI-based-SDI technique in THz electric field measurement..... | 66 |
| 3.5.3 The optimal OPD between the two OPB interfering signals | 67 |
| 3.5.4 Dynamic range (DR) of MZI-based SDI technique in THz electric field measurement | 68 |
| 3.5.5 MZI-based-SDI technique at different THz peak electric field..... | 69 |
| Chapter 3 references..... | 70 |
| Chapter 4: Innovative coherent THz detection techniques using SDI part II: Cross-polarized (CP) based SDI in terahertz electric field measurement | 72 |
| 4.1 The idea of the fiber interferometer: Concept of the CP-SDI scheme | 72 |
| 4.2 Experimental realization of CP-SDI technique for THz electric field measurement..... | 74 |
| 4.3 THz electric field measurements obtained with CP-SDI technique | 76 |
| 4.4 Characterization of the CP-SDI THz detection technique | 78 |
| 4.4.1 Fiber length choice..... | 78 |
| 4.4.2 Signal-to-noise ratio (SNR)..... | 81 |
| 4.4.3 Over-rotation limitation..... | 81 |
| 4.4.4 Dynamic range (DR) of CP-SDI technique | 82 |
| 4.4.5 CP-SDI technique at different THz electric field | 83 |
| 4.4.6 Measurement of polarization dependence using CP-SDI technique | 85 |
| 4.5 Attempting to improve the SNR of the CP-SDI technique for THz electric field measurement | 87 |
| 4.5.1 New referencing method in CP-SDI technique for THz electric field measurement . | 88 |
| 4.5.2 Compact CP-SDI module scheme | 92 |
| 4.6 Comparison between standard SDI, MZI based SDI and CP-SDI techniques in THz electric field measurement..... | 95 |
| Chapter 4 references..... | 97 |

| | |
|---|-----|
| Chapter 5: Application of CP-SDI detection technique in THz spectroscopy of high-permittivity materials | 99 |
| 5.1 Introduction | 99 |
| 5.2 Barium Strontium Titanate (BST) - A case study | 101 |
| 5.3 THz spectroscopy applied to BST ceramic | 104 |
| 5.3.1 Experimental realization | 104 |
| 5.4 THz waveforms acquisition for BST dielectric response extraction using conventional EOS THz detection technique | 106 |
| 5.4.1 Extraction of dielectric constants of stoichiometric BST sample using data obtained via conventional EOS technique | 109 |
| 5.5 THz Z-scan of BST ceramic | 111 |
| 5.6 THz waveforms acquisition for BST dielectric response extraction using CP-SDI THz detection technique | 114 |
| 5.6.1 Extraction of dielectric constants of stoichiometric BST sample using data obtained via CP-SDI THz detection technique | 117 |
| Chapter 5 references | 120 |
| Chapter 6: Conclusions and perspectives | 124 |
| Résumé en français | 128 |
| Références | 146 |

List of Figures

| | |
|---|----|
| Figure 1.1: The spectrum of electromagnetic radiation with THz frequencies..... | 1 |
| Figure 2.1: Schematic illustration of THz generation via photoconductive antenna..... | 9 |
| Figure 2.2: Interdigitated electrodes in the LAPCA for THz generation scheme..... | 10 |
| Figure 2.3: THz generation with collinear optical pump via OR..... | 12 |
| Figure 2.4: THz generation with non-collinear in LiNbO ₃ crystal via OR configuration..... | 14 |
| Figure 2.5: Schematic of experimental setup for THz generation by tilted-pulse-front technique in LiNbO ₃ | 15 |
| Figure 2.6: Schematic of the experimental setup for THz generation in plasma..... | 16 |
| Figure 2.7: Schematic illustration of THz pulse detection via PCA scheme..... | 19 |
| Figure 2.8: Schematic illustration of THz detection using EOS technique..... | 20 |
| Figure 2.9: Schematic illustration of experimental setup for THz- ABCD technique..... | 23 |
| Figure 2.10: Schematic for the concept of SDI..... | 27 |
| Figure 2.11: Schematic for electric and magnetic field vectors after reflection and transmission of an incident electromagnetic wave incident on a semi-infinite non-conducting surface..... | 30 |
| Figure 2.12: Schematic illustration for the experimental set up commonly used in THz-TDS..... | 31 |
| Figure 2.13: Schematic of OPITP spectroscopy with a non-collinear configuration..... | 36 |
| Figure 3.1: Schematic of the experimental setup of Michelson interferometer-type based SDI technique for THz electric field measurement..... | 48 |
| Figure 3.2: Schematic of the home-made spectrometer used in the SDI project..... | 48 |
| Figure 3.3: Schematic of interference in the SDI (a) and the corresponding FFT signal (b)..... | 51 |
| Figure 3.4: Interference OPB pulses in SDI (a), the intensity distribution (b), and the corresponding FFT peak (c)..... | 52 |
| Figure 3.5: Measured signal phase in <i>wave-number space</i> and the corresponding unwrapped phase signal using SDI technique..... | 54 |
| Figure 3.6: THz electric field obtained with the standard SDI technique (a) and the corresponding Fourier transform power spectrum (b)..... | 55 |
| Figure 3.7: THz electric field obtained with the conventional EOS technique (a) and the corresponding Fourier transform power spectrum (b)..... | 55 |
| Figure 3.8: The spatial profile of the THz beam focal spot on the ZnTe detection (a) and the image of the focused THz beam pulse measured via pyroelectric IR camera (b)..... | 56 |
| Figure 3.9: Mechanical vibrations on the glass plate used in standard SDI affecting phase change measurement via OPB..... | 57 |
| Figure 3.10: Schematic of SR-SDI idea..... | 59 |
| Figure 3.11: THz electric field measurement obtained with the standard SDI technique (a) without using the self-referencing method and (b) the corresponding Fourier power spectrum..... | 60 |
| Figure 3.12: THz electric field measurement obtained with the standard SDI technique (a) with using the self-referencing method and (b) the corresponding Fourier power spectrum..... | 60 |
| Figure 3.13: Schematic of the experimental setup of Mach-Zehnder interferometer (MZI) based spectral domain interferometry technique for THz electric field measurement..... | 62 |

| | |
|---|----|
| Figure 3.14: THz electric field trace obtained with the conventional EOS technique (a). Fourier power spectrum of the THz temporal trace obtained by conventional EOS technique (b) ... | 64 |
| Figure 3.15: THz electric field trace obtained with the MZI based SDI technique (a). Fourier power spectrum of the THz temporal trace obtained by MZI based SDI technique (b)..... | 65 |
| Figure 3.16: THz electric field measurement obtained with the MZI based SDI technique at different OPD between the interfering optical probe beam pulses..... | 67 |
| Figure 3.17: Signal-to-noise ratio (SNR) of the THz electric field measurements dependence on optical path difference (OPD) between the two signals at MZI two arms ... | 68 |
| Figure 3.18: THz signal amplitude measurements dependence on THz peak electric field using conventional EOS and MZI based SDI techniques. The red line is the linear fit | 69 |
| Figure 4.1: PM fiber introduces optical path difference between the two polarization components(a) and the evolution process of introducing a fixed OPD between the two polarization components(b) | 74 |
| Figure 4.2: Experimental set up of the CP-SDI technique for THz detection | 75 |
| Figure 4.3: THz electric field trace obtained with conventional EOS technique (a), and the corresponding Fourier power spectrum (b) | 77 |
| Figure 4.4: THz electric field trace obtained with CP-SDI technique (a), and the corresponding Fourier power spectrum of the THz trace (b)..... | 77 |
| Figure 4.5: Dependence of noise and sensitivity of SDI technique on optical path difference between the interfering signals. (a) Normalized sensitivity drop and (b) normalized RIN are plotted against optical path difference (OPD)..... | 78 |
| Figure 4.6: THz electric field measurement obtained with the CP-SDI technique at different (fiber length) OPD between the interfering optical probe beam pulses..... | 80 |
| Figure 4.7: Dependence of the signal-to-noise ratio of the THz electric field measurements on the optical path difference between the two signals at the exit end of the optical fiber in the CP-SDI technique for THz electric field measurement... .. | 80 |
| Figure 4.8: Short temporal scans of different THz electric fields (E_{THz}) obtained with (a) the conventional EOS and (b) the CP SDI techniques at various E_{THz} | 82 |
| Figure 4.9: THz electric field measurement obtained with the CP-SDI technique using 80 cm length PM fiber at different THz peak electric field E_{THz} | 83 |
| Figure 4.10: Comparison between SNR of the conventional EOS and CP-SDI techniques for THz electric field measurement..... | 84 |
| Figure 4.11: Schematic representation of ZnTe detection crystal with angles of the THz beam and optical probe beam (OPB) polarization orientation with respect to the crystal Z axis | 86 |
| Figure 4.12: ZnTe detection crystal's azimuthal angle dependence on the detected THz electric field amplitude..... | 87 |
| Figure 4.13: Partial schematic of new referencing method in CP-SDI technique | 89 |
| Figure 4.14: THz electric field trace obtained with conventional EOS technique (a) and the corresponding Fourier power spectrum (b)..... | 90 |
| Figure 4.15: THz electric field trace obtained with CP-SDI technique without referencing (a), and with referencing method (b), the noise amplitude subtracted using the referencing method (c), and the corresponding Fourier power spectra of the THz trace obtained with and without the new referencing method (d)..... | 91 |

| | |
|---|-----|
| Figure 4.16: Schematic illustration of the experimental setup of the CP-SDI compact module for THz electric field measurement | 93 |
| Figure 4.17: THz electric field trace obtained with CP-SDI compact module (a) and the corresponding Fourier power spectrum of the THz trace (b)..... | 94 |
| Figure 5.1: The elementary cell for the ferroelectric perovskite compounds structure (ABO ₃)..... | 100 |
| Figure 5.2: The elementary cell along with the eigenvector of the soft mode for the ferroelectric perovskite compound (Ba, Sr)TiO ₃ | 102 |
| Figure 5.3: The schematic of THz-TDS setup used to characterize the stoichiometric BST sample <i>in transmission</i> geometry..... | 105 |
| Figure 5.4: Measurement of the THz temporal waveform (a) reference (air) and (b) transmitted through stoichiometric BST sample A/B=1.00, both measured via conventional EOS. The corresponding power spectra are shown in (c) and (d) respectively... .. | 107 |
| Figure 5.5: Extracted THz (a) amplitude and (b) phase data obtained from the Fourier transform of the waveforms with conventional EOS THz detection technique..... | 108 |
| Figure 5.6: Extracted THz (a) magnitude of transmission coefficient and (b) phase difference obtained from Fourier transform of the waveforms with conventional EOS THz detection technique... .. | 109 |
| Figure 5.7: The extracted real (n) and imaginary (k) parts of the complex index of refraction for BST sample using THz-TDS <i>in transmission</i> geometry with conventional EOS THz detection technique... .. | 110 |
| Figure 5.8: Conventional EOS measured THz spectra of (a) real part of permittivity ϵ' , and (b) imaginary part of permittivity ϵ'' at an average thickness of 31.2 \pm 4 μ m of stoichiometric BST sample..... | 111 |
| Figure 5.9: Measurement of the transmitted E_{THz} through stoichiometric BST sample for different positions of the Z-scan at room temperature..... | 112 |
| Figure 5.10: Measurement of the temporal shift and the transmitted THz peak amplitude through BST for different positions of the Z-scan | 113 |
| Figure 5.11: Measurement of the THz waveform (a) reference and (b) transmitted through stoichiometric BST sample, both measured via CP-SDI THz detection technique at high $E_{\text{THz}} \approx 439$ kVcm ⁻¹ at room temperature. The corresponding power spectra are shown in (c) and (d) | 114 |
| Figure 5.12: Measurement of THz (a) amplitude and (b) phase data obtained from the Fourier transform of the waveforms using CP-SDI THz detection technique... .. | 115 |
| Figure 5.13: Measurement of THz (a) Transmission coefficient and (b) phase difference obtained from Fourier transform of the waveforms using CP-SDI THz detection technique. | 116 |
| Figure 5.14: Extracted real (n) and imaginary (k) parts of the complex index of refraction for a 30.3 \pm 2 μ m -thick stoichiometric BST sample using THz-TDS in transmission geometry with CP-SDI technique in detection | 116 |
| Figure 5.15: Different measured values obtained by CP-SDI THz detection technique for (a) ϵ' and (b) ϵ'' spectra at different thicknesses of the stoichiometric BST sample | 117 |
| Figure 5.16: CP-SDI technique measured spectra of (a) real part of permittivity ϵ' , and (b) imaginary part of permittivity ϵ'' at an average thickness of 30.3 \pm 2 μ m of BST sample..... | 118 |
| Figure 5.17: Frequency dependence of the loss tangent of stoichiometric BST sample | 120 |

List of Tables

| | |
|--|----|
| Table 2.1: Properties of common materials used for THz generation via OR..... | 13 |
| Table 2.2: Comparison between common THz generation techniques..... | 17 |
| Table 4.1: Parameters of the PM fiber used in the CP-SDI technique | 76 |
| Table 4.2: Comparison between SNR of THz electric field measurements obtained with conventional EOS technique and different SDI schemes..... | 94 |
| Table 4.3: Comparison between different SDI techniques for THz detection | 96 |

Acknowledgement

My Ph.D. work at INRS would not have been successful without interactions with many people at INRS and throughout the scientific community. I have had the pleasure of knowing and working with them, all of whom I am indebted to.

I am extremely grateful to my thesis advisor, Prof. Tsuneyuki Ozaki for his endless support, guidance, constant enthusiasm, and patience those have an impact in driving the research described in this thesis work. His enormous knowledge always inspired me. I have learned from him many problem-solving strategies in both scientific and personal levels, those will be an asset to me wherever I go in my future. This work would not have taken its present shape without him.

I am indebted to Dr. I. Al Naib who has helped me a lot in the start of my Ph.D. program by elucidating lots of THz concepts. I am very thankful to Prof. D. Cooke of McGill University and his group for allowing us to work in his THz laboratory and discussing our new THz detection technique. Moreover, I extended my thanks to Prof. F. Blanchard of École de technologie supérieure (ÉTS) for his technical advice whenever needed. I am thankful to Prof. T. Teranishi, of Okayama University, Japan and his group for BST samples fabrication.

My previous and current colleagues in Prof. Ozaki's group have been an invaluable resource: G. Sharma, K. Singh, X. Ropagnol, M. K.-Turmel, H. A. Hafez, and D. Férachou.

I would like to thank the fantastic technical staff especially Philippe Lassondé and Antoine Laramée for their genius efforts in solving many technical problems in ALLS laboratory. Many thanks to Mr. C. Morissette from INRS machine shop for helping in fabricating the needed experimental-setup parts. Also, many thanks to the administrative staff especially Ms. H. Sabourin.

Finally, I would like to express my gratitude to members of the Sudanese community in London Ontario for their moral support especially brothers Hatim Bakri and Abdulkhalig Abdoon.

Chapter 1

Introduction and motivation

1.1 Terahertz gap: Historical background

Terahertz (THz = 10^{12} Hz) radiation is a part of the electromagnetic (EM) spectrum, typically defined as the radiation with frequencies from 0.1 to 10 THz, which corresponds to wavenumbers between 3 and 300 cm^{-1} , photon energies between 0.4 and 40 meV, and wavelengths between 3 mm and 30 μm . This part of the EM spectrum has not been well explored due to the lack of practical efficient sources and sensitive detectors, consequently giving that frequency band the name the “THz gap”. In the past, technological applications in the THz region were hindered due to the fact that this frequency range is situated in between electronics and optics, *i.e.* it is in the upper limit to what is accessible by electronics and in the lower limit to what is accessible by optics. Fig. 1.1 depicts the THz band within in the EM spectrum [1-3].

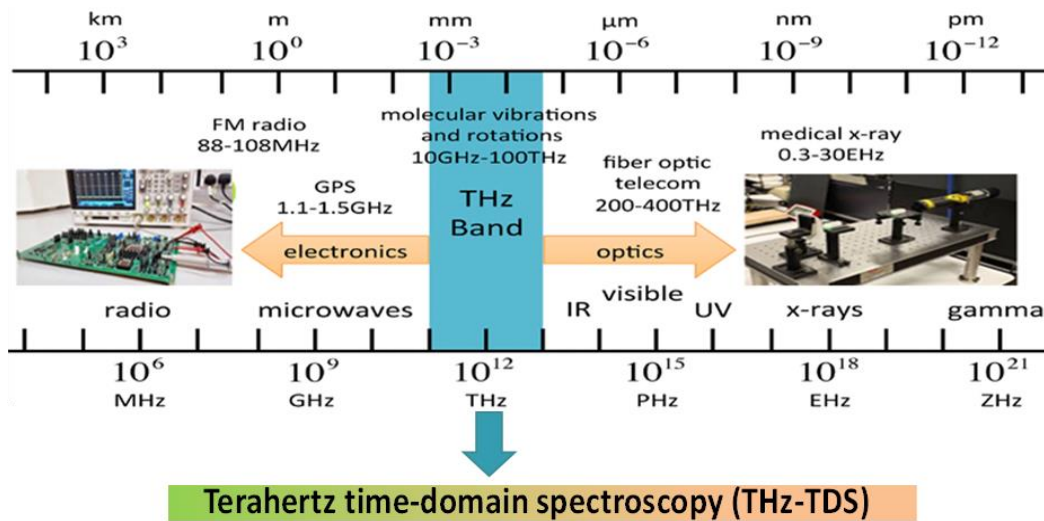


Figure 1.1 | The spectrum of electromagnetic radiation with THz frequencies situated in between microwave and infrared frequencies [3].

The interaction of electromagnetic radiation with matter has been the center of interest for scientists and researchers. One of the milestones in studying novel phenomenon in physics and chemistry is the availability of light sources and detectors that can enable spectroscopic techniques in the linear and nonlinear regimes. While microwave and optical frequency regions

are well established with many light sources along with detectors, the THz region had remained well-unexplored for a long time. Recent years have witnessed significant successful developments of techniques related to static and transient terahertz (THz) time-domain spectroscopy (THz-TDS) and imaging. The versatility of these techniques has been demonstrated in a wide range of applications in many disciplines, such as in spectroscopic imaging and tomography [4,5], label-free genetic diagnostics and analysis [6], biomolecular spectroscopy [7], and biomedical applications such as T-ray biosensor [8].

1.2 Motivation of this thesis work

1.2.1 The imperative need for intense THz sources and detectors

The need for intense THz sources is on the rise, due to recent significant advances in studying the nonlinear optical responses of materials in THz frequencies and at picosecond or even sub-picosecond timescale. Such remarkable progress has undoubtedly been accelerated by the incredible advances in both generating and detecting coherent THz radiation. For example, the recent surge in the availability of intense THz radiation sources is allowing new solutions to long-standing challenges, as well as opening new avenues in both science and technology. For example, intense THz sources have the potential to enable THz-TDS of aqueous samples, such as those related to biology and medicine [9,10], with high signal-to-noise ratio (SNR) [11]. Due to the high absorption of THz radiation by water, such THz spectroscopic experiments have been difficult to perform in transmission configuration. Techniques such as THz time-domain attenuated total reflection (ATR) spectroscopy [12,13] has been exploited instead to avoid the limitations in such experiment. However, data analysis of this technique is rather complicated.

The availability of THz sources with high flux is opening the possibility to perform THz-TDS of aqueous and other highly absorptive media *in transmission configuration*. Humidity also has significant influence in THz applications, such as large-scale object imaging and remote sensing for security purposes [14,15], and wireless communications [16,17], in which the THz pulse may need to propagate long distances through the atmosphere. Furthermore, intense THz sources are also enabling the observation of fascinating nonlinear phenomena in light-matter interaction processes [18-25]. For example, THz nonlinear spectroscopy offers a unique characterization method of novel materials for future THz electronics, such as graphene [26-28] and topological insulators [29,30]. In turn, such demand is pushing the limits of tabletop, intense,

and ultrafast broadband THz emitting sources, resulting in peak THz electric fields of sub-MV/cm to several MV/cm [31-35].

For such THz-based technological applications to be fully implemented, it is of crucial importance to have coherent THz detection techniques with both high dynamic range (DR) and high SNR [11]. Where DR is defined as the maximum measurable phase divided by the standard deviation of the phase noise when no THz signal is present. High DR measurement is especially important in many of the above applications, where one needs to compare the waveform of intense THz pulses with relatively weak THz signals (such as the THz signal after experiencing strong absorption, or the nonlinear THz signal). Large DR is also required in THz-TDS measurements in order to avoid misinterpretation of experimentally obtained data [36]. However, electro-optic sampling (EOS) [37-39], which is currently one of the most popular methods for THz detection, has achieved limited DR. This limited DR of conventional EOS technique can be attributed to the mechanism by which the THz field is measured. In conventional EOS, a linearly polarized femtosecond laser pulse co-propagates with a picosecond THz pulse in an electro-optic (EO) detection crystal [37]. The THz-electric-field-induced birefringence in the EO crystal (due to the Pockels effect) changes the polarization of the co-propagating optical probe pulse. The resulting ellipticity of the probe pulse is measured by using a detection system that consists of a quarter-wave plate, a polarizer and a pair of balanced photodiodes placed after the detection crystal. The change in phase, which is proportional to the THz electric field, is manifested as a modulation in the intensity of the two polarization components of the optical probe beam (OPB) pulse. However, if the induced phase change in the probe pulse components is more than $\pi/2$, a reversal in the intensity modulation of the probe pulse will take place. This, in turn, results in ambiguities in measuring THz fields that induce phase differences of more than $\pi/2$ [40] in the conventional EOS configuration. This limitation is known as over-rotation [40] and hence severely limits the DR of conventional EOS. In addition, over-rotation poses several other restrictions. For example, higher spectral resolution in THz-TDS requires thicker EO detection crystals [40]. However, a thicker crystal increases the possibility of over-rotation, as induced birefringence in the EO crystal is proportional to both the THz electric field and the thickness of the crystal. One could use thin (less than 50 μm) detection crystals, but the DR will still suffer from lower THz electric field modulation on the OPB pulse. Furthermore, the limited DR of conventional EOS makes it very difficult to measure intense THz signals and weak signals at the

same time. Currently, researchers are forced to use THz filters (such as high resistivity float-zone silicon plates) to make sure that their measurements are within the DR of the conventional EOS technique, and then calibrate them against reference data. However, dispersion and wavelength-dependent absorption of such plates would modify the THz waveform, thus complicating the correct measurement of intense THz waves using conventional EO sampling [41].

1.3 The objectives and scope of this thesis work

The core objective of this thesis work is to establish a novel THz detection technique that comprises no over-rotation limitation, ultra-high DR, and high SNR characteristic features. Furthermore, the second objective of the thesis is to exploit this detection technique in exploring the THz response of high-permittivity materials, such as Barium Strontium Titanate (BST). In the new THz detection techniques, we make use of spectral-domain interferometry (SDI) to develop different detection schemes, such as Mach-Zehnder interferometer based SDI (MZI-SDI) and fiber-based SDI (later we distinguish it as cross-polarized SDI (CP-SDI)) schemes to detect intense THz electric fields without over-rotation and with ultrahigh DR. Worth to note, in the initial stage of the SDI-THz project, we have used a Michelson-type (later we distinguish it as standard SDI) technique to measure the THz waveform. The standard SDI technique for THz electric field measurement provided a large DR however it was limited in the duration of the pulse that could be measured (3 ps), which is far too short for most applications. The SNR of the standard SDI technique was also limited, being far inferior compared with the popular conventional EOS technique.

The thesis is organized into four main chapters. Chapter 2 covers the literature survey on various techniques of generating and detecting THz pulses via optical methods based on employing ultrashort Ti: sapphire laser pulses, with the emphasis on generating and detecting intense THz pulses. Moreover, in the same chapter, some applications of intense THz radiation are discussed.

In the first part of Chapter 3, we started with discussion and reproduction of the THz electric field measurement by using Michelson-type interferometer based-SDI technique (we later distinguish it as the standard SDI technique), illustrating its drawbacks (e.g. limited temporal scan range and inferior SNR) and the possible means to overcome such drawbacks. In the second part of Chapter 3, we discuss the experimental demonstration of the use of MZI in SDI technique

for THz electric field measurement and how it helped in eliminating some drawbacks experienced in the standard SDI for THz electric field measurement.

In Chapter 4 we describe, once more for the first time, a novel technique for detecting coherent THz radiation, possessing tremendous DR $\sim 7 \times 10^6$, while at the same time having high SNR that is comparable to that of the commonly used EOS technique. In this new technique, we have exploited the birefringence in a single mode polarization-maintaining (PM) fiber that creates two cross-polarized signals at the exit end of the fiber. Thus, we name this technique the cross-polarized (CP)-SDI technique. As mentioned earlier, THz technology is extending into various domains of science and technology and is rapidly becoming an important tool. Many such applications require measurements of the THz waveform with both high DR and high SNR. Further, we have discussed and experimentally demonstrated two attempts to increase the SNR of the CP-SDI technique by (i) introducing a new referencing method and (ii) using a compact CP-SDI module that reduces the mechanical vibration in the setup.

In Chapter 5, meriting from the characteristics of the new technique (e.g. ultrahigh DR and excellent SNR), we experimentally demonstrate the second objective of this thesis, which is the validation of the CP-SDI technique in THz spectroscopy application. We have chosen to perform THz-TDS measurements- in transmission geometry- on material that encounters challenges in the THz frequency range, such as high permittivity sample of Barium Strontium Titanate (BST) that notoriously has significant losses in THz frequencies region thus affecting the SNR of the measurement. The experiment was an excellent testing opportunity to evaluate our new technique capabilities in determining BST dielectric response in the THz frequency region. Furthermore, we hold a comparison between dielectric response results obtained via CP-SDI THz detection technique and those obtained via conventional EOS THz detection technique for the same BST sample and under the same experimental conditions. We show that from the comparison, the CP-SDI technique enables obtaining more accurate results.

References

- [1] A. Handi, *Int. J. Infrared Millim. Waves* **24**, 91-118 (2003).
- [2] M. F. Kimmitt, *J. Biol. Phys.* **29**, 77-85 (2003).
- [3] <http://pratt.duke.edu/about/news/willie-padilla-exploring-technologys-terahertz-gap>.
- [4] Y. Watanabe, K. Kawase, T. Ikari, H. Ito, Y. Ishikawa and H. Minamide, *Appl. Phys. Lett.* **83**, 800-802 (2003).
- [5] S. Wang, B. Ferguson, D. Abbott, and X. C. Zhang, *J. Biol. Phys.* **29**, 247-256 (2003).

- [6] M. Nagel, P. H. Bolivar, M. Brucherseifer, H. Kurz, A. Bosserhoff and R. Buttner, *Appl. Phys. Lett.* **80**, 154-156 (2002).
- [7] A. Markelz, S. Whitmire, J. Hillebrecht, and R. Birge, *Phys. Med. Biol.* **47**, 3797-3805 (2002).
- [8] S. P. Mickan, A. Menikh, H. Liu, C. A. Mannella, R. MacColl, D. Abbott, J. Munch and X.-C. Zhang, *Phys. Med. Biol.* **47**, 3789-3795 (2002).
- [9] X.-C. Zhang, *Phys. Med. Biol.* **47**, 3667-3677 (2002).
- [10] E. Pickwell and V. P. Wallace, *J. Phys. D: Appl. Phys.* **39**, R301-R310 (2006).
- [11] G. Zhao, R. N. Schouten, N. Van der Valk, W. T. Wenckebach, and P. C. M. Planken, *Phys. Med. Biol.* **47**, 3699-3704 (2002).
- [12] M. Nagai, H. Yada, T. Arikawa and K. Tanaka, *Int. J. Infra. Milli. Waves* **27**, 4 505–515 (2006).
- [13] A. Nakanishi, Y. Kawada, T. Yasuda, K. Akiyama, and H. Takahashi, *Rev. Sci. Inst.* **83**, 033103 (2012).
- [14] M. Tonouchi, *Nature Photon.* **1**, 97-105 (2007).
- [15] H.-B. Liu, H. Zhong, N. Karpowicz, Y. Chen, and X.-C Zhang, *Proc. IEEE* **95**, 1514-1527 (2007).
- [16] S. Koenig, D. Lopez-Diaz, J. Antes, F. Boes, R. Henneberger, A. Leuther, A. Tessmann, R. Schmogrow, D. Hillerkuss, R. Palmer, T. Zwick, C. Koos, W. Freude, O. Ambacher, J. Leuthold and I. Kallfass, *Nature Photon.* **7**, 977- 981 (2013).
- [17] K.-C. Huang and Z. Wang, *IEEE Microw. Mag.* **12**,108-116 (2011).
- [18] C. Vicario, C. Ruchert, F. Ardana-Lamas, P. M. Derlet, B. Tudu, J. Luning and C. P. Hauri, *Nature Photon.* **7**, 720-723 (2013).
- [19] K. Tanaka, H. Hirori, and M. Nagai, *IEEE Trans. THz Sci. Technol.* **1**, 301-312 (2011).
- [20] T. Kubacka, J. A. Johnson, M. C. Hoffmann, C. Vicario, S. de Jong, P. Beaud, S. Grubel, S.-W. Huang, L. Huber, L. Patthey, Y.-D. Chuang, J. J. Turner, G. L. Dakovski, W.-S. Lee, M. P. Miniti, W. Schlotter, R. G. Moore, C. P. Hauri, S. M. Koohpayeh, V. Scagnoli, G. Ingold, S. L. Johnson, U. Staub, *Science* **343**, 1333-1336 (2014).
- [21] H. Y. Hwang, S. Fleischer, N. C. Brandt, B. G. Perkins Jr., M. Liu, K. Fan, A. Sternbach, X. Zhang, R. D. Averitt and K. A. Nelson, *J. Mod. Opt.* **62**, 1447-1479 (2015).
- [22] T. Kampfrath, A. Sell, G. Klatt, A. Pashkin, S. Mahrlein, T. Dekorsy, M. Wolf, M. Fiebig, A. Leitenstorfer and R. Huber, *Nature Photon.* **5**, 31-34 (2011).
- [23] L. Razzari, F. H. Su, G. Sharma, F. Blanchard, A. Ayesheshim, H. -C. Bandulet, R. Morandotti, J. -C. Kieffer, T. Ozaki, M. Reid, and F. A. Hegmann, *Phys. Rev. B* **79**, 193204 (2009).
- [24] F. H. Su, F. Blanchard, G. Sharma, L. Razzari, A. Ayesheshim, T. L. Cocker, L. V. Titova, T. Ozaki, J.-C. Kieffer, R. Morandotti, M. Reid, and F. A. Hegmann, *Opt. Express* **17**, 9620-9629 (2009).

- [25] M. Liu, H. Y. Hwang, H. Tao, A. C. Strikwerda, K. Fan, G. R. Keiser, A. J. Sternbach, K. G. West, S. Kittiwatanakul, J. Lu, S. A. Wolf, F. G. Omenetto, X. Zhang, K. A. Nelson and R. D. Averitt, *Nature* **487**, 345-348 (2012).
- [26] H. A. Hafez, I. Al-Naib, K. Oguri, Y. Sekine, M. M. Dignam, A. Ibrahim, D. G. Cooke, S. Tanaka, F. Komori, H. Hibino, and T. Ozaki, *AIP Adv.* **4**, 117118 (2014).
- [27] H. A. Hafez, I. Al-Naib, M. M. Dignam, Y. Sekine, K. Oguri, F. Blanchard, D. G. Cooke, S. Tanaka, F. Komori, H. Hibino, and T. Ozaki, *Phys. Rev. B.* **91**, 035422 (2015).
- [28] L. Vicarelli, M. S. Vitiello, D. Coquillat, A. Lombardo, A. C. Ferrari, W. Knap, M. Polini, V. Pellegrini, and A. Tredicucci, *Nat. Mater.* **11**, 865–871(2012).
- [29] X. Zhang, J. Wang, and S.-C. Zhang, *Phys. Rev. B.* **82**, 245107 (2010).
- [30] L. Wu, M. Brahlek, R. Valdes Aguilar, A. V. Stier, C. M. Morris, Y. Lubashevsky, L. S. Bilbro, N. Bansal, S. Oh and N. P. Armitage, *Nature Phys.* **9** 410-414 (2013).
- [31] H. Hirori, A. Doi, F. Blanchard, and K. Tanaka, *Appl. Phys. Lett.* **98**, 091106 (2011).
- [32] F. Blanchard, L. Razzari, H.-C. Bandulet, G. Sharma, R. Morandotti, J.-C. Kieffer, T. Ozaki, M. Reid, H. F. Tiedje, H. K. Haugen, and F. A. Hegmann, *Opt. Express* **15**, 13212-13220 (2007).
- [33] K. L. Yeh, M. C. Hoffmann, J. Hebling, and K. A. Nelson, *Appl. Phys. Lett.* **90**, 171121 (2007).
- [34] X. Ropagnol, F. Blanchard, T. Ozaki, and M. Reid, *Appl. Phys. Lett.* **103**, 161108 (2013).
- [35] A. Sell, A. Leitenstorfer and R. Huber, *Opt. Lett.* **33**, 2767-2769 (2008).
- [36] P. U. Jepsen, and B. M. Fischer, *Opt. Lett.* **30**, 29-31 (2005).
- [37] Q. Wu and X. -C. Zhang, *Appl. Phys. Lett.* **67**, 3523-3525 (1995).
- [38] Q. Wu and X.-C. Zhang, *Appl. Phys. Lett.* **71**, 1285-1286 (1997).
- [39] Q. Wu and X.-C. Zhang, *Appl. Phys. Lett.* **70**, 1784-1786 (1997).
- [40] G. Sharma, K. Singh, I. Al-Naib, R. Morandotti, and T. Ozaki, *Opt. Lett.* **37**, 4338-4340 (2012).
- [41] J. Dai, J. Zhang, W. Zhang and D. Grischkowsky, *JOSA B* **21**, 1379 (2004).

Chapter 2

Theoretical background

Outline

In this chapter, we will discuss commonly used methods for THz pulse generation and detection as well as some THz applications, with emphasis on laser based intense few-cycle THz sources. In the first part of this chapter, we will discuss the various methods for THz pulse generation, namely photoconductive (antennas) switches (PCA), difference frequency mixing or optical rectification (OR), and air plasma THz sources. In the second part of this chapter, we will discuss the common methods for coherent THz detection, namely the PCA, the electro-optic sampling (EOS), and THz-air-biased coherent detection (THz-ABCD) techniques. Furthermore, we will highlight the limitations of these techniques in measuring intense THz pulse radiation. A novel detection technique based on spectral-domain interferometry (SDI) that suits well intense THz electric field measurement and avoids limitations suffered in the other THz detection techniques will be discussed as well. In the third part of this chapter, we will discuss conventional THz application such as THz-time domain spectroscopy (THz-TDS) as well as two applications that have been made feasible with intense THz sources.

2.1 Conventional femtosecond laser methods for generating few-cycle THz pulse

Despite a wide range of applications and needs, the availability of suitable sources for THz experimental investigation is yet limited. However, there has been an important advancement in developing tabletop THz pulse sources by exploiting femtosecond lasers. The ultrafast photoconductive switch (antenna), optical rectification in nonlinear crystals, and air plasma sources are examples of such techniques widely adopted in the THz community.

2.1.1 Photoconductive switches (antennas)

The photoconductive antenna (PCA) scheme is typically designed from a high resistivity semiconductor substrate with two electrodes fabricated on the substrate, as schematically

depicted in Fig. 2.1. The operational concept of the PCA is based on generating rapidly varying currents that in turns emit electromagnetic radiation. The current variation is caused by modulation of the resistance of a semiconductor by the absorption of the short laser pulse. This method of generating picosecond THz pulses was invented by Auston in 1984 [1,2]. Nowadays PCA scheme for THz generation still finds widespread applications with the most common exploited substrate material is GaAs [3-11]; other materials used are silicon [2,1,12,13] and InP [5,7].

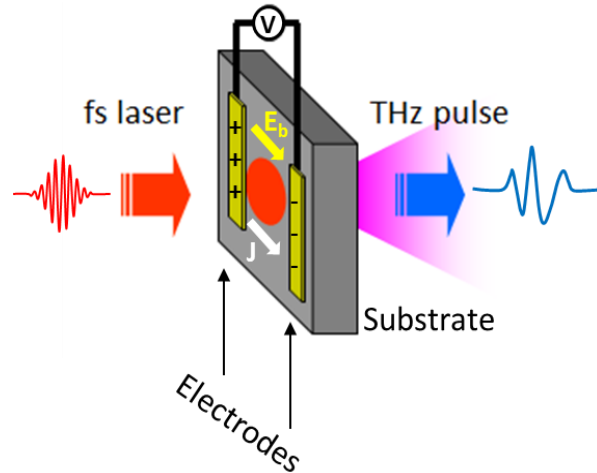


Figure 2.1 | Partial schematic illustrates THz generation via the photoconductive antenna (PCA). E_b is the applied static electric field and J is the surface current density [adapted from ref. 14].

The THz pulse generated via PCA scheme is distinguished by unique characteristics, namely the strong asymmetry in the magnitude of the positive and negative components of the THz field, the quasi-half-cycle nature, and the relatively lower central frequency. Such unique characteristics accompanied by the accelerated development in amplified Ti:sapphire laser technology has driven the interest in generating intense THz pulses from PCAs. In order to achieve this objective, the aperture of the PCA is increased and eventually, large aperture photoconductive antenna (LAPCA) scheme has been introduced for intense THz pulse generation [6]. In this scheme, the generated THz field in the far field is typically described by using Maxwell's equations, the THz electric field is proportional to the time derivative of the transient current, [15]:

$$E(t) \propto \frac{dJ}{dt} \propto E_b \frac{dn(t)}{dt} \quad (2.1)$$

Here $E(t)$ is the envelope of the emitted THz field, J is the current density, E_b is the applied bias field and n is the carrier density.

Therefore, in order to generate intense THz pulses via LAPCA scheme, one needs to apply the highest voltage possible between the electrodes. The LAPCA scheme differs from other intense THz sources that rely on nonlinear optical process, since the THz energy is extracted from the bias field and not directly from the laser pulse energy [5].

The current golden standard for substrate material for PCA is GaAs, which has been the popular choice owing to its suitable electrical and optical properties. For LAPCAs there are limitations in using GaAs with gaps sizes of a few millimeters. For example, carriers would be accelerated to energies high enough to cause damage to the semiconductor substrate beside the degradation with usage and subsequent failure [16], resulting primarily from increased temperature due to Joule heating. Thus in order to circumvent these limitations in GaAs, other wide bandgap semiconductor materials with suitable thermal and electrical properties are attempted, for instance, diamond [17], ZnO [18], GaN [19] and ZnSe [20,21] crystals have been experimentally tested for LAPCAs substrates.

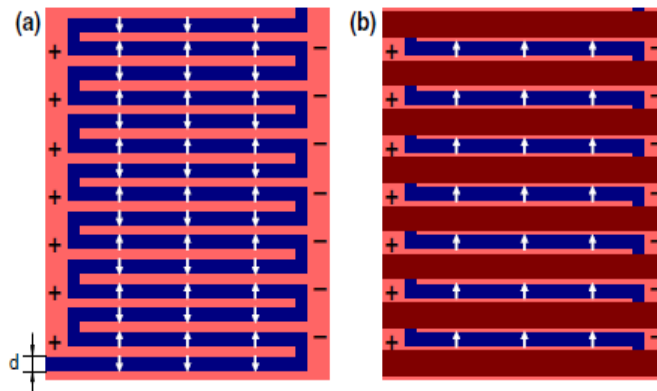


Figure 2.2| (a) Interdigitated electrodes in the LAPCA for THz generation scheme. Adjacent gaps between the electrodes have opposite directions of the static electric field (white arrows). (b) To prevent canceling of the oppositely directed contributions all gaps with a field directed downwards are blocked [adapted from ref. 28].

Nowadays there is an emerging trend in using interdigitated LAPCA as an alternative approach to reducing the bias voltage (and thus the requirement for the high-voltage source) while maintaining a large aperture for illumination [22]. Fig. 2.2 shows a schematic diagram of a typical interdigitated LAPCA. Interdigitated LAPCAs have many advantages compared to simple LAPCAs. For instance, they (i) increase the THz efficiency due to the trap field enhancement near the multiple anodes [23], (ii) allow the possibility to apply higher bias fields [24], and (iii) limit Joule heating, since the interdigitated structure typically uses a shadow mask

that allows the illumination of less than half of the LAPCA [24,25]. On the other hand, these structures have some limitations. For example, if the gap size is too small (below 100 μm for a GaAs LAPCA), a relatively large capacitance is created in the antenna, which tends to limit the maximum radiated THz power. In this case the LAPCA works in the space-charge screening regime, which saturates the radiated field [26,27]. The application of the shadow mask also limits the maximum efficiency of the LAPCA, since at least half of the total area is shadowed. However, despite these limitations, the highest optical-to-THz conversion efficiency ($\sim 1.6\%$) is obtained with a GaAs interdigitated LAPCA [16].

Enhanced performance of the interdigitated LAPCA scheme has been proposed by using a phase mask instead of a shadow mask, thus exploiting the total aperture of the interdigitated LAPCA [25].

2.1.2 Difference frequency mixing or optical rectification in nonlinear media

Difference frequency mixing or optic rectification (OR) is a popular method for intense THz generation, which is based on the second order nonlinear process in noncentrosymmetric materials [29-32]. This method offers high THz pulse energies as well as high electric fields with broader bandwidth THz pulses compared to PCA approach [33,34]. The first attempt to generate THz radiation using OR technique was carried out by Zernike and Berman [35]. In this process, an optical pulse that is propagating through a nonlinear crystal induces a time dependent polarization change that leads to the radiation of an electromagnetic wave (as depicted schematically in Fig. 2.3) whose polarization depends on the crystal orientation and on the incident pump beam polarization [36], the temporal THz field is proportional to the second derivative of the change of this polarization with respect to time t :

$$E_{THz}(t) \propto \frac{\partial^2}{\partial t^2} P^2(t) \quad (2.2)$$

Here, E_{THz} is the electric field, $P(t)$ is the polarization induced in the crystal by the electric field associated with an intense optical pulse. Eq. (2.2) contains not only a term linear in the electric field but also higher-order terms and can be expressed as the following expansion in powers of the electric field:

$$P = \varepsilon_0(\chi^{(1)}E + \chi^{(2)}EE + \chi^{(3)}EEE + \chi^{(4)}EEEE + \dots + \chi^{(n)}E^{(n)}) \quad (2.3)$$

Here, $\chi^{(n)}$ is the n^{th} -order electric susceptibility tensor of the material. THz generation via difference frequency mixing process is related to the second order susceptibility of the material, given by:

$$P^{(2)}(\Omega) = \varepsilon_0 \chi^{(2)}(\Omega = \omega_2 - \omega_1; \omega_1, -\omega_2) E(\omega_1) E^*(\omega_2) \quad (2.4)$$

Here, Ω is the frequency difference between two frequency components of the optical pump ω_1 and ω_2 . If the frequencies ω_1 and ω_2 are contained in the electric field in Eq. (2.4), the resultant polarization will contain two important effects:

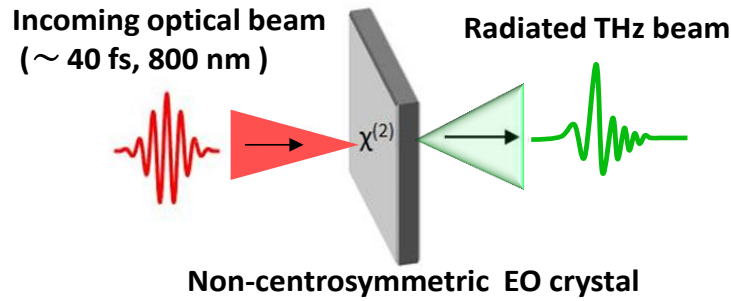


Figure 2.3| THz generation with collinear optical pump by ultrashort laser pulse in a nonlinear crystal via OR method.

(i) second-harmonic generation [37], and optical rectification [38]. The former is attributed to the sum of frequencies $\omega_1 + \omega_2$ (sum frequency generation) or (for $\omega_1 = \omega_2$, the second-harmonic generation) and the latter is due to the difference of the frequencies $\omega_1 - \omega_2$ (difference frequency generation) or (for $\omega_1 = \omega_2$, optical rectification). Several requirements should be satisfied in the material of choice for THz generation via OR process, for instance, the material should have relevant nonlinear susceptibility and it should be transparent at all the frequencies involved in order to maximize the effective interaction length and mitigate absorption limitation. Furthermore, the material should have high damage threshold owing to the use of high intensities in such a nonlinear process. Other material properties should be carefully considered, such as diffraction, saturation, and phase matching conditions. The matching between the optical group velocity and the THz phase velocity is one of the most crucial factors for an efficient OR process. THz waves are generated at different positions in the media upon passage of the optical pump beam, and maximum output is expected when all the waves add up constructively, leading to continually increasing electrical field propagation along the entire interaction depth of the medium. The phase matching condition is given by the following formula [39]:

$$k(\omega_2) - k(\omega_1) = k(\Omega) \quad (2.5)$$

Here, k is the wave vector depending on the electromagnetic frequency and their corresponding refractive indexes. Defining the coherence length as the interaction length at which the phase change reaches π [40], during which THz waves can have a positive build up thus avoiding the effects of phase mismatch

$$\delta k L_c = \pi \quad (2.6)$$

Here, $\delta k = k_{\omega_2} - k_{\omega_1} - k_{THZ}$ and L_c is the coherence length. Some relevant parameters of common nonlinear materials for OR scheme are summarized in Table 2.1 [41]. In the past, a tremendous number of materials have been exploited for generation of THz radiation from OR scheme, for instance semiconductors such as GaSe [42-56], ZnGeP₂ [47], and the zinc blende semiconductors such as GaAs [45,57,58], CdTe [59], InP [57], ZnTe [10,60,61] and GaP [47,48,62].

| Crystal | EO coefficient [pm/V] | Index of refraction | THz Index of refraction | THz Absorption coefficient (cm ⁻¹) |
|--------------------|---|--|----------------------------------|--|
| ZnTe | $r_{41} = 4.0$ (0.633 μm) | 2.85 (0.8 μm) | ~3.17 | 1.3 |
| LiNbO ₃ | $r_{33} = 30.9$ $r_{51} = 32.6$ (0.633 μm) | $n_o = 2.29$, $n_e = 2.18$ (0.633 μm) | $n_o \sim 6.8$, $n_e \sim 4.98$ | 16 |
| LiTaO ₃ | $r_{33} = r_{51} = 30.5$ (0.820 μm) | $n_o = 2.176$, $n_e = 2.180$ (0.633 μm) | $n_o \sim 6.5$, $n_e \sim 6.4$ | 46 |
| CdTe | $r_{41} = 4.5$ (1.00 μm) | 2.84 (0.8 μm) | ~3.23 | 4.8 |
| DAST | $r_{11} = 160$ (0.82 μm) | $n_o = 2.46$, $n_e = 1.70$ (0.820 μm) | ~2.4 | 150 |
| GaSe | 1.7 (0.8 μm) | 2.85 (0.8 μm) | ~3.72 | 0.07 |
| GaAs | $r_{41} = 1.43$ (1.15 μm) | 3.61 (0.886 μm) | ~3.4 | 0.5 |

Table 2.1 | Properties of common materials used for THz generation via OR [41].

Dielectrics materials such as LiNbO₃ [48,63–68], LiIO₃ [69], LiTaO₃ [70-72] and SiO₂ [35,73] have been reported as well. Moreover, organic crystal such as 4-*N,N*-dimethylamino-4-*N*-methyl-stilbazolium tosylate (DAST) has been successfully exploited for intense THz generation [74–80]. However, currently, the most often used materials for THz generation are ZnTe, GaSe,

and LiNbO₃. ZnTe is favorable as THz emitter because of its relatively high nonlinear coefficient, high-damage threshold, and excellent phase matching between the laser pulse group velocity and the THz pulse phase velocity that results in achieving the phase matching collinearly. However, ZnTe has the disadvantage of competing nonlinear processes, *e.g.* white-light generation at high pump intensities, thus limiting upscaling of the optical pump intensity. On the other hand, GaSe tolerates high optical pump intensities, but phase matching condition is met only for mid-infrared frequencies. Furthermore, ZnTe and GaSe are usually pumped in a collinear arrangement (as depicted in Fig. 2.3), while LiNbO₃ yields very high THz pulse energies in non-collinear arrangement [68] (as depicted in Fig. 2.4). LiNbO₃ crystal has the following advantages over ZnTe: higher electro-optic coefficient, the generated THz energy is orders of magnitude higher than in ZnTe generation [81], and higher pumping laser energy can be used without suffering from two photon absorption of the pump energy [61,64,82,83]. However, there is a certain condition that must be satisfied in order to achieve phase matching between the optical group velocity and THz phase velocity and thus emitting THz efficiently from LiNbO₃.

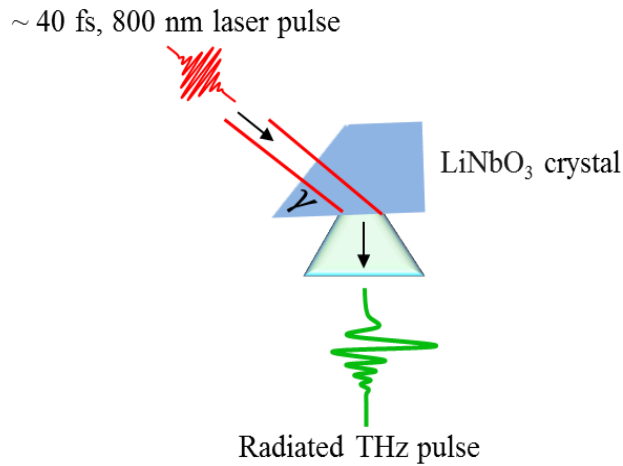


Figure 2.4 | THz generation with non-collinear optical pump by ultrashort laser pulse in LiNbO₃ crystal via optical rectification configuration.

This condition is achieved via a technique known as tilted-pulse-front (TPF) technique, in which non-collinear phase matching is satisfied and can be expressed mathematically as:

$$v_{op}^{gr} \cdot \cos\gamma = v_{THz}^{ph} \quad (2.7)$$

Here, v_{op}^{gr} is the group velocity of the optical pulse, γ is the tilt angle, and v_{THz}^{ph} is the phase velocity of the THz pulse. The pulse front of the optical pulse is titled typically using a diffraction grating, and a telescope is then used to image the titled-pulse at the crystal position with an appropriate demagnification ratio M that is determined by using d_o (object distance from the lens) and d_i (image distance from the lens) shown in Fig. 2.5 where a schematic diagram of the setup for ultrafast THz pulse generation using a titled-pulse-front arrangement, employing a single lens and an optical diffraction grating.

Moreover, the crystal is cut at γ angle to fulfill the phase matching condition inside the crystal. In this configuration, γ is given by [84]:

$$\tan \gamma = \frac{m N \lambda_{pump} M}{n_{pump} \cos \beta} \quad (2.8)$$

Here, m is the diffraction order; N is the grating groove number density, n_{pump} is the refractive index of the LiNbO₃ crystal at the pump laser wavelength and β is the diffraction angle of the incident beam on the grating.

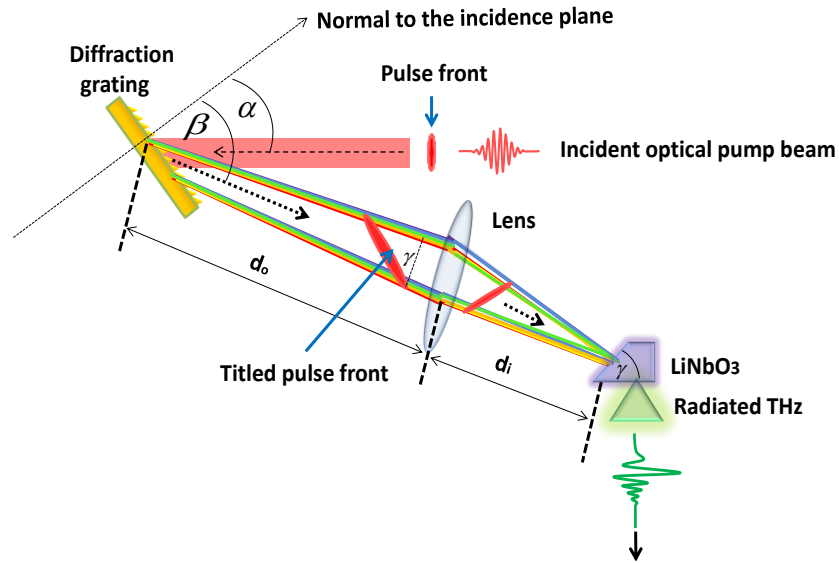


Figure 2.5| Partial schematic of experimental setup for THz generation by titled-pulse-front technique in LiNbO₃. An optical diffraction grating is used to title the pulse front. A tilt angle γ is introduced between the pulse front and the phase front.

Typical experimental setups of the LiNbO₃ THz source based on the titled-pulse-front technique use an amplified Ti:sapphire laser, which delivers several mJ, femtosecond pulses at kHz repetition rates [84]. In order to avoid the photorefractive effect in the LiNbO₃ crystal and thus, in turn, to mitigate THz radiation absorption, the crystal is commonly doped with Mg at 1-mol%

[85]. Typical tilted-pulse-front LiNbO₃ THz sources provide peak electric fields of > 200 kV/cm in the 0.1-2.5 THz spectral range, with conversion efficiencies of $\sim 10^{-3}$, which is ~ 30 times higher than large aperture ZnTe sources.

In addition to its suitability to LiNbO₃ crystal, the tilted-pulse-front technique can also be applied to other materials. For example, THz generation in room temperature gallium arsenide (GaAs) crystal using pump laser at a wavelength of 1.8 μm has been reported with the tilted-pulse-front technique [86].

2.1.3 THz waves generation in plasma

Another method for intense THz wave generation from plasma has been developed in the past years, where an intense ultrafast laser pulse with a center wavelength of 800 nm is frequency doubled by a nonlinear crystal such as Barium-Borate (BBO) (as shown in Fig. 2.6). Both the 800 nm (the fundamental) and 400 nm (the second harmonic (SH)) pulses are focused together and ionize some gas, creating a filament of plasma and intense, broadband THz radiation.

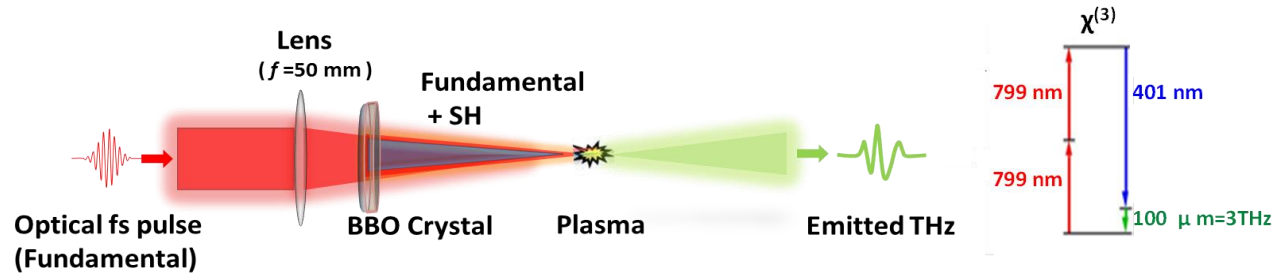


Figure 2.6 | Partial schematic of the experimental setup for THz generation in plasma. The pulse at the fundamental contains wavelengths between 770 and 830 nm, the second harmonic (SH) between 385 and 415 nm [adapted from ref. 28].

The generation mechanism could be described by four-wave optical rectification with a third-order nonlinear process [87-91] $\chi^{(3)}(\Omega_{\text{THz}}: 2\omega + \Omega_{\text{THz}}, -\omega, -\omega)$, where Ω_{THz} is the frequency of the emitted THz wave. Following the four-wave mixing theory, the THz field is proportional to:

$$E_{\text{THz}} \propto \chi^{(3)} E_{2\omega}(t) E_{\omega}^*(t) E_{\omega}^*(t) \cos(\varphi) \quad (2.9)$$

Here, φ is the relative phase difference between the fundamental and the SH frequencies [88].

Compared to PCA or OR schemes, THz radiation generated from plasma sources offers much broader bandwidth because plasmas do not have phonons and dispersion is very small [92]. For example, OR in LiNbO₃ crystals offers spectral bandwidth only up to 1.5 THz despite its intense

radiation [93] while the plasma source spectral range can reach up to 200 THz [92]. Another feature that distinguishes plasma sources for THz generation is the absence of breakdown field and therefore, it is possible to generate very high electric fields ($>1\text{MV/cm}$).

| THz generation technique | Generated THz radiation | Limitations and demerits |
|---|---|--|
| <p>Photoconduction</p> <p>Requirements:</p> <ul style="list-style-type: none"> *Photoconductive antenna. *High bias voltage. | <ul style="list-style-type: none"> *Half-cycle THz pulses with a few hundreds of kV/cm peak electric field. *Relatively narrow band width ranging from 0.1 THz to 2 THz. | <ul style="list-style-type: none"> *Laser damage threshold of the antenna. *Bias voltage breakdown of the antenna. |
| <p>Optical rectification</p> <p>Requirements:</p> <ul style="list-style-type: none"> *Noncentrosymmetric nonlinear medium with a high nonlinear coefficient. | <ul style="list-style-type: none"> *Single cycle THz pulses with peak field of several hundreds of kV/cm. *Bandwidth typically from 0.1 THz up to 6 THz maximum depending on the nonlinear crystal. | <ul style="list-style-type: none"> *Phase matching condition. *Laser damage threshold of the nonlinear medium. *Thermal effects in the crystal when pumping at high laser intensities. |
| <p>Air and metal-surface plasma generation</p> <p>Requirements:</p> <ul style="list-style-type: none"> *Tight focusing of intense short laser pulses in air or onto the metal surface. | <ul style="list-style-type: none"> *Intense broadband single- and multicycle THz pulses with high peak fields in the MV/cm range. | <ul style="list-style-type: none"> *Very sensitive to environmental fluctuations that can affect the stability of both the generated plasma and in turn the THz pulses. *Damage effects on the metal surface, which requires pumping at various positions on the metal surface and in turn high consumption of metal samples. *Difficulties in employing proper filtration to extract pure THz pulses. *Plasma fluctuations that can affect stability of the source. |

Table 2.2 | Comparison between common THz generation techniques [41]

Furthermore, the experimental setups implemented for such generation method do not require reflective surfaces and hence leads to the elimination of echoes, which in turn allows for very long temporal scan length (*i.e.* high-frequency resolution). In addition to gases, solid targets can be also used for intense THz pulse generation from high-intensity laser-plasma interaction at

relativistic intensities [94]. Table 2.2 summarizes the techniques commonly exploited for intense THz generation along with their requirements, specifications of the pulse, spectral band width, and limitations.

2.2 Intense THz pulse detection

2.2.1 Conventional techniques for coherent THz detection

Measurement of subpicosecond single-cycle electromagnetic transients with femtosecond laser pulses is acquiring widespread acceptance as a convenient method of accessing the THz frequency range. As far as the detection of THz pulses is concerned, three main schemes have been commonly used and well described in the literature: bolometers [6,95], time-gated antennas [96], and time-gated electro-optic detectors [97]. The advantage of time-gated detection over bolometric detection is the measurement of the THz pulse electric field amplitude and phase rather than average power of the THz pulse; therefore, the latter cannot provide a coherent measurement. Furthermore, the time-gated detection is superior in suppressing of the thermal background compared to bolometric detection. In principle, the THz emission mechanisms discussed in section 2.1 can be reversed and exploited for the THz pulses detection. For instance, the same PCAs structures can be reversed and used as THz detectors while the reverse mechanism for OR is electro-optical sampling (EOS). Both detection techniques are routinely used for measuring THz electric field waveform. The reversed mechanism for plasma THz generation is known as THz-air-biased-coherent detection (THz-ABCD).

2.2.1.1 PCA for THz electric field measurement

Using a PCA scheme in THz detection (schematically shown in Fig. 2.7) involves measuring the photocurrent generated by the probe beam across the electrode gap and biased by the THz electric field. In absence of THz field across the gap, photo-carriers created by the probe beam diffuse randomly and do not generate any net current. However, the presence of THz field across the gap cause the separation of the electron hole pairs and a net current is generated. The measured photocurrent $I(t)$ depends not only on the incident THz electric field but also on the transient surface conductivity $\sigma_s(t)$ [98]:

$$I(t) \propto \int_{-\infty}^t \sigma_s(t-t') E_{\text{THz}}(t') dt' \quad (2.10)$$

The time dependent conductivity implies that the current cannot flow instantaneously in response to the THz field. The photocurrent is a convolution of the THz field with the conductivity.

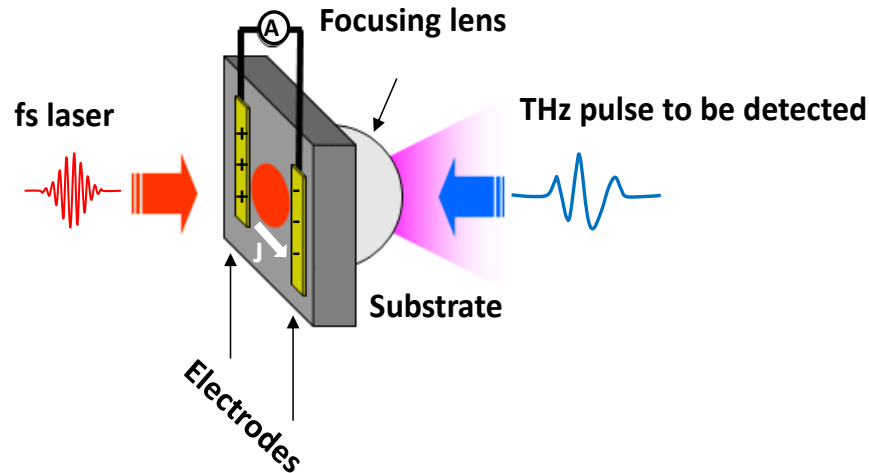


Figure 2.7| Partial schematic illustrates THz pulse detection via photoconductive antenna scheme [adapted from ref. 14].

As a consequence, the characteristics of the laser pulse and the semiconductor substrate will affect the detected THz waveform. In order to limit the effects of conductivity, materials with short carrier lifetime (such as low-temperature grown GaAs (LT-GaAs) and doped GaAs) are usually selected [99-101]. LT-GaAs has a carrier lifetime that is shorter than 0.5 ps. For increasing the maximum detected bandwidth, one should also combine a substrate with short carrier lifetime and an optical pulse with short duration. Another factor that influences the bandwidth of the detected THz pulse is the geometry of the PCA. There are four different structures of PCA that are currently used for THz electric field measurement: strip-line, bowtie, butterfly and logarithmic antennas. These PCAs each have different characteristics. For example, the butterfly PCA is very efficient for detecting low THz frequencies, while a strip-line PCA is sensitive for detecting high THz frequencies. Another factor that will greatly influence the detected signal is the dimension of the PCA. For example, a smaller gap size will allow the detection of higher frequencies and larger amplitude signals, while longer electrodes will increase the amplitude of the detected signal but will be more sensitive to low frequencies [102].

2.2.1.2 Electro-optic sampling technique

Electro-optic sampling (EOS) technique is emerging as the most popular choice for THz electric field measurement and that is primarily due to two reasons: (i) electro-optic materials are readily commercially available, unlike time-gated antennas, which typically require the usage of microfabrication techniques to make them. (ii) electro-optic detection is suitable for signals with a large bandwidth, much larger than the bandwidth offered by the PCA scheme [103]. In the

EOS technique, an applied electric field induces a refractive-index change in an electro-optic (EO) material at visible and near-IR frequencies that is proportional to the applied field. The technique is based on the linear Pockels effect in an EO crystal together with a femtosecond optical gating pulse, to probe the electric field of the THz pulse [98].

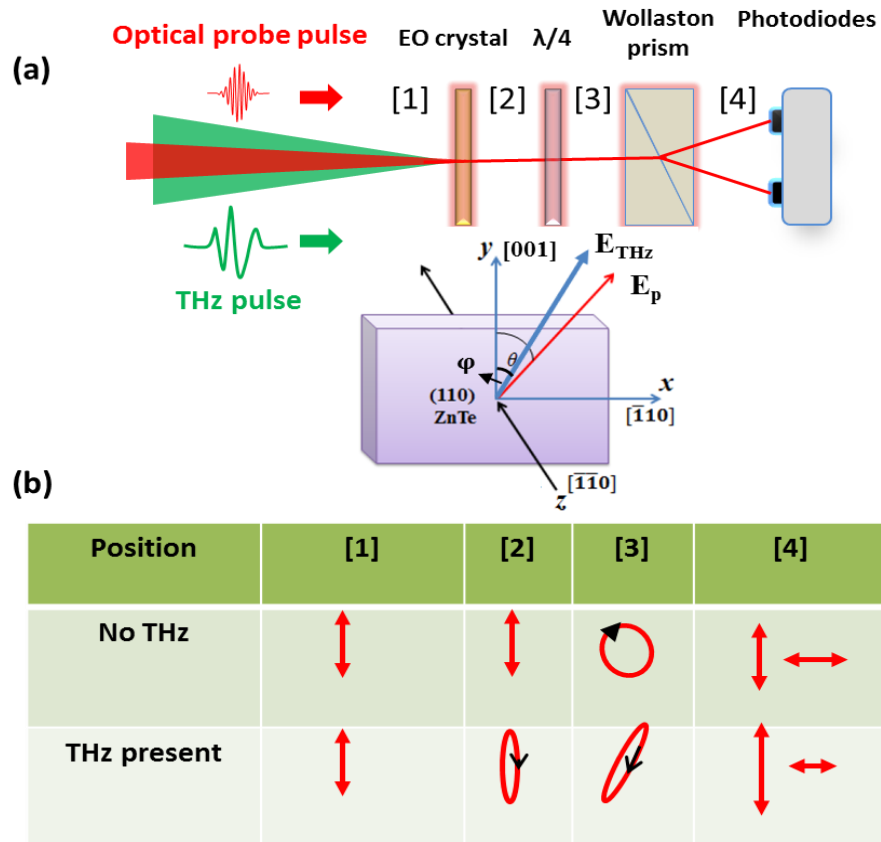


Figure 2.8| THz detection using EOS technique with balanced detection (a). The evolution of optical probe beam polarization components without and with THz presence (b) [adapted from ref. 41].

The refractive-index change in the EO crystal affects the ellipticity of a circularly polarized, synchronized, ultrashort laser pulse that is co-propagating with the THz pulse through the same material. This change in ellipticity is measured with a polarizing beam splitter that separates the two orthogonal polarization components of the optical probe beam. Due to the Pockels effect, the induced birefringence in the nonlinear EO crystal is directly proportional to the THz electric field strength. A balanced photodetector measures the intensity difference between the two components and gives a signal that is directly proportional to the THz electric field. By varying

the delay between the THz pulse and the probe-laser pulse, one obtains the complete time-dependent electric field.

A typical schematic diagram of the balanced measurement using this EOS technique is shown in Fig. 2.8(a) while Fig. 2.8(b) illustrates the evolution of the optical probe beam polarization components without and with THz presence. Without the presence of THz pulse, a linearly polarized (position 1) optical probe pulse traverses the EO crystal without experiencing birefringence (position 2), which then passes through a quarter-wave plate and becomes circularly polarized (position 3). A polarization-state analyzer, such as a Wollaston prism, is then used to separate the orthogonal polarization components (position 4), and each is sent to one of the photodiodes of a balanced detector. The detector connected to a lock-in amplifier, measures the difference signal $I_y - I_x$ from the two photodiodes, giving zero reading without the THz pulse. On the other hand, when the optical probe pulse and the THz pulse co-propagate through the EO crystal in time, the THz field induced birefringence that rotates the polarization of the probe pulse, making it elliptical (position 3), thus introducing a signal imbalance between I_y and I_x (position 4). This difference between the two signals can directly give the electric field amplitude information of the THz pulse [98] by using the following equations:

$$I_s = I_y - I_x = I_0 \Delta\phi \propto E_{THz} \quad (2.11)$$

Here,

$$I_x = \frac{I_0}{2} (1 - \sin\Delta\phi) \approx \frac{I_0}{2} (1 - \Delta\phi) \quad (2.12)$$

$$I_y = \frac{I_0}{2} (1 + \sin\Delta\phi) \approx \frac{I_0}{2} (1 + \Delta\phi) \quad (2.13)$$

I_0 is the total intensity of the optical probe beam and $\Delta\phi$ is the phase retardation between the two polarization components. In Eq. (2.12) and Eq. (2.13), an approximation of $\Delta\phi \ll 1$ is used, and thus a linear relationship between the THz electric field and the signal is seen in Eq. (2.11). Therefore, the dynamic range (DR) of the EOS technique is limited. For the detection of intense THz radiation, to assure linearity of the measurement, several high-resistivity float-zone silicon plates are often used to reduce the THz field to an appropriate value. However, dispersion and wavelength-dependant absorption of such plates would modify the THz waveform, thus complicating the correct measurement of intense THz waves using conventional EOS technique [104]. The entire THz waveform can be mapped in time by employing an optical delay stage to scan the time delay between the femtosecond probe pulse and the THz pulse. The quasi-DC THz

electric field approximation used above is reasonable for femtosecond optical probe pulses. However, for an ultra-short THz pulse with broad spectrum, temporal walk-off due to velocity mismatch between the probe pulse and the THz pulse should be considered carefully. THz detection sensitivity will increase as the EO crystal thickness increases, but the corresponding detection bandwidth will decrease because of this walk-off. For this reason, the thickness of the EO crystal should be chosen properly. Thinner crystals are used for broadband detection, such that velocity matching can be fulfilled. In addition, phonon absorption is also a crucial factor that limits the detection bandwidth. For example, phonon absorption at 1.6 and 3.7 THz and the transverse optical phonon at 5.31 THz in commonly used ZnTe crystal limit its use to low THz frequency detection. Alternatively, other EO crystals such as GaP and GaSe are generally better choices for broadband detections when using EOS technique for THz electric field measurement.

2.2.1.3 THz-air-biased coherent detection (THz-ABCD)

In this detection technique, the underlying mechanism can be described by a four-wave mixing model with the generation of a second harmonic field, which depends on the THz pulse shape [105,106]. The interaction of the fundamental laser field ω and the THz pulse can be described by the following equation:

$$E_{2\omega} \propto \chi_{air}^{(3)} E_{\omega} E_{\omega} E_{THz} \quad (2.14)$$

Here, $\chi_{air}^{(3)}$, $E_{2\omega}$, E_{ω} and E_{THz} are the third-order susceptibility of air, the electric field amplitude of the second harmonic 2ω , the electric field amplitude of the fundamental ω and electric field amplitude of the THz waves, respectively. From this equation, one can see that the second harmonic electric field is proportional to the THz electric field. However, in practice, we measure the intensity or power of the second harmonic, but not its electric field. From Eq. (2.14), we see that the intensity of the second harmonic $I_{2\omega}$ is proportional to the intensity of the THz wave I_{THz} . The consequence is that the measured signal would be proportional to the square of the THz field, and thus phase information cannot be extracted, resulting in an incoherent measurement. To realize coherent measurements, a local oscillator at the 2ω frequency $E_{2\omega}^{LO}$ is generated to interfere with the second harmonic induced by the THz field, as expressed by the following equation:

$$I_{2\omega} \propto |E_{2\omega}|^2 = (E_{2\omega}^{THz} + E_{2\omega}^{LO})^2 = E_{2\omega}^{THz^2} + 2E_{2\omega}^{THz} E_{2\omega}^{LO} + E_{2\omega}^{LO^2} \quad (2.15)$$

Here, $E_{2\omega}^{LO}$ is the second harmonic local oscillator, which is provided by the second-harmonic component of the white light in the laser-induced air plasma. The second cross term in this equation is the key term for coherent THz detection. The local oscillator $E_{2\omega}^{LO}$ depends on the probe beam intensity. In the case of low probe energy, the first term of this equation is dominant, leading to $I_{2\omega} \propto I_{THz}$, which results in incoherent detection. With probe intensity higher than the air ionization threshold, the local oscillator becomes sufficiently strong and the second term of Eq. (2.15) becomes dominant, and thus $I_{2\omega} \propto E_{THz}^2$, which leads to coherent detection. As the probe intensity has to be high enough to break down the air for coherent detection, this technique was first named THz air breakdown coherent detection (ABCD) [105].

Figure 2.9 shows a schematic illustration of the experimental set up of a refined version of this technique where an AC bias voltage was applied at the focus point of the collinear THz and optical beams [106].

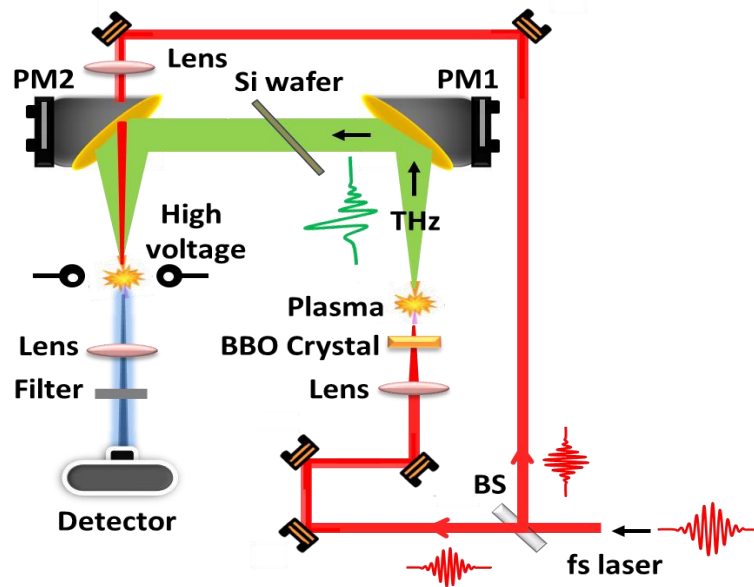


Figure 2.9| Schematic illustration of typical experimental setup for THz detection via THz-air-biased coherent detection (ABCD) technique. BS: beam splitter, PM1 and PM2: parabolic off-axis mirror. The optical pump beams are blocked by a Si filter. The THz and probe pulses are focused together in a gas which is biased by a high voltage. The resulting second harmonic (400 nm) light is detected by a photo-multiplier tube [adapted from ref. 36]

The new version of the technique is termed as air-biased coherent detection (which is also ABCD in short). The AC bias voltage is synchronized with the laser repetition rate. The bias voltage breaks the symmetry, providing an additional source of second harmonic, which could be

used as the local oscillator $E_{2\omega}^{\text{LO}}$. The THz field induced second harmonic $E_{2\omega}^{\text{THz}}$ and the AC bias second harmonic $E_{2\omega}^{\text{LO}}$ can be written as:

$$E_{2\omega}^{\text{THz}} \propto \chi_{\text{air}}^{(3)} I_{\omega} E_{\text{THz}} \quad (2.16)$$

$$E_{2\omega}^{\text{LO}} \propto \chi_{\text{air}}^{(3)} I_{\omega} E_{\text{bias}} \quad (2.17)$$

Here, E_{bias} is the bias electric field. Then Eq. (2.15) becomes

$$I_{2\omega} \propto \left(\chi_{\text{air}}^{(3)} I_{\omega} \right)^2 \left(E_{\text{THz}}^2 + 2E_{\text{THz}}E_{\text{bias}} + E_{\text{bias}}^2 \right) \quad (2.18)$$

In practice, the first and third terms of Eq. (2.18) can be eliminated when the AC bias voltage is synchronized with the lock-in amplifier. And the signal is demodulated at a singular frequency corresponding to the sum or difference of the modulation rates of the THz pulse and LO bias. Only the cross term is measured, thus resulting in $I_{2\omega} \propto E_{\text{THz}}E_{\text{bias}}$ and allowing coherent measurements. This method has the great advantage to reduce the probe power needed to generate the second harmonic and detect the THz pulse. Furthermore, the SNR has been improved [106] compared to the method without AC biasing [105], the DR is larger and once more the THz bandwidth is only limited by the optical pulse duration [107].

2.3 Conventional THz detection techniques in measuring intense THz electric field: challenges and limitations

Advances in tabletop, intense, few-cycle broadband THz sources have pushed the achievable peak THz electric fields from the sub-MV/cm level to well into the several MV/cm regimes [108-110,68]. Such intense THz fields are of great interest, since they enable studies of fascinating nonlinear phenomena in materials within the THz frequency range, at picosecond and even sub-picosecond timescales and thus paving the way for their future technological applications. High-intensity THz sources and their detection methods are the main tools that are driving such technology to boom. Coherent detection of such intense THz electric fields is currently performed by various methods [111,112], as described in section 2.2. However, these conventional techniques for THz detection have several challenges when they are exploited in intense THz electric field measurement. For example, with the EOS technique, if the THz electric field is intense enough, a phase difference of more than $\pi/2$ will be introduced to the optical probe beam, which leads to reversal in the intensity modulation of the probe pulse. This, in turn, will lead to ambiguities in the measured THz field, hence posing a limitation in detecting

intense THz electric fields using conventional EOS technique [113]. This limitation is known as over-rotation. As mentioned earlier, the over-rotation poses some restrictions in THz electric field measurement via the EOS technique. For instance usage of a thicker detection crystal (which is required for enhancing both the spectral resolution and the signal-to-noise ratio (SNR) of the THz measurement) is limited because of the increased chance for over-rotation, since the birefringence introduced in the detection crystal is proportional to both the THz electric field and the thickness of the EO detection crystal.

The increased availability of robust high-intensity THz sources and the urgent need to characterize their peak electric fields and waveforms has become a challenge for conventional EOS techniques. This is because high power THz measurements require high DR detection techniques, where DR is defined as the ratio of the maximum measurable signal to the standard deviation of the noise signal. The current conventional EOS technique suffers from the limited achievable DR once again because of over-rotation limitation in measuring intense THz electric field. On the other hand, PCA detectors are not commonly used for detecting intense THz pulses, despite their quality. One reason for this is that the PCA detector is very sensitive to the ambient electromagnetic noise, which could be relatively high when using high-energy amplified laser systems. However, the major disadvantage of using PCA for the detection of intense THz pulse is the possible presence of nonlinear effects in the semiconductor substrate induced by the intense THz field, thus leading to incorrect interpretation of the detected THz signal. The THz-ABCD technique does not have the problem of over-rotation, but the need for a high voltage supply makes it more complicated to use when compared with the EOS techniques. Therefore, a simple technique is yet desirable to satisfy the requirement for measuring intense THz electric fields.

2.4 Advanced technique for coherent THz detection based on spectral-domain interferometry (SDI) technique

In this section, we will discuss a new novel coherent THz detection method that is especially well adapted to intense THz sources. This new method is based on spectral-domain interferometry (SDI) technique.

2.4.1 Concept of spectral-domain interferometry (SDI) technique

The general idea of spectral-domain interferometry (SDI) technique can be explained with the help of spectral-domain low-coherence interferometry technique (which is based on a Michelson interferometer [114]) as depicted in Fig. 2.10. Here a broadband laser source is divided into two arms in a Michelson interferometer scheme. One arm illuminates the reference and the other illuminates the sample. The sample comprises two surfaces: top (T) and lower (L). The two beams from the reference and sample are reflected back and recombine on the same beam splitter, and then they travel to a diffraction grating where the diffracted spectral components of the beam are focused by a lens and the interference pattern between the various spectral components of the beams is detected using a CCD camera [114]. The phase difference between signals reflected from the reference and the top sample's surface (T) is given by [115,116]

$$\phi_T(k) = \phi_o + 2kx_1 \quad (2.19)$$

While the phase difference between signals reflected from the reference and lower sample's surface (L) is given by:

$$\phi_L(k) = \phi_o + 2kx_2 \quad (2.20)$$

Here, ϕ_o is the phase change due to reflection, $k (= \frac{2\pi}{\lambda})$ is the wave number and x_1, x_2 are the optical path difference (OPD) of signals from the top and lower sample's surface with respect to the reference, respectively. The rate of change of the phase with respect to the wavenumber (f_{k1}) along k -axis for the top sample's surface (T) pulse can be expressed as:

$$f_{k1} = \left(\frac{1}{2\pi}\right) \times \frac{\partial \phi_T(k)}{\partial k} = \frac{x_1}{\pi} \quad (2.21)$$

For the pulse from the lower sample's surface (L), the rate of change of the phase with respect to the wavenumber (f_{k2}) can be written as

$$f_{k2} = \left(\frac{1}{2\pi}\right) \times \frac{\partial \phi_L(k)}{\partial k} = \frac{x_2}{\pi} \quad (2.22)$$

Analysis is carried out in k -space rather than λ -space owing to the fact that the frequency will be independent of k . The frequency spectrum will broaden as sampling of the interferogram intensity data is carried out uniformly in the k -axis [115,116]. The intensity distribution along k -axis on the CCD camera as a result of interference between the two pulses from the two surfaces of the sample and reference surface is given by:

$$I(k) = I_o(k) + 2\sqrt{I_r(k)I_T(k)} \cos(\phi_T(k)) + 2\sqrt{I_r(k)I_L(k)} \cos(\phi_L(k)) \quad (2.23)$$

Here I_o is the dc term, I_r , I_T , I_L are the intensities of signals from reference surface, top (T), and lower (L) surfaces of the sample, respectively. Due to the cosine term and phase difference dependency on k , a modulation in the spectrum intensity is introduced along k -axis. Eq. (2.23) is an illustration of the modulation of the two frequencies x_1/π and x_2/π , which are directly proportional to x_1 and x_2 , respectively.

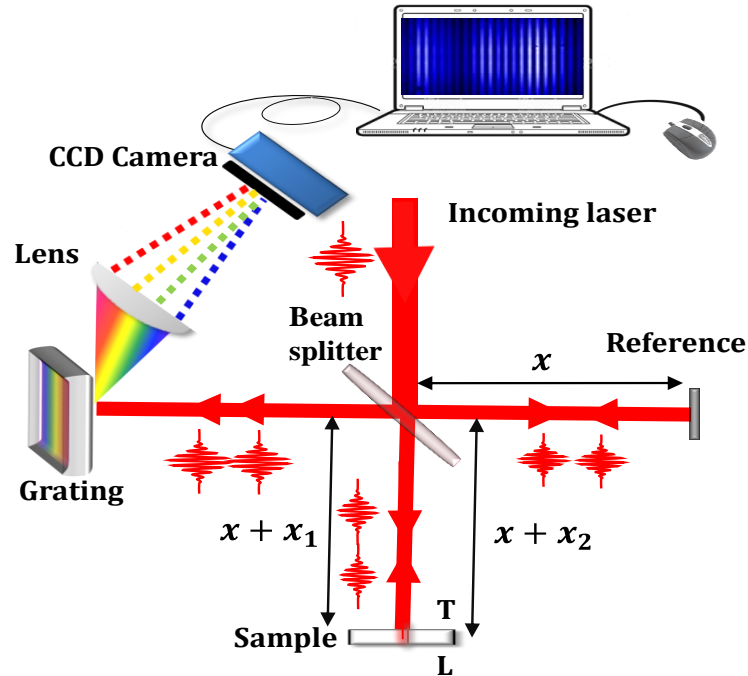


Figure 2.10| Schematic illustration for the experimental realization of the concept of spectral-domain interferometry (SDI) based on Michelson interferometer scheme.

The Fourier transform of the intensity pattern on the camera after conversion from pixel to k -space directly leads to the frequency of the modulation in Eq. (2.21) and Eq. (2.22), and consequently the position of the reflecting layer within the sample with respect to the reference surface [116,117].

The SDI technique is proven to be a robust tool to measure phase changes in the micro-radian range in various applications[114-118]. For instance, the field most impacted by SDI is the spectral-domain low-coherence interferometry (SD-LCI) technique, which is developed as a biomedical diagnostic tool for early stage Glaucoma disease [119, 120].

2.4.2 Pursuing SDI technique for THz electric field measurement

The SDI technique in THz electric field measurement is a novel emerging technique that has been recently demonstrated [113,121,122]. The new SDI technique for THz detection has proven to overcome the challenges associated with the coherent detection of intense THz radiation, such as over-rotation and its consequent limitations that are commonly observed in EOS detection techniques. One of the consequences of over-rotation limitation is the limited DR of the THz measurement. The SDI technique has been demonstrated in enhancing the DR to $\sim 7 \times 10^6$, thus offering an excellent tool for spectroscopic measurement that will result in obtaining accurate experimental results. Furthermore, the new technique also eliminates usage of lock-in amplifier from the experimental set-up. This in turns results in reducing the cost of the THz set-up.

Accelerated improvement efforts in this THz detection technique have resulted in developing different versions: Michelson-type interferometer SDI, Mach-Zehnder interferometer SDI, and Cross-polarized SDI (The experimental setups for different SDI versions used for THz electric field measurement will be discussed later in chapter 3 and 4). Each of these versions uses specific interferometer; but shares the same concept. The concept is based on creation of two optical probe beam signals via the interferometer (in the case of Michelson-type interferometer and Mach-Zehnder interferometer SDI, those two signals are labeled as sample and reference signals). The sample signal experiences the THz birefringence effect on the EO detection crystal, while the reference signal does not. The signals from the reference and sample are then recombined and sent to a spectrometer where they are spectrally dispersed onto a CCD camera using a diffraction grating. At the CCD camera plane, this interference signal can be written as:

$$I(k) = I_r(k) + I_s(k) + 2\sqrt{I_r(k)I_s(k)}\cos[\varphi_o + kL] \quad (2.24)$$

Here, $k = 2\pi/\lambda$ is the wave number, φ_o is the phase constant, L is the optical path difference (OPD) between the reference signal and the sample signal, and I_r and I_s are the intensities of the reference and sample signals, respectively. Interference after the diffraction grating is recorded using a CCD camera and rescaled from wavelength space to wavenumber (k) space, and then Fourier transformed to obtain the corresponding FFT spectrum. The instantaneous phase difference between the two signals is calculated using the relation [115]:

$$\varphi(L) = \tan^{-1}\left[\frac{\hat{H}(I(L))}{I(L)}\right] \quad (2.25)$$

Here, $\tilde{H}(I(L))$ and $I(L)$ are the Hilbert transform and the interference signal intensity of Eq. (2.24) at an OPD of L . The change in the OPD over time can be traced by monitoring the phase change in Eq. (2.25). This phase difference is proportional to the THz electric field. Thus, as with other conventional techniques, the THz waveform is measured in the SDI technique by varying the delay time between the THz pulse and the optical pulse using an optical delay line.

2.5 Applications of THz radiation

2.5.1 THz spectroscopy

Owing to the unique characteristics inherent in THz radiation and the abundant THz spectral fingerprints unlike from the corresponding infrared signature, THz spectroscopy has been realized as a powerful tool for sensing and material characterization. The two widely exploited techniques in THz spectroscopy are: (i) THz time-domain spectroscopy (THz-TDS) with coherent pulsed THz radiation and (ii) THz frequency-domain spectroscopy with narrow tunable continuous-wave (CW) THz radiation (CW-THz spectroscopy).

2.5.1.1 Terahertz time-domain spectroscopy (THz-TDS)

THz-TDS is now a well-established method of materials science and it covers a broad frequency range extending from tens of GHz up to few THz thus bridging a large gap between microwave and conventional infrared spectroscopies. Moreover, as a phase-sensitive method, THz-TDS has the advantages of extracting both amplitude and phase information coherently, which in turn can be used to extract the real and imaginary parts of the index of refraction (or equivalently, the complex conductivity or dielectric function) without the use of Kramers-Kronig relations. The particular attraction of THz-TDS is the energy range that is probed (0.41 - 12.3 meV), which contains spectroscopic signatures for many material systems [123]. In liquid systems, torsional or damped rotational excitations of large molecules are in the THz range [124]. The analysis of either the traditional Fourier transformed [125] or the raw time-domain [126] THz transmission data can be used to identify various gaseous species. Rotational excitations of smaller molecules are often in the 2 meV range, and thus may be probed by a THz pulse [127]. In a simple dielectric, the index of refraction and absorption can be evaluated easily and unambiguously [128]. In condensed matter systems, quasiparticle scattering rates in doped semiconductors are in the THz range, and so THz pulses have been used to characterize both the overall conductivity of the wafer [129,130] and the spatially resolved variations in carrier density

and mobility [131]. Furthermore, superconducting energy gaps [132], and intersubband energy spacing in quantum wells [133] are all in the THz range. This makes the THz region an extremely important yet relatively unexplored part of the spectrum for new and old material systems.

Fresnel equations are the basic equations describing reflection and transmission of an electromagnetic field at an interface (Fig. 2.11).

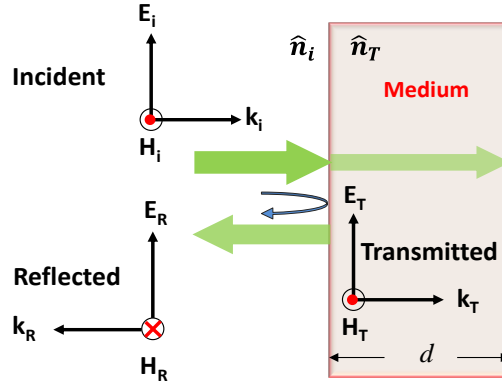


Figure 2.11 | Schematic illustration for electric and magnetic field vectors after reflection and transmission of an incident electromagnetic wave incident on a semi-infinite (thickness $\gg \lambda$) non-conducting (no free carriers) surface.

Those equations establish the foundation for THz-TDS and can be derived knowing the requirement that the boundary conditions for the tangential components of the electric (\vec{E}) and magnetic (\vec{H}) fields and the normal components of the electric displacement (\vec{D}) and magnetic flux (\vec{B}), be continuous across the interface of a medium to determine the reflection and transmission of radiation. One can correlate between the amplitudes of the incident (E_i , H_i), transmitted (E_T , H_T) and reflected (E_R , H_R) fields by the following equations

$$E_T = E_i + E_R \quad (2.26)$$

$$H_T = H_i - H_R \quad (2.27)$$

From the relations $H = B/\mu = B/\mu_0$, $|\vec{E}| = v|\vec{B}|$ and $v = c/n$ where n is the index of refraction one can write

$$E_T n_T = E_i n_i - E_R n_R \quad (2.28)$$

which when combined with Eq.(2.26) gives the amplitude reflection (\tilde{R}) and transmission (\tilde{T}) coefficients at normal incidence, that in general are complex valued.

$$\tilde{R} = \frac{\tilde{n}_i - \tilde{n}_T}{\tilde{n}_i + \tilde{n}_T} \quad (2.29)$$

$$\tilde{T} = \frac{2\tilde{n}_i}{\tilde{n}_i + \tilde{n}_T} \quad (2.30)$$

These equations completely describe the change in amplitude and phase of electromagnetic radiation as it traverses an interface of a bulk material. Once it traverses the interface and is in the material, its vacuum wave vector $\mathbf{K} = \frac{\omega}{c} \hat{z}$ must be replaced by the complex wave vector $\vec{q} = \frac{\omega}{c\tilde{n}} \hat{z}$.

In the case when a distance (d) is travelled in the medium, another additional transmission factor can be defined as:

$$P = e^{i\frac{\omega\tilde{n}d}{c}} = e^{i\frac{\omega}{c}[n+ik]d} = e^{i\frac{\omega nd}{c}} e^{-\frac{\omega kd}{c}} \quad (2.31)$$

which results in both a phase shift term proportional to the real index of refraction (n) and an attenuation term proportional to the extinction coefficient (k), the imaginary component of the complex index of refraction ($\tilde{n} = n + ik$).

Figure 2.12 depicts a typical THz-TDS experimental set up required to measure the temporal profile of the electric field of THz pulse transmitted through the investigated sample [134].

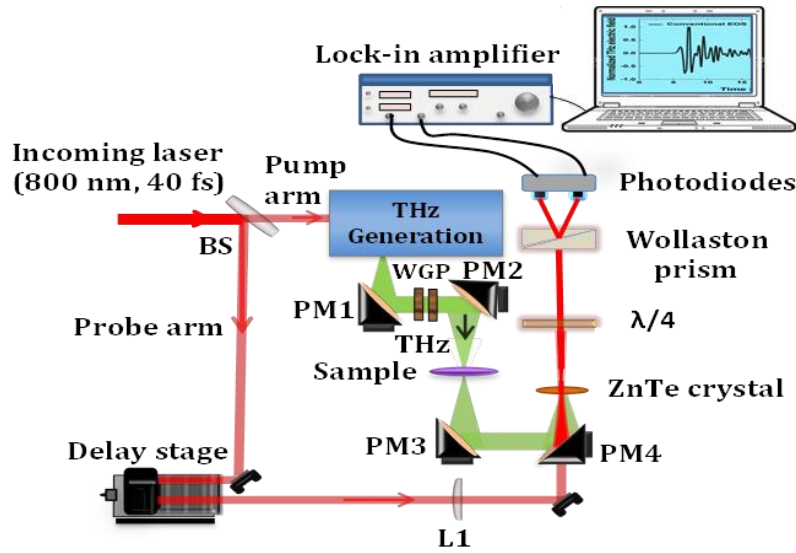


Figure 2.12 | Schematic illustration for the experimental set up commonly used in THz-TDS. The sample mounted on focus position. BS: beam splitter, PM1-PM4: off axis parabolic mirror, WGP: wire grid polarizer. The measurement of the THz waveforms is achieved via EOS technique.

Utilizing conventional EOS THz detection technique, the temporal waveforms of the THz pulses are measured: (i) a reference THz waveform $E_R(t)$ without mounting the sample on the THz radiation path, and (ii) a sample THz waveform $E_S(t)$ transmitted through the investigated sample when mounted onto the sample holder filling the whole aperture.

Fast Fourier transform is carried on both signals and the Fourier components are deduced. Then we could define the sample complex transmission function, $T(\omega)$ as:

$$T(\omega) = \frac{E_S(\omega)}{E_R(\omega)} \quad (2.32)$$

The complex refractive index can be written in terms of refractive index n , and the extinction coefficient k

$$\hat{n} = n + ik \quad (2.33)$$

Then the complex transmission function $T(\omega)$ can be rewritten as:

$$T(\omega) = \frac{4\hat{n}}{(\hat{n}+1)^2} \exp\left[\frac{i\omega(\hat{n}-1)d}{c}\right] \sum_{x=0}^m \left[\left(\frac{\hat{n}-1}{\hat{n}+1}\right) \exp\left[\frac{i\omega\hat{n}d}{c}\right]\right]^{2x} \quad (2.34)$$

Here d is the sample thickness, c is the speed of light and m is the number of internal reflections (Fabry-Pérot (FP)) in the sample. If these reflections are experimentally resolved (for thick samples) they form separate pulses in the measured signal so that the value of the coefficient m can be easily determined; for thin samples, the FP reflections overlap in time and the geometrical series should be summed up to the infinity. By splitting Eq. (2.34) into magnitude $|T(\omega)|$ and phase $\Phi(\omega)$ components, a coupled set of nonlinear equations is obtained

$$|T(\omega)| = \frac{2\sqrt{n^2+k^2}}{(n+1)^2+k^2} \exp\left(\frac{-\omega kd}{c}\right) \quad (2.35)$$

And

$$\Phi(\omega) = \omega(n-1)\frac{d}{c} + \arctan\left(-k\frac{n^2+k^2-1}{n(n+1)^2+k^2(n+1)}\right) \quad (2.36)$$

In order to obtain n and k , the two Eqs. (2.35) and (2.36) should be solved numerically. From the values of n and k , then the real and imaginary parts of the permittivity can be written as:

$$\epsilon' = n^2 - k^2 \quad (2.37)$$

$$\epsilon'' = 2nk \quad (2.38)$$

2.5.1.2 Terahertz frequency -domain spectroscopy (THz-FDS)

Another method that has been exploited in THz spectroscopic characterization is the THz-FDS technique in which, a continuous-wave THz radiation is generated, for example via photo-mixing of the combined output of two single-frequency diode lasers in a PCA. The wavelength of one (or both) of the lasers is tuned to vary the THz output frequency. Coherent detection of the output THz beam from the PCA can be achieved at room temperature by mixing the same optical radiation from the diode lasers in a detector PCA [135-137].

Well-known the THz-TDS technique uses optical pulses from a mode-locked laser to generate THz pulses through a demodulation process in a PCA [100,132,138,139]. The THz pulse is then passed through the sample of interest before being focused on a second PCA for detection that is driven by a delayed optical pulse from the same mode-locked laser. The photocurrent measured as a function of delay time to obtain the THz autocorrelation function. Normalization and Fourier transformation then yields the frequency-dependent transmission through the sample of interest. The spectral resolution is determined primarily by the travel of the delay line, which is very difficult to increase much past 1 cm, rendering a typical resolution of ~30 GHz. In other words, the THz-TDS has the merit of providing a broad spectral coverage but suffer from poor spectral resolution owing to mechanical time-delay scanning. In contrast, the THz-FDS technique can provide high spectral resolution, however, the accessible spectral range is usually narrower than that accessible by THz-TDS.

The THz-FDS technique offers greater sensitivity and faster data acquisition, moreover, it preserves phase information. Here we note some of the merits of the THz-FDS technique compared to the THz-TDS technique as follows: i) no moving parts (i.e. no mechanical scanning delay line), ii) higher frequency resolution, and iii) the ability to selectively scan specific frequency regions of interest with adjustable resolution. Despite their merits, it has been difficult to realize practical FD spectrometers and that is due to the challenges associated with the construction and control of the dual lasers, namely mode-matching and collimation of the two laser beams [140] and precise control of their difference frequency. However, recently, THz frequency combs have been demonstrated [141] to reveal their potential in improving the THz-FDS [142,143]. A THz comb, which is a description of pulsed THz radiation in the frequency domain, is composed of a series of continuous wave (CW)-THz waves regularly separated by the mode-locked frequency of the pulsed THz radiation.

2.5.2 Applications of intense field THz pulses

Intense-field THz sources have attracted numerous interests from researchers in various fields, with the driving force being the exploration of potential applications of such intense THz fields in areas including biomedicine [144], condensed matter physics [145,146], imaging and security [147] and communication [148]. For example, the recent surge in the availability of intense THz radiation sources is allowing new solutions to long-standing challenges, as well as opening up new avenues in both science and technology. For instance, intense THz sources have the potential to enable THz-TDS of aqueous samples, such as those related to biology and medicine [149,150], with high SNR [151]. Due to the high absorption of THz radiation by water, such experiments have been difficult to perform up to now. However, the availability of THz sources with high flux is opening the possibility to perform THz-TDS of aqueous and other highly absorptive media *in transmission configuration*. Humidity also has significant influence in THz applications such as large-scale object imaging and remote sensing for security purposes [152,153], and wireless communications [148,154], in which the THz pulse may need to propagate long distances through the atmosphere.

Intense THz fields are also enabling the observation of fascinating new physical phenomena such as collective vibrational excitations and the plasma frequency of a dilute free electron gas in doped semiconductors [155]. Furthermore, such intense THz sources offer high spectral brightness with broadband spectral range, which in turn are crucial for THz-TDS systems with enhanced SNR. Such systems are required as a characterization method of novel materials for future THz electronics (such as graphene [156-158] and topological insulators [159,160]) and also required for THz-based technological applications such as spatially resolved chemical recognition [161].

Moreover, at the fundamental level, the nonlinear behavior of semiconductors under intense THz field excitation has been investigated using THz sources based on gas lasers [162] and free electron lasers (FELs) [163,164]. However, owing to the long pulse duration and challenges in synchronizing a femtosecond laser to an FEL-based intense THz source, the temporal resolution of the experiment was limited. Meanwhile, the OR-based sources offer sub-picosecond single or few-cycle pulses with extremely intense THz field strengths and broad bandwidth. Moreover, the synchronization of the pump and probe pulses that resulted from their derivation from the same femtosecond laser source, permits for time resolved experiments where

the influence of the intense THz field on a sample can be observed directly with tens of femtosecond resolution.

The intense THz domain has evolved rapidly during the last decade, with many new and exciting experimental findings surfacing recently. In this section, two of those applications namely nonlinear THz spectroscopy of condensed matter and Ponderomotive effect will be briefly discussed.

2.5.2.1 Nonlinear THz spectroscopy of condensed matter

Numerous studies on the interaction of THz radiation with semiconductors have been carried out revealing effects such as free-carrier absorption, the photon drag effect and inter-band transitions [163]. However, and especially with the development of intense THz sources, a number of studies have been reported on the nonlinear THz characteristics of semiconductors using intense fields [163,165,166]. For instance, the observation of ponderomotive effects has been possible by using light source with significantly longer wavelength than the band gap of the semiconductor. The tunneling ionization of shallow impurities is one manifestation of the large ponderomotive potential of THz pulses where the energy levels of deep centers are tilted by the external electric field of the THz radiation and consequently tunneling ionization takes place [167]. Furthermore, another manifestation of ponderomotive potential in semiconductor is the Franz-Keldysh effect where direct acceleration of free carriers by the THz field can be observed in n-type semiconductors with high mobility. In these materials mobile free carriers establish an electron gas with maximum absorption in the THz frequency range [168] at room temperature. Further, ballistic acceleration of electrons in doped semiconductor can take place where the electron velocity exceeds the DC drift velocity at equilibrium [169]. A nonlinear effect such as strong absorption bleaching has been reported in GaAs [81], InGaAs [170], Ge, Si [171] as well as in photoexcited GaAs [172]. Moreover, the enhanced THz transmission in bulk samples furnishes the application ground for those materials to be exploited as saturable THz absorbers at room temperature [173].

2.5.2.1.1 Optical-pump/intense THz-probe and THz-pump/THz-probe experiments

In optical-pump/THz-probe (OPTP) experiments, the material sample is first pumped with laser pulses in the visible to the near-infrared range, and then its photoinduced dynamics is

probed by THz pulses. In semiconductors, photoexcitation of electrons from the valence band into unoccupied states in the conduction band takes place linearly only when the exciting photon-energy exceeds the bandgap energy. On the other hand, the photoexcitation of carriers in zero-bandgap graphene from the valence band to the conduction band requires the photon energy of the pump beam to exceed twice the Fermi-level energy of the graphene sample; otherwise, the interband transition will be blocked (Pauli blocking effect) [174-176].

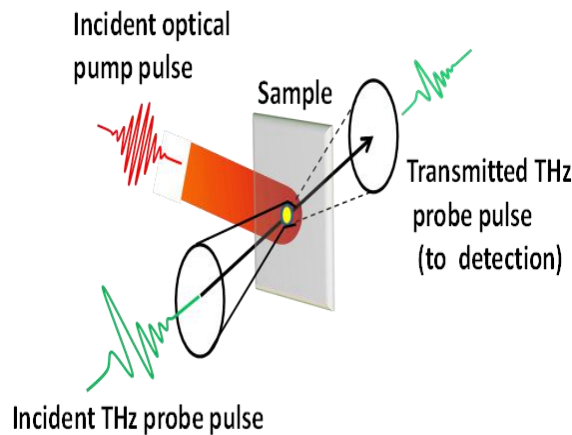


Figure 2.13| Partial schematic of OPITP spectroscopy with a non-collinear configuration. The sample is placed at the focus of intense THz beam that probes the photo-induced effects by the optical pump beam.

After photoexcitation of the material sample in OPTP experiments, the THz probe field then reveals the transport dynamics of the free carriers (holes in the valence band and electrons in the conduction band), through transmission and/or reflection measurements. In OPTP experiments, the THz probe beam is sufficiently weak so that the THz interaction is in the *linear* regime. However, by using optical-pump/*intense*-THz-probe (OPITP) spectroscopy, new and interesting phenomena begin to evolve, such as the *nonlinear* THz-induced carrier dynamics of various materials such as bulk GaAs semiconductor [177,178] and two-dimensional graphene[157].

THz-pump/THz-probe (TPTP) spectroscopy [164] using an intense THz pump beam, is an efficient but quite challenging technique for exploring the nonlinear THz properties of materials. The TPTP technique is commonly used in studying impact ionization and intervalley scattering in doped semiconductors [179].

The choice of a technique from the two mentioned techniques for a certain study depends on the nature of the dynamics to be explored. For instance, OPTP spectroscopy is suitable for studying carrier dynamics of free carriers generated by photoexcitation, especially in undoped semiconductors. It can also reveal information about the interaction of hot photoexcited carriers and cold carriers in doped semiconductors. On the other hand, pumping with intense THz field and probing with a weaker optical or THz field can reveal nonlinear THz effects such as impact ionization in doped semiconductors.

2.5.2.1.2 Ponderomotive effect

The ponderomotive potential can be defined as the time-averaged kinetic energy of an electron in matter driven by an oscillating electric field and expressed as:

$$U_p = \frac{e^2 E^2}{4m_e \omega^2} = \frac{2\pi e^2}{mc} \frac{I}{\omega^2} \quad (2.39)$$

Here m is the electron mass and I is the intensity of the light that oscillates with frequency ω . In the case that the ponderomotive potential of the light electric field exceeds the photon energy $\hbar\omega$, the system is then in a non-perturbative state. From Eq. (2.39) one can deduce that when the electric field is intense with very low frequency, the value of the ponderomotive potential U_p is higher.

The most benefited system from the large ponderomotive potential in a single-cycle THz pulse is the Rydberg atom or molecule [180] in electronically excited state. These systems are uniquely characterized by large orbital radius, and hence dipole moment. As a result, Rydberg atoms have characteristic properties such as small binding energy, high state density and long lifetime, which make them easy to ionize under the action of an external electric field [180-182].

References

- [1] D. H. Auston, K. P. Cheung and P. R. Smith, *Appl. Phys. Lett.* **45**, 284–6 (1984).
- [2] D. H. Auston, *Appl. Phys. Lett.* **26**, 1013 (1975).
- [3] G. P. Williams, *Rep. Prog. Phys.* **69**, 301–26 (2006).
- [4] G. Mourou, C. V. Stancampiano, A. Antonetti and A. Orszag, *Appl. Phys. Lett.* **39**, 295–6 (1981).
- [5] J. T. Darrow, X. C. Zhang, D. H. Auston and J. D. Morse, *IEEE J. Q. Elec.* **28**, 1607–16 (1992).
- [6] D. You, R. R. Jones, P. H. Bucksbaum and D. R. Dykaar, *Opt. Lett.* **18**, 290–2 (1993).

- [7] P. K. Benicewicz, J. P. Roberts and A. J. Taylor, *J. Opt. Soc. Am. B* **11**, 2533–46 (1994).
- [8] G. Rodriguez, S. R. Caceres and A. J. Taylor, *Opt. Lett.* **19**, 1994–6 (1994).
- [9] J. Darmo, T. Muller, W. Parz, J. Kroll, G. Strasser and K. Unterrainer, *Phil. Trans. R. Soc. Lond. A* **362**, 251–62 (2004).
- [10] T. Löffler, M. Kress, M. Thomson, T. Hahn, N. Hasegawa and H. G. Roskos, *Semicond. Sci. Technol.* **20**, S134–41 (2005).
- [11] J. H. Kim, A. Polley and S. E. Ralph, *Opt. Lett.* **30**, 2490–2 (2005).
- [12] B. B. Hu, J. T. Darrow, X. C. Zhang, D. H. Auston and P. R. Smith, *Appl. Phys. Lett.* **56**, 886–8 (1990).
- [13] L. Xu, X. C. Zhang, D. H. Auston and B. Jalali, *Appl. Phys. Lett.* **59**, 3357–9 (1991).
- [14] <http://phome.postech.ac.kr/user/indexSub.action?codyMenuSeq=2853646&siteId=nbtp&menuUIType=top>.
- [15] M. R. Stone, M. Naftaly, R. E. Miles, J. R. Fletcher and D. P. Steenson, *IEEE Trans. Microw. Theory* **52**, 2420–9 (2004).
- [16] S. B. Qadri, D. H. Wu, B. D. Graber, N. A. Mahadik and A. Garzarella, *Appl. Phys. Lett.* **101**, 011910 (2012).
- [17] H. Yoneda, K. Tokuyama, K. Ueda, H. Yamamoto and K. Baba, *Appl. Optics* **40**, 6733–6 (2001).
- [18] S. Ono, H. Murakami, A. Quema, G. Diwa, N. Sarukura, R. Nagasaka, Y. Ichikawa, H. Ogino, E. Ohshima, A. Yoshikawa and T. Fukuda, *Appl. Phys. Lett.* **87**, 261112 (2005).
- [19] O. Imafuji, B. P. Singh, Y. Hirose, Y. Fukushima and S. Takigawa, *Appl. Phys. Lett.* **91**, 071112 (2007).
- [20] X. Ropagnol, R. Morandotti, T. Ozaki and M. Reid, *IEEE Photonics J.* **3**, 174–86 (2011).
- [21] J. Holzman and A. Elezzabi, *Appl. Phys. Lett.* **83**, 2967–9 (2003).
- [22] A. Dreyhaupt, S. Winnerl, T. Dekorsy and M. Helm, *Appl. Phys. Lett.* **86**, 121114 (2005).
- [23] W. Shi, L. Hou and X. Wang, *J. Appl. Phys.* **110**, 023111 (2011).
- [24] T. Hattori, K. Egawa, S. Ookuma and T. Itatani, *Jpn. J. Appl. Phys.* **2**, 45 L422–4 (2006).
- [25] X. Ropagnol, R. Morandotti, T. Ozaki and M. Reid, *Opt. Lett.* **36**, 2662–4 (2011).
- [26] D. Kim and D. Citrin, *Appl. Phys. Lett.* **88**, 161117 (2006)
- [27] G. Rodriguez and A. Taylor, *Opt. Lett.* **21**, 1046–8 (1996).
- [28] K. Reimann, *Rep. Prog. Phys.* **70**, 1597–1632(2007).
- [29] N. Bloembergen, *Nonlinear Optics*, 4th edition, (Benjamin Inc. 1965).
- [30] Y. R. Shen, *Rev. Mod. Phys.* **48**, 1–32 (1976).
- [31] P. N. Butcher and D. Cotter, *The Elements of Nonlinear Optics* (Cambridge: Cambridge University Press, 1990).
- [32] M. Wegener, *Extreme Nonlinear Optics* (Berlin: Springer, 2005).
- [33] S. W. Huang, E. Granados, W. R. Huang, K. H. Hong, L. E. Zapata and F. X. Kartner, *Opt. Lett.* **38**, 796–8 (2013).
- [34] C. Vicario, A. V. Ovchinnikov, S. I. Ashitkov, M. B. Agranat, V. E. Fortov and C. P. Hauri, *Opt. Lett.* **39**, 6632 (2014).

- [35] F. Jr. Zernike and P. R. Berman, *Phys. Rev. Lett.* **15**, 999–1001 (1965).
- [36] http://dl.z-thz.com/eBook/zomega_ebook_pdf_1206_sr.pdf.
- [37] P. A. Franken, A. E. Hill, C. W. Peters and G. Weinreich, *Phys. Rev. Lett.* **7**, 118–19 (1961).
- [38] M. Bass, P. A. Franken, J. F. Ward and G. Weinreich, *Phys. Rev. Lett.* **9**, 446–8 (1962).
- [39] D. Mittleman, M. Gupta, R. Neelamani, R. Baraniuk, J. Rudd and M. Koch, *Appl. Phys. B Lasers O* **68**, 1085–94 (1999).
- [40] Z. Jiang and X. Zhang, *Opt. Lett.* **23**, 1114–6 (1998).
- [41] H. A. Hafez, X. Chai, A. Ibrahim, S. Mondal, D. F erachou, X. Ropagnol and T. Ozaki, *J. Opt.* **18**, 093004 (2016).
- [42] W Shi, Y. J. Ding, N. Fernelius and K. Vodopyanov, *Opt. Lett.* **27**, 1454–6 (2002).
- [43] W. Shi and Y. J. Ding, *Opt. Lett.* **30**, 1861–3 (2005).
- [44] R. A. Kaindl, F. Eickemeyer, M. Woerner and T. Elsaesser, *Appl. Phys. Lett.* **75**, 1060–2 (1999).
- [45] J. P. Likforman, M. Mehendale, D. M. Villeneuve, M. Joffre and P. B. Corkum, *Opt. Lett.* **26**, 99–101 (2001).
- [46] C. Kubler, R. Huber and A. Leitenstorfer, *Semicond. Sci. Technol.* **20**, S128–33 (2005).
- [47] Y. J. Ding and W. Shi, *Laser Phys.* **16**, 562–70 (2006).
- [48] B. Bartal, I. Z. Kozma, A. G. Stepanov, G. Almasi, J. Kuhl, E. Riedle and J. Hebling, *Appl. Phys. B* **86**, 419–23 (2007).
- [49] T. Dahinten, U. Plodereder, A. Seilmeier, K. L. Vodopyanov, K. R. Allakhverdiev and Z. A. Ibragimov, *IEEE J. Q. Elec.* **29**, 2245–50 (1993).
- [50] S. Ehret and H. Schneider, *Appl. Phys. B* **66**, 27–30 (1998).
- [51] R. A. Kaindl, D. C. Smith, M. Joschko, M. P. Hasselbeck, M. Woerner and T. Elsaesser, *Opt. Lett.* **23**, 861–3 (1998).
- [52] N. B. Singh, D. R. Suhre, V. Balakrishna, M. Marable, R. Meyer, N. Fernelius, F. K. Hopkins and D. Zelmon, *Prog. Cryst. Growth* **37**, 47–102 (1998).
- [53] R. Huber, A. Brodschelm, F. Tauser and A. Leitenstorfer, *Appl. Phys. Lett.* **76**, 3191–3 (2000).
- [54] R. A. Kaindl, M. Wurm, K. Reimann, P. Hamm, A. M. Weiner and M. Woerner, *J. Opt. Soc. Am. B* **17**, 2086–94 (2000).
- [55] K. Reimann, R. P. Smith, A. M. Weiner, T. Elsaesser and M. Woerner, *Opt. Lett.* **28**, 471–3 (2003).
- [56] C. W. Chen, Y. K. Hsu, J. Y. Huang, C. S. Chang, J. Y. Zhang and C. L. Pan, *Opt. Express* **14**, 10 636–44 (2006).
- [57] S. L. Chuang, S. Schmitt-Rink, B. I. Greene, P. N. Saeta and A. F. J. Levi, *Phys. Rev. Lett.* **68**, 102–05 (1992).
- [58] X. -C. Zhang, Y. Jin, K. Yang and L. J. Schowalter, *Phys. Rev. Lett.* **69**, 2303 (1992).
- [59] A. Rice, Y. Jin, X. F. Ma, X. C. Zhang, D. Bliss, J. Larkin and M. Alexander, *Appl. Phys. Lett.* **64**, 1324–6 (1994).

- [60] J. Ahn, A. V. Efimov, R. D. Averitt and A. J. Taylor, *Opt. Express* **11**, 2486–96 (2003).
- [61] T. Löffler, T. Hahn, M. Thomson, F. Jacob and H. G. Roskos, *Opt. Express* **13**, 5353–62 (2005).
- [62] T. Tanabe, K. Suto, J. Nishizawa, K. Saito and T. Kimura, *J. Phys. D.* **36**, 953–7 (2003).
- [63] J. A. Lquoterighthuillier, G. Torosyan, M. Theuer, Y. Avetisyan and R. Beigang, *Appl. Phys. B* **86**, 185–96 (2007).
- [64] J. A. Lquoterighthuillier, G. Torosyan, M. Theuer, C. Rau, Y. Avetisyan and R. Beigang, *Appl. Phys. B* **86**, 197–208 (2007).
- [65] J. R. Morris and Y. R. Shen, *Opt. Commun.* **3**, 81–4 (1971).
- [66] J. Hebling, A. G. Stepanov, G. Almaasi, B. Bartal and J. Kuhl, *Appl. Phys. B* **78**, 593–9 (2004).
- [67] A. G. Stepanov, J. Kuhl, I. Z. Kozma, E. Riedle, G. Almaasi and J. Hebling, *Opt. Express* **13**, 5762–8 (2005).
- [68] K. -L. Yeh, M. C. Hoffmann, J. Hebling and K. A. Nelson, *Appl. Phys. Lett.* **90**, 171121 (2007).
- [69] T. Elsaesser and M. C. Nuss, *Opt. Lett.* **16**, 411–13 (1991).
- [70] D. H. Auston, *Appl. Phys. Lett.* **43**, 713–15 (1983).
- [71] D. H. Auston, K. P. Cheung, J. A. Valdmanis and D. A. Kleinman, *Phys. Rev. Lett.* **53**, 1555–8 (1984).
- [72] D. H. Auston, A. M. Glass and A. A. Ballman, *Phys. Rev. Lett.* **28**, 897–900 (1972).
- [73] K. E. Niebuhr, *Appl. Phys. Lett.* **2**, 136–7 (1963).
- [74] N. A. van Dantzig, P. C. M. Planken and H. J. Bakker, *Opt. Lett.* **23**, 466–8 (1998).
- [75] P. Y. Han, M. Tani, F. Pan and X. C. Zhang, *Opt. Lett.* **25**, 675–7 (2000).
- [76] A. Schneider, I. Biaggio and P. Gunter, *Opt. Commun.* **224**, 337–41 (2003).
- [77] H. Adachi, T. Taniuchi, M. Yoshimura, S. Brahadeeswaran, T. Higo, M. Takagi, Y. Mori, T. Sasaki and H. Nakanishi, *Jpn. J. Appl. Phys.* **43**, L1121–3 (2004).
- [78] I. Taniuchi, H. Adachi, S. Okada, T. Sasaki and H. Nakanishi, *Electron. Lett.* **40**, 549–51 (2004).
- [79] A. Schneider and P. Gunter, *Ferroelectrics* **318**, 83–8 (2005).
- [80] A. Schneider, M. Neis, M. Stillhart, B. Ruiz, R. U. A. Khan and P. Gunter, *J. Opt. Soc. Am. B* **23**, 1822–35 (2006).
- [81] M. C. Hoffmann, J. Hebling, H. Y. Hwang, K.-L. Yeh, and K. A. Nelson, *J. Opt. Soc. Am. B.* **26**, A29 (2009).
- [82] A. Syouji, S. Saito, K. Sakai, M. Nagai, K. Tanaka, H. Ohtake, T. Bessho, T. Sugiura, T. Hirosumi, and M. Yoshida, *J. Opt. Soc. Am. B.* **24**, 2006 (2007).
- [83] A. Schneider, M. Stillhart, and P. Gunter, *Opt. Express* **14**, 5376 (2006).
- [84] F. Blanchard, G. Sharma, L. Razzari, X. Ropagnol, H. C. Bandulet, F. Vidal, R. Morandotti, J. Kieffer, T. Ozaki, H. Tiedje, H. Haugen, M. Reid and F. Hegmann, *IEEE J. Selec. Top. Q. Elect.* **17**, 5–16 (2011).

- [85] L. Palfalvi, J. Hebling, G. Almasi, A. Peter, K. Polgar, K. Lengyel and R. Szipocs, *J. Appl. Phys.* **95**, 902–8 (2004).
- [86] F. Blanchard, B. E. Schmidt, X. Ropagnol, N. Thire, T. Ozaki, R. Morandotti, D. G. Cooke and F. Legare, *Appl. Phys. Lett.* **105**, 241106 (2014).
- [87] D. Cooke and R. Hochstrasser, *Opt. Lett.* **25**, 1210–2 (2000).
- [88] M. Kress, T. Löffler, S. Eden, M. Thomson and H. G. Roskos, *Opt. Lett.* **29**, 1120–2 (2004).
- [89] T. Bartel, P. Gaal, K. Reimann, M. Woerner and T. Elsaesser, *Opt. Lett.* **30**, 2805–7 (2005).
- [90] M. D. Thomson, M. Kress, T. L. Offler and H. G. Roskos, *Laser and Photon. Rev.* **1**, 349–68 (2007).
- [91] X. Xie, J. Dai and X.-C. Zhang, *Phys. Rev. Lett.* **96**, 075005 (2006).
- [92] E. Matsubara, M. Nagai, and M. Ashida, *Appl. Phys. Lett.* **101**, 011105 1–4 (2012).
- [93] J. A. Fulop, L. Palfalvi, S. Klingebiel, G. Almasi, F. Krausz, S. Karsch, and J. Hebling, *Opt. Lett.* **37**, 557–559 (2012).
- [94] H. Hamster, A. Sullivan, S. Gordon, W. White and R. Falcone, *Phys. Rev. Lett.* **71**, 2725–8 (1993).
- [95] M. Joffre, A. Bonvalet, A. Migus, and J.-L. Martin, *Opt. Lett.* **21**, 964-966 (1996).
- [96] M. van Exter and D. R. Grischkowsky, *IEEE Trans. Microw. Theo. Tech.* **38**, 1684-1691 (1990).
- [97] Q. Wu and X.-C. Zhang, *Appl. Phys. Lett.* **68**, 1604-1606 (1996).
- [98] Y. -S. Lee, *Principles of Terahertz Science and Technology* (Berlin: Springer 2009).
- [99] S. Kono, M. Tani and K. Sakai, *Appl. Phys. Lett.* **79**, 898 (2001).
- [100] J. Zhang, Y. Hong and S. L. Braunstein, and K. Shore, *IEEE Proc.: Optoelectronics* **151**, 98–101 (2004).
- [101] A. Singh, S. Pal, H. Surdi, S. S. Prabhu, S. Mathimalar, V. Nanal, R. G. Pillay and G. H. Dohler, *Opt. Express* **23**, 6656-6661 (2015).
- [102] P. U. Jepsen, R. H. Jacobsen and S. R. Keiding *J. Opt. Soc. Am. B* **13**, 2424–36 (1996).
- [103] A. Leitensdorfer, S. Hunsche, J. Shah, M. C. Nuss, and W. Knox, *Phys. Rev. Lett.* **82**, 5140-5143 (1999).
- [104] J. Dai, J. Zhang, W. Zhang and D. Grischkowsky, *JOSA B* **21**, 1379 (2004).
- [105] J. Dai, X. Xie and X.-C. Zhang, *Phys. Rev. Lett.* **97**, 103903 (2006).
- [106] N. Karpowicz, J. Dai, X. Lu, Y. Chen, M. Yamaguchi, H. Zhao, X.-C. Zhang, L. Zhang, C. Zhang, M. Price-Gallagher, C. Fletcher, O. Mamer, A. Lesimple and K. Johnson, *Appl. Phys. Lett.* **92**, 011131 (2008).
- [107] I. -C. Ho, X. Guo and X.-C.Zhang, *Opt. Express* **18**, 2872–83 (2010).
- [108] X. Ropagnol, F. Blanchard, T. Ozaki and M. Reid, *Appl. Phys. Lett.* **103**, 161108 (2013).
- [109] F. Blanchard, L. Razzari, H.-C. Bandulet, G. Sharma, R. Morandotti, J.-C. Kieffer, T. Ozaki, M. Reid, H. F. Tiedje, H. K. Haugen and F. A. Hegmann, *Opt. Express* **15**, 13212–20 (2007).

- [110] H. Hirori, A. A. Doi, F. Blanchard and K. Tanaka, *Appl. Phys. Lett.* **98**, 091106 (2011)
- [111] Q. Wu and X.-C. Zhang, *Appl. Phys. Lett.* **67**, 3523–5 (1995).
- [112] J. R. Fletcher, *Opt. Express* **10**, 1425 (2002).
- [113] G. Sharma, K. Singh, I. Al-Naib, R. Morandotti and T. Ozaki, *Opt. Lett.* **37**, 4338–40 (2012).
- [114] A. F. Fercher, C. K. Hitzenberger, G. Kamp, and S. Y. El-Zaiat, *Opti. Comm.* **117**, 43 (1995).
- [115] K. Singh, C. Dion, M. R. Lesk, T. Ozaki, and S. Costantino, *Rev. Sci. Inst.* **82**, 023706 (2011).
- [116] K. Singh, C. Dion, M. Wajszilber, T. Ozaki, M. R. Lesk, and S. Costantino, *Invest. Ophthalmol. Vis. Sci.* **52**, 8927 (2011).
- [117] M. H. De la Torre-Ibarra, P. D. Ruiz, and J. M. Huntley, *Opt. Express* **14**, 9643-9656 (2006).
- [118] J. Zhang, R. Bin, L. Yu and Z. Chen, *Opt. Lett.* **34**, 3442–4 (2009).
- [119] K. Singh, C. Dion, S. Costantino, M. Wajszilber, M.R. Lesk, T. Ozaki, *Exp. Eye. Res.* **91**, 63–68 (2010).
- [120] K. Singh, C. Dion, A. G. Godin, F. Lorghaba, D. Descovich, M. Wajszilber, T. Ozaki, S. Costantino, and M. R. Lesk, *Invest. Ophthalmol. Vis. Sci.* **53**, 7819-7824 (2012).
- [121] G. Sharma, K. Singh, A. Ibrahim, I. Al-Naib, R. Morandotti, F. Vidal and T. Ozaki, *Opt. Lett.* **38**, 2705–7 (2013).
- [122] A. Ibrahim, D. Ferachou, G. Sharma, K. Singh, M. K.-Turmel, and T. Ozaki, *Sci. Rep.* **6**, 23107 (2016).
- [123] D. Middleman, *Sensing with terahertz radiation* (Springer, Berlin; New York, 2003).
- [124] M. Walther, B. Fischer, M. Schall, H. Helm, and P. U. Jepsen, *Chem. Phys. Lett.* **332**, 389 (2000).
- [125] R. A. Cheville and D. Grischkowsky, *Opt. Lett.* **20**, 1646 (1995).
- [126] R. H. Jacobsen, D. M. Middleman, and M. C. Nuss, *Opt. Lett.* **21**, 2011 (1996).
- [127] H. Harde, S. Keiding, and D. Grischkowsky, *Phys. Rev. Lett.* **66**, 1834 (1991).
- [128] D. Grischkowsky, S. Keiding, M. Vanexter, and C. Fattinger, *J. Opt. Soc. Am. B* **7**, 2006 (1990).
- [129] T. I. Jeon and D. Grischkowsky, *Phys. Rev. Lett.* **78**, 1106 (1997).
- [130] T. I. Jeon and D. Grischkowsky, *Appl. Phys. Lett.* **72**, 3032 (1998).
- [131] D. M. Middleman, J. Cunningham, M. C. Nuss, and M. Geva, *Appl. Phys. Lett.* **71**, 16 (1997).
- [132] M. C. Nuss, K. W. Goossen, J. P. Gordon, P. M. Mankiewich, M. L. Omalley, and M. Bhushan, *J. Appl. Phys.* **70**, 2238 (1991).
- [133] P. C. M. Planken, M. C. Nuss, I. Brener, K. W. Goossen, M. S. C. Luo, S. L. Chuang, and L. Pfeiaeer, *Phys. Rev. Lett.* **69**, 3800 (1992).
- [134] I. Wilke, M. Khazan, C. T. Rieck, P. Kuzel, C. Jaekel, H. Kurz, *Physica C* **341**, 2271-2272 (2000).

- [135] I. S. Gregory, C. Baker, W. R. Tribe, I. V. Bradley, M. J. Evans, E. H. Linfield, A. G. Davies, and M. Missous, *IEEE J. Quantum Electron.* **41**, 717 (2005).
- [136] S. Verghese, K. A. McIntosh, and E. K. Duerr, *Proc. SPIE* **3828**, 118 (1999).
- [137] S. Verghese, K. A. McIntosh, S. Calawa, W.F. Dinatale, E. K. Duerr, and K. A. Molvar, *Appl. Phys. Lett.* **73**, 3824 (1998).
- [138] Y. -C. Shen, P. F. Taday, D. A. Newnham, M. C. Kemp, and M. Pepper, *Proc. SPIE* **5727**, 24 (2005).
- [139] D. M. Mittleman, *AIP Conf. Proc.* **760**, 25 (2005).
- [140] K. K. Wong, R. T. Logan Jr., *Proc. of European Optical Society, Paris* (2006).
- [141] T. Yasui, R. Ichikawa, Y. D. Hsieh, K. Hayashi, H. Cahyadi, F. Hindle, Y. Sakaguchi, T. Iwata, Y. Mizutani, H. Yamamoto, K. Minoshima and H. Inaba, *Sci. Rep.* **5**, 10786 (2015).
- [142] T. Yasui, Y. Kabetani, E. Saneyoshi, S. Yokoyama, and T. Araki, *Appl. Phys. Lett.* **88**, 241104 (2006).
- [143] T. Yasui, M. Nose, A. Ihara, K. Kawamoto, S. Yokoyama, H. Inaba, K. Minoshima, and T. Araki, *Opt. Lett.* **35**, 1689 (2010).
- [144] J. -H. Son, *Terahertz Biomedical Science and Technology* (Taylor and Francis Group, 2014).
- [145] K. Tanaka, H. Hirori and M. Nagai, *IEEE Trans. Terahertz Sci. Technol.* **1**, 301–12 (2011).
- [146] S. L. Dexheimer, *Terahertz Spectroscopy: Principles and Applications* (Taylor and Francis Group CRC Press 2007).
- [147] X. -C. Zhang and J. Xu, *Introduction to THz Wave Photonics* (Boston, MA: Springer Science and Business Media 2009).
- [148] S. Koenig, D. Lopez-Diaz, J. Antes, F. Boes, R. Henneberger, A. Leuther, A. Tessmann, R. Schmogrow, D. Hillerkuss, R. Palmer, T. Zwick, C. Koos, W. Freude, O. Ambacher, J. Leuthold and I. Kallfass, *Nat Photonics* **7**, 977–81 (2013).
- [149] X. -C. Zhang, *Phys. Med. Biol.* **47**, 3667-3677 (2002).
- [150] E. Pickwell, and V. P. Wallace, *J. Phys. D: Appl. Phys.* **39**, R301-R310 (2006).
- [151] G. Zhao, R. N. Schouten, N. Van der Valk, W. T. Wenckebach, and P. C. M. Planken, *Phys. Med. Biol.* **47**, 3699-3704 (2002).
- [152] M. Tonouchi, *Nature Photon.* **1**, 97-105 (2007).
- [153] H. -B. Liu, H. Zhong, N. Karpowicz, Y. Chen, and X.-C. Zhang, *Proc. IEEE* **95**, 1514-1527 (2007).
- [154] K. -C. Huang and Z. Wang, *IEEE Microw. Mag.* **12**, 108-116 (2011).
- [155] V. K. Thorsmølle, R. D. Averitt, M. P. Maley, M. F. Hundley, A. E. Koshelev, L. N. Bulaevskii and A. J. Taylor, *Phys. Rev. B* **66** 012519 (2002).
- [156] H. A. Hafez, I. Al-Naib, K. Oguri, Y. Sekine, M. M. Dignam, A. Ibrahim, D. G. Cooke, S. Tanaka, F. Komori, H. Hibino, and T. Ozaki, *AIP Adv.* **4**, 117118 (2014).
- [157] H. A. Hafez, I. Al-Naib, M. M. Dignam, Y. Sekine, K. Oguri, F. Blanchard, D. G. Cooke, S. Tanaka, F. Komori, H. Hibino and T. Ozaki, *Phys. Rev. B* **91**, 035422 (2015).

- [158] L. Vicarelli, M.S. Vitiello, D. Coquillat, A. Lombardo, A.C. Ferrari, W. Knap, M. Polini, V. Pellegrini, A. Tredicucci, *Nat. Mater.* **11**,865–871(2012).
- [159] X. Zhang, J. Wang, and S.-C. Zhang, *Phys. Rev. B.* **82**, 245107 (2010).
- [160] L. Wu, M. Brahlek, R. Valdes Aguilar, A. V. Stier, C. M. Morris, Y. Lubashevsky, L. S. Bilbro, N. Bansal, S. Oh, and N. P. Armitage, *Nature Phys.* **9** 410-414 (2013).
- [161] B. Fischer, M. Hoffmann, H. Helm, G. Modjesch and P. U. Jepsen, *Semicond. Sci. Technol.* **20** S246-S53 (2005).
- [162] T. Y. Chang, T. J. Bridges and E. G. Burkhardt, *Appl. Phys. Lett.* **17** 249-51 (1970).
- [163] S. Ganichev and W. Prettl, *Intense Terahertz Excitation of Semiconductors*, (Oxford University Press 2005).
- [164] A. F. G. van der Meer, *Nucl. Instrum. Methods Phys. Res. Sect. A-Accel. Spectrom. Dect. Assoc. Equip.* **528** 8-14 (2004).
- [165] S. D. Ganichev and W. Prettl, *Appl. Phys. Lett.* **64** 1977-80 (1994).
- [166] M. Wagner, H. Schneider, D. Stehr, S. Winnerl, A. M. Andrews, S. Schartner, G. Strasser and M. Helm, *Phys. Rev. Lett.* **105** 167401 (2010).
- [167] S. D. Ganichev, I. N. Yassievich and W. Prettl, *J. Phys. Condes. Matt.* **14** R1263-R95 (2002).
- [168] M. Dressel and G. Gruner, *Electrodynamics of Solids* (Cambridge: Cambridge University Press 2002).
- [169] P. Gaal, W. Kuehn, K. Reimann, M. Woerner, T. Elsaesser and R. Hey, *Nature* **450** 1210–3 (2007).
- [170] L. Razzari, F. H. Su, G. Sharma, F. Blanchard, A. Ayesheshim, H. C. Bandulet, R. Morandotti, J. C. Kieffer, T. Ozaki, M. Reid and F. A. Hegmann, *Phys. Rev. B* **79** 4 (2009).
- [171] J. Hebling, M. C. Hoffmann, H. Y. Hwang, K.-L. Yeh and K. A. Nelson, *Phys. Rev. B* **81** 035201 (2010).
- [172] F. H. Su, F. Blanchard, G. Sharma, L. Razzari, A. Ayesheshim, T. L. Cocker, L. V. Titova, T. Ozaki, J. C. Kieffer, R. Morandotti, M. Reid and F. A. Hegmann, *Opt. Express* **17** 9620-9 (2009).
- [173] M. C. Hoffmann and D. Turchinovich, *Appl. Phys. Lett.* **96** 3 (2010).
- [174] F. Wang, Y. Zhang, C. Tian, C. Girit, A. Zettl, M. Crommie and Y. R. Shen, *Science* **320**, 206–9 (2008).
- [175] Z. Q. Li, E. A. Henriksen, Z. Jiang, Z. Hao, M. C. Martin, P. Kim, H. L. Stormer and D. N. Basov, *Nat. Phys.* **4**, 532–5 (2008).
- [176] X. Gan, R.-J. Shiue, Y. Gao, K. F. Mak, X. Yao, L. Li, A. Szep, D. Walker, J. Hone, T. F. Heinz and D. Englund, *Nano Lett.* **13**, 691–6 (2013).
- [177] F. H. Su, F. Blanchard, G. Sharma, L. Razzari, A. Ayesheshim, T. L. Cocker, L. V. Titova, T. Ozaki, J. C. Kieffer, R. Morandotti, M. Reid and F. A. Hegmann, *Opt. Express* **17**, 9620–9 (2009).

- [178] G. Sharma, I. Al-Naib, H. Hafez, R. Morandotti, D. G. Cooke and T. Ozaki, *Opt Express* **20**, 18016–24 (2012).
- [179] M. C. Hoffmann, J. Hebling, H. Y. Hwang, K.-L. Yeh and K. A. Nelson, *Phys. Rev. B* **79**, 161201 (2009).
- [180] R. R. Jones, D. You and P. H. Bucksbaum, *Phys. Rev. Lett.* **70** 1236-9 (1993).
- [181] T. J. Bensity, G. Haefliger and R. R. Jones, *Phys. Rev. Lett.* **79** 2018–21 (1997).
- [182] S. Li and R. R. Jones, *Phys. Rev. Lett.* **112** 143006 (2014).

Chapter 3

Innovative coherent THz detection techniques using SDI part I: Michelson-type and Mach-Zehnder interferometer based SDI techniques in THz electric field measurement

Outline

In this chapter, we discuss the first utilization of SDI in THz electric field measurement. Two schemes of SDI in THz electric field measurements are discussed (i) Michelson-type interferometer-based SDI (the standard SDI) scheme, which was the pioneer version developed by our group (Sharma *et al.* [1]) in initial stage of the SDI-THz project, and (ii) Mach-Zehnder interferometer-based SDI (MZI-based SDI) scheme. The latter has been developed in the second stage of the project to eliminate the short THz temporal scan range that notoriously limited the exploitation of the standard SDI in any THz spectroscopic measurements and applications that imperatively require higher spectral resolution. The self-referencing method which has been demonstrated successfully in increasing the SNR of the standard SDI technique will be discussed here as well. Comparison between the standard SDI and MZI-based SDI techniques for THz electric field measurement is held in order to illustrate the advantages and shortcomings of each technique.

3.1 SDI in THz electric field measurement

Owing to its capability in measuring small distances (optical path differences) and eventually, small phase changes with high phase sensitivity, SDI lends itself readily as a robust tool for measuring small phase changes due to birefringence induced by the THz electric field in the electro-optic (EO) detection crystal. In this thesis work, three main SDI schemes for THz electric field measurement are developed, exploited and comparatively discussed (i) Michelson-type interferometer-based SDI (or the standard SDI), (ii) Mach-Zehnder interferometer-based SDI, and (iii) the fiber based-SDI (or CP-SDI). The first and second schemes are discussed in this chapter while the third scheme will be discussed separately in Chapter 4. The experimental

works in this thesis are carried out at the Advanced Laser Light Source (ALLS) facility, Varennes, Quebec, Canada. The laboratory facility provides a high power multi-beam Ti:sapphire based laser system, providing laser pulses in a wide range of electromagnetic spectrum, ranging from THz to soft X-rays [2-6]. ALLS offers a limited competitive beam time, since it has many users. Therefore, the experimental work presented in this thesis has been accomplished in different beam times. We always made sure to compare the same set of data obtained in the same beam time, since the experimental conditions (*e.g.* Ti:sapphire laser conditions and the THz set up alignment) differ from one beam time to another, which consequently affect our THz set up parameters (*e.g.* THz pulse shape, THz electric field, and SNR).

3.2 Michelson-type interferometer based SDI in THz electric field measurement

In the initial course of this thesis work, we started with reproducing THz electric field measurements using Michelson-type interferometer-based SDI (the standard SDI) that has been initiated by my colleague G. Sharma [1].

3.2.1 Experimental realization of standard SDI technique for THz electric field measurement

The layout of the standard SDI technique for THz electric field measurement is schematically illustrated in Fig. 3.1. The Ti:sapphire laser (DragonTM, KM Labs. Inc.) provides a femtosecond pulse of 40 fs duration, with a repetition rate of 2.5 kHz, a wavelength of 800 nm, 4 mJ energy per pulse, and a beam diameter of ~10 mm. The incoming laser beam is split by the beam splitter (BS1) into a probe beam arm and a pump beam arm. The pump beam is used to generate the THz pulse using the tilted-pulse-front technique from a LiNbO₃ crystal [7,8] pumped with 0.96 mJ optical pulses. Single-cycle THz pulses with energies up to 0.3 μ J are generated with bandwidth extending from 0.1 to 3 THz from that arrangement. The beam splitter (BS2) splits the optical probe beam (OPB) into two equal parts: the transmitted part (blocked by a blocker in Fig. 3.1) and reflected part. The reflected part of the beam is sent to a 0.3 mm-thick glass plate. The two surfaces of the glass plate each reflects ~ 4% of the incident beam. Half of the probe beam that is reflected from the glass plate is transmitted through the 50% beam splitter

(BS2). The reflected signal from the glass plate comprises two pulses, one that is reflected from the front surface, and the second reflected from the back surface of the glass plate.

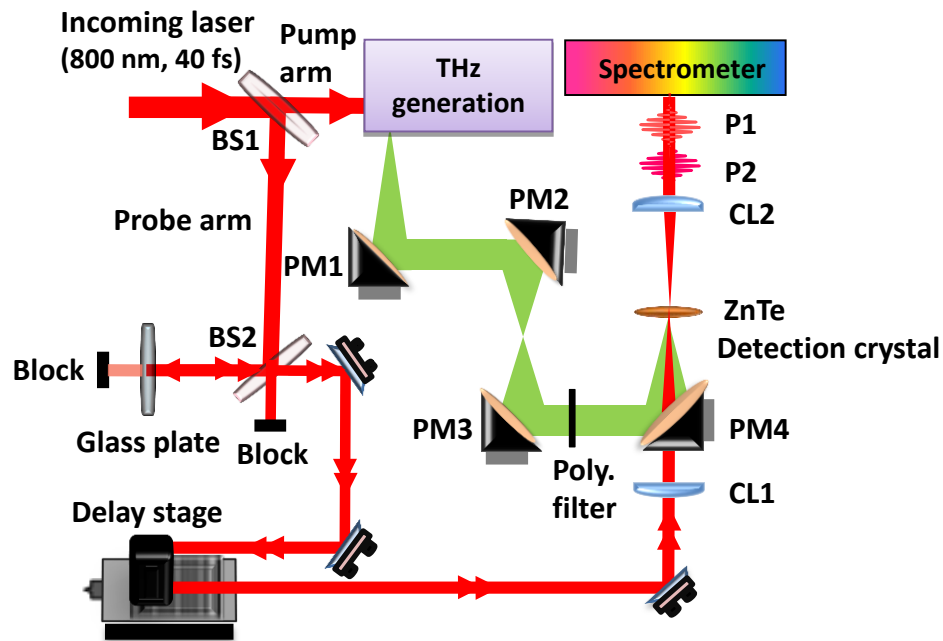


Figure 3.1 | Schematic of the experimental setup of Michelson interferometer-type based SDI (the standard SDI) technique for THz electric field measurement incorporated into the THz setup. BS: beam splitter, CL: cylindrical lens, PM: parabolic off-axis mirror, poly. filter is a black polyethylene filter, and P1,P2: reference and sample optical pulses.

Using a cylindrical lens (CL1), these two pulses are focused onto the 1-mm-thick ZnTe detector

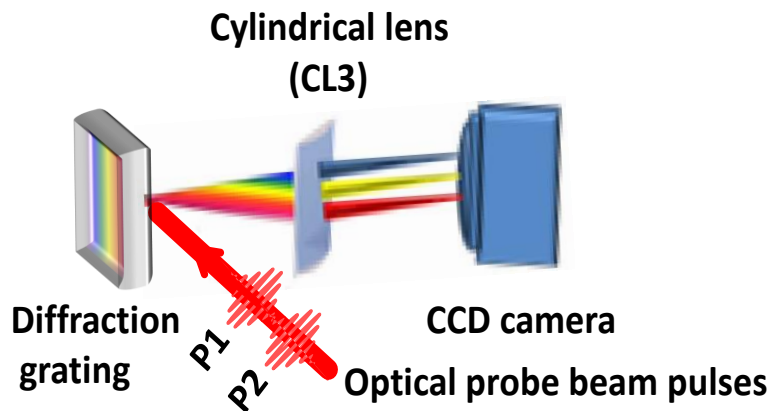


Figure 3.2 | Schematic of the home-made spectrometer used in the SDI project, P1 and P2 are the reference and sample optical probe beam pulses coming from the front and back surfaces of the glass plate respectively.

crystal, overlapping with the focused THz beam. In order to block any residual of the OPB, a black polyethylene sheet was used as an absorbing filter for the optical beam but transparent for

the THz beam. The THz beam is guided and refocused on the ZnTe detection crystal by a set of four parabolic off-axis mirrors (PM1-PM4). A cylindrical lens (CL2) is used to collimate the probe beam, which is then sent to a spectrometer. In this thesis work, we used a home-made spectrometer, schematically depicted in Fig. 3.2, which consists of a diffraction grating (1200 grooves/mm, Richardson Gratings™), a cylindrical lens (CL3, $f = 100$ mm) and a 2D CCD camera (Dalsa Inc. CR-GM00-H6400, 480×640 pixels). The presence of the THz electric field induces birefringence in the ZnTe detection crystal due to the Pockels effect. The induced birefringence is experienced by the pulse reflected from the back surface of the glass plate (referred to as the sample pulse P2). However, the pulse reflected from the front surface of the glass plate (referred to as the reference pulse P1) will traverse the ZnTe detection crystal without experiencing the birefringence effect. In other words, the pulse P2 temporally matches the THz pulse on the ZnTe detection crystal. Interference between the OPB pulses (P1 and P2), takes place and the spectral interference fringes are detected after the diffraction grating on a CCD camera of the spectrometer. Immediately the change in OPD (or phase change) due to the phase difference between P1 and P2 can be measured from the obtained interference fringes, which is, in turn, proportional to the THz electric field when it exists and overlapped with the OPB on the detection crystal.

One can express mathematically the interference between the two OPB pulses P1 and P2 in the standard SDI scheme, as [9]:

$$I(k) = I_R(k) + I_S(k) + 2\sqrt{I_R(k)I_S(k)}\cos[\varphi_o + kL] \quad (3.1)$$

Here, $k = 2\pi/\lambda$ is the wave number, I_R is the reference pulse intensity, I_S is the sample pulse intensity, φ_o is the phase constant, L is the OPD introduced between the reference and the sample pulses.

In phase measurement with SDI, the oscillation of the fringes in the spectral domain due to OPD between the reference and sample arms is detected, and the information from the instantaneous phase difference between the two pulses P1 and P2 is extracted from [10]

$$\varphi(L) = \tan^{-1}\left[\frac{\tilde{H}(I(L))}{I(L)}\right] \quad (3.2)$$

Here, $\tilde{H}(I(L))$ and $I(L)$ are the Hilbert transform and the interference signal intensity of Eq. (3.1) at an OPD of L , which corresponds to the OPD introduced between P1 and P2 due to the thickness of the glass plate. The change in OPD over time can be traced by monitoring the phase change in Eq. (3.2), which is in turn, as mentioned previously, proportional to the THz electric field strength. Indeed, in the SDI technique, the available spectral bandwidth of the light source is spread over the limited number of CCD pixels. Moreover, if we consider the total bandwidth Δk of the interfering signal acquired with a certain number of pixels (N) of the spectrometer's CCD camera, then the distance per pixel (Δd) after performing Fourier transform is given by

$$\Delta d = \frac{1}{2} \frac{2\pi}{\Delta k} \quad (3.3)$$

A factor of 2 in the denominator of Eq. (3.3) accounts for the change in OPD due to the change in refractive index of the EO detection crystal in a single-pass. Therefore, the distance increment per pixel in this case given by $\Delta d = 2\pi/\Delta k$, and thus the maximum OPD that can be measured as a function of the number of pixels N of the spectrometer's CCD camera [1]

$$d_{max} = \frac{N}{2} \Delta d = \frac{N}{2} \frac{2\pi}{\Delta k} = \frac{N}{2} \frac{\lambda_o^2}{\Delta \lambda} \quad (3.4)$$

Here λ_o is the central wavelength of the laser source. A factor of 2 appears in the denominator of Eq. (3.4), since the signal after performing fast Fourier transform (FFT) is symmetric around zero OPD. Thus, the signals on the opposite side of zero give in principle the same information. Thus, for a Gaussian profiled spectrum, we can express the maximum OPD (or the depth range) that can be measured using the SDI technique as [1]:

$$d_{max} = \frac{2 \ln 2}{\pi} \frac{N_p}{2} \frac{\lambda_o^2}{\Delta \lambda} \quad (3.5)$$

In Fig. 3.3(a), we show a typical SDI interference pattern between the two pulses (P1 and P2) coming from the two surfaces of the glass plate in the standard SDI technique. After performing FFT on the interference signal in (a), the frequency (FFT) peak (which is proportional to the optical path difference between the reference (P1) and sample (P2) pulses) is obtained, as illustrated in Fig. 3.3(b). The first peak (at $\sim 20 \mu\text{m}$) in Fig. 3.3(b) corresponds to a stationary peak representing the light source spectrum while the second peak of amplitude multiplied by the

fringes visibility constant (at $\sim 800 \mu\text{m}$) centered exactly at the OPD between the interfering signals. The maximum change in optical path difference that can be measured is given by Eq. (3.5), which in turn depends on the spectrometer used and the bandwidth of the laser source. Moreover, the theoretical phase (or OPD) sensitivity (*i.e.* the minimum measurable phase (or OPD) variation) is determined by the SNR of the phase measurement in SDI system, which is defined as [11,12]:

$$\langle \Delta\varphi^2 \rangle = \frac{1}{SNR_{SDI}} \quad (3.6)$$

Here the SNR for an SDI system is calculated as [13]:

$$SNR_{SDI} = \frac{|\tilde{I}|}{\sigma} \quad (3.7)$$

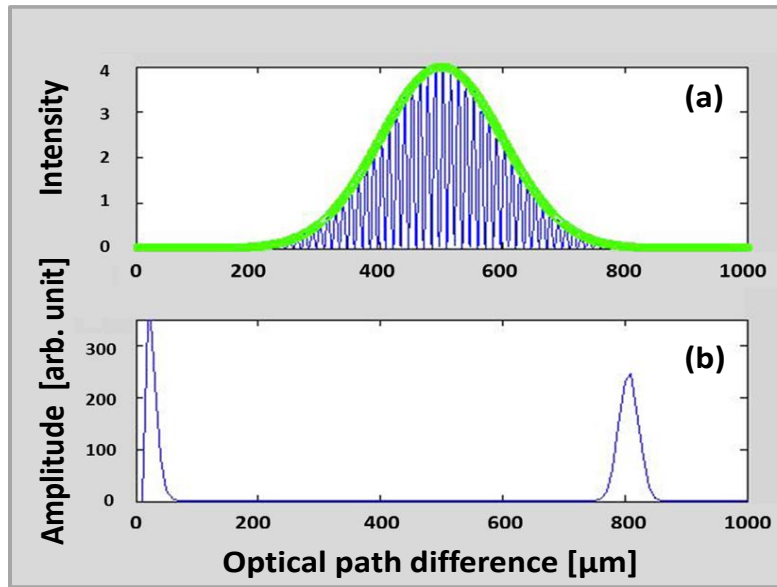


Figure 3.3| The interference pattern between the two pulses coming from surfaces of the glass plate in the standard SDI (a), and the corresponding FFT amplitude signal proportional to the optical path difference between the reference (P1) and the sample (P2) pulses (b).

Here, $|\tilde{I}|$ is the magnitude of the FFT peak in Fourier transformed signal of the spectrometer, and σ is the standard deviation of the noise signal away from the FFT peak. Thus, the minimum measurable OPD can be written as [9]:

$$\Delta x_{min} = \frac{\lambda_o}{4\pi} \langle \varphi^2 \rangle \quad (3.8)$$

Here, $\langle \varphi^2 \rangle$ is the phase stability (or standard deviation). From Eq. (3.8), it is obvious that the minimum measurable OPD depends on σ of the measured phase, which in turns depends on the SNR. Therefore, to enhance the SDI system performance in OPD measurements, the system SNR is imperatively required to be optimized to its highest values.

An argument can be raised on how the two 40-fs OPB pulses reflected from the glass plate surfaces interfere despite they are temporally separated by (>1.33 ps)? One can explain that based on the difference between common interferometric methods and the SDI technique. In the latter, the two separated pulses in time interfere as two waves with different frequency beat in the time domain. Despite being temporally separated by more than the pulse duration, their spectral interference can be detected. The mode-locked laser pulse is transformed into individual spectral components owing to the linear dispersion of the diffraction grating in the spectrometer [14,15]. Several different directions will be taken by the different propagating spectral components, which in turn create a frequency-dependent time delay [16]. Therefore, individual spectral components are spatially separated and hence are not mode-locked anymore after the diffraction grating. Consequently, the two temporally separated pulses can physically overlap on the CCD camera plane *i.e.* pulses interfere for much longer time scales.

3.2.2 Phase change data acquisition by SDI technique

After optimizing the alignment of the THz setup along with the incorporated standard SDI detection scheme, the interference between the two probe pulses (P1 and P2) takes place on the CCD camera plane of the spectrometer.

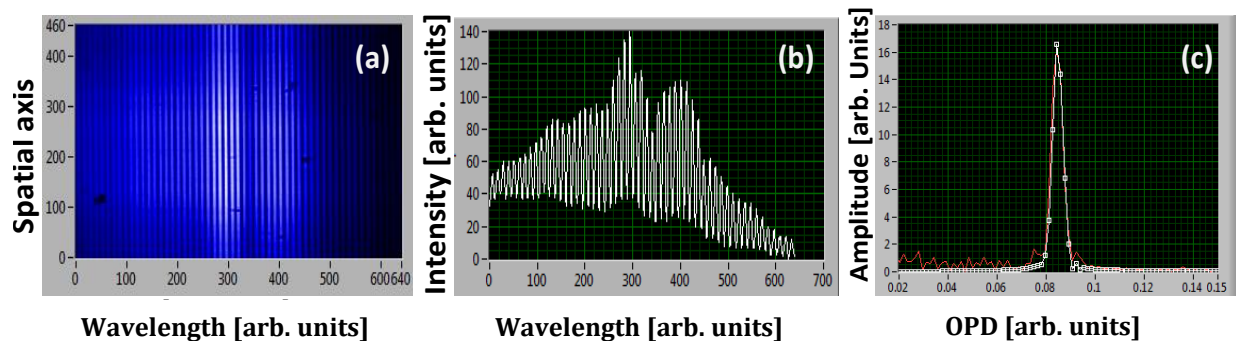


Figure 3.4 | Interference pattern of the two OPB pulses (P1 and P2) coming from front and back surfaces of the glass plate (a), the intensity distribution of the interference pattern at line 240 of the CCD camera of the spectrometer (b), and the corresponding FFT peak (c).

The data obtained by the CCD camera are recorded using LabVIEW software (LabVIEW; National Instruments Inc.) that was developed in our THz group [1], as depicted in Fig. 3.4(a), and the image of the interference fringes is recorded along with their intensity distribution (Fig. 3.4(b)). Fast Fourier transform is performed and the corresponding FFT signal for the interference is acquired (Fig. 3.4(c)). In order to enhance the SNR of the THz electric measurement using the standard SDI technique, the FFT signal is first maximized prior to THz electric field measurement, which is achieved by optimizing the standard SDI spectrometer alignment while the THz beam was blocked. Indeed, the FFT signal serves as an indicator for the quality of the interference pattern and thus for the quality of the SDI signal. Numerical treatment of the data is performed in order to reconstruct the THz pulse using the following steps: First, data are converted *to wave number-space* from *wavelength-space*. Then, Fourier transform is performed on the data in order to obtain the corresponding frequency for OPD between the reference (P1) and sample (P2) pulses. In the next step, the phase change between the two signals is measured using the relation expressed in Eq. (3.2). In fact, high sensitivity phase measurement of the fringes can provide an ultrahigh accuracy measurement of the OPD, which is due to phase oscillation in 2π rad steps at every shift of half a wavelength of the OPD. However, the measurement of the OPD using the SDI technique is restricted to less than half a wavelength, owing to the 2π ambiguity. To measure OPD longer than half a wavelength, phase unwrapping algorithms are needed. Conventional phase unwrapping algorithms require that the phase shift varies slowly and gradually [17], which limits the dynamic range (DR) of the phase measurement in the case of large phase discontinuity. Phase unwrapping by synthesizing a beat wavelength between two wavelengths was demonstrated for the correction of the 2π ambiguity [18,19]. However, additional phase noise or spikes were generated. We used a LabVIEW phase unwrapping function in this work. We show in Fig. 3.5 [13] a typical measured wrapped phase signal in *wave-number space* in Fig. 3.5(a). In order to attain the highest DR the phase signal is unwrapped as depicted in Fig. 3.5(b) [13]. Next, the measured phase will be traced over time as a delay is introduced between the THz signal and the OPB signal by using a translational stage. Finally, the phase waveform is directly proportional to the THz electric field strength, and hence the temporal shape of the THz electric field can be reconstructed by varying the delay time between the THz pulse and the probe pulse [1].

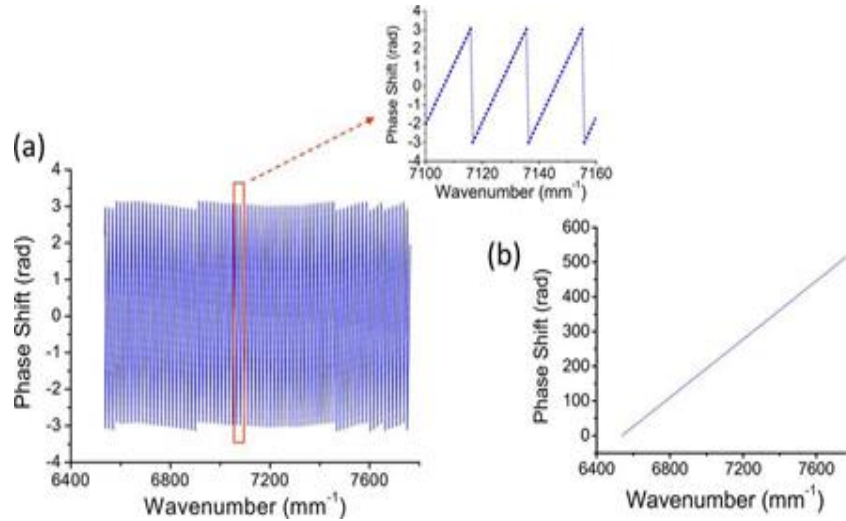


Figure 3.5 | Measured signal phase in wave-number space (a) and the corresponding unwrapped phase signal using SDI technique [adopted from ref. 13].

3.2.3 Experimental results and discussion

3.2.3.1 THz electric field measurement obtained with the standard SDI technique

Employing the standard experimental setup for the SDI technique (Fig. 3.1), a THz pulse has been measured, as depicted in Fig. 3.6(a). For comparison, we have also measured the same THz electric field temporal waveform with conventional EOS, which is depicted in Fig. 3.7(a). The corresponding Fourier power spectra for the standard SDI and conventional EOS techniques are depicted in Fig. 3.6(b) and 3.7(b), respectively. The pulse width (full-width at half-maximum, FWHM) is measured to be ~ 0.45 ps for THz pulses obtained with both techniques. There is a slight change in shape of the THz waveform obtained by the standard SDI technique, which is attributed to a slight change in the alignment of the optical probe beam and the THz beam while replacing the detection scheme. Moreover, a short temporal scan range in the standard SDI is clearly observed, posing a challenge in the standard SDI technique, as will be discussed in more detail in section 3.2.4.2, whereas the temporal window in the case of conventional EOS is unlimited. However, we have chosen 30 ps temporal scan length that is just enough to show the first THz reflection from the ZnTe detection crystal that is peaked at ~ 28 ps. It is worth mentioning that although the THz peak electric field was high (~ 70 kV cm⁻¹) we did not observe any over-rotation effects on the temporal waveform obtained with the standard SDI technique even though we did not use silicon wafer to reduce the THz field value.

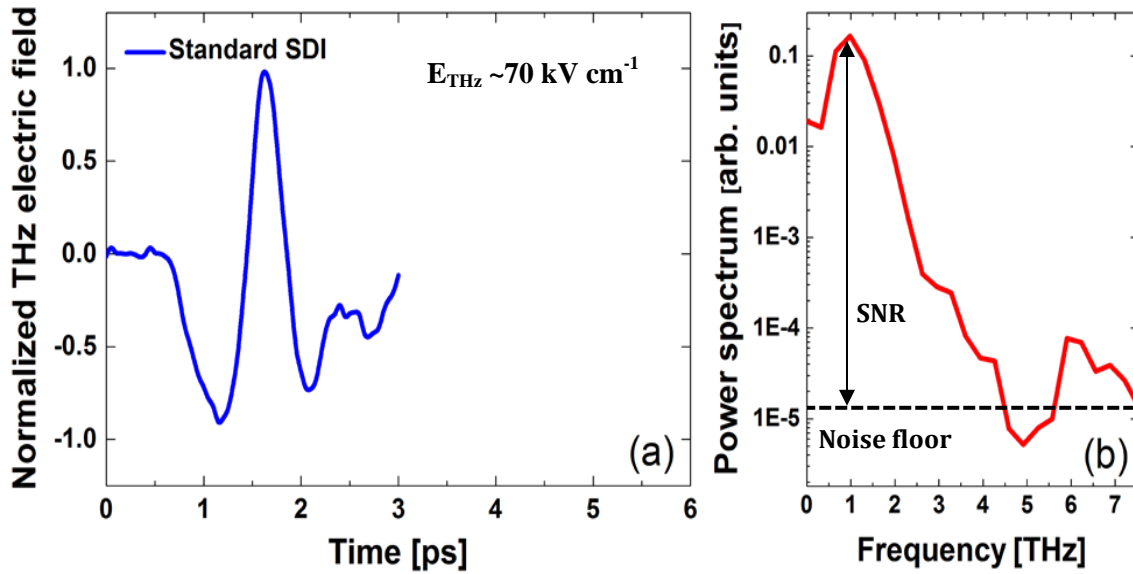


Figure 3.6| THz electric field obtained with the standard SDI technique (a) and the corresponding Fourier transform power spectrum (b).

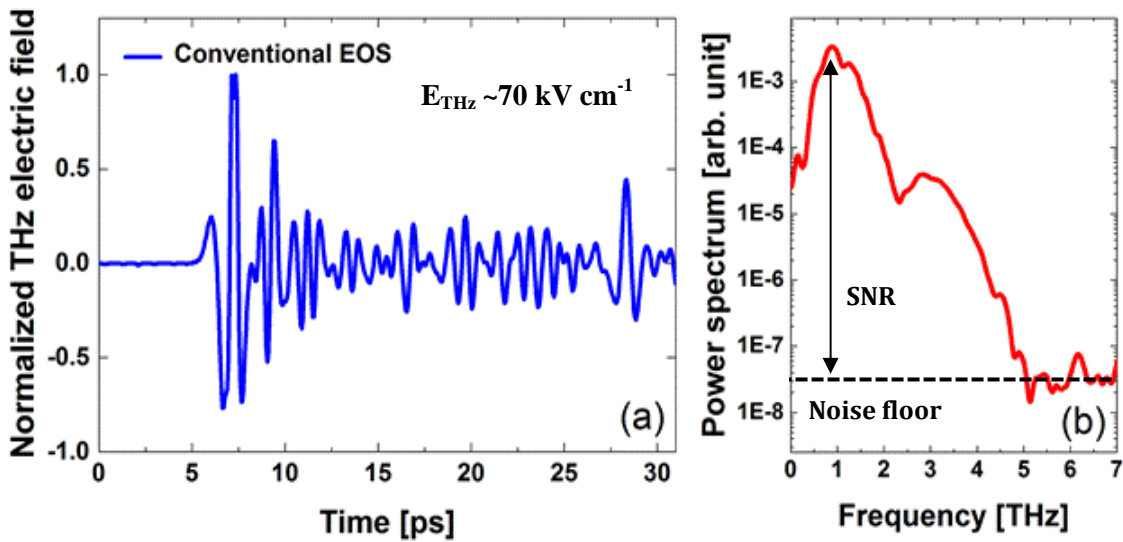


Figure 3.7| THz electric field obtained with the conventional EOS technique (a) and the corresponding Fourier transform power spectrum (b).

In contrast, over-rotation effect has been detected in measuring the same THz field by the conventional EOS technique. The SNR from the Fourier power spectrum plot is observed to be higher for conventional EOS technique ($\sim 52.17 \text{ dB}$) than standard SDI technique ($\sim 38.12 \text{ dB}$). We could also evaluate the SNR from the temporal shape of the THz pulse, by taking the ratio of the THz peak value to the standard deviation of the baseline (the signal that is before 1 ps) in the THz temporal trace. Following such approach, the SNR of the THz pulse obtained with the

standard SDI technique (Fig. 3.6(a)) is (~ 45) compared to (~ 418) for the THz pulse obtained with the conventional EOS technique (Fig. 3.7(a)).

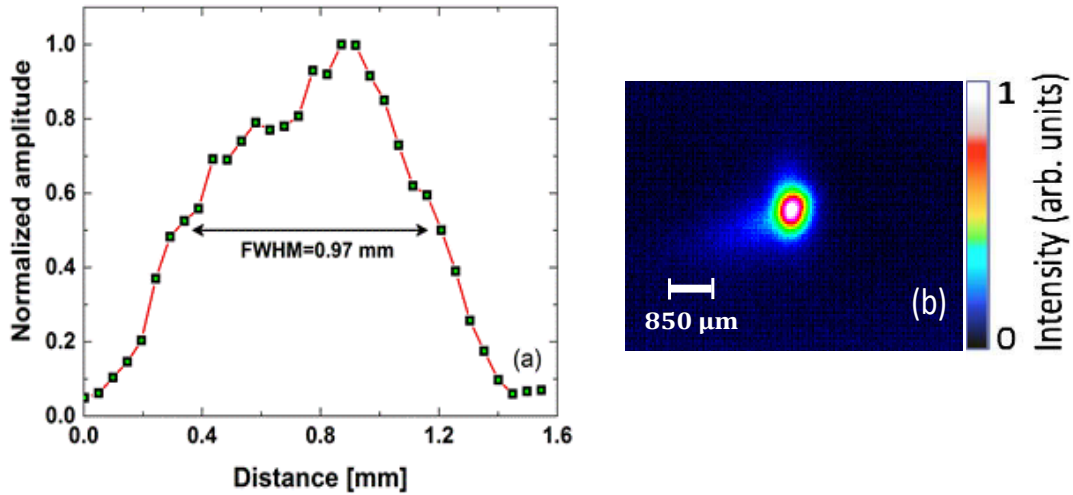


Figure 3.8| The spatial profile of the THz beam focal spot on the ZnTe detection (a) and the image of the focused THz beam pulse measured via pyroelectric IR camera (b).

Moreover, by exploiting the standard SDI technique, we could plot the spatial profile of the THz pulse at the focal plane on the detection crystal by manipulating the interference interferogram in a single temporal measurement.

This can be achieved by focusing the OPB on the ZnTe detection crystal in a line using a cylindrical lens [1]. The focused line is then imaged by another cylindrical lens on the 2D CCD camera along the vertical direction that is perpendicular to the diffraction plane of the spectrometer grating. Following this arrangement, the OPD (or phase change) measurement along the vertical direction of the CCD camera yields the spatial profile of the THz pulse at the focus, as depicted in Fig. 3.8(a). From the spatial profile, we could measure the THz focal spot size to be ~ 0.97 mm (FWHM) of the field amplitude. Moreover, in order to determine the physical dimension of the THz beam at the focus, we have captured the image of the focused THz beam using BaSrTiO₃ (BST) pyroelectric infrared (IR) camera (Electrophysics Inc., PV320-L2V), as depicted in Fig. 3.8(b). The measured spot size is $\sim 0.97 \times 1.05$ mm² at $1/e^2$ of the intensity profile.

3.2.4 Challenges and limitation of the standard SDI technique for THz electric field measurement

Despite its first successful demonstration [1], the new standard SDI THz detection technique is still encountering primarily two challenges (i) lower signal-to-noise ratio (SNR)

compared to that of conventional EOS detection, and (ii) limited temporal scan length. These challenges are limiting its practical laboratory usage for THz spectroscopic measurements. In order to expand its practical usage, those challenges imperatively need to be addressed.

3.2.4.1 Signal-to-noise ratio (SNR)

In SDI systems, phase noise originates from the noise in the light source, noise from the detector (CCD camera), and mechanical vibrational noise present in the system itself. In a shot-noise-limited system, the minimum phase variation (standard deviation of the phase) or phase sensitivity that can be detected is limited by the SNR of the system, given by Eq. (3.6) [9,13]. We measured SNR of our SDI system (from FFT peak, similar to the one depicted in Fig. 3.4(c)) to be $\sim 14,000$, resulting in a theoretical phase sensitivity of $\sim 70 \mu\text{rad}$.

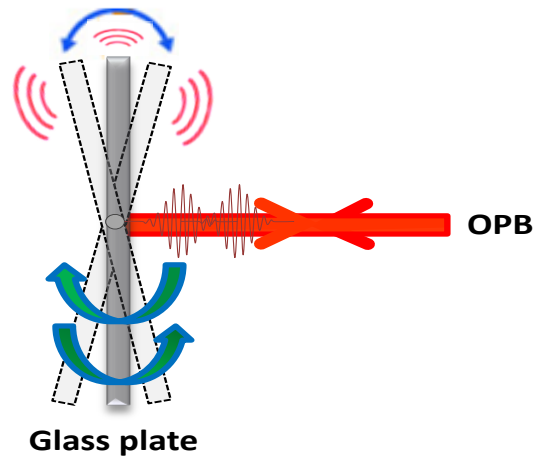


Figure 3.9 | Mechanical vibrations on the glass plate used in standard SDI affecting phase change measurement via OPB. The amplitude of the plate vibration is exaggerated for clarity.

In order to measure the phase sensitivity of the system experimentally, the THz signal was blocked and the phase from the FFT spectrum at the FFT peak corresponding to the interference between the two OPB pulses coming out from the two surfaces of the glass plate (Fig. 3.9) was measured for a probe delay of 3 ps. The measured phase sensitivity was found to be $\sim 890 \mu\text{rad}$, which is considerably inferior to the theoretically expected value of $\sim 70 \mu\text{rad}$. This reduced phase sensitivity can be attributed to the mechanical vibrations present in the system. One of the sources for mechanical noise is the angular vibration of the glass plate, as depicted in Fig. 3.9. Owing to this angular vibration, even if there is no THz signal, some phase difference will still be introduced between the reflected pulses from the front and back surfaces of the glass plate. In fact, angular variations of only 10 milli-degree between the 0.3 mm thick glass plate and the

laser beam can introduce a phase change of 140 μrad [20]. The noise from the spectrometer's CCD camera could be mitigated by using a high dynamic range CCD camera, while we attempted to mitigate the noise from the laser source and mechanical vibration using the self-referencing method [20], which is primarily introduced in order to reduce the phase noise due to mechanical vibrations and also to improve the phase sensitivity, as we will discuss it later in section 3.3.

3.2.4.2 Limited temporal scan length

One can realize the short temporal scan length in measuring the THz electric field via standard SDI technique (Fig. 3.6(a)) where we could measure only 3 ps. That short temporal scan length poses a limitation to the exploitation of the technique in THz spectroscopic measurements, which require a longer scanning time (and thus higher spectral resolution). This shorter scan length is dictated by the thickness of the glass plate in use (0.3 mm). One can use a thicker glass plate, but that will result in increasing the OPD between the two reflected signals (P1 and P2) which in turn results in reducing the sensitivity of the SDI technique and thus will lead to a reduction in the SNR of the measurement. One approach to eliminate the limitation in the temporal scanning window is by getting rid of the finite thickness glass plate that constrains the short temporal scanning window. The approach can be achieved for instance by employing different interferometer scheme in the detection line, which can divide the optical probe beam into two signals, one signal traverses through the EO detection crystal (modulated by the THz field) and referred to as the sample signal, while the other signal does not traverse through the detection crystal (and thus will not be modulated by the THz field) and referred to as the reference signal. Mach-Zehnder interferometer (MZI) scheme in SDI set up is an excellent demonstration of that concept. Moreover, the MZI scheme offers extra advantage by enabling one to work at around zero-OPD between the interfering signals, and thus increasing the SNR of the SDI technique as well as the THz scanning time.

3.3 The idea of self-referencing in the standard SDI technique for THz electric field measurement

In order to mitigate the phase noise signals in the standard SDI technique for THz electric field measurement, a new method called self-referencing SDI (SR-SDI) was introduced and experimentally demonstrated, which will be described in this section [20]. The idea is based on

creating a line-like focus of the OPB on the ZnTe detection crystal when overlapping with the focused THz beam, as depicted in Fig. 3.10. The probe beam was focused in a line with a length of ~ 4 mm using a cylindrical plano-convex lens, whereas the diameter of the THz spot is ~ 0.97 mm. The THz electric field is maximal at the center of the focused beam and it decreases while moving towards the edges of the beam.

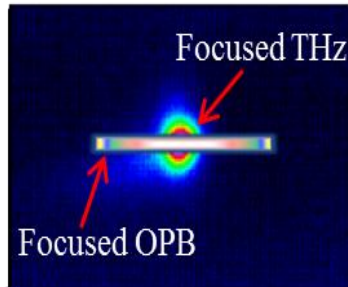


Figure 3.10 | Schematic of SR-SDI idea: THz beam and OPB at the ZnTe detection crystal position. The OPB is line focused using a cylindrical lens, and the THz beam spot is circularly focused using an off-axis mirror.

Thus, the optical probe beam will experience maximum phase change at the center of the THz spot and as we move towards the edges, the phase change decreases as well. At the edge of the optical probe beam, there will be no effect of the THz electric field on the OPB. Although the phase change along the probe beam would be proportional to the THz electric field, the phase change due to mechanical vibrations present in the system will be the same along the complete probe beam diameter. Thus, the mechanical noise in the system and noise due to laser fluctuations can be mitigated by subtracting the phase value measured at the edge of the probe beam from the phase values of the rest of the beam. In other words, we can look at it as spatial referencing where OPB can sample two points: one point without THz and serves as a reference (at the edge of OPB) and the other with a finite THz electric field (at the center of OPB). Hence, when subtracting the reference phase values from the sample phase values while scanning the THz temporal waveform we could successfully enhance the SNR of the THz electric field measurement [20].

We show in Fig. 3.11(a) the THz electric field trace obtained with standard SDI technique without implementing the SR-SDI method, and the THz electric field trace when implementing the SR-SDI method in Fig. 3.12(a). In Fig. 3.11(b), we depict the normalized Fourier power

spectrum of the THz temporal trace of Fig. 3.11(a), while Fig. 3.12(b) depicts the normalized Fourier power spectrum of the THz temporal trace of Fig. 3.12(a).

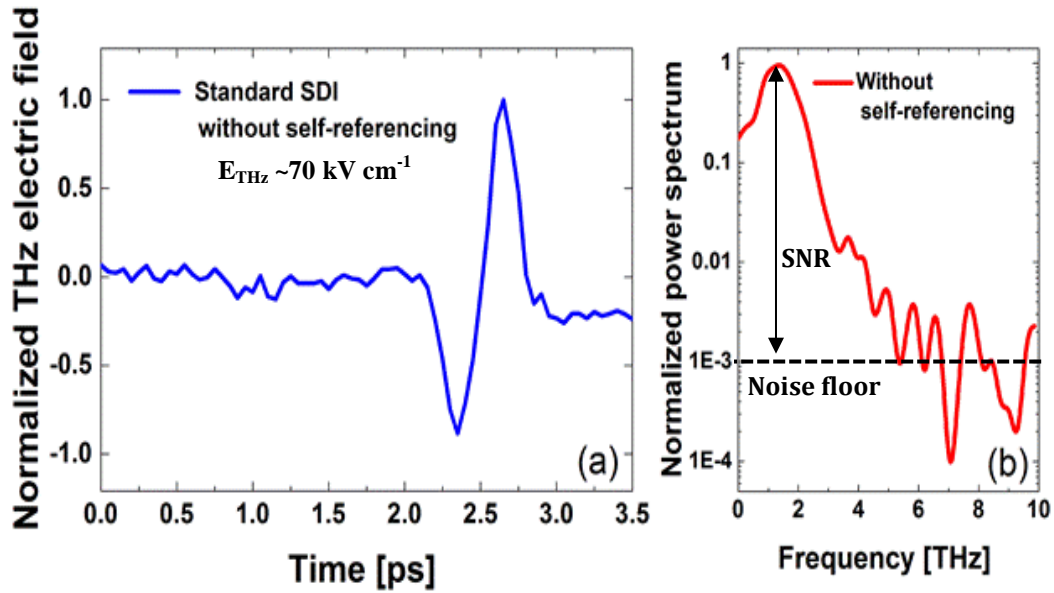


Figure 3.11 | THz electric field measurement obtained with the standard SDI technique (a) without using the self-referencing method and (b) the corresponding Fourier power spectrum.

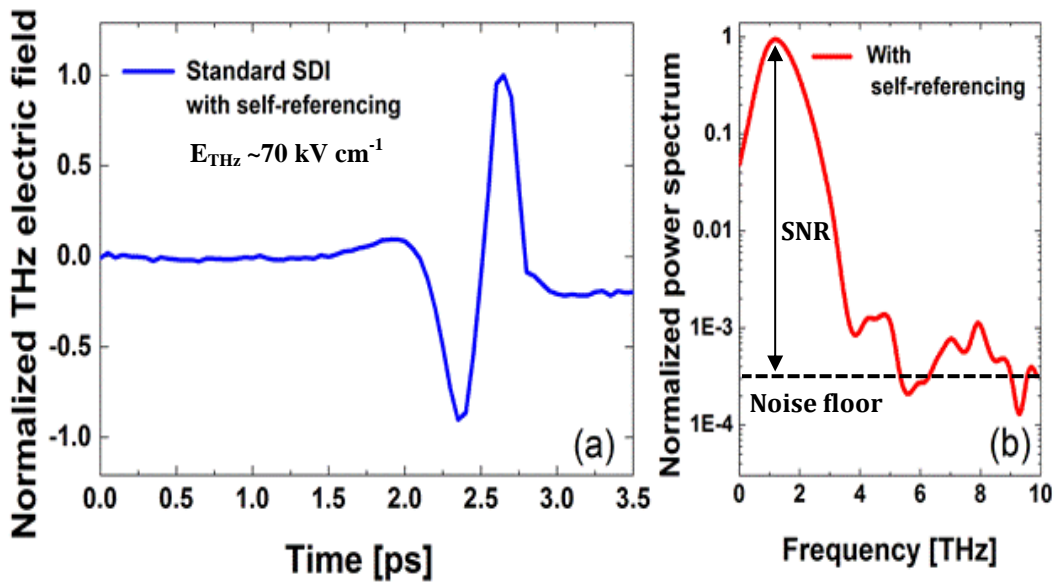


Figure 3.12 | THz electric field measurement obtained with the standard SDI technique (a) with using the self-referencing method and (b) the corresponding Fourier power spectrum.

From the Fourier power spectra, we could measure the SNR as the ratio between the maximum power signal to the noise floor signal (indicated in the figures). Using the following relation

$$\text{SNR [dB]} = 10 \log_{10} \left(\frac{\text{maximum signal}}{\text{noise}} \right) \quad (3.9)$$

we measure SNR~29.03 dB for THz electric field trace obtained with the standard SDI without self-referencing, compared to ~36.53 dB for THz electric field trace obtained with the standard SDI with self-referencing method. We could also measure the SNR of the THz electric field measurement from the temporal traces by taking the ratio of the peak to the standard deviation of the baseline (signal before 1 ps time in Fig. 3.11(a) and Fig. 3.12(a)) with and without SR-SDI method.

We found that the SNR of the THz signal measured without SR-SDI method is ~19, but is increased to ~118 after implementing the self-referencing method. Thus, the SNR of the THz electric field measurement obtained with SR-SDI is increased by more than six-fold, as compared to the SNR of THz electric field measurement obtained with standard SDI without self-referencing method.

3.4 MZI based SDI technique for THz electric field measurement

Although the standard SDI THz detection technique overcomes the limitation of over-rotation, it still suffers from poor SNR compared to the conventional EOS THz detection technique [1,20]. Increased SNR of the THz electric field measurement obtained with standard SDI technique by six folds has been demonstrated by implementing SR-SDI technique, as discussed in section 3.3 [20]. However, the SR-SDI technique for THz electric field measurement lacks the longer temporal scanning window imperatively required for higher spectral resolution in THz spectroscopic measurements. This limitation in the temporal scanning window is due to the finite thickness of the glass plate used in the standard SDI techniques for THz detection [1,20]. For example, a 300 μm thick glass plate provides a temporal scanning window of only 3 ps [1]. Even if longer scanning times could be realized by using thicker glass plates, the larger OPD between the two pulses, reflected from the glass plate surfaces, would drastically reduce the visibility of the interference, and that is due to inherent sensitivity drop of the SDI technique as working away from zero-OPD. Thus using a thicker glass plate (>300 μm) will result in reducing the SNR of the THz electric field measurement.

To enable unlimited temporal scanning window without the loss of SNR, and to simultaneously avoid over-rotation in detecting intense THz pulses, we propose and demonstrate a new interferometric technique for THz detection via SDI. The new technique uses a Mach-Zehnder

interferometer (MZI) configuration instead of a glass plate used in the standard SDI techniques for THz detection [10]. We show that the new technique enables the detection of intense THz signals without over-rotation while eliminating the limitation in the temporal scanning window suffered in the standard SDI technique. In this thesis work, as a proof of concept, we demonstrate a 30 ps temporal scanning window, which represents a ten-fold increase compared with the scanning window of the standard SDI techniques [1,20]. In this new MZI based SDI technique, we exploit the advantage of being able to work at smaller OPD between the two probe pulses enabled by the MZI arrangement, consequently increasing the visibility of the interference signal.

3.4.1 Experimental realization of MZI-based-SDI technique for THz electric field measurement

We show in Fig. 3.13 the schematic illustration of the experimental setup used to demonstrate the MZI configuration for SDI-THz electric field measurement [10].

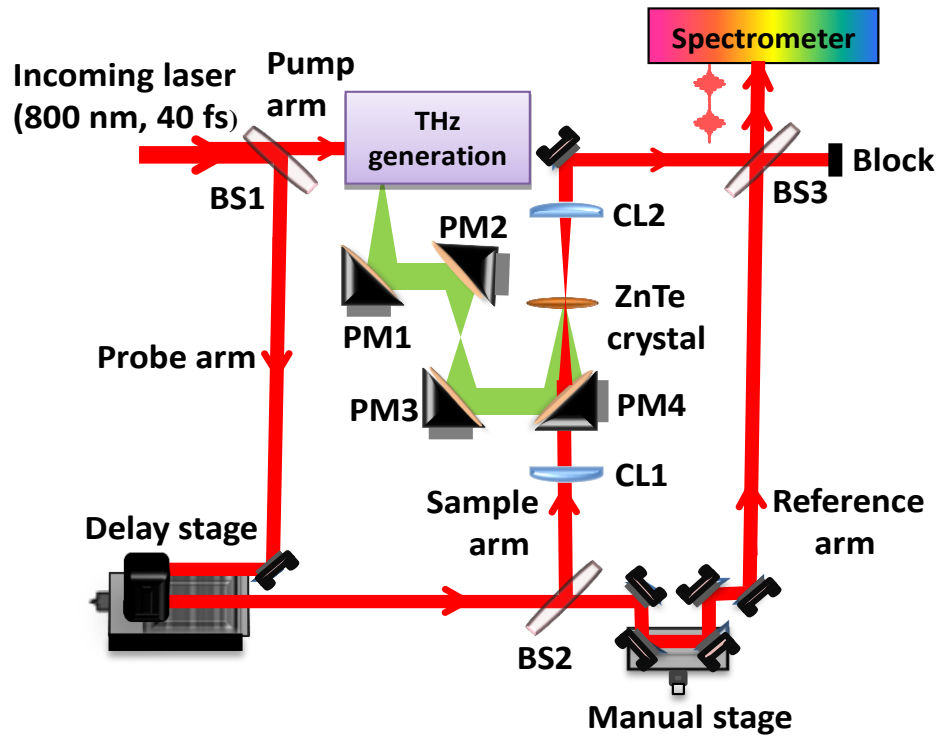


Figure 3.13 | Schematic of the experimental setup of Mach-Zehnder interferometer (MZI) based spectral domain interferometry technique for THz electric field measurement. BS: beam splitter, PM: parabolic off-axis mirror, and CL1, CL2: plano-convex cylindrical lenses [10].

A femtosecond 800 nm laser beam is split by a beam splitter (BS1) into two arms: the pump arm and the probe arm. The laser pulse in the pump arm is used to generate the THz signal, as previously discussed in the standard SDI setup [7,8]. In an MZI configuration, the probe arm is further split by a beam splitter (BS2) into two arms, the sample arm, and the reference arm. The probe pulse in the sample arm is then focused by a cylindrical plano-convex lens (CL1), propagates through a hole (diameter of ~ 1.3 mm) in a parabolic off-axis mirror (PM4), and onto a 1-mm-thick $\langle 110 \rangle$ ZnTe detection crystal, where it overlaps with the focused THz pulse. Another cylindrical plano-convex lens (CL2) is used to collimate the sample arm beam after the ZnTe detection crystal. The other arm of the MZI is the reference arm, which does not traverse through the ZnTe detection crystal (and thus will not be modulated by the THz field). Both reference and sample arms of the MZI are recombined together using a beam splitter (BS3). After BS3, the probe pulses are then sent to a spectrometer (same as discussed in section 3.2.1 and depicted in Fig. 3.2) that is used to observe the spectral interference fringes between the two MZI arm pulses. At the CCD camera plane, the sample and reference pulses interfere, thus allowing one to measure the phase difference between their spectral components. A manual micrometer stage is used to vary the OPD between the pulses in the two arms of the MZI. At the ZnTe detection crystal, the THz pulse is aligned in a polarization state vertical to the paper plane and parallel to the polarization state of the probe pulse. The presence of the THz electric field will induce birefringence in the ZnTe detection crystal via the Pockels effect. This birefringence is read out by the sample probe pulse as a change in the OPD between the two interfering signals at the CCD camera plane. Therefore, one can measure the change in the phase difference introduced by the THz pulse using the spectral interference of the two pulses in MZI arms. We noted that the sample beam after ZnTe detection crystal is elliptically polarized compared to the reference beam polarization which is linear. Nevertheless, we still observed the interference between both them, however, that may affect the interference fringe and the signal quality those in turns affects the SNR of the measurement depending on the intensity of the sample beam relative to reference beam in polarization direction same as the reference beam. Moreover, the hole in the off-axis mirror (PM4) is cut with a diameter of ~ 5 mm at the back of the mirror while at the front surface of the mirror its diameter is reduced to ~ 1.3 mm. This geometry allows us to minimize the clipping of the OPB and at the same time minimize the loss in the THz electric

field reflected by this mirror. We estimated the loss in the THz electric field due to this hole to be $<0.7\%$.

3.4.2 Experimental results and discussion

3.4.2.1 THz electric field measurement obtained with MZI-based-SDI technique

We show in Fig. 3.14(a) the trace of the multi-cycle THz pulse measured using the conventional EOS at THz peak electric field of $\sim 70 \text{ kV cm}^{-1}$.

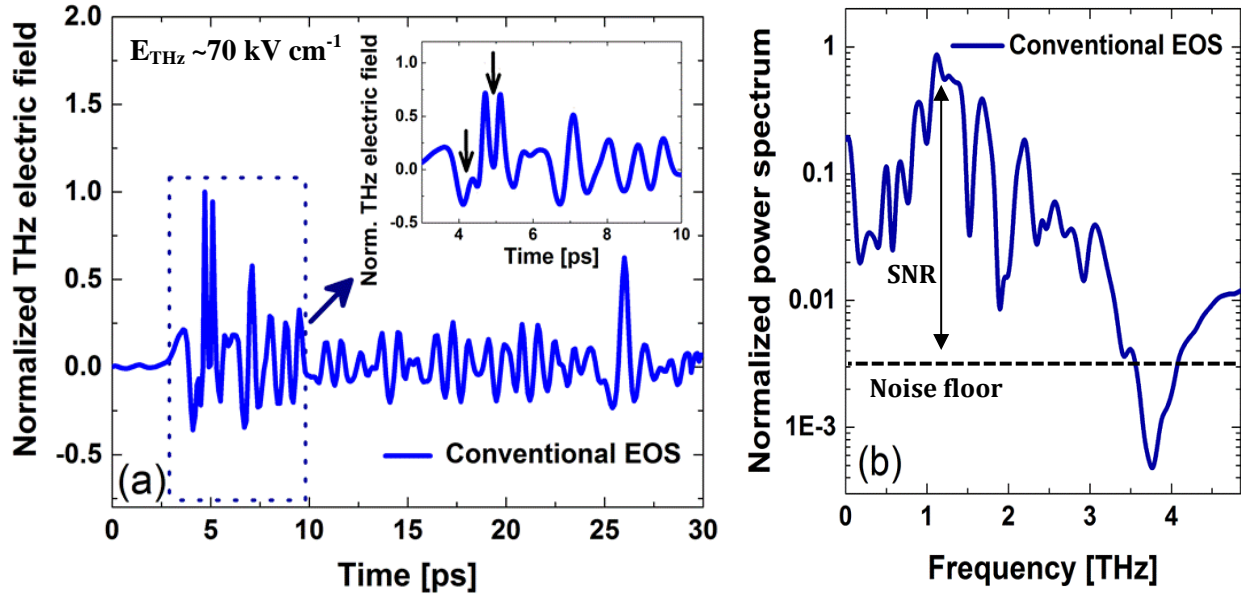


Figure 3.14 | THz electric field trace obtained with the conventional EOS technique (a). The inset shows a short scan of 7 ps where over-rotation limitation affecting parts of the THz pulse indicated by arrows. Fourier power spectrum of the THz temporal trace obtained by conventional EOS technique (b) [10].

The inset illustrates a short scan window (7 ps) to better visualize limitations due to over-rotation. As we can see, over-rotation is evident in some parts of the THz main pulse (at ~ 5 ps) indicated by arrows, thus severely altering the shape of the THz pulse. At time ~ 26 ps, the THz signal amplitude starts to increase again, indicating the first THz reflection from the ZnTe detection crystal. Fig. 3.14(b) shows the corresponding Fourier power spectrum of the THz trace obtained in Fig. 3.14(a). In Fig. 3.15(a), we show the few-cycle THz pulse measured with the MZI based SDI technique at an OPD of $\sim 450 \mu\text{m}$ between the reference and sample pulses of the MZI. We note that at the time ~ 5 ps, the THz signal increases with higher amplitude, indicating the main THz pulse, while at the time ~ 26 ps the THz signal starts to increase again with a smaller amplitude, corresponding to the first reflection of the THz electric field in the

ZnTe detection crystal. The oscillations from ~ 7 ps to ~ 24.5 ps are caused mainly by the absorption and subsequent emission of light by water-vapor molecules. We demonstrate that over-rotation limitation can be avoided when using MZI based SDI technique in measuring temporal waveform of THz electric field (~ 70 kV cm $^{-1}$), as shown in the inset of Fig. 3.15(a), in contrast to the conventional EOS technique.

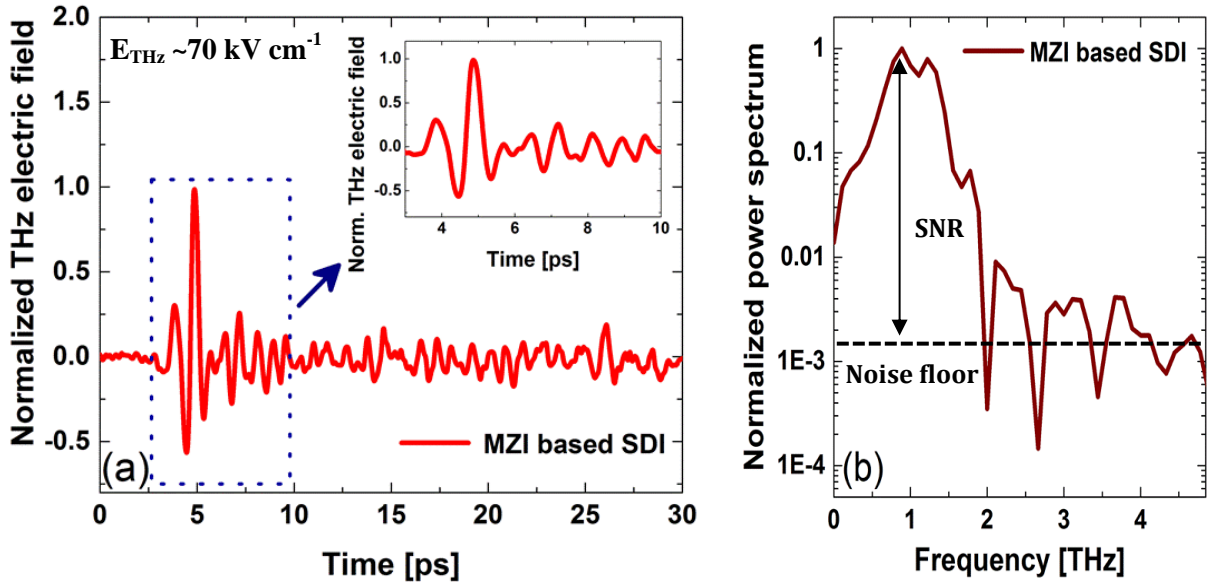


Figure 3.15 | THz electric field trace obtained with the MZI based SDI technique (a). The inset shows a short scan of 7 ps where over-rotation limitation in the conventional EOS technique has been avoided in the MZI-SDI technique. Fourier power spectrum of the THz temporal trace obtained by MZI based SDI technique (b) [10].

3.5 Characterization of MZI-based-SDI technique for THz electric field measurement

3.5.1 Temporal scan range

One can notice that the temporal scan window has been extended (we show only ten-fold increment) compared to the standard SDI techniques for THz detection [1,20]. In the standard SDI techniques [1,20], both the front and the back pulse reflected from the glass plate surfaces propagate through the ZnTe detection crystal, with a temporal delay defined by the thickness of the glass plate (3 ps for 300 μm thick glass). As previously explained, the back pulse is modulated by the THz electric field in the ZnTe detection crystal, while the front pulse passes through the crystal without modulation. Therefore, with the standard SDI method, the scanning window is limited by the temporal delay between the two pulses, which is determined by the

thickness of the glass plate. However, in the new MZI technique, we have overcome such limitation, since now the two probe pulses propagate through two different arms in the MZI. Birefringence of the ZnTe detection crystal due to the THz electric field is uniquely experienced by the probe pulse in the sample arm, while the probe pulse in the reference arm does not experience such birefringence effect.

3.5.2 SNR of MZI-based-SDI technique in THz electric field measurement

Fig. 3.14(b) depicts the Fourier power spectrum of the THz trace obtained with the conventional EOS technique (Fig. 3.14(a)) while Fig. 3.15(b) depicts the Fourier power spectrum of the THz trace obtained with the MZI based SDI technique (Fig. 3.15(a)). From Fourier power spectra, one can see that the SNR of the THz measured with the MZI based SDI technique is still inferior to that measured with the conventional EOS and even with that obtained in the standard SDI technique (Fig. 3.6(a)). The SNR for THz measurements is calculated to be ~ 31.21 dB for MZI based SDI technique, compared to ~ 38.12 dB for the standard SDI technique. In order to ensure a fair comparison between the SNR of both THz measurements (conventional EOS and MZI-based SDI), we kept the same averaging time (300 ms), the same step size of the delay stage (0.1 ps), and the same number of steps (301 steps). Moreover, the time taken to register a THz trace is the same for both techniques ~ 2 minutes. One can see the water vapor absorption lines clearly in the spectrum of the THz trace obtained with the MZI based SDI technique (Fig. 3.15(b)), while they are absent in the THz spectrum obtained with the standard SDI technique (Fig. 3.6(b)). This is attributed to the fact that the temporal scanning window in the standard SDI technique is limited to 3 ps, while the oscillations in the THz field due to water vapor extend to later times (longer than 3 ps), and thus cannot be recorded with the standard SDI technique. On the contrary, the MZI based SDI technique has a longer temporal scanning window and consequently clearly shows water vapor lines. This indicates clearly the advantage of the MZI technique compared with the standard SDI technique. Indeed, we were expecting that the enhancement in the SNR of the THz electric field measurement obtained with MZI based SDI technique would be greater than the obtained value since, by default, using MZI based SDI grants us the privilege of working away from the zero-OPD region where significant noise may exist, while also keeping the OPD at a sufficiently small value to avoid low SNR due to loss in interference of the two probe pulses. The noise stems from mechanical vibrations and laser fluctuations in the set up seems to be greater in the MZI technique configuration than in the

standard SDI technique configuration. However, the SNR of the former could be further improved if the self-referencing method is used, which has been shown to improve the SNR by six times [20], by reducing the phase noise due to laser fluctuations and mechanical vibrations in the setup. We note that the potential improvement by using the common self-referencing technique could be much larger compared with the standard SDI techniques in THz detection, since in the MZI technique, there are more optics involved to interfere the two pulses, and thus measurements are much more sensitive to vibrations in the setup. However, these further improvements are out of the scope of this thesis work.

3.5.3 The optimal OPD between the two OPB interfering signals

Moreover, in an effort to maximize the SNR of the THz electric field measurement using the MZI based SDI technique, we have varied the OPD between the two probe pulses of the MZI by using a manual micrometer in the reference arm. At each OPD, a temporal THz trace is measured, as depicted in Fig. 3.16.

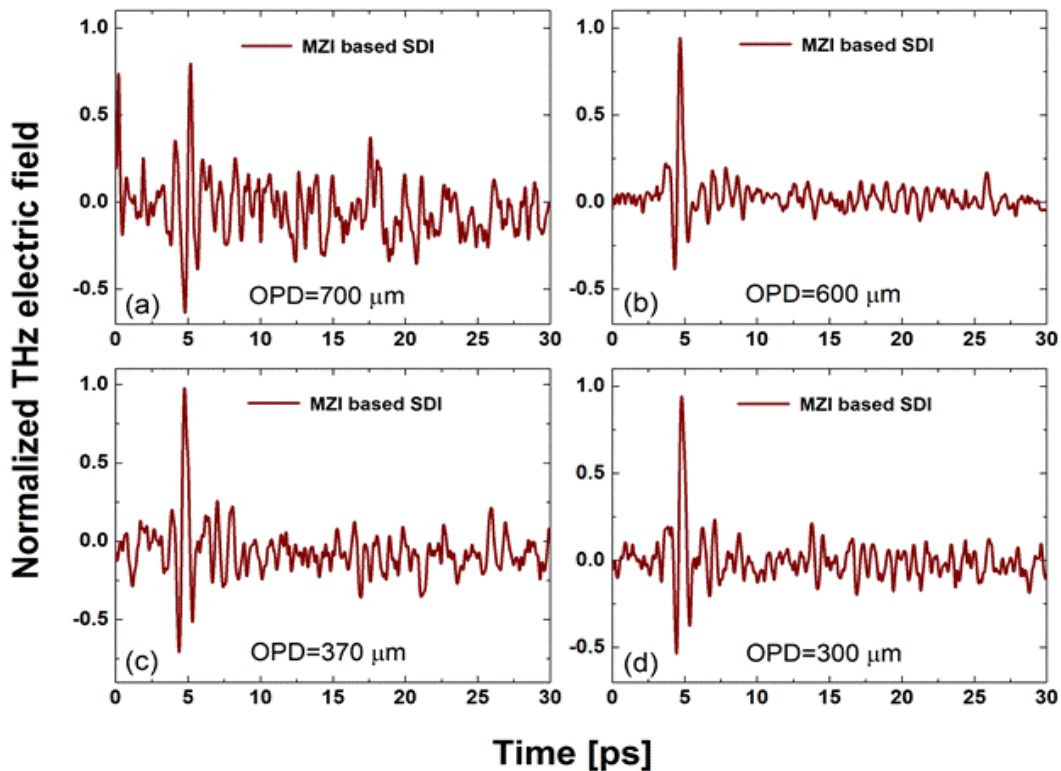


Figure 3.16 | THz electric field measurement obtained with the MZI based SDI technique at different OPD between the interfering optical probe beam pulses (a) 700 μm , (b) 600 μm , (c) 370 μm , and (d) 300 μm .

The SNR is calculated at each OPD from the corresponding Fourier power spectrum and plotted as we vary the OPD, as shown in Fig. 3.17. We find that the SNR increases as the OPD between the probe pulses decreases from 700 μm to 450 μm . However, further decreasing the OPD from 450 μm to 300 μm reduces the SNR. One could attribute this reduction in the SNR to the fact that working closer to the DC component of the interference signal (that is, closer to zero-OPD between the two interfering signals) will result in a situation where the signal is subject to many low-frequency noises in the laboratory environment. On the other hand, the reduction in the SNR for OPD above 450 μm could be attributed to the reduced contrast of the interference fringes when working far away from zero-OPD [10].

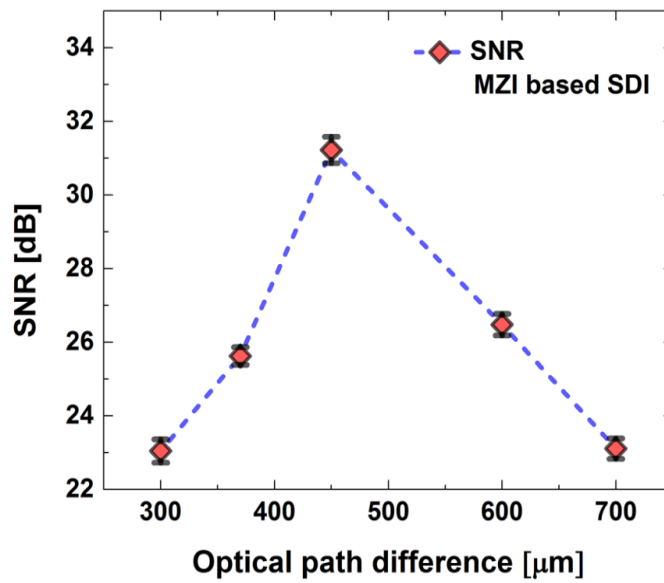


Figure 3.17 | Signal-to-noise ratio (SNR) of the THz electric field measurements dependence on optical path difference (OPD) between the two signals at MZI two arms. The dashed blue line is to guide the eye [10].

3.5.4 Dynamic range (DR) of MZI-based SDI technique in THz electric field measurement

In order to evaluate the DR of the MZI based SDI in THz electric field measurement, we applied the characteristic parameters of the laser used in the experiment (*i.e.* central wavelength $\lambda_o = 790 \text{ nm}$, and bandwidth $\Delta\lambda = 40 \text{ nm}$) along with the characteristic parameter of the spectrometer CCD camera (*e.g.* number of pixels of the CCD camera $N = 640$) in Eq. (3.5), which in turn defines the depth range of the SDI technique. We obtained a theoretical depth range of 2.203 mm. Hence, by considering that a change of 2π in phase is equivalent to a one

wavelength change in the OPD, with the depth range of our spectrometer, an OPD equivalent to $5,577\pi$ can be measured. In the EOS technique, the maximum measurable phase change is $\pi/2$. Therefore, the maximum measurable phase difference for the MZI based SDI technique is approximately 11,000 times greater than that for the conventional EOS technique. The maximum achievable DR, defined as the maximum measurable phase divided by the standard deviation of the phase noise when no THz is present, is measured to be $\sim 4 \times 10^5$ for the MZI based SDI technique, compared with $\sim 4 \times 10^2$ for the conventional EOS technique. This large DR of our system provides the potential for future THz nonlinear spectroscopic and imaging applications that require such large DR.

3.5.5 MZI-based-SDI technique at different THz peak electric field

Furthermore, in order to study the capabilities of the MZI based SDI technique and evaluate its performance in measuring different THz fields with reasonable SNR, we varied the THz electric field from 70 kV cm^{-1} to 4 kV cm^{-1} by varying the angle between the wire grid polarizers and without changing the THz wave polarization state.

The experiment is carried out for the same THz electric field values using the conventional EOS technique as well. Comparison between the THz amplitude signals measured from the temporal waveform with conventional EOS technique and MZI-based-SDI technique at different THz electric fields is depicted in Fig. 3.18.

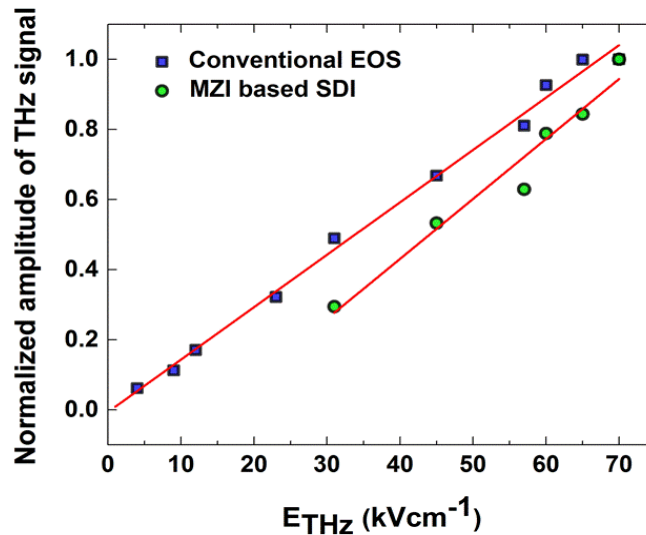


Figure 3.18| THz signal amplitude measurements dependence on THz peak electric field using conventional EOS (blue squares) and MZI based SDI (green circles) techniques. The red line is the linear fit.

Immediately, it is clear that using the conventional EOS, we could measure THz signals at lower THz electric field values ($\sim 4 \text{ kV cm}^{-1}$). However, when using MZI based SDI, we could not measure THz signal waveform when the THz electric field is $< 31 \text{ kV cm}^{-1}$.

This is attributed to inferior SNR of the THz measurement obtained with MZI-based SDI compared to conventional EOS. In other words, the inferior SNR of the MZI-based SDI measurement does not allow us to measure lower THz electric field signals ($< 31 \text{ kV cm}^{-1}$). As mentioned in section 3.5.2, there is potential for enhancing SNR in MZI-based SDI by employing the common self-referencing method [20], whereas this further enhancement is out of the scope of this thesis work.

References

- [1] G. Sharma, K. Singh, I. Al-Naib, R. Morandotti and Tsuneyuki Ozaki, *Opt. Lett.* **37**, 4338 (2012).
- [2] L. B. Elouga Bom, Y. Pertot, V. R. Bhardwaj, and T. Ozaki, *Opt. Express* **19**, 3077 (2011).
- [3] T. Ozaki, J. C. Kieffer, R. Toth, S. Fourmaux, and H. Bandulet, *Laser Part. Beams* **24**, 101 (2006).
- [4] N. Thiré, S. Beaulieu, V. Cardin, A. Laramée, V. Wanie, B. E. Schmidt, and F. Légaré, *Appl. Phys. Lett.* **106**, 091110 (2015).
- [5] X. Ropagnol, F. Blanchard, T. Ozaki, and M. Reid, *Appl. Phys. Lett.* **103**, 161108 (2013).
- [6] F. Blanchard, B. E. Schmidt, X. Ropagnol, N. Thiré, T. Ozaki, R. Morandotti, D. G. Cooke, and F. Légaré, *Appl. Phys. Lett.* **105**, 241106 (2014).
- [7] J. Hebling, A. G. Stepanov, G. Almási, B. Bartal, and J. Kuhl, *Appl. Phys. B* **78**, 593-599 (2004).
- [8] J. A. Fulop, L. Palfalvi, S. Klingebiel, G. Almasi, F. Krausz, S. Karsch, and J. Hebling, *Opt. Lett.* **37**, 557-559 (2012).
- [9] K. Singh, C. Dion, M. R. Lesk, T. Ozaki, and S. Costantino, *Rev. Sci. Instrum.* **82**, 023706 (2011).
- [10] A. Ibrahim, G. Sharma, K. Singh, T. Ozaki, *J. Infrared. Milli. Terahz. Waves* **37**, 837 (2016).
- [11] M. A. Choma, A. K. Ellerbee, C. Yang, T. L. Creazzo, and J. A. Izatt, *Opt. Lett.* **30**, 1162 (2005).
- [12] C. Joo, T. Akkin, B. Cense, B. H. Park, and J. F. de Boer, *Opt. Lett.* **30**, 2131 (2005).
- [13] J. Zhang, B. Rao, L. Yu, and Z. Chen, *Opt. Lett.* **34**, 3442 (2009).
- [14] N. F. Scherer, R. J. Carlson, A. Matro, M. Du, A. J. Ruggiero, V. Romero-Rochin, J. A. Cina, G. R. Fleming, and S. A. Rice, *J. Chem. Phys.* **95**, 1487 (1991).
- [15] E. Tokunaga, A. Terasaki, and T. Kobayashi, *Opt. Lett.* **17**, 1131 (1992).
- [16] X. D. Cao and D. D. Meyerhofer, *Opt. Lett.* **19**, 1837-1839 (1994).

- [17] T. J. Flynn, J. Opt. Soc. Am. A **14**, 2692 (1997).
- [18] D. Parshall and M. K. Kim, Appl. Opt. **45**, 451 (2006).
- [19] H. C. Hendargo, M. Zhao, N. Shepherd, and J. A. Izatt, Opt. Express **17**, 5039 (2009).
- [20] G. Sharma, K. Singh, A. Ibrahim, I. Al-Naib, R. Morandotti, F. Vidal and T. Ozaki, Opt. Lett. **38**, 15 2705 (2013).

Chapter 4

Innovative coherent THz detection techniques using SDI part II: Cross-polarized (CP) based SDI in terahertz electric field measurement

Outline

In this chapter, we discuss our novel fiber-based spectral domain interferometry (cross-polarized spectral-domain interferometry (CP-SDI)) scheme for THz-electric field measurement. The concept of the technique is explained, while the experimental realization of the concept is characterized and compared to the well-known conventional electro-optic sampling (EOS) THz detection technique, as well as the other SDI versions. The advantageous characteristics of the CP-SDI THz detection technique are superior to all of the aforementioned THz based on SDI detection techniques and that was manifested in the ultrahigh DR offered by the CP-SDI technique ($\sim 10^7$) compared to conventional EOS ($\sim 10^2$). Although the SNR of the technique is already comparable to the conventional EOS THz detection technique, two attempts to enhance the SNR of the CP-SDI THz detection technique are discussed: (i) by introducing a new referencing method to this version, and (ii) by designing a compact module of this version that has mitigated the vibrational noise significantly. Comparison between CP-SDI and MZI- SDI for THz electric field measurement is held, aiming at illustrating the advantages and the shortcomings of each technique.

4.1 The idea of the fiber interferometer: Concept of the CP-SDI scheme.

The major breakthrough of the CP-SDI design is that it offers a demonstration of an effective scheme for improved THz electric field measurement with higher DR and SNR, which is crucial for various applications of THz technology, including spectroscopic measurements. In

this new version of the SDI technique, we exploit the intrinsic phase delay between the fast and the slow axes of the birefringent fiber [1] (see Fig. 4.1(a) and Fig. 4.1(b)). The s - and p -polarization components of the probe pulse experience different refractive indices in the polarization-maintaining (PM) fiber, which results in the modification of the polarization state at its output, depending on the length of the fiber (l). In other words, the PM fiber creates two pulses; one propagating along the fast axis and the other propagating along the slow axis of the PM fiber, resulting in an OPD between the two. This is in addition to the OPD between the s - and p - components of the probe pulse that results from the birefringence introduced by the EO detection crystal, when the THz pulse and the probe pulse overlap in space and time. A common polarization direction that is neither of s - nor p -polarization (by using, for example, a polarizer) is chosen, to allow these two pulses to interfere. The OPD introduced by the THz electric field is measured from the interference signal of the two probe pulses as a change in the phase. The measured phase can be unwrapped by the same algorithms described earlier when the standard SDI version was discussed [2], leading to ultra-high DR for this new technique. The two orthogonal components of the probe pulse exiting the fiber cannot interfere, as they are cross polarized. In order to enable their interference, a polarizer is placed at the exit end of the PM fiber with its transmission axis at 45° with respect to the fast and slow axes. This allows a component of both s - and p -polarizations to pass through and to interfere in the spectrometer attached to the set up (same as the spectrometer discussed in section 3.2.1, Fig. 3.2). At the CCD camera plane, the spectral components of the two pulses interfere, thus allowing one to measure the phase difference between them. Just as in the conventional EOS methods, the THz electric field induces birefringence in the ZnTe detection crystal, which is read out by the probe pulse when it overlaps with the THz pulse within the crystal in space and time. However, in the CP-SDI method, this birefringence is converted into a change in the OPD (or the phase) between the two probe pulses using a PM fiber and a polarizer. Using the interference signal between the spectral components of these two pulses; one can measure the THz electric field as a change in the phase difference introduced by the THz pulse. Fig. 4.1(a) schematically depicts the concept of the PM fiber in which the fiber introduces a fixed OPD between the polarization components of the OPB. In Fig. 4.1(b) we explain the evolution of the process.

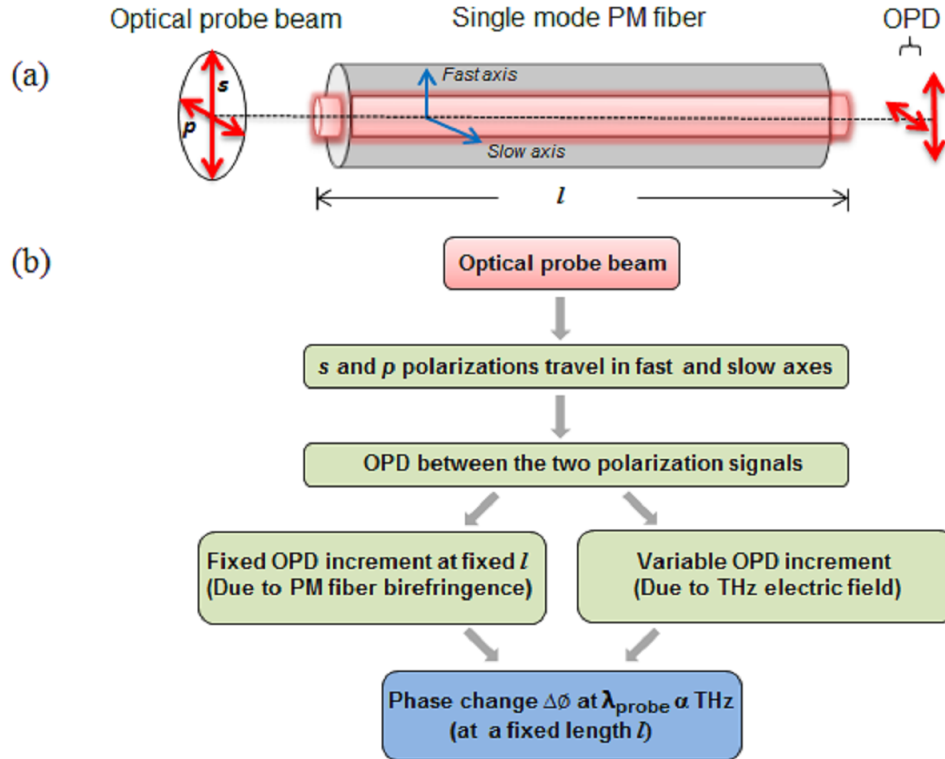


Figure 4.1 | PM fiber introduces optical path difference. (a) Elliptically polarized optical probe beam after traversing the detection crystal is coupled into the single-mode PM optical fiber where polarization components travel into fast and slow axes and at the output, an OPD is introduced between the two signals (b) The evolution process of the optical fiber introducing a fixed OPD between the two polarization components. In the presence of the THz signal, an additional OPD that is proportional to THz field strength is introduced between the two polarization states. The fixed OPD due to birefringence of the fiber will be systematic in the phase calculation while the variable OPD due to THz electric field induced birefringence in the ZnTe detection crystal is used to measure THz electric field pulse shape [3].

4.2 Experimental realization of CP-SDI technique for THz electric field measurement

Here we use the experimental setup illustrated in Fig. 4.2, where a femtosecond 800 nm laser beam is split by a beam splitter (BS) into two arms: the pump arm and the probe arm. The pump beam is used to generate the THz pulse using the tilted-pulse-front technique from a LiNbO₃ crystal [4,5] pumped with 0.96 mJ pulses. Single-cycle THz pulses with energies up to 0.3 μJ are generated with bandwidth extending from 0.1 to 3 THz from that arrangement. The probe beam is focused by a spherical plano-convex lens (L1), and then propagates through a hole in a parabolic off-axis mirror (PM4) and onto a 1-mm-thick <110> ZnTe detection crystal, where

it overlaps with the focused THz pulse. Another spherical plano-convex lens (L2) is used to collimate the optical probe beam after the ZnTe detection crystal.

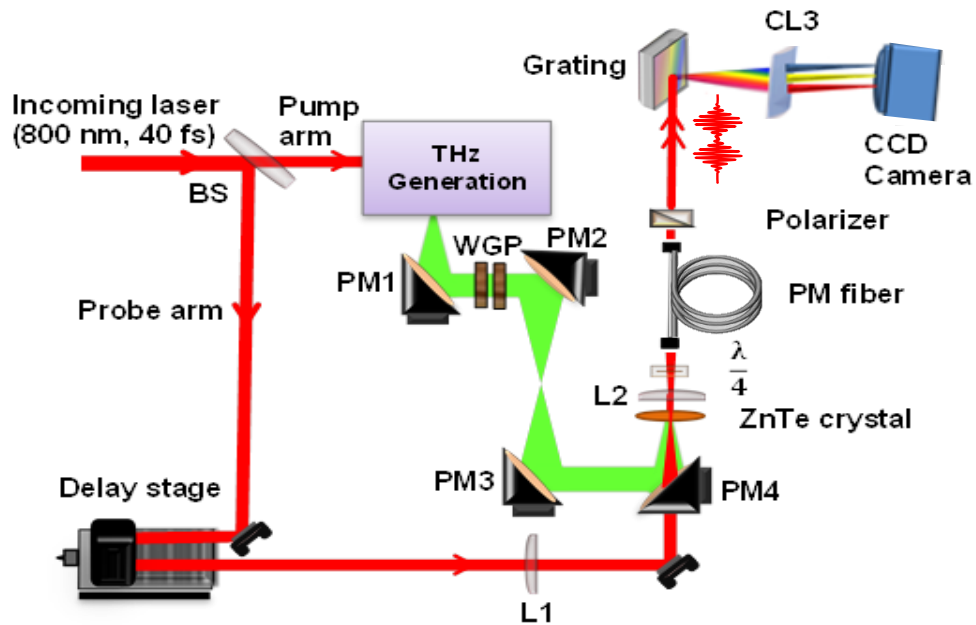


Figure 4.2 | Experimental set up of the CP-SDI technique for THz detection. A beam splitter (BS) splits the beam into a pump and probe arms for the generation and detection of THz, respectively. Spherical plano-convex lenses (L1, L2) focus and collimate the probe beam on and after the detection crystal respectively. Parabolic off-axis mirrors (PMs) guide the THz radiation to the detection crystal, where it spatially overlaps with the probe beam. Two wire grid polarizers (WGP) are used to control the electric field strength of THz radiation at the detection crystal. The spectrometer consists of a diffraction grating, a plano-convex cylindrical lens (CL3), and a two-dimensional (2D) CCD camera [3].

A quarter-wave plate is used before a single-mode PM optical fiber (Thorlabs, PM 780-HP) to convert the linear polarization state of the probe pulse to circular polarization without the presence of the THz pulse. Then the probe pulse is coupled into the PM fiber, with its polarization components (*s*- and *p*-) set along the two orthogonal birefringent axes of the PM fiber depending on the birefringence introduced in the ZnTe crystal by the THz electric field. The wire grid polarizers (WGP) are used to vary the THz peak electric field. The custom-made spectrometer (as discussed in section 3.2.1) consists of a diffraction grating (1200 grooves/mm), a plano-convex cylindrical lens CL3 ($f = 150$ mm), and a two-dimensional (2D) CCD camera (Dalsa Inc., CR-GM00-H6400, 480×640 pixels). We measure the phase change between the spectral components of the two polarization signals exiting the single mode PM fiber at a fixed

length, which is proportional to the THz electric field strength only. By varying the delay time between the THz pulse and the optical probe pulse using a delay stage, the temporal shape of the THz electric field can be plotted. The experimental data extraction is straightforward and carried out in real time by a LabView code that has been developed by our group [2]. Moreover, the measurement does not require any longer time than that taken by the conventional EOS technique.

The parameters of the PM optical fiber used in this study are summarized in Table 4.1.

| Parameter | Value |
|--|--------------------------------------|
| Numerical aperture | 0.12 |
| Core diameter | 4.5 μm |
| Attenuation | ≤ 4 dB/km @ 850 nm |
| Operating wavelength | 770 - 1100 nm |
| Second mode cut-off | 710 \pm 60 nm |
| Mode field diameter (1/e² fit -near field) | 5.3 \pm 1.0 μm @ 850 nm |
| Beat length | 2.4 mm @ 850 nm |
| Birefringence | 3.5 $\times 10^{-4}$ |

Table 4.1 | Parameters of the PM fiber used in the CP-SDI technique [3].

We note that propagation of 40 fs OPB pulses in such small core fiber (4.5 μm) could result in nonlinear effects those, in turn, will affect the SNR of the measurement. In order to avoid such undesirable nonlinear effects, we have attenuated the OPB power to ~ 3.5 mW (at 2.5 kHz repetition rate) before coupling it into the fiber by using a set of neutral density filters.

4.3 THz electric field measurements obtained with CP-SDI technique

We show in Fig. 4.3(a) a long temporal scan (> 30 ps) for the trace of the THz electric field measured using the conventional EOS technique, and in Fig. 4.3(b) the corresponding Fourier power spectrum. Further, by employing the CP-SDI technique, we obtained long temporal scan (> 30 ps) for the trace of the THz electric field, as depicted in Fig. 4.4(a) along with the corresponding Fourier power spectrum in Fig. 4.4(b). For both THz traces, the peak THz electric field was measured to be ~ 64 kVcm⁻¹. In the experiment to acquire the THz trace with the CP-SDI technique (shown in Fig. 4.4 (a)), we used an optical fiber length of 80 cm. At this length, the OPD between the two probe pulses will be ~ 400 μm (a temporal separation of ~ 1.33 ps) at a central wavelength $\lambda_0 = 790$ nm when they exit the fiber.

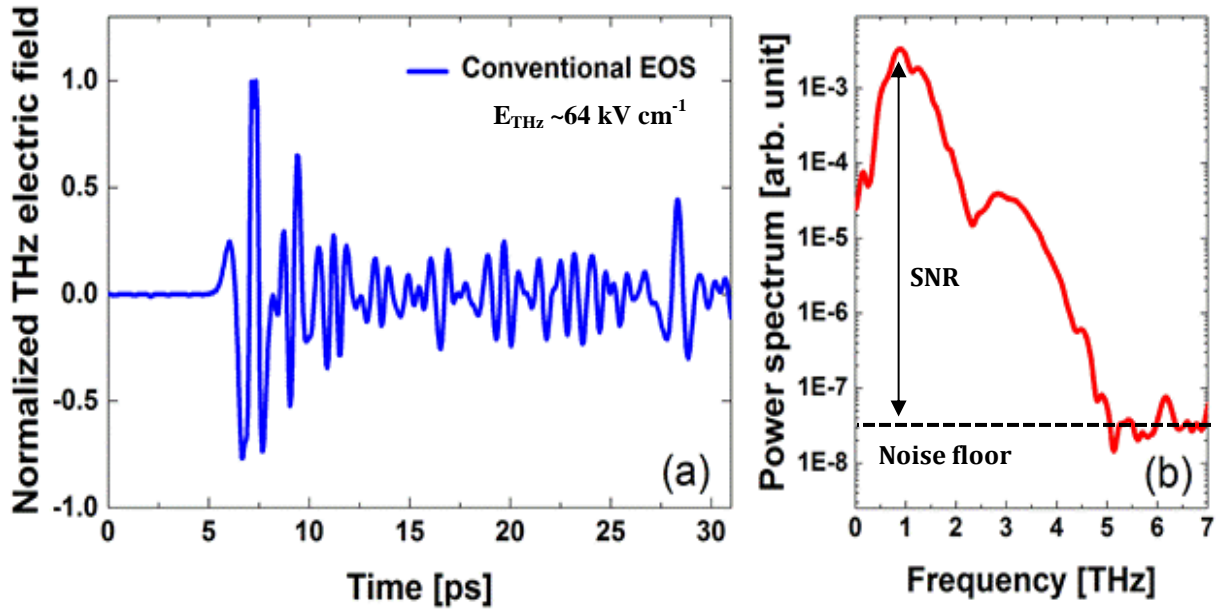


Figure 4.3| THz electric field trace obtained with conventional EOS technique (a), and the corresponding Fourier power spectrum of the THz trace obtained with the conventional EOS technique (b).

Both THz traces obtained with EOS (Fig. 4.3(a)) and CP-SDI (Fig. 4.4(a)) techniques show a few-cycle THz pulse. Further, for both THz traces at a time ~ 7.3 ps, the THz signal increases

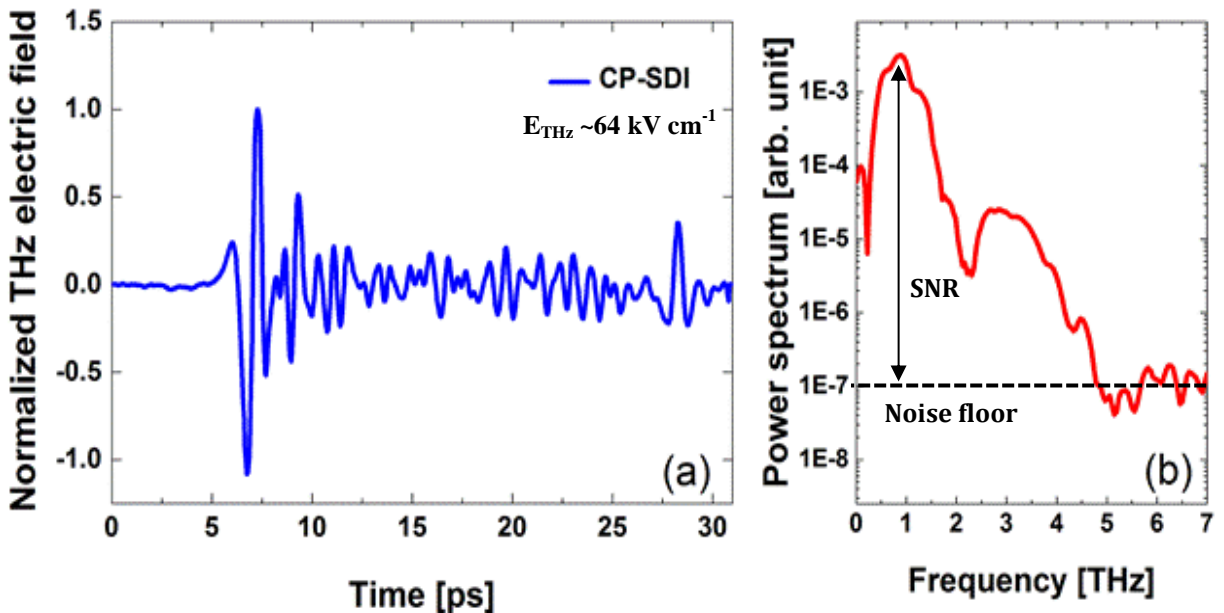


Figure 4.4| THz electric field trace obtained with CP-SDI technique (a), and the corresponding Fourier power spectrum of the THz trace obtained with CP-SDI technique (b).

with considerable amplitude, indicating the main peak of the THz pulse, while at a time ~ 28.3 ps, the signal increases again with a smaller amplitude, corresponding to the first reflection of the THz electric field in the ZnTe detection crystal. The oscillations from ~ 8 ps to ~ 26.5 ps are caused primarily by the absorption and subsequent emission of light by water-vapor molecules. Once more, if we compare between THz traces obtained with the standard SDI technique (Fig. 3.6(a)) -where a 300 μm -thick glass plate was utilized to introduce a fixed OPD between the two probe pulses reflecting from its front and the back surfaces- and that obtained with the CP-SDI technique (Fig. 4.4(a)), we can see that the temporal scanning window limitation of only 3 ps is eliminated in the THz trace obtained with the CP-SDI technique. Moreover, the slight discrepancy in the main pulse shape in Fig. 4.3(a) and Fig. 4.4(a) is due to the over-rotation effect on the trace obtained with the conventional EOS technique, as we will discuss in the coming section.

4.4 Characterization of the CP-SDI THz detection technique

4.4.1 Fiber length choice

In SDI measurements, the choice of a working point in OPD (*i.e.* fixed OPD) is crucial in determining the SNR of the measurement.

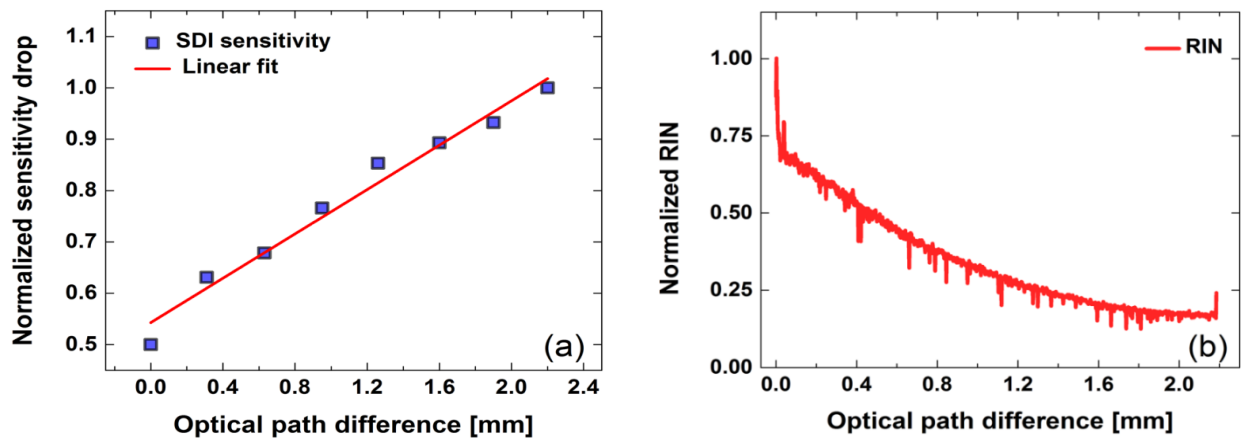


Figure 4.5| Dependence of noise and sensitivity of SDI technique on OPD between the interfering signals. (a) Normalized sensitivity drop and (b) normalized RIN are plotted against OPD. The red solid line in (a) is a linear fit. The drop in the sensitivity of the detection technique is low for smaller OPD whereas RIN is high for smaller OPD [3].

Error in the phase measurement is dominated by relative intensity noise (RIN) at lower OPD, whereas at higher OPD it is dominated by low sensitivity, as depicted in Fig. 4.5(a) and Fig.

4.5(b) [3]. RIN is calculated as the standard deviation of the Fourier transformed data measured at the spectrometer over 60 seconds. RIN primarily arises due to intensity fluctuations in the laser pulses and is different for different laser sources. Sensitivity drop is a fundamental problem in the SDI technique, and arises due to limited bandwidth falling on each pixel of the CCD camera. The interference fringes are convolved with the *rec.* function representing a single pixel of the CCD camera. However when carrying out the Fourier transform, the *rec.* function will transform to *sinc* function. In SDI the width of the *sinc* function depends on the pixel width [6]. Thus with the limited size of the camera pixels causes averaging of the interferometric fringes, leading to lower fringe contrast or higher sensitivity drop at longer OPD where modulation frequency is higher [6]. A balance is achieved somewhere between minimum and maximum OPD, where phase measurement error is minimum. The sensitivity of the SDI detection technique is enhanced for smaller OPD, whereas the RIN is higher for smaller OPD as depicted in Fig. 4.5(a) and Fig. 4.5(b). Bearing that in mind, we attempt to choose the appropriate length of the fiber that can provide the best SNR for our THz electric field measurement. For this purpose, PM fibers of different lengths, ranging from 40 to 240 cm (with the corresponding OPD between the optical probe pulses at the exit end of the PM fiber of 200 to 1200 μm) were used. At each fiber length, a THz temporal trace was recorded for the same THz peak electric field (64 kV cm^{-1}).

We show in Fig. 4.6 the different THz waveforms obtained at different selected fiber lengths (different OPD between signals exiting the PM fiber). One can see from the temporal waveforms that the smoother baseline (zero-line before THz main pulse) is observed at OPD=600 μm (*i.e.* fiber length =120 cm). However, even smoother THz temporal waveform and smoother baseline (better SNR) is registered for OPD=400 μm (*i.e.* fiber length 80 cm). In Fig. 4.6(d) one can notice that the THz waveform is slightly different than those in (a), (b) and (c). A possible reason for this difference could be due to a slight change in the alignment of the OPB and THz during the process of replacing different fiber lengths. Moreover, we show in Fig. 4.7 the SNR measured using the CP-SDI THz detection technique for various OPD between the optical probe pulses. Here the SNR is measured from Fourier power spectra of each THz waveform. Our experimental findings show that the SNR increases as the OPD between the probe pulses decreases from 1200 μm to 400 μm . However, further decreasing the OPD from 400 μm to 200

μm reduces the SNR. This could be explained using Fig. 4.5(a) and Fig. 4.5(b), as the sensitivity of the SDI technique is enhanced when the OPD decreases at $\text{OPD} > 400 \mu\text{m}$, while the low

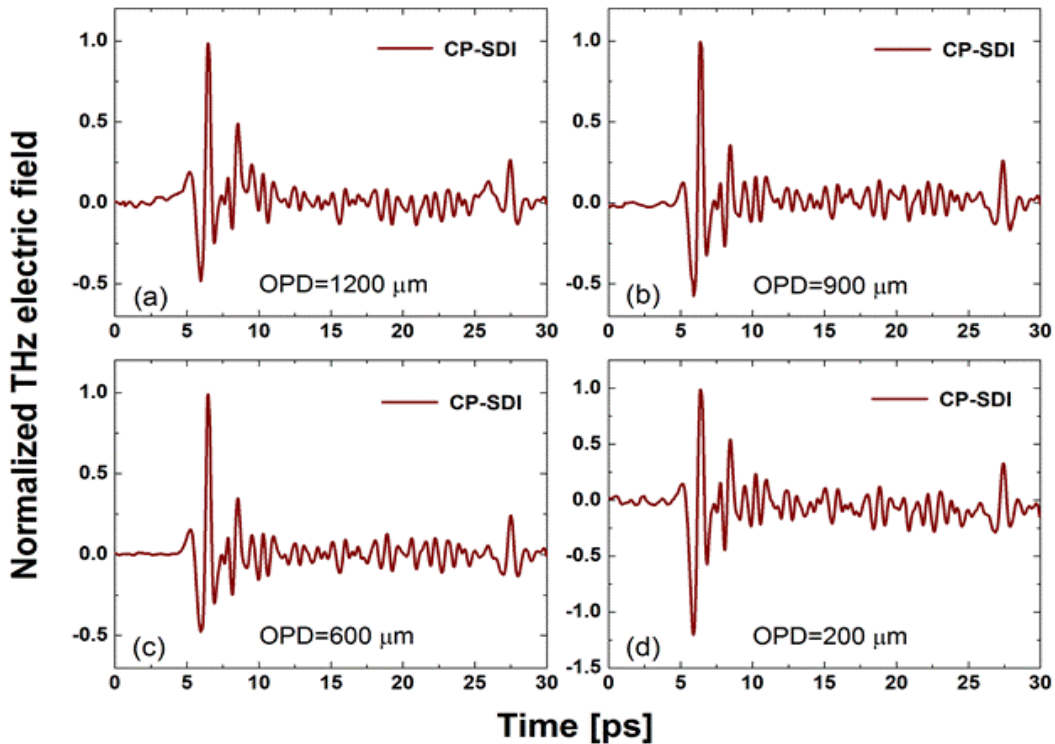


Figure 4.6 | THz electric field measurement obtained with the CP-SDI technique at different (fiber length) OPD between the interfering optical probe beam pulses (a) (240 cm) $1200 \mu\text{m}$, (b) (180 cm) $900 \mu\text{m}$, (c) (120 cm) $600 \mu\text{m}$, and (d) (40 cm) $200 \mu\text{m}$.

-frequency noises of the laboratory environment affecting the measurement in a great deal could be the reason for decreasing the SNR at smaller OPD ($< 400 \mu\text{m}$).

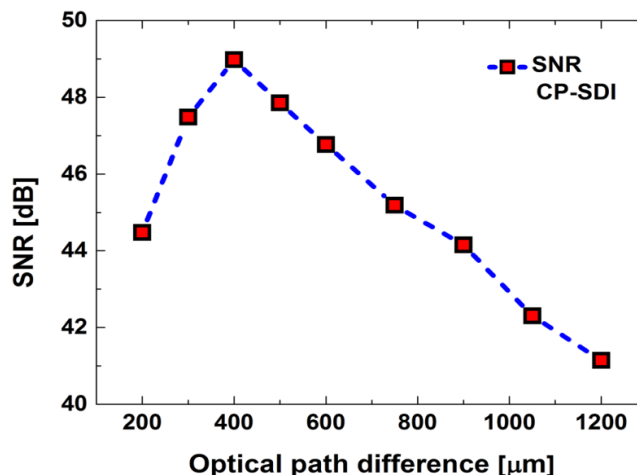


Figure 4.7 | Dependence of the signal-to-noise ratio of the THz electric field measurements on the optical path difference between the two signals at the exit end of the optical fiber in the CP-SDI technique for THz electric field measurement [3].

According to these experimental results, we concluded that 400 μm OPD (offered by 80-cm fiber length) is the best for our THz electric field measurement. Thus, we used 80 cm fiber length for all CP-SDI THz electric field measurement in this thesis work [3].

4.4.2 Signal-to-noise ratio (SNR)

Figure 4.3(b) shows the corresponding Fourier power spectrum of the THz electric field obtained from the conventional EOS technique, while Fig. 4.4(b) shows the corresponding Fourier power spectrum of the THz electric field obtained from the CP-SDI technique (at fiber length 80 cm). From these spectra, we find that the measured SNR is ~ 48.97 dB for the CP-SDI technique compared to ~ 52.17 dB for conventional EOS technique. As discussed in section 3.2.3.1, the SNR for the standard SDI technique was measured to be ~ 38.12 dB, compared to ~ 48.97 dB for the CP-SDI technique. We could also evaluate the SNR from the temporal shape of the THz pulse, by taking the ratio of the THz peak to the standard deviation of the baseline (the signal that is before 1 ps) in the THz temporal trace. Following such approach, the SNR of the THz pulse measured with the CP-SDI technique (Fig. 4.4(a)) is ~ 279 compared to ~ 418 for the THz pulse obtained with the conventional EOS technique (Fig. 4.3(a)). At the same time, the SNR of THz pulse obtained with the standard SDI (Fig. 3.6(a)) is ~ 45 [3].

4.4.3 Over-rotation limitation

In order to compare the shape of the THz main pulse obtained with the conventional EOS and the CP-SDI techniques, short temporal scans (5 ps-long each) at different THz electric fields are shown in Fig. 4.8(a) and 4.8(b). One can see that the THz pulse obtained at high THz electric fields (64 kV cm^{-1} - 54 kV cm^{-1}) with conventional EOS in Fig. 4.8(a) suffers from over-rotation in the parts indicated by arrows, which alter the shape of the pulse. At lower THz electric fields ($\leq 47 \text{ kV cm}^{-1}$) the THz pulse measured with the conventional EOS technique returns to its normal shape. Meanwhile, when using the CP-SDI technique for the same THz electric fields, over-rotation is always avoided even at higher values of the THz electric field, as shown in Figure 4.8(b) [3]. Worth to note that there is a slight change in THz waveform obtained by both techniques, which can be attributed to the change of the alignment of the OPB and THz beam on the detection crystal. That could take place during replacing the detection schemes.

4.4.4 Dynamic range (DR) of CP-SDI technique

Indeed, both high DR and high SNR [7] are crucially required in coherent THz detection techniques. For instance, high DR measurement is especially important in THz electric field measurement where one needs to compare the waveform of intense THz pulses with relatively weak THz signals (such as the THz signal after experiencing strong absorption, or the nonlinear THz signal). Large DR is also required in THz-TDS measurements in order to avoid misinterpretation of experimentally obtained data [8].

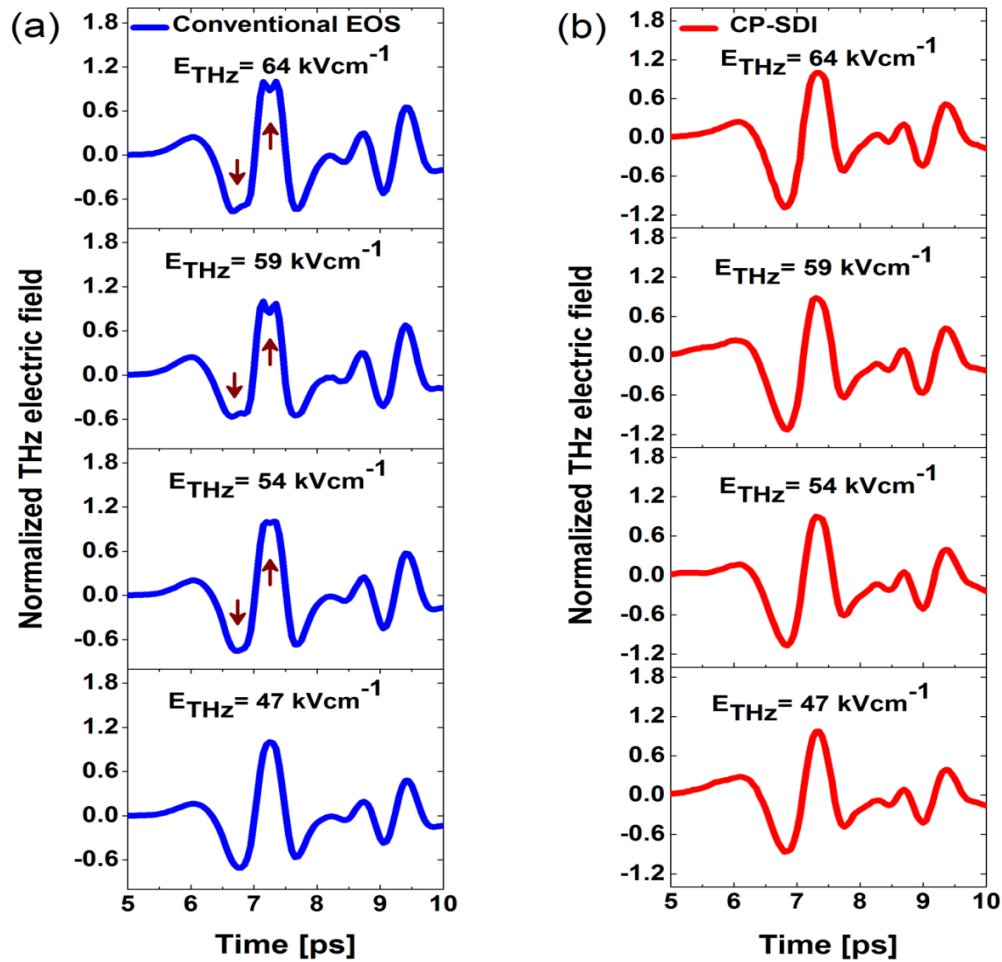


Figure 4.8 | Short temporal scans of different THz electric fields (E_{THz}) obtained with (a) the conventional EOS (blue line) and (b) the CP-SDI (red line) techniques at various E_{THz} from 64 kVcm^{-1} to 47 kVcm^{-1} . Over-rotation effect is evident in the conventional EOS (indicated by the arrows) at E_{THz} of 64 kVcm^{-1} , 59 kVcm^{-1} , and 54 kVcm^{-1} . At lower $E_{\text{THz}} \leq 47 \text{ kVcm}^{-1}$, the pulse obtained with the conventional EOS returns to its normal shape, while in the CP-SDI technique over-rotation effect has been avoided even at higher $E_{\text{THz}} = 64 \text{ kVcm}^{-1}$ [3].

When we apply the parameters of our system (central wavelength $\lambda_0 = 790$ nm, bandwidth $\Delta\lambda = 40$ nm, and the number of pixels of the CCD camera $N = 640$) in Eq. (3.5) (which defines the depth range of the SDI technique) yields a theoretical OPD range of 2.203 mm. Considering a change of 2π in the phase for one wavelength change in the OPD, the maximum overall phase change that we can measure with our CP-SDI technique is $5,577\pi$ which is approximately 11,000 times greater than the maximum measurable phase change obtained with the conventional EOS technique. Moreover, the maximum achievable DR for CP-SDI technique with our current setup is measured to be 7×10^6 , which is 4 orders of magnitude higher than the maximum achievable DR for our conventional EOS configuration of 6×10^2 . Meanwhile in the standard SDI the maximum achievable DR is 6×10^5 when using the same spectrometer and laser source.

4.4.5 CP-SDI technique at different THz electric field

In order to evaluate the capability of our technique to measure different THz peak electric fields

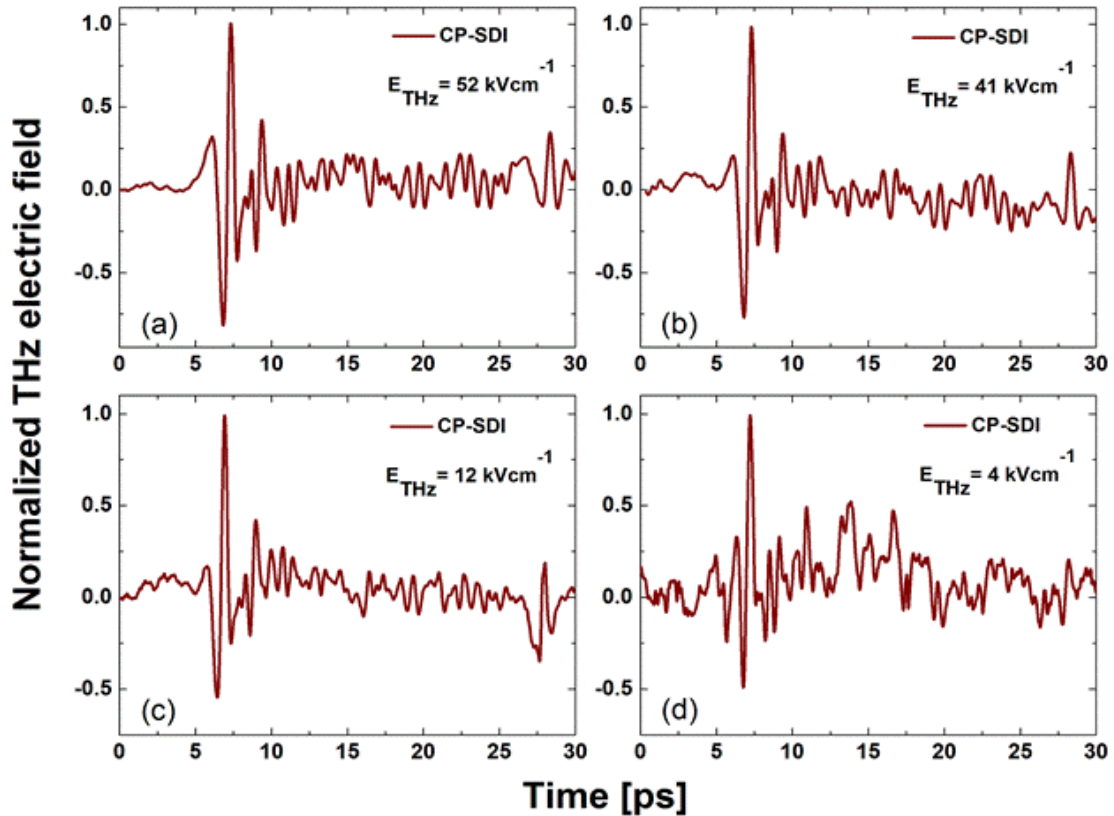


Figure 4.9 | THz electric field measurement obtained with the CP-SDI technique using 80 cm length PM fiber at different THz peak electric field E_{THz} (a) ~ 52 kVcm $^{-1}$, (b) ~ 41 kVcm $^{-1}$, (c) ~ 12 kVcm $^{-1}$, and (d) ~ 4 kVcm $^{-1}$.

with reasonable SNR, the THz peak electric field was varied from $\sim 4 \text{ kV cm}^{-1}$ to $\sim 64 \text{ kV cm}^{-1}$ by using two wire-grid polarizers. The value of the THz peak electric field amplitude (E_{THz}) is measured with conventional EOS technique using the modulation formula in Eq. (4.1) [9,10].

$$\frac{A - B}{A + B} = \sin \theta = \frac{2\pi r_{41} n_o^3 L t_{\text{ZnTe}} t_{\text{Si}}^N E_{\text{THz}}}{\lambda_o} \quad (4.1)$$

Here, A and B are the signals from the balanced photodetectors in EO detection configuration, θ is the phase shift induced by the THz peak electric field, r_{41} is the electro-optic coefficient of the ZnTe detection crystal, n_o is the refractive index of ZnTe, L is the ZnTe thickness, Fresnel transmission coefficients t_{ZnTe} for ZnTe and t_{Si} for the silicon wafer, N is the number of silicon wafers, and λ_o is the central wavelength.

We show in Fig. 4.9 the long THz temporal traces (30 ps) obtained with the CP-SDI technique at different selected THz electric fields. One can see as we decrease the THz electric field from 52 kV cm^{-1} to 4 kV cm^{-1} , the trace becomes noisier.

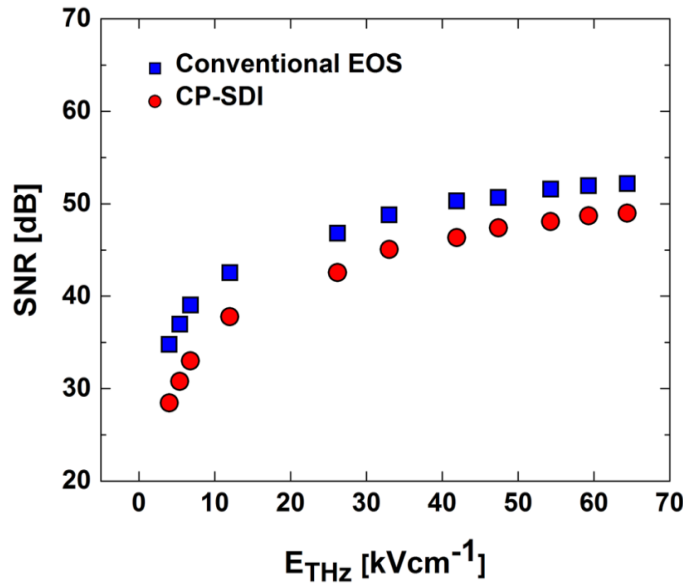


Figure 4.10 | Comparison between SNR of the conventional EOS (blue squares) and CP-SDI (red circles) techniques for THz electric field measurement.

However, even at a lower THz electric field ($E_{\text{THz}} \sim 4 \text{ kV cm}^{-1}$), we could detect THz pulse, but with a considerable amount of noise (due to vibration) to the extent that we could not distinguish the first THz reflection peak from the 1 mm-thick ZnTe detection crystal.

We show in Fig. 4.10 the variation of SNR (calculated from the Fourier power spectra) at different THz peak electric fields for both conventional EOS and CP-SDI techniques. At THz peak electric field of 64 kV cm^{-1} , we could measure SNR of $\sim 48.97 \text{ dB}$ for the THz electric field measurement obtained with CP-SDI technique, compared to $\sim 52.17 \text{ dB}$ obtained with conventional EOS technique. Meanwhile, at THz field of 4 kV cm^{-1} , we could measure SNR of 28.45 dB for the CP-SDI technique compared to 34.77 dB for the conventional EOS technique. These experimental findings are indicative of the potentials of the new technique in measuring higher THz electric fields as well as lower fields. Further enhancement in SNR of the new CP-SDI technique could be achieved if a subtle referencing method is implemented in the setup, which could enhance the SNR considerably by mitigating the noise due to mechanical vibration and laser fluctuations in the setup. The vibrations in our optical table originate from different sources, for example, there are several pumps and chillers required for operating the Ti: sapphire laser and its amplifiers. These motorized equipment create vibrations in the ground and upper building in the range $10\text{-}500\text{Hz}$, as well they cause acoustic noise ($>20 \text{ Hz}$). All the aforementioned vibrations sources can affect by adding more phase values (noise values) on the top of the phase value due to THz. However, with the current existing vibrational noises, we believe that our experimental findings manifest the potentiality of the CP-SDI technique in measuring lower THz electric field signals with good SNR.

4.4.6 Measurement of polarization dependence using CP-SDI technique

In order to enhance the SNR of the THz electric field measurement, several parameters in the experimental setup required to be optimized. Among those parameters are, for instance, polarization directions of both the optical probe beam (OPB) and the THz beam with respect to the ZnTe detection crystal (001) axis. Optimal orientation for those polarizations with respect to the ZnTe detection crystal (001) is crucial in determining the SNR of any THz electric field measurement using EOS techniques [11]. We, therefore attempted measurements of the THz pulse in (110)-oriented ZnTe aiming at enhancing the THz measurement efficiency as a function of the angles of the OPB polarization and the THz polarization with respect to the crystal (001) axis. In Fig.4.11, we schematically illustrate the THz beam and OPB polarizations with respect to ZnTe (001) axis. Moreover, we denote α and ϕ as the angles of the THz beam polarization and the OPB polarization respectively both with respect to the ZnTe crystal (001) axis. We varied the azimuthal angle of the ZnTe detection crystal in 10° -step in the range from 0° to 360° while at

each step we measured the THz electric field temporal waveform using CP-SDI technique (similar to temporal waveform depicted in Fig. 4.4(a)). Further, the maximum THz amplitude was determined at each step from the temporal waveform. We show in Fig. 4.12 the measured maxima of the THz amplitude as a function of the ZnTe crystal's azimuthal angle α . We have studied three cases: (i) when the THz polarization is perpendicular to the OPB polarization (*i.e.* $\varphi = \alpha + 90^\circ$), (ii) when the THz beam polarization is at 45° with the OPB polarization (*i.e.* $\varphi = \alpha + 45^\circ$), and (iii) when the THz beam polarization is parallel with the OPB polarization (*i.e.* $\varphi = \alpha$).

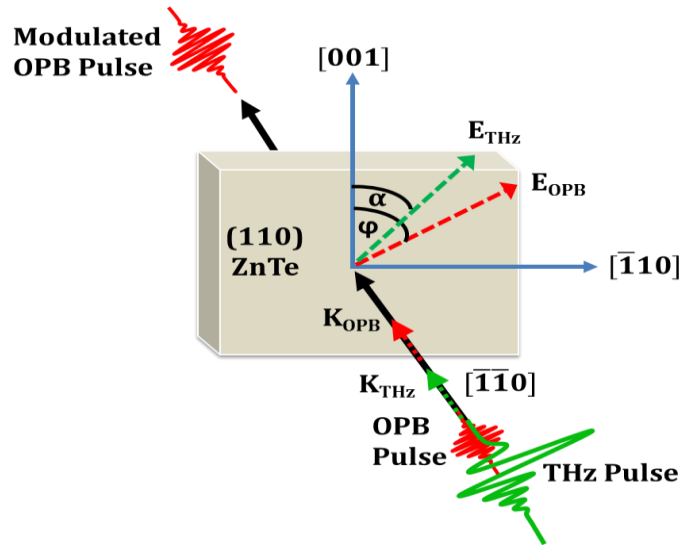


Figure 4.11 | Schematic representation of (001) ZnTe detection crystal with angles of the THz beam and optical probe beam (OPB) polarization orientation with respect to the crystal [001] axis. K_{THz} and K_{OPB} indicate the propagation directions of the THz and the OPB, respectively.

We observed, while rotating the crystal around the (110) axis, in case (i) the measured THz amplitude shows two absolute maxima at 90° and 270° as depicted in Fig. 4.12(a), in case (ii) the THz amplitude shows four absolute maxima, as depicted in Fig. 4.12(b), and in case (iii) the THz amplitude shows two absolute maxima similar to those observed in case (i) but inverted, as depicted in Fig. 4.12(c). We ignored the sign of the amplitude in all three cases. Our experimental findings in Fig. 4.12 agree well with results in P. Planken *et al.* carried out via conventional EOS technique [11] and we concluded that the maximum THz signal is realized when $\varphi = \alpha + 90^\circ$ or $\varphi = \alpha$. Consequently, for enhancing the SNR of the THz measurement, one should adopt the precise polarization angles of the THz beam and OPB with respect to (001) axis of ZnTe detection crystal.

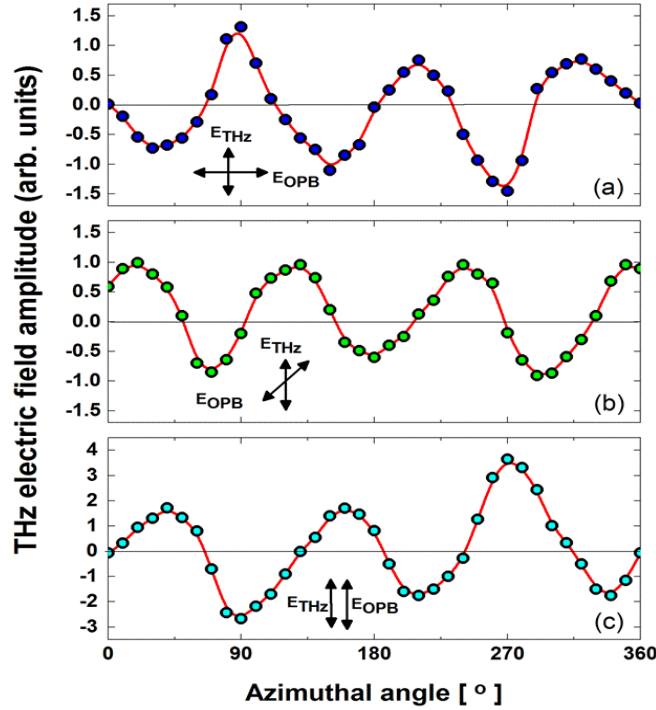


Figure 4.12 | ZnTe detection crystal's azimuthal angle dependence on the detected THz electric field amplitude for different angles between the OPB and THz beam polarizations. (a) $\varphi = \alpha + 90^\circ$, (b) $\varphi = \alpha + 45^\circ$, and (c) $\varphi = \alpha$.

In this thesis work, we have chosen to work with the orientation depicted in Fig. 4.12(c): OPB polarization parallel to THz beam polarization in ZnTe detection crystal since that orientation offers maximum birefringence around $\alpha = 270^\circ$.

4.5 Attempting to improve the SNR of the CP-SDI technique for THz electric field measurement

Two attempts are carried out in order to enhance the SNR of the CP-SDI technique for THz electric field measurement by (i) employing a new referencing method and (ii) designing a compact module for CP-SDI. Both attempts for increasing the SNR have been carried out in a different beam time at the Advanced Laser Light Source (ALLS) laboratory of the INRS, with different experimental conditions. For instance, our THz setup has been moved to a new optical table far away from the main Ti:sapphire laser sources and consequently a new major realignment of the THz set up took place, resulting in a slightly different THz pulse shape from previously discussed results in section 4.3. Moreover, we have observed a significant amount of vibrations in the new location of our THz set up, which significantly affects the SNR of the THz

electric field measurement via CP-SDI technique. Moreover, in this section, we used a 2-mm-thick ZnTe detection crystal instead of 1 mm-thick ZnTe in an attempt to compensate for the SNR and to increase the spectral resolution for the THz measurement. Therefore, the SNR of the THz electric field measurements obtained in this section cannot be compared with those obtained previously in section 4.3.

4.5.1 New referencing method in CP-SDI technique for THz electric field measurement

We have demonstrated successfully the novel idea of CP-SDI in THz electric field measurement so far, as discussed in section 4.2 and 4.3. However, the SNR of the CP-SDI is still inferior to that of the conventional EOS technique for THz electric field measurement. Indeed the self-referencing method has proven itself capable of eliminating the phase noise due to vibration and laser fluctuations and thus in turn enhances the overall SNR of the THz measurement in the standard SDI technique [12]. However, employing the common self-referencing method in CP-SDI technique is challenging and not viable, because in the common self-referencing method, the probe beam must sample at least two spatial points, one with finite THz field and the other with zero THz field. Further, the two beams must propagate through a similar optical path, so that the information from the probe beam at zero THz field point could be used as the reference. However, the use of the fiber in the CP-SDI technique limits the spatial information to only one point in the THz beam, thus making the common self-referencing a challenge. Thus, to further enhance the SNR of the CP-SDI technique for THz electric field measurement, we have attempted a new method for referencing, as depicted in Fig. 4.13. Here, the schematic of this new method is illustrated, where an optical chopper is placed in the THz beam path, thus alternately blocking and unblocking the THz beam by the chopper blade while the CCD camera (SK1024VPD, 1024 pixel, $10 \times 10 \mu\text{m}$, Schäfter+Kirchhoff Inc.) alternately records fringe frames without and with carrying the effect of the THz on them. The THz waveform is reconstructed by sampling in equivalent time while the delay between the THz pulse and the optical probe laser pulse is varied by using a delay line. At each position of the delay line, two consecutive image frames (Frame 1 and Frame 2 as depicted in Fig. 4.13) are acquired within a short time, so that the noise contained in the two image frames have approximately the same value. We denote the signal information obtained from Frame 1 as the reference signal that contains only the noise information, while the one obtained from Frame 2 as

the THz signal plus the noise signal information. By subtracting the former from the latter, we obtain the resulting pure THz waveform information without vibrational noise for one temporal point in the scan length.

Data acquisition and processing are carried out through a LabVIEW code developed in our THz group, as described earlier in section 3.2.2. Thus, by following such an approach, we could eliminate the noise present in the THz measurement. Before employing the new referencing method in the CP-SDI technique, a THz temporal trace was obtained by the conventional EOS technique for comparison purposes, as shown in Fig. 4.14(a).

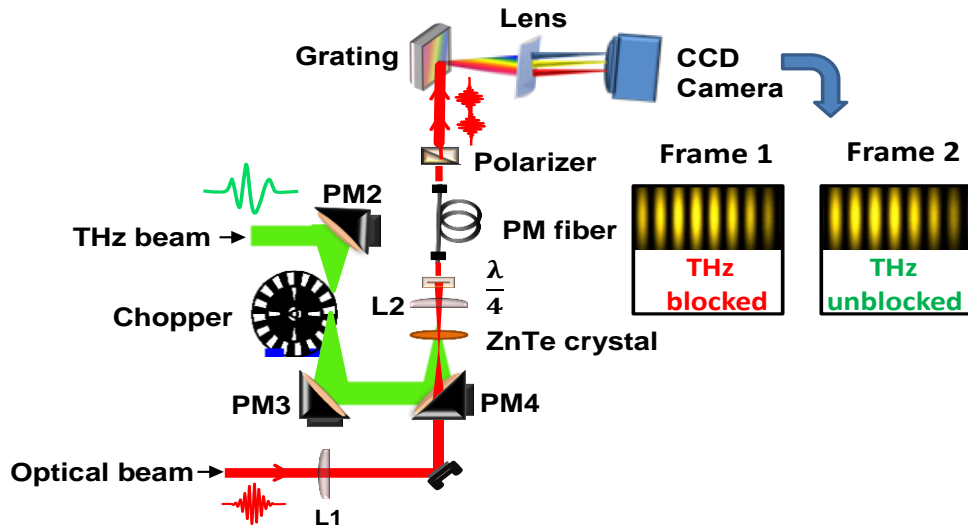


Figure 4.13 | Partial schematic of the THz experimental set up where the CP-SDI technique for THz detection incorporated with the chopper used to realize the new referencing method in CP-SDI technique. The chopper synchronously block-unblock the THz beam. The interferograms in the CCD camera frames 1 and 2 are representing THz blocked and unblocked states respectively.

A THz pulse was recorded, where the THz signal increases with considerable amplitude indicating the main peak of the THz pulse at ~ 6.2 ps, while at a time ~ 48.5 ps, the signal increases again with smaller amplitude, corresponding to the first reflection of the THz electric field in the 2 mm-thick ZnTe detection crystal. The oscillations from ~ 7.4 ps to ~ 46 ps are caused primarily by the absorption and subsequent emission of light by water-vapor molecules. The inset shows a magnified region of the THz baseline (1 – 4 ps), where we could measure the temporal SNR as the ratio between the THz peak value and the standard deviation of the baseline. In order to avoid over-rotation effects in the THz electric field measurement via conventional EOS technique, we have lowered E_{THz} to ~ 31 kV cm $^{-1}$ by using wire-grid polarizers. In Fig. 4.14(b) we show the corresponding Fourier power spectrum of a part of the THz pulse

(only 7 ps) in Fig. 4.14(a). From the Fourier power spectrum, we calculate the SNR to be better than 51.46 dB while the temporal SNR is measured to be better than 637. By exploiting standard CP-SDI technique (*i.e.* CP-SDI technique without implementing the new referencing method), a THz temporal trace was obtained, as shown in Fig. 4.15(a). A THz pulse was recorded, where the THz signal increases with considerable amplitude indicating the main peak of the THz pulse at ~ 5.5 ps.

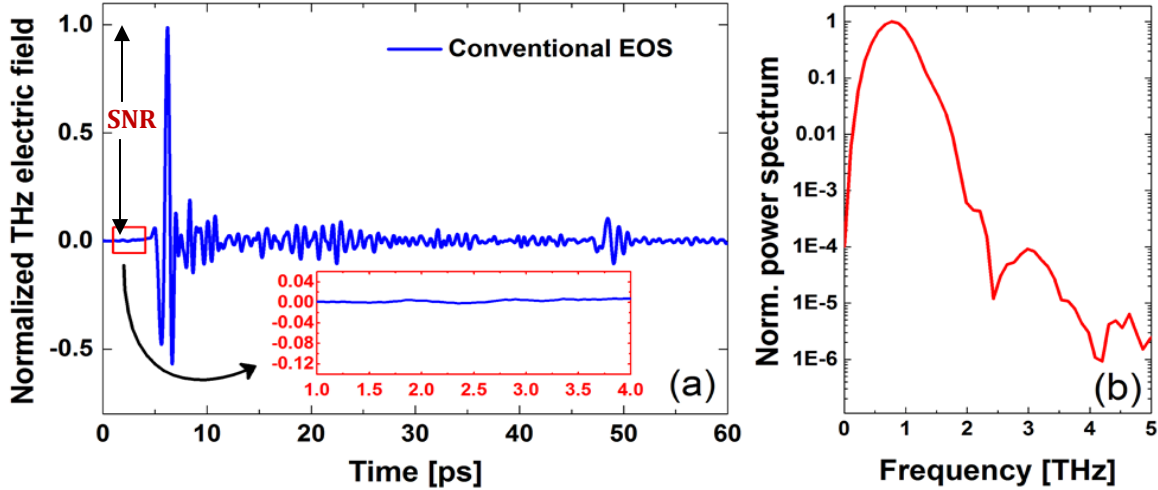


Figure 4.14 | THz electric field trace obtained with conventional EOS technique (a) the inset in (a) shows a magnified temporal noise. The corresponding Fourier power spectrum of the THz trace obtained with conventional EOS technique (b).

Owing to the significant vibrational noise level in the setup, we could not distinguish the first THz reflection signal from the noise signal level in the measurement. The inset shows a magnified region of the THz baseline (1 – 4 ps) where we could measure the temporal SNR. Here, we have not lowered the THz electric field when using the standard CP-SDI technique ($E_{\text{THz}} = 54 \text{ kV cm}^{-1}$) and yet, over-rotation effects in the THz trace are avoided. Now by implementing the new referencing method in the CP-SDI technique, a THz temporal trace was obtained at $E_{\text{THz}} = 54 \text{ kV cm}^{-1}$, as shown in Fig. 4.15(b). We note that the waveform in this case is smooth, with the main peak of the THz pulse at ~ 5.5 ps accompanied this time by a clear first THz reflection peak at ~ 48.3 ps. The appearance of the first reflection peak is an indicative of the efficiency of our new referencing method in removing a considerable amount of vibrational noise level in the setup. The inset shows a magnified region of the THz baseline (1–4 ps) where we could measure the temporal SNR. In Fig. 4.15(c) we show the amount of phase noise that the

new referencing method has successfully removed. Moreover, we show in Fig. 4.15(d) a comparison between the Fourier spectra of the THz traces obtained with and without employing the new referencing method.

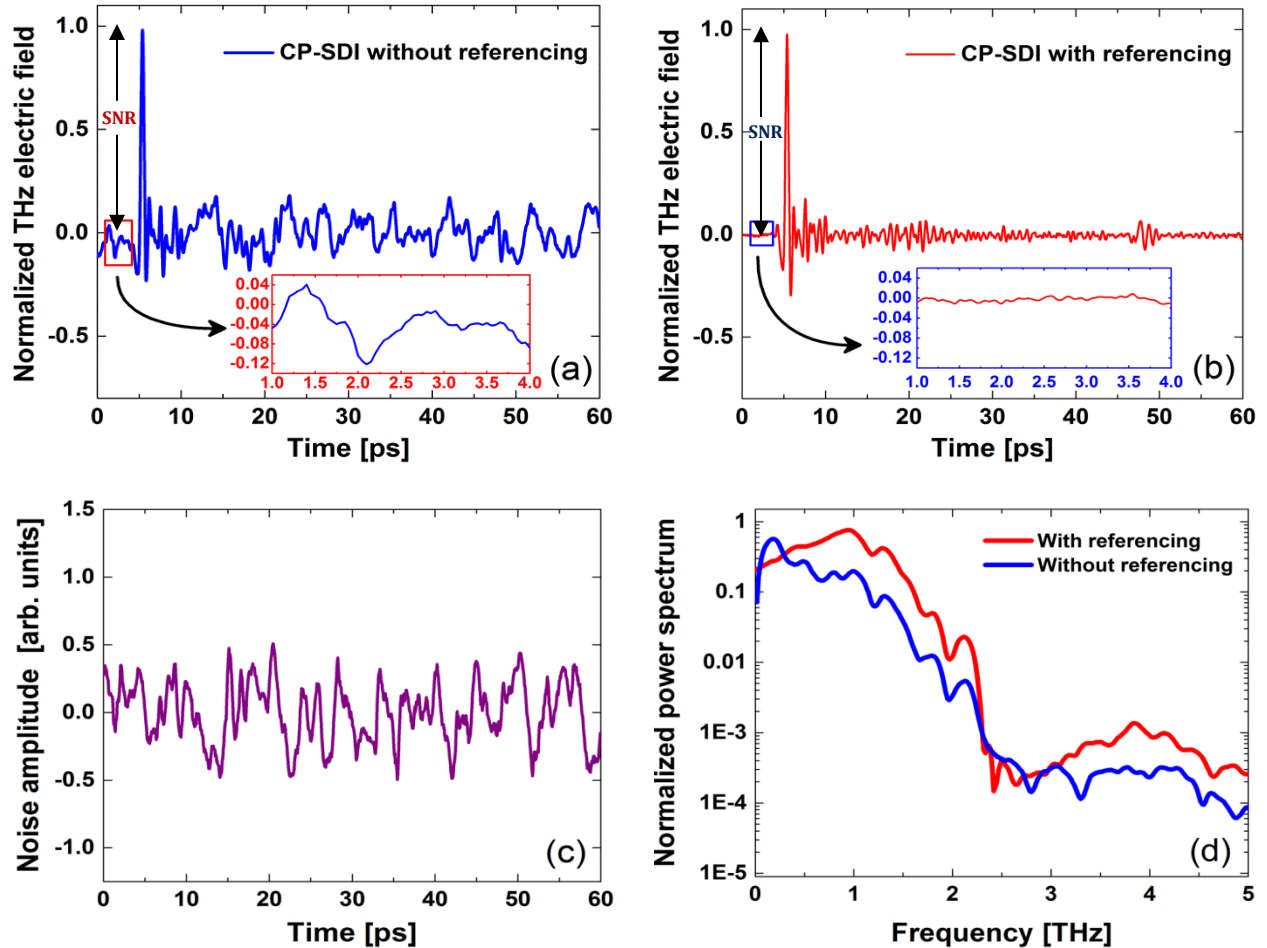


Figure 4.15 | THz electric field trace obtained with CP-SDI without referencing (a), the inset in (a) shows a magnified temporal noise, THz electric field trace obtained with CP-SDI with referencing method (b), the inset in (b) shows a magnified temporal noise, the noise amplitude subtracted using the referencing method (c), and the corresponding Fourier power spectra of the THz trace obtained with (red line) and without (blue line) the new referencing method (d).

As seen at lower THz frequencies some noise components have been successfully mitigated. From the Fourier power spectra, we measured the SNR to be ~ 41.14 dB without using the new referencing method, while it is calculated to be ~ 43.13 dB when applying the referencing method. We note that when we followed the approach of measuring temporal SNR, the measured SNR is ~ 25 for THz measurement without referencing and ~ 250 when applying the new referencing method, which represents ten-fold enhancement in temporal SNR. From our

experimental findings, we concluded that the new referencing method is efficient in removing low-frequency noise, and has successfully improved the temporal shape of the THz pulse; one can see the excellent agreement with the THz pulse obtained with conventional EOS technique shown in Fig. 4.14(a). Further, we investigated the effect of changing the chopping frequency and the CCD camera exposure time on the SNR of the THz measurement. We experimentally found that lower chopping frequency is better in getting better SNR for our THz measurement. In fact, increasing the chopping frequency inevitably requires decreasing the exposure time of the CCD camera. We noted that the CCD camera exposure time has no significant effect on the SNR when the interference fringes have a constant contrast and therefore it is only a tool to enhance the interference contrast. For the experimentally obtained results in this section, we have tuned the chopping rate at 11 Hz while the CCD camera exposure time was set to 8 ms. Indeed, we hoped that the method can contribute to a significant enhancement in the SNR of the measurement. However, the method has contributed in reducing the noise signal only at lower THz frequencies, as can be seen from Fig. 4.15(d). At this current stage, we believe the reason behind the limited improvement in SNR when applying the new referencing method is the leakage of the OPB beam signal that is carrying both THz and noise information (Frame 2) into the CCD camera reference signal frame that presumably contains solely pure noise signal (Frame 1). Thus, when we apply our algorithm to obtain the THz wave form, we were actually subtracting frames carrying (slightly leaked THz information+noise information signal) from frames carrying (THz information signal + noise information signal) rather than subtracting frames carrying (pure noise signal when the THz is momentarily blocked by the chopper blade (*e.g.* Frame 1)) from frames carrying (THz information + noise information signal (*e.g.* Frame 2)). Ineffectively, this leads to slightly reducing the THz signal itself while we were attempting to eliminate the noise signals and thus in turn the obtained enhancement in SNR is unforeseen. However, more investigation on the new referencing method is required for further enhancement in its performance to eliminate the vibrational noise.

4.5.2 Compact CP-SDI module scheme

Another effort was made in order to reduce the noise stemming from vibration in the setup. That has been achieved by using a small CP-SDI compact module as depicted schematically in Fig. 4.16. The compact module consists of a collimating aspheric lens (L1) with short focal length ($f = 30$ mm). After collimation, the OPB passes through a quarter waveplate

placed with its transmission axis at 45° with respect to the fast and slow axis of the PM fiber (780HP, MDF= $5\mu\text{m}$, 80 cm length, connectors FC/APC both ends, slow axis oriented).

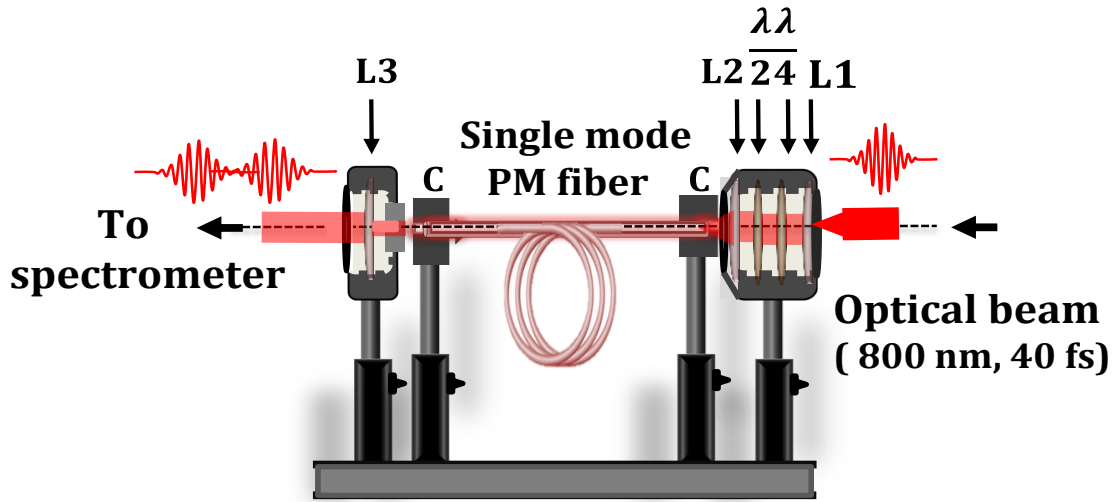


Figure 4.16 | Schematic illustration of the experimental setup of the CP-SDI compact module for THz electric field measurement. L1, L2, and L3 are collimating, focusing, and collimating aspheric lenses respectively. C stands for FC/APC connector.

A half-waveplate was used to adjust a small error in the polarization alignment into the axes of the PM fiber. Focusing aspheric lens (L2) ($f = 20\text{ mm}$) was used to couple the laser into the PM fiber. The PM fiber is connected marked to the module with an FC/APC connector. At the exit end of the PM fiber, a collimating aspheric lens (L3) ($f = 13.8\text{ mm}$) was used to send the beam collimated to the spectrometer. The compact module in its current design (15 cm in length) is fabricated by Doric Lenses Inc. The rest of components *e.g.* the polarizer and the spectrometer optical components are not part of the compact module yet. We are planning in the next stage to include all of them in one compact module. We anticipate that can double the current SNR.

Exploiting the CP-SDI compact module, we could measure the THz electric field temporal waveform, as depicted in Fig. 4.17(a). We note that the waveform is smooth with the main THz peak at $\sim 4.2\text{ ps}$, while the first THz reflection peak is at $\sim 46.7\text{ ps}$. Once more, the appearance of the first reflection peak is indicative of the efficiency of the module in mitigating vibrational noise level in the setup. The inset shows a magnified region of the THz baseline ($0 - 2\text{ ps}$) where we could measure the temporal SNR. Fig. 4.17(b) depicts the Fourier power spectrum of the THz traces obtained with the compact module. The measured SNR from the power spectrum is better than 45.44 dB the temporal SNR evaluated from the temporal trace is better than 370.

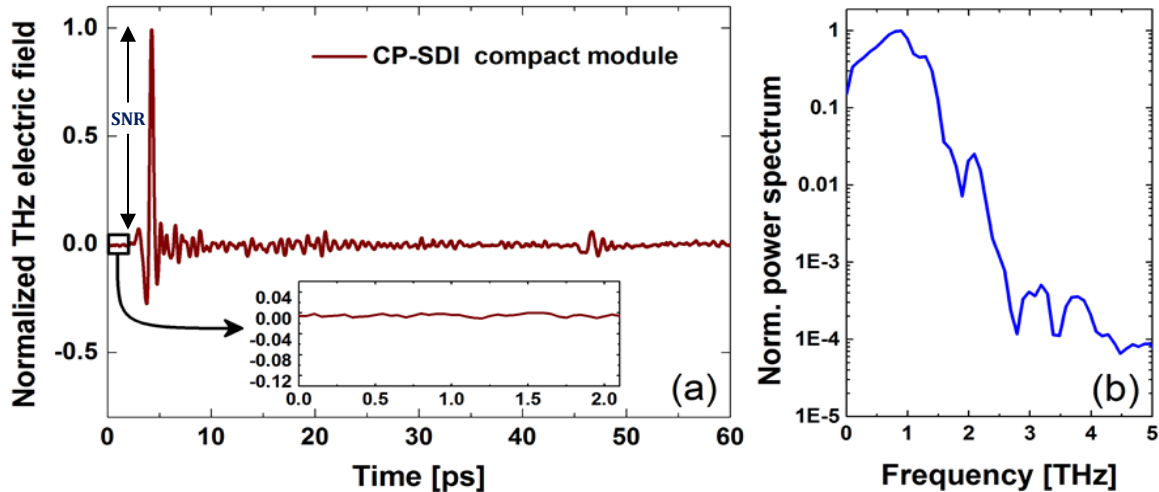


Figure 4.17 | THz electric field trace obtained with CP-SDI compact module (a) inset in (a) shows a magnified temporal noise. The corresponding Fourier power spectrum of the THz trace obtained with CP-SDI compact module (b).

The performance of the compact module is efficient in eliminating considerable low frequencies vibrational noise signal that is due to the fact that all the optical components in the module are all held fixed together and with higher stability, and thus they vibrate with similar frequency leading to much less impact on the system in contrast to the standard CP-SDI technique (THz trace in Fig. 4.15 (a), hereafter we used standard CP-SDI in order to distinguish it from CP-SDI with referencing, and CP-SDI compact module) where the optical components were separately mounted (not held together) and thus each optical component vibrates separately leading to poor performance (poor SNR).

| Detection scheme | SNR (Spectral) | SNR (Temporal) |
|---|-------------------|-------------------|
| EOS technique | 51.46 dB | 637 |
| Standard CP-SDI technique | 41.14 dB | 25 |
| CP-SDI with referencing method | 43.13 dB | 250 |
| Compact module of CP-SDI technique | 45.44 dB | 370 |

Table 4.2 | Comparison between SNR of THz electric field measurements obtained with conventional EOS technique and different SDI schemes.

Moreover, in the standard CP-SDI, both fiber ends are fixed in an XYZ micro-block stages with their tips free in air, subject to mechanical vibrations in the set up thus leading to influencing the

quality of the coupling and the motion on the fringes pattern. This in turn affects the SNR of the THz electric field measurement carried out with standard CP-SDI technique. We concluded that the compact module reduces a great deal the CP-SDI sensitivity to mechanical vibrations in the setup, and thus enhances the SNR. In Table 4.2, we compare the SNR of conventional EOS technique along with different CP-SDI schemes under same beam time experimental conditions. From the SNR given in Table 4.2, we conclude that the compact CP-SDI module offers the best SNR among all CP-SDI versions. Consequently, we will use the compact module scheme for spectroscopic applications discussed in Chapter 5.

4.6 Comparison between standard SDI, MZI based SDI and CP-SDI techniques in THz electric field measurement

As we have seen, the conventional EOS technique for intense THz electric field measurement suffers from over-rotation effects. However, by using our newly designed CP-SDI technique for THz electric field measurement, we could circumvent this limitation while maintaining comparable SNR. By eliminating over-rotation, we could achieve a DR of 7×10^6 . On the other hand, the standard SDI technique in THz electric field measurement first presented by Sharma *et al.* [2] achieved inferior SNR and DR compared to SNR and DR offered by the CP-SDI technique. In the standard SDI technique, one of the major sources of phase noise, as discussed previously in section 3.2.4.1, is angular vibration in the glass plate owing to the angular variation between its two surfaces [2]. Furthermore, the OPD between the two pulses reflecting from the glass plate surfaces was relatively large (900 μm), which results in working relatively far from zero-OPD, which in turn causes a loss in interference signal of the two pulses and consequently lowers the SNR and the DR. However, in the CP-SDI technique, introducing the PM fiber increases the SNR in THz measurement primarily because of working closer to zero-OPD where the sensitivity of the technique is maximal. Moreover, by using the PM fiber, the noises associated with the glass plate vibrations that change the OPD between two interfering signals are eliminated. A change in OPD because of the glass plate vibration in the standard SDI technique will result in an additional change in phase, on top of the phase change introduced by the THz electric field, and appears as noise. This noise is eliminated in the CP-SDI technique, since both interfering signals are traveling through the same fiber and any change in OPD is common to both signals. The PM fiber also enables higher DR, since the interfering signals are

generated after the detection crystal, whereas in the standard SDI technique, the interfering signals are generated before the detection crystal, limiting the scan length to the temporal thickness of the glass plate. Consequently, the CP-SDI technique has achieved higher SNR and DR compared to the standard SDI technique. Furthermore, the new CP-SDI technique in THz measurement eliminates the limit in the temporal scan length which is crucially required for any THz spectroscopic application. This was a drawback in the standard SDI version of the technique [2] in THz detection, due to the limit imposed by the thickness of the glass plate. However, in the CP-SDI technique the PM fiber imposes no limit in the scan length. Indeed, the PM fiber plays a critical role in adjusting a suitable working point on the OPD where the detection sensitivity is high and at the same time, the noises are minimal. Alternatively, this effect could also be achieved by using a birefringent crystal with appropriate dimensions. However, this comes with the expense of growing such a crystal, whereas PM fibers are commercially available at affordable prices and can be manipulated easily in small size setup. However, the SNR of the CP-SDI is still inferior to that of the conventional EOS technique, and further enhancement in the SNR is limited, due to challenges in employing the common self-referencing method [12].

| SDI detection scheme | SNR (Spectral) | SNR (Temporal) | Merits | Demerits |
|----------------------------------|----------------|----------------|---|---|
| Standard CP-SDI technique | 38.12 dB | 45 | <ul style="list-style-type: none"> No over-rotation. DR=high $\sim 6 \times 10^5$ Common self-referencing can be applied to improve the SNR. | <ul style="list-style-type: none"> Short temporal scanning window that limits the spectroscopic applications. |
| MZI-SDI technique | 31.21 dB | 37 | <ul style="list-style-type: none"> No over-rotation. DR=high $\sim 4 \times 10^5$ No limit imposed in the temporal scanning window. Common self-referencing can be applied to improve the SNR. | <ul style="list-style-type: none"> Poor SNR due to significant vibrational noise in optical components used to interfere the MZI signals. |
| CP-SDI technique | 48.97 dB | 279 | <ul style="list-style-type: none"> No over-rotation. DR=ultra-high $\sim 7 \times 10^6$ No limit imposed in the temporal scanning window. The best SNR. Can be used in the spectroscopic measurement and application. | <ul style="list-style-type: none"> The common self-referencing cannot be applied to improve the SNR. Sophisticated referencing method is yet required to improve the SNR. |

Table 4.3 | Comparison between different SDI techniques in THz electric field measurement.

This is because, in the common self-referencing method, the probe beam must sample at least two spatial points, one with finite THz field and the other with zero THz field. The information from the probe beam at zero THz field point could be used as the reference. However, the use of the fiber in the SDI (CP-SDI) technique limits the spatial information to only one point with the THz information only, thus making the common self-referencing a challenge. On the other hand, the potential for enhancing the SNR and consequently the DR in the MZI based SDI technique for THz electric field measurement is high, by employing the common self-referencing method, which could be realized much easier compared with the CP-SDI technique. Thus, for potential and profound further improvement in SNR and DR, MZI based SDI has the advantage compared to CP-SDI technique, which as of yet requires a complicated method to carry out referencing. In Table 4.3 we compare the different SDI techniques for THz electric field measurement attempted in the framework of this thesis, illustrating their merits and demerits. It is clear that the CP-SDI technique offers the best performance resulting in excellent SNR of the THz measurement.

References

- [1] X. D. Cao and D. D. Meyerhofer, *Opt. Lett.* **19**, 1837-1839 (1994).
- [2] G. Sharma, K. Singh, I. Al-Naib, R. Morandotti, and T. Ozaki, *Opt. Lett.* **37**, 4338-4340 (2012).
- [3] A. Ibrahim, D. Férachou, G. Sharma, K. Singh, M. K.-Turmel, and T. Ozaki, *Sci. Rep.* **6**, 23107 (2016).
- [4] J. Hebling, A. G. Stepanov, G. Almasi, B. Bartal, and J. Kuhl, *Appl. Phys. B.* **78**, 593-599 (2004).
- [5] J. A. Fulop, L. Palfalvi, S. Klingebiel, G. Almasi, F. Krausz, S. Karsch, and J. Hebling, *Opt. Lett.* **37**, 557-559 (2012).
- [6] N. Bosschaart, M. C. G. Aalders, T. G. van Leeuwen, and D. J. Faber, *Biom. Opt. Express* **3** 2263 (2012).
- [7] G. Zhao, R. N. Schouten, N. Van der Valk, W. T. Wenckebach, and P. C. M. Planken, *Phys. Med. Biol.* **47**, 3699-3704 (2002).
- [8] P. U. Jepsen, and B. M. Fischer, *Opt. Lett.* **30**, 29-31 (2005).
- [9] H. Hirori, A. Doi, F. Blanchard, and K. Tanaka, *Appl. Phys. Lett.* **98**, 091106 (2011).
- [10] F. Blanchard, L. Razzari, H.-C. Bandulet, G. Sharma, R. Morandotti, J.-C. Kieffer, T. Ozaki, M. Reid, H. F. Tiedje, H. K. Haugen, and F. A. Hegmann, *Opt. Express* **15**, 13212-13220 (2007).
- [11] P. C. M. Planken, H.-K. Nienhuys, H. J. Bakker, and T. Wenckebach, *J. Opt. Soc. Am. B* **18**, 3 (2001).

- [12] G. Sharma, K. Singh, A. Ibrahim, I. Al-Naib, R. Morandotti, F. Vidal and T. Ozaki, *Opt. Lett.* **38** (15), 2705 (2013).

Chapter 5

Application of CP-SDI detection technique in THz spectroscopy of high-permittivity materials

Outline

In this chapter, we discuss the experimental results obtained via our newly developed THz detection technique (CP-SDI compact module version), which is used for the first time in THz-time domain spectroscopy (THz-TDS). The advantages offered by CP-SDI THz detection technique in detecting intense THz signals, *e.g.* avoidance of over-rotation and inherent ultrahigh DR, enables THz measurements that were difficult and challenging when using the conventional EOS THz detection technique. The work presented in this chapter simultaneously serves two main objectives: i) validate our novel CP-SDI THz detection technique and test its capabilities in THz-TDS, as well as ii) performing THz-TDS measurements *-in transmission geometry-* on material that encounters challenges in THz frequency range. In order to achieve the aforementioned objectives, we have chosen a high permittivity sample Barium Strontium Titanate (BST) as a test material to evaluate its dielectric response in the THz frequency region. Further, we have compared the obtained dielectric response results obtained via CP-SDI THz detection technique with those obtained via conventional EOS THz detection technique for the same BST sample. We show that the results obtained via the former are more accurate than those obtained via the latter, and that they are comparable to the results published in the literature.

5.1 Introduction

The class of dielectric materials that exhibit unique properties such as field dependent dielectric permittivity is widely known as ferroelectric materials [1-3]. In such materials, upon application of an electric field, some of their charges are displaced while the remaining charges are bound and oscillate, resulting in creation of electric dipoles per unit volume; in such a state, the material is forenamed to have a polarization. The polarization can exist without application

of an electric field in some materials, which are said to have spontaneous polarization. Altering or reversing the spontaneous polarization in ferroelectric materials can be achieved by application of an electric field. Fig. 5.1 illustrates the perovskite unit cell structure (ABO_3) that ferroelectric composites generally exhibit, here (A) stands for the large cations located at the corners of the unit cell, (B) stands for the smaller cations located at the body center and (O) stands for the oxygen atoms at the face centers [4]. Crystallographic phase changes often accompany ferroelectricity. For instance, ferroelectrics transform to paraelectric phase above a certain transition temperature called Curie temperature T_c [5]. At T_c , the ferroelectrics undergo a structural change from ferroelectric to paraelectric, attaining the highest dielectric constant value. Due to their (ferroelectric-paraelectric) phase transition, ferroelectrics lend themselves readily for a plethora of very promising applications, *e.g.* the strong hysteresis behavior below T_c (in ferroelectric phase) makes ferroelectric materials suitable candidates for memory applications. Above T_c (in the paraelectric phase), the spontaneous polarization disappears while the dielectric constant remains at its highest value, and thus in such phase the ferroelectric materials are appealing for dynamic and non-volatile random access memories (DRAM) applications [6], as well as for tunable high-frequency microwave (MW) devices [5, 7-11].

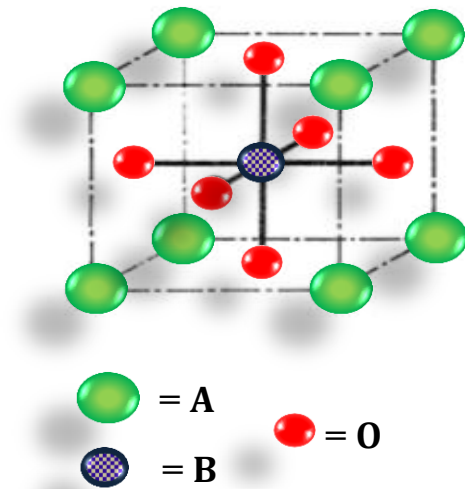


Figure 5.1 | The elementary cell for the ferroelectric perovskite compounds structure (ABO_3) [12].

Moreover, ferroelectrics are foreseen to play a significant role in providing excellent technological components such as pyroelectric sensors, high permittivity capacitors, ferroelectric

memories, piezoelectric transducers, and electro-optic devices [13]. The past decade has witnessed intensive development efforts in ferroelectric materials studies, and a surge in their interests has been driven mainly by the potential for significant miniaturization of MW components as well as large cost reduction [13,14]. Once more the development in thin and thick ferroelectric films technology has influenced the potential for integration with microelectronic circuits [15]. Regarding the desired properties for the applicability of ferroelectric materials, the high tunability and low dielectric losses are the most sought [13]. However, ferroelectrics in thin-film forms often exhibit lower permittivity, lower tunability, and considerable losses compared to bulk materials of similar composition [13,16].

Currently, the THz spectral range attracts attention for investigating the dielectric properties of such materials. The deriving motive stems from the desire to understand the fundamental processes in these materials using THz-far infrared spectral signatures, as well as to develop new THz technological applications based on these ferroelectric materials [17,18]. For instance, the switchable and tunable dielectric materials operating in the THz range are currently of high interest for THz-based technology with conceivable applications in future short-range wireless communications [19-22].

5.2 Barium Strontium Titanate (BST) - A case study

The perovskite Barium Strontium Titanate $\text{Ba}_x\text{Sr}_{1-x}\text{TiO}_3$ [(BST), $0 \leq x \leq 1$] is a classical prototype solid solution ferroelectric material that has been investigated and reviewed in literature since 1946 [5]. Its structure is derived from the prototype BaTiO_3 (BTO) perovskite, as depicted in Fig. 5.2. The BTO structure is a simple cubic arrangement that consists of large barium ions at each corner of the unit cell, surrounded by twelve nearest oxygen ions. The titanium ion is at the center and has six oxygen ions in an octahedral arrangement. BST displays a well-defined ferroelectric phase transition at T_c , which in turn depends on the Ba/Sr ratio [24]. For instance, the phase changes from the simple cubic (C) paraelectric to ferroelectric phases are almost linear from ~ 127 °C for pure BaTiO_3 (BT) to ~ -193 °C for $x = 0.1$, where x is the Ba content [5,25,26].

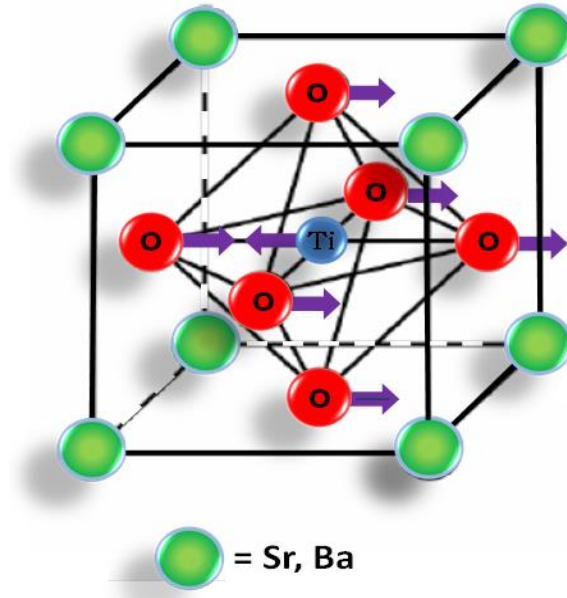


Figure 5.2|The elementary cell along with the eigenvector of the soft mode (indicated by arrows) for the ferroelectric perovskite compound $(\text{Ba}, \text{Sr})\text{TiO}_3$ [23].

Upon cooling, the BST attains tetragonal (T), orthorhombic (O) and rhombohedral (R) structures, whose ferroelectric phases are characterized by significant dielectric losses. Therefore, BST in those phases is an excellent candidate for applications in non-volatile memories [27,28]. On the other hand, in its paraelectric C phase (above T_c), BST exhibits high dielectric constants and low dielectric losses, while there is no hysteresis effect, and consequently this phase is desirable for tunable MW application and devices such as phase shifters, tunable filters and varactors [29-31]. Moreover, its unique characteristic features, such as composition dependent T_c , electric field dependent dielectric permittivity, high and tunable dielectric permittivity combined with low dielectric losses [13], attract attention to BST for potential applications not only in tunable MW, but also in designing electronic devices required for controlling radiation in the optical and MW frequencies [32], as well as functional elements in devices [33,34]. Evidenced by experimental findings, the best BST composition suitable for room temperature applications corresponds to composition with $x = 0.5-0.6$, where its T_c is close to room temperature, and where the material remains in the paraelectric C phase exhibiting steadily huge permittivity with strong tunability combined with minimal dielectric losses [7]. As a typical ferroelectric, BST is characterized by the existence of a strong polar soft lattice vibrational mode (SM) responsible for the phase transition. Moreover, its dielectric behavior

close to the phase transition is entirely governed by the SM dynamics, which slows down close to T_c and exhibits a softening trend upon cooling. The SM contributes substantially to the dielectric permittivity according to:

$$\varepsilon = \frac{f}{\omega_0^2} \quad (5.1)$$

Here f is the oscillator strength (the effective charge associated with the soft mode eigenvector) and ω_0 is the frequency of SM [35].

Basically, BST samples can be fabricated in bulk (dense ceramic) or thin film forms, and significant differences are often noticed between the two [13,36]. For instance, BST thin films are important for technological applications, *e.g.* thin films of BST are now replacing silica-nitride laminates in DRAM. However, their capacitance is much inferior to that expected from bulk BST [36]. It has been revealed that ferroelectric and/or high-permittivity thin films (including BST) exhibit both lower permittivity and inferior tunability compared with bulk samples [13,37-39]. For instance, the bulk form displays paraelectric-to-ferroelectric phase transition near room temperature, where the dielectric constant is maximal featuring a sharp peak at room temperature. As such, owing to the larger exhibited permittivity, bulk BST ceramics have long been exploited in high charge-density capacitors. On the other hand, BST thin films exhibit much lower dielectric constant without a sharp peak at room temperature [36]. The inferior permittivity in the thin film is attributed to fine grains, interfacial capacitance, and residual stress [36]. This explains the recent emerging interest in investigating self-standing bulk (platelet ceramic) for potential technological applications that require reasonably high permittivity, tunability, and lower dielectric losses.

BST in both film and bulk forms have a well-established history of published works to determine its dielectric properties, owing to numerous research studies mostly at different frequency ranges (kHz-GHz) [24, 40-44]. However, the amount of reported works is greatly reduced in the THz frequency range, studied directly by using THz time-domain spectroscopy (THz-TDS) both *in reflection* [32,45] and *in transmission* geometries [46-50]. From a BST-based technological applications point of view, it is important to realize the permittivity modulation over a wide frequency range (including THz) and close to room temperature. Furthermore, the importance of detailed investigation on BST dielectric properties in the THz frequency range stems from new emerging experimental findings suggesting the potential for BST for THz optical components,

e.g. THz modulators [18]. The majority of the work carried out using THz-TDS in *transmission geometry* on BST thin films rather than bulk ceramic samples, which is due to the limitation imposed by the THz signal absorption losses. Indeed, one advantage of using bulk BST sample is that the dielectric losses are expected to be inferior to those in the case of thin films where inhomogeneous broadening increases the damping of the soft phonon mode [47]. On the other hand, it is practically difficult to prepare a very thin platelet of a single crystalline sample, and consequently bulk absorption is significantly higher than that exhibited by the thin film due to the sample thickness. This considerable thickness related loss in the THz frequency range limits THz-TDS technique -in *transmission geometry*-, especially for optically thick samples. Such absorptive samples pose a challenge for conventional EOS THz detection technique in measuring the transmitted THz signal through thick samples with an adequately good SNR. Poor SNR and lower DR for the THz transmission measurements using conventional EOS detection technique will consequently affect the accuracy for extracting dielectric constants when using the THz-TDS technique.

In this thesis work, we exploit our new CP-SDI THz detection technique -taking advantage of the following inherent features: i) avoidance of over-rotation in measuring higher THz signals and ii) ultra-high DR, to measure THz waveforms over large THz field strengths, which is required for determine the dielectric properties of the BST ceramic sample. Thus, BST has offered an excellent reference material to benchmark and validate our new CP-SDI THz detection technique, benefitting its aforementioned features.

5.3 THz spectroscopy applied to BST ceramic

5.3.1 Experimental realization

Thick stoichiometric BST sample (platelet) was fabricated by Prof. T. Teranishi group, Okayama University, Japan. They have synthesized the BST sample by mixing BaTiO₃ (BT; Sakai Chemical Industry, Osaka, Japan) and SrTiO₃ (ST; Sakai Chemical Industry) powders. Excess TiO₂ (Ishihara Sangyo Kaisha, Osaka, Japan) and BaCO₃ (Kojundo Chemical Laboratory, Saitama, Japan) were added to the BT-ST mixed powder to prepare cation-defective samples. The mixed powders were milled with ethanol for 4 hours using a planetary ball mill (Model P-6; Fritsch Idar Oberstein, Germany), followed by drying. The dried powder was calcined at 1,150°C for 20 minutes. The calcined powders were uniaxially pressed in 10-mm-

diameter dies, followed by cold isostatic pressing at 125 MPa. The sample was sintered at 1470°C for 4 hours. Phase identification was performed by powder X-ray diffraction (XRD; Model MultiFlex; Rigaku, Tokyo, Japan) with CuK_α radiation over $2\theta=20^\circ\text{-}80^\circ$. Pure Si powder was added as a standard to the sample to correct the measured diffraction angles. The sample then thinned to platelet of $\sim 35\text{-}40\ \mu\text{m}$ -thickness and $\sim 7\text{-}10\ \text{mm}$ diameter.

THz-TDS technique *-in transmission geometry-* experimental setup (schematically depicted in Fig. 5.3) was utilized to determine the dielectric constants of the stoichiometric BST sample. In the setup, a mode-locked Ti:sapphire femtosecond laser beam (central wavelength of 800 nm, repetition rate 1 kHz, and pulse width 40 fs) was divided into two beams via a beam splitter (BS). The pump beam was focused on a LiNbO_3 crystal for the generation of THz waves via electro-optical rectification process, while the optical probe beam was focused into a 2-mm-thick ZnTe crystal for the detection of the THz wave by conventional EOS, and later by the CP-SDI technique. Two parabolic off-axis mirrors (PM1 and PM2) were used to collimate and focus the emitted THz radiation onto the sample. The transmitted THz wave was collected and focused on the ZnTe detection crystal using two additional parabolic off-axis mirrors (PM3 and PM4).

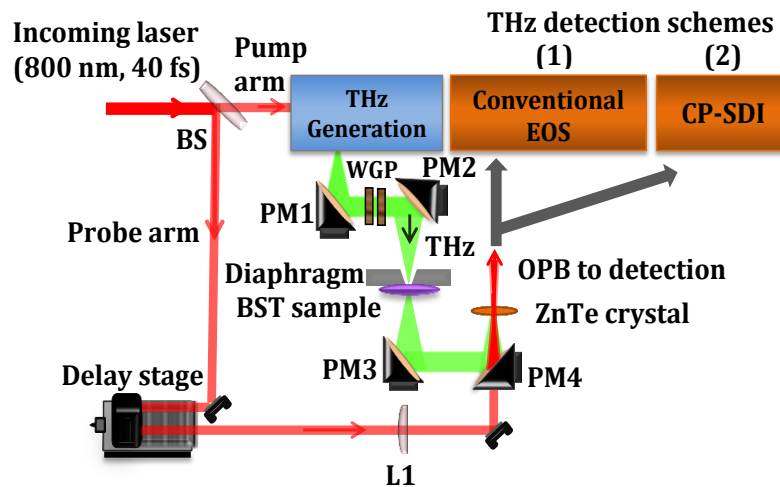


Figure 5.3 | The schematic of THz-TDS setup used to characterize the stoichiometric BST sample *in transmission geometry*.

The set up offers usable spectral range from 0.15 to 2.5 THz, and the THz focal spot size at sample position is 0.5mm. When using the conventional EOS for THz waveform measurement, the SNR is better than 10^4 in the THz power spectrum, while the DR of the measurement is better than 10^2 . However, the DR is significantly enhanced to better than 10^6 when using the CP-SDI THz detection technique. Moreover, it is well-known that the spectral resolution of the

measurements is related to the length of the temporal scan T via the Nyquist criterion $\Delta f = 1/T$, while the upper and lower frequency limits are governed by the properties of the THz emitter and receiver. In our case, we have attained a spectral resolution of 33 GHz. Utilizing both THz detection techniques, we could measure the temporal waveforms of the THz pulses: a reference waveform $E_R(t)$ was measured without mounting BST sample on diaphragm (*i.e.* an empty diaphragm), while a signal waveform $E_S(t)$ transmitted through the investigated BST sample was measured when mounted onto the diaphragm filling the whole aperture. Fast Fourier transform was carried out on both signals and the Fourier components are calculated. Then, we could calculate the complex transmission function of the BST sample, $T(\omega)$ using Eq. (2.32). In order to obtain n and k , Eq. (2.35) and Eq. (2.36) are solved numerically. Then, the real and imaginary parts of the permittivity can be written using the values of n and k as:

$$\epsilon' = n^2 - k^2 \quad (5.2)$$

$$\epsilon'' = 2nk \quad (5.3)$$

While the loss tangent can be expressed as:

$$\tan \delta = \frac{\epsilon''}{\epsilon'} \quad (5.4)$$

5.4 THz waveforms acquisition for BST dielectric response extraction using conventional EOS THz detection technique

The terahertz temporal waveforms that are required for determining the dielectric response of stoichiometric BST sample obtained via conventional EOS THz detection technique are depicted in Fig. 5.4. Here, the solid red line represents the reference terahertz transient (air) waveform (Fig. 5.4(a)) and the blue solid line is the THz waveform transmitted through a stoichiometric BST sample ($A/B=1.00$) at room temperature. Here A/B is the ratio between Ba, Sr, and Ti ions described by the flowing formula $(Ba+Sr)/Ti$ [41].

Both waveforms are measured using 2-mm-thick ZnTe detection crystal. Immediately, one can notice a small time lag of ~ 0.35 ps between the measured waveforms of the reference and the sample, indicating the finite thickness of the BST sample.

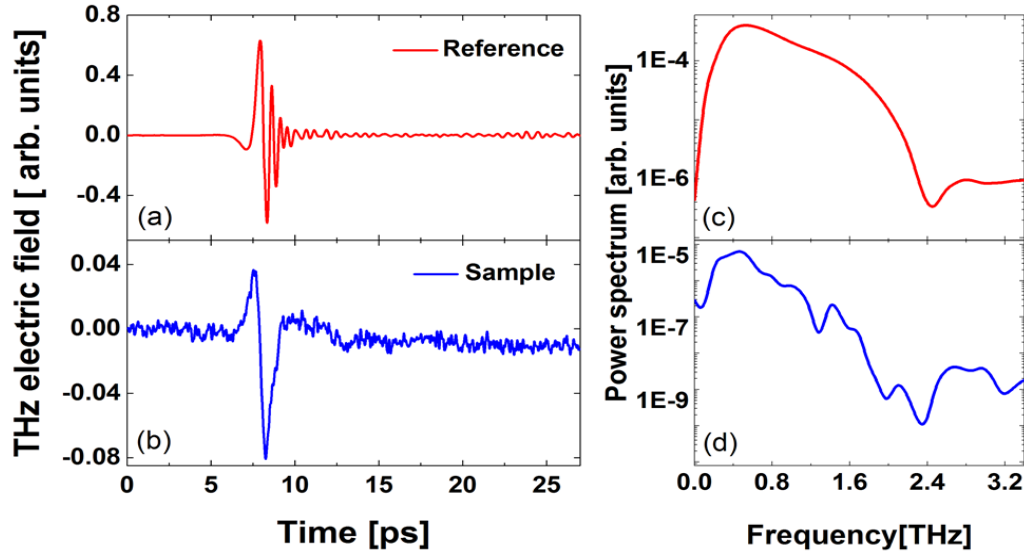


Figure 5.4 | Measurement of the THz temporal waveform (a) reference (air) and (b) transmitted through stoichiometric BST sample $A/B=1.00$, both measured via conventional EOS at low $E_{\text{THz}} \approx 28 \text{ kVcm}^{-1}$ at room temperature. The corresponding power spectra are shown in (c) and (d) respectively.

The thickness was determined to be $31.2 \pm 4 \text{ }\mu\text{m}$, where the error in the sample thickness stems from the mechanical thinning process carried out in order to reduce its thickness, thus resulting in a non-uniform sample thickness. For THz propagation through a sample with finite thickness, it is well-known that a fraction of the THz wave is typically reflected at the interface. The detected THz signal commonly consists of the directly transmitted pulse, as well as the multiple reflections at the sample interfaces (FP oscillations). However, the small thickness of our sample and its significant loss did not allow us to distinguish these reflections from the directly transmitted pulse. Therefore, we exclude FP oscillations in our measurements, since they are weak within the noise level of the measurement [17]. Performing the complete complex analysis, first by taking the Fourier transform of the reference and transmitted (sample) THz waveforms in Fig. 5.4(a) and Fig. 5.4(b), one can obtain the corresponding power spectra of each temporal waveform, as depicted in Fig. 5.4(c) and Fig. 5.4(d), respectively. From the power spectra, the measured SNR of the THz reference pulse is $\sim 34.77 \text{ dB}$, while the SNR of the transmitted waveform through the BST sample was found to be $\sim 26.98 \text{ dB}$. Indeed, we could not exploit the full value of the THz peak electric field (E_{THz}) when measuring the temporal waveforms (Fig. 5.4(a) and Fig. 5.4(b)) using conventional EOS detection technique before the over-rotation effects start to appear in the reference waveform. Consequently, this poses a limitation on the

value of E_{THz} to be used in such measurement. Therefore, we have been constrained to reduce E_{THz} in order to avoid over-rotation limitation, especially in measuring the reference THz waveform. For this purpose, a set of a wire-grid polarizer (WGP) was used to reduce $E_{\text{THz}} \approx 28 \text{ kV cm}^{-1}$, and consequently, such reduction in the THz signal significantly deteriorates the SNR of the measurement. Clearly, the poor SNR will affect the extraction of the dielectric constants as noticed in this measurement. Figure 5.5 (a) illustrates a comparison between the Fourier transform amplitude of the reference and sample waveforms depicted in Fig. 5.4(a) and Fig. 5.4(b). Fig. 5.5(b) illustrates a comparison between the phases of the same waveforms, which in turn helps in identifying the most trusted spectral region where the phase data are reliable and not distorted.

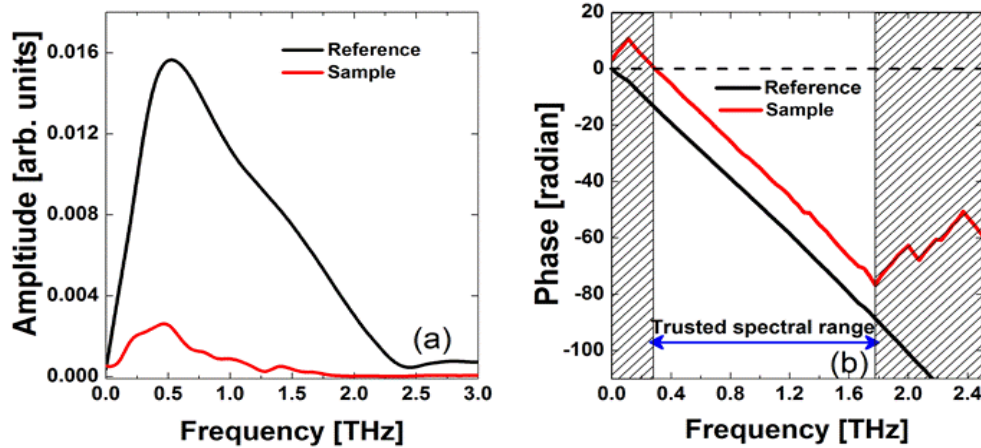


Figure 5.5 | Extracted THz (a) amplitude and (b) phase data obtained from the Fourier transform of the waveforms given in Fig. 5.4(a) and Fig. 5.4(b) with conventional EOS THz detection technique. The dashed areas highlight phase irregularities.

Choosing the most trusted spectral region to extract the dielectric response will result in enhancing the accuracy of the extraction process.

The dashed areas in Fig. 5.5(b) highlight the irregularity in the phase information, and the spectral range between the dashed areas represents the most trusted phase region. As can be seen in Fig. 5.5(b), the most trusted spectral range of our THz measurement extends from 0.28 to 1.8 THz, allowing THz broadband dielectric response measurements.

The magnitude of the complex transmission function, $|T(\omega)| = \left| \frac{E_{Sample}(\omega)}{E_{Reference}(\omega)} \right|$ and the phase, $\Phi(\omega) = \Phi_{Sample}(\omega) - \Phi_{Reference}(\omega)$ in radians, are calculated by taking the ratio of the THz amplitudes of the sample and reference, as depicted in Fig. 5.6(a) and Fig. 5.6(b) respectively.

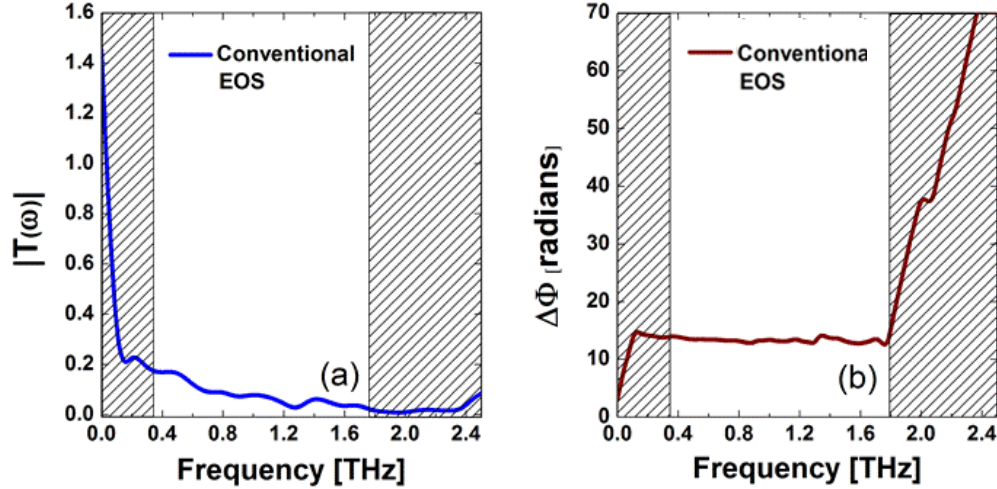


Figure 5.6 | Extracted THz (a) magnitude of Transmission coefficient and (b) phase difference obtained from Fourier transform of the waveforms given in Fig. 5.4(a) and Fig. 5.4(b) with conventional EOS THz detection technique. The dashed areas highlight the border of the most trusted spectral region.

5.4.1 Extraction of dielectric constants of stoichiometric BST sample using data obtained via conventional EOS technique

In order to determine the complex refractive index and dielectric dispersion functions of the stoichiometric BST sample, the THz waveforms in Fig. 5.4(a) and Fig. 5.4(b) were Fourier transformed to derive the amplitude and phase. Now, one has all the information needed to extract the complex dielectric function.

In this thesis work, we have used a software [51] in order to solve numerically the complex transmission function and hence to extract the refractive index $n(\omega)$ and extinction coefficient $k(\omega)$ of the stoichiometric BST sample ($A/B=1.00$), as depicted in Fig. 5.7. The dashed areas highlight the irregularities in the extracted values of n and k , and the most trusted spectral region can be found at frequencies of 0.28 - 1.8 THz. In this frequency range, the refractive index $n(\omega)$ of the stoichiometric BST sample exhibits a decreasing trend as the frequency increases. For instance, the magnitude of n is ~ 11.4 at 0.28 THz, decreasing to 5.2 at 1 THz and down to 0.14 at 1.8 THz.

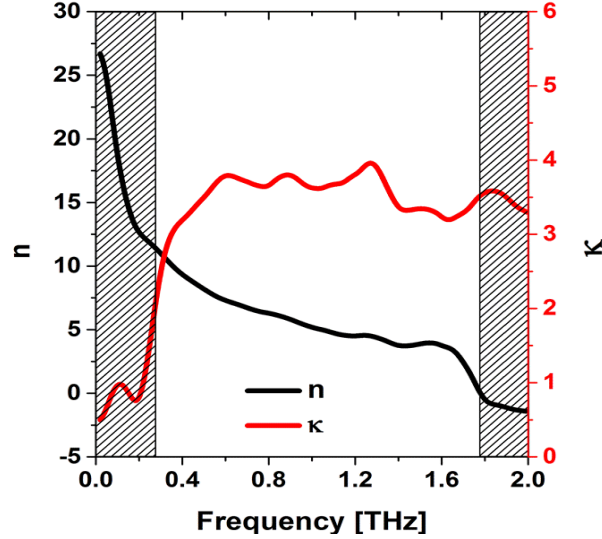


Figure 5.7 | The extracted real (n) and imaginary (k) parts of the complex index of refraction for a $31.2 \pm 4 \mu\text{m}$ -thick stoichiometric BST sample using THz-TDS *in transmission* geometry with conventional EOS THz detection technique. The dashed areas highlight the border of the most trusted spectral region.

As one can see at higher frequencies ($>1.6\text{THz}$) and as the SNR of the measurement starts to deteriorate, the values for n become misleading. Figure 5.8 depicts the extracted (a) real part of complex permittivity $\epsilon'(\omega)$ and (b) imaginary part of complex permittivity $\epsilon''(\omega)$ of the stoichiometric BST sample in the frequency range of 0.15 -2 THz.

As can be seen in the trusted spectral region from 0.28 – 1.8 THz (sandwiched by the dashed areas) the magnitude of $\epsilon'(\omega)$ is peaked at ~ 120 while $\epsilon''(\omega)$ peaks with a lower magnitude ~ 62 , with both constants decreasing as the frequency increases. The observed oscillation on some part of the data can be attributed to the fact that the sample thickness varies, and its accurate determination is limited by poor SNR of the measurement. The average thickness of the sample was determined numerically [52-55] using a software which is described in reference [51]. Briefly, the reference and sample THz waveforms are fed to the software that solves numerically the complex transmission function (Eq. 2.34) and estimates the thickness based on Fabry-Pérot reflections. Using the software the sample thickness was determined to be $31.2 \pm 4 \mu\text{m}$, after averaging five thickness values.

The error in extracting the thickness is calculated from the standard deviation of the five thickness measurements. Indeed, accurate determination of the sample thickness is crucial for the accurate numerical extraction of permittivity constants using software [51].

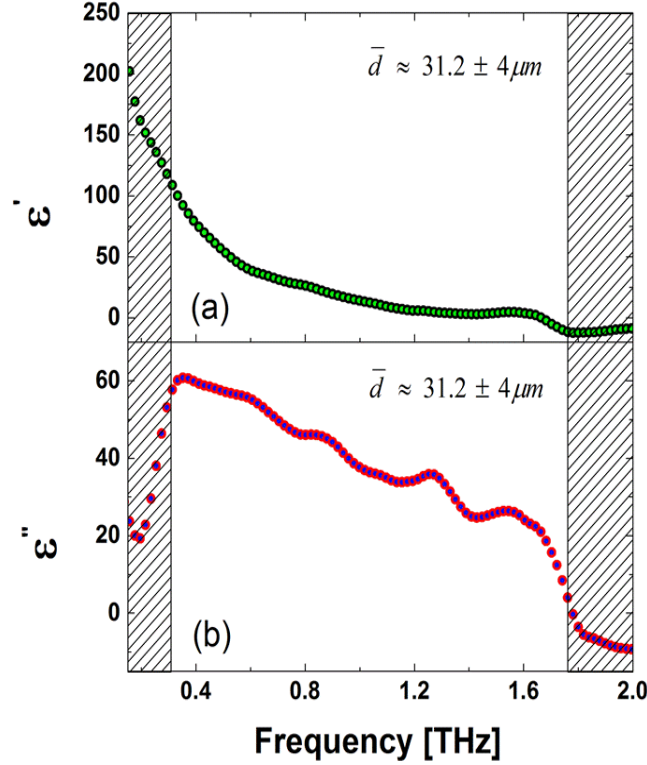


Figure 5.8 | Conventional EOS measured THz spectra of (a) real part of permittivity ϵ' , and (b) imaginary part of permittivity ϵ'' at an average thickness of $31.2 \pm 4 \mu m$ of stoichiometric BST sample A/B=1.00 from 0.15 – 2 THz. The dashed areas highlight the border of the most trusted spectral region.

However, poor SNR of the THz reference and sample temporal waveforms (Fig. 5.4(a) and Fig. 5.4(b)) significantly affect the capability of the software to accurately determine the thickness, which in turn affect the results of numerical solution of the transmission function, thus contributing to less accurate values of $\epsilon'(\omega)$ and $\epsilon''(\omega)$ [56]. This explains the observed inferior values of the dielectric constants of the BST sample when extracted from THz waveforms obtained via conventional EOS detection technique.

5.5 THz Z-scan of BST ceramic

Prior to switching to higher E_{THz} regime ($>28 \text{ kV cm}^{-1}$), we have investigated the effect of E_{THz} on our sample by performing open-aperture Z-scan measurements to investigate nonlinear THz effects in our sample. The Z-scan is a nonlinear characterization technique commonly exploited to study intensity dependent transmission changes in a sample. The sample transmission is measured as the sample is translated along the propagation path (Z-axis) of a

focused THz beam. For a Gaussian beam, the maximum intensity will be achieved at the focus, which reduces while moving away from the focus position. Indeed, if a nonlinear THz absorption occurs, the intensity of the transmitted THz beam through the sample under investigation will depend on the spot size, which is in its turn depends on the sample position [57]. The THz measurements for BST sample have been carried out at McGill University THz laboratory. Their high-field time-domain THz spectrometer was developed and based on tilted-pulse front optical rectification in lithium niobate with peak THz field amplitude of $\sim 439 \text{ kVcm}^{-1}$. The bandwidth of the THz pulses was $\sim 2.3 \text{ THz}$ and was detected using EOS in a 2 mm thick (110)-cut ZnTe crystal. The emitted THz pulses were collected and focused by a set of off-axis parabolic mirrors to $\sim 570 \mu\text{m}$ spot size as determined by an uncooled micro-bolometer camera.

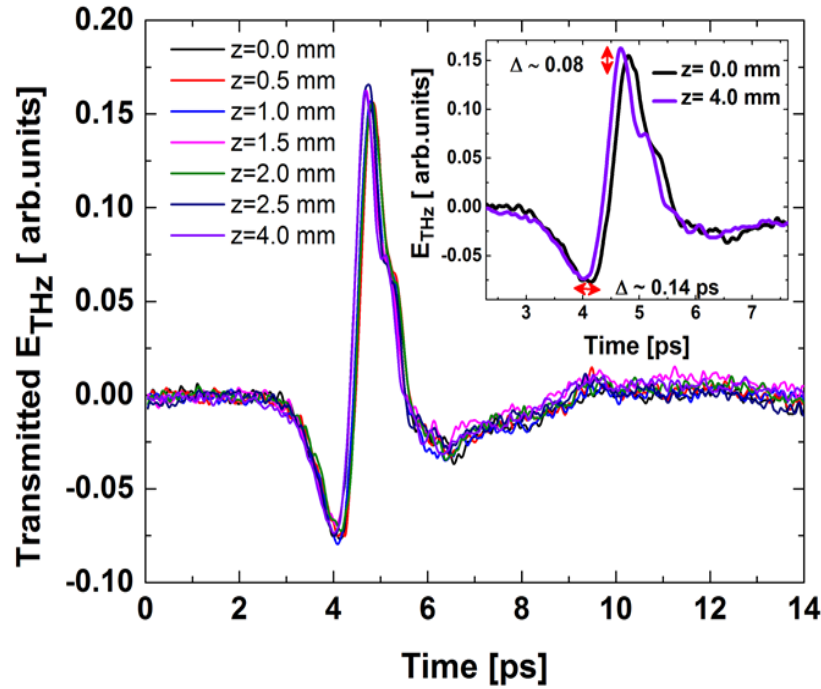


Figure 5.9 | Measurement of the transmitted E_{THz} through stoichiometric BST sample $A/B=1.00$ for different positions of the Z-scan at room temperature. The inset shows a magnified plot for traces in position $z=0 \text{ mm}$ and $z=4 \text{ mm}$.

We show in Fig. 5.9 the THz waveform transmitted through stoichiometric BST sample $A/B=1.00$ at high $E_{\text{THz}} \approx 439 \text{ kV cm}^{-1}$ while the sample was moved translationally in the Z-direction away from the THz focus plane in steps. For better visualization, the inset in Fig. 5.9 shows a magnification of the transmitted waveforms when the sample positioned at the focus and at 4 mm away from the focus. We could see an insignificant temporal shift ($\Delta \sim 0.14 \text{ ps}$) between

the traces as well as an insignificant increase in the amplitude ($\Delta \sim 0.08$ arb. units). Both observed insignificant changes can be explained based on non-uniform sample thickness and its non-parallel surfaces as a result of mechanical thinning of the sample. Clearly, as we move the sample away from the focus, the THz spot size illuminates a larger surface area of the sample, which in turns entails larger thickness variation.

In the case of Fig. 5.9, the sample thickness varies as we moved away from the focal plane and hence both the THz transmission and phase shift vary as well. Fig. 5.10 shows the variation trend in both temporal shift and the transmitted THz amplitude of BST sample A/B=1.00 for different positions of the Z-scan at room temperature.

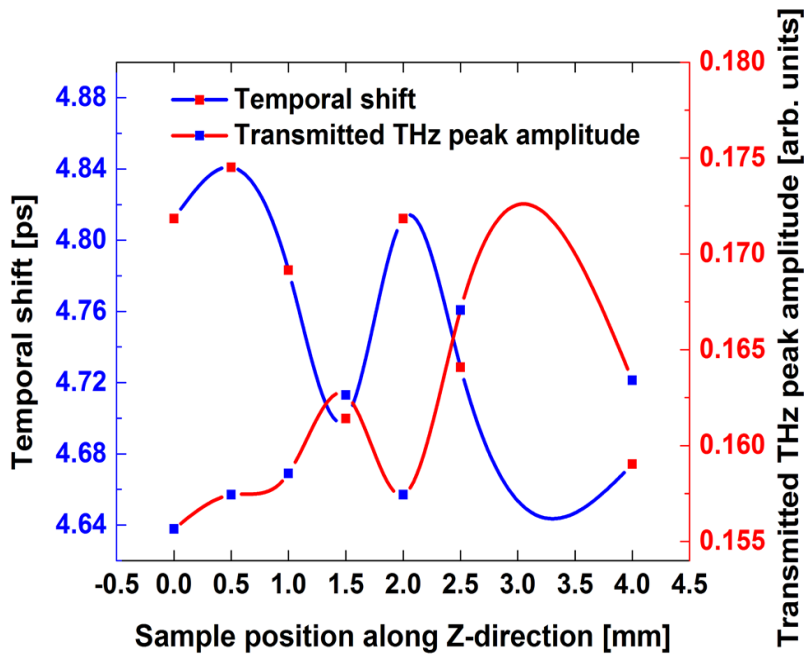


Figure 5.10 | Measurement of the temporal shift (blue line + red square) and the transmitted THz peak amplitude through stoichiometric BST sample A/B=1.00 for different positions of the Z-scan at room temperature.

One can see that both parameters do not exhibit consistent trend as we change the position of the sample along the Z- direction. That can explain the non-uniform sample thickness and its non-parallel surfaces. Based on the data presented in Fig. 5.9 and Fig. 5.10, we could not conclude the presence of nonlinear change in the stoichiometric BST sample A/B=1.00 parameters as we vary the E_{THz} and now we can exploit the maximum value of the E_{THz} in our set up in order to enhance the SNR of the measurement, which is crucial for accurate dielectric response characterization of our sample.

5.6 THz waveforms acquisition for BST dielectric response extraction using CP-SDI THz detection technique

We used the CP-SDI THz detection technique to measure the temporal waveforms of the THz electric field, as shown in Figure 5.11 (a) for the reference (air), and in Fig. 5.11(b) for the transmitted THz waveform through stoichiometric BST sample ($A/B=1.00$).

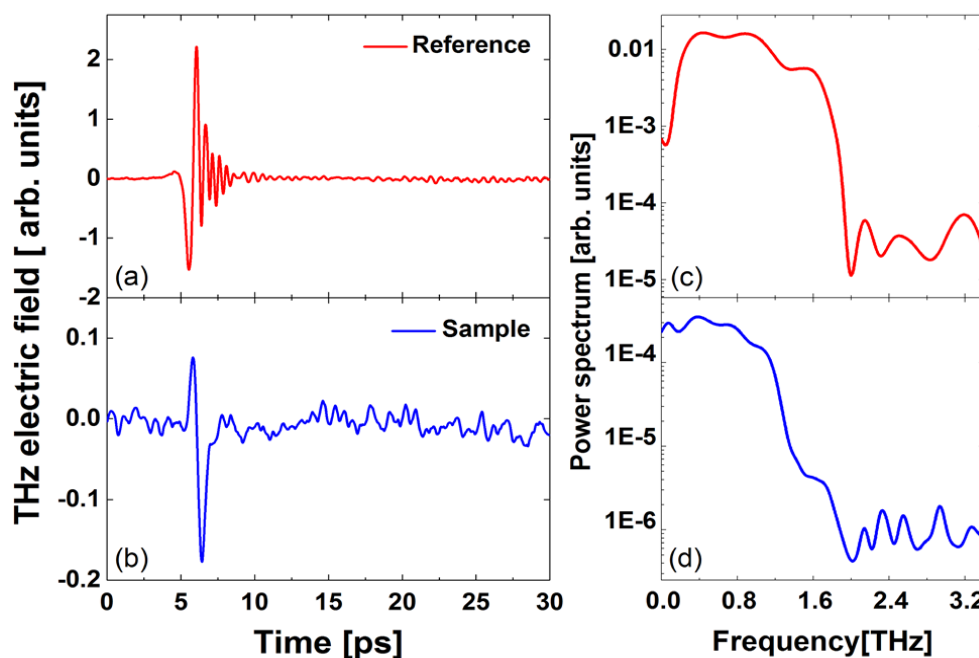


Figure 5.11 | Measurement of the THz waveform (a) reference and (b) transmitted through stoichiometric BST sample, both measured via CP-SDI THz detection technique at high $E_{\text{THz}} \approx 439 \text{ kVcm}^{-1}$ at room temperature. The corresponding power spectra are shown in (c) and (d) respectively.

Both waveforms were obtained with 2-mm ZnTe detection crystal. Fig. 5.11(c) and Fig. 5.11(d) depict the corresponding power spectra of the measured THz pulses, respectively. From the power spectra, the measured SNR of the transmitted waveform through the sample was measured to be $\sim 36.25 \text{ dB}$, while the SNR of the reference was measured to be $\sim 44.47 \text{ dB}$. Immediately, one can notice the enhancement in SNR of the THz waveforms measured using the CP-SDI technique compared to the SNR of the THz waveforms measured using EOS technique for the same sample, but measured at lower E_{THz} . The enhancement in SNR is attributed to the fact that the CP-SDI technique allows us to exploit the full maximum value of E_{THz} offered by our THz set up at $\approx 439 \text{ kV cm}^{-1}$ without experiencing over-rotation effect in the obtained THz reference

pulse, contrary to the conventional EOS THz detection technique where we were forced to reduce the value of E_{THz} to avoid over-rotation effect. Thus further increasing E_{THz} will result in further enhancing the SNR of the THz measurements.

Analogous to what we have carried out on THz waveforms acquired by conventional EOS technique, we have performed Fourier transform on the temporal waveforms acquired by CP-SDI THz detection technique (Fig.5.11(a) and Fig. 5.11(b)) and extracted Fourier amplitude and phase data for both reference and sample, as depicted in Fig. 5.12(a) and Fig. 5.12(b), respectively.

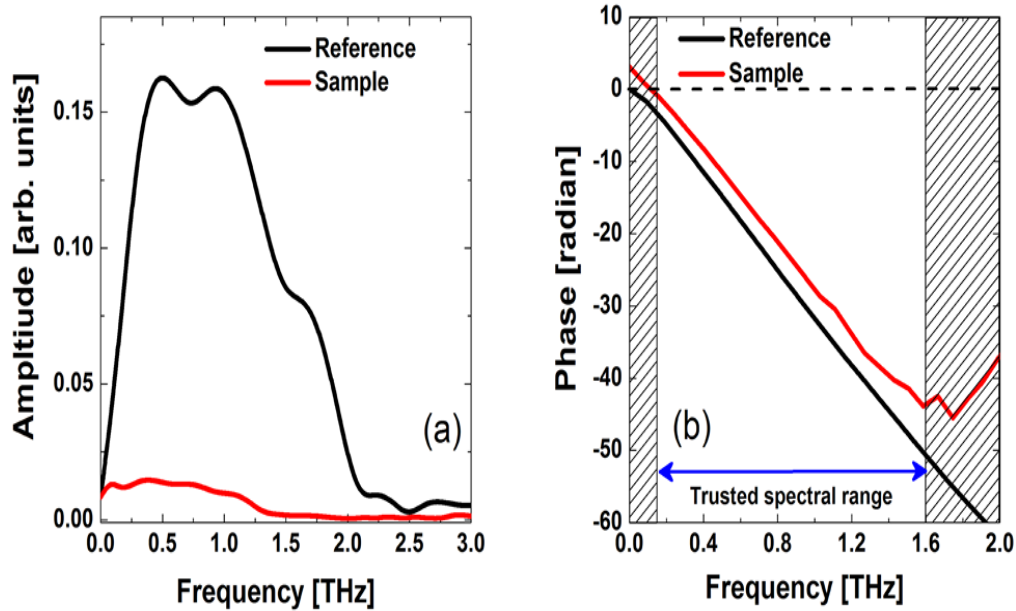


Figure 5.12| Measurement of THz (a) amplitude and (b) phase data obtained from the Fourier transform of the waveforms given in Fig. 5.9 using CP-SDI THz detection technique. The dashed areas highlight the border of the most trusted spectral region.

The magnitude of the transmission function as well as the phase change extracted from Fourier transform of the THz waveforms acquired via CP-SDI THz detection technique (Fig. 5.11(a) and Fig. 5.11(b)) are depicted in Fig. 5.13(a) and Fig. 5.13(b), respectively. The most trusted spectral region is sandwiched between the dashed areas.

Figure 5.14 illustrates the frequency dependence of $n(\omega)$ and $k(\omega)$ of the stoichiometric BST sample $A/B=1.00$. The THz waveforms used for this extraction are acquired via CP-SDI THz detection technique.

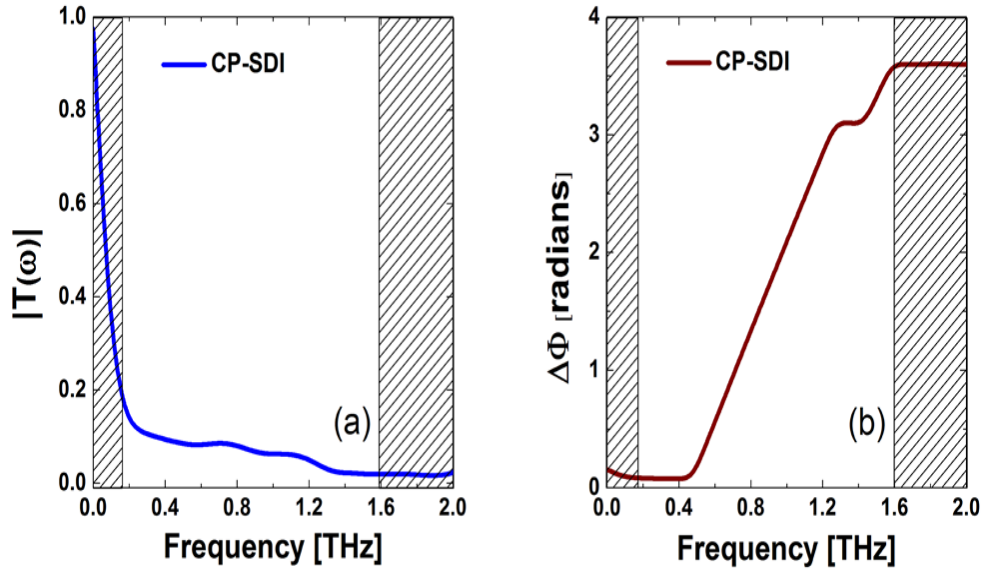


Figure 5.13 | Measurement of THz (a) Transmission coefficient and (b) phase difference obtained from Fourier transform of the waveforms given in Fig. 5.11 using CP-SDI THz detection technique. The dashed areas highlight the border of the most trusted spectral region.

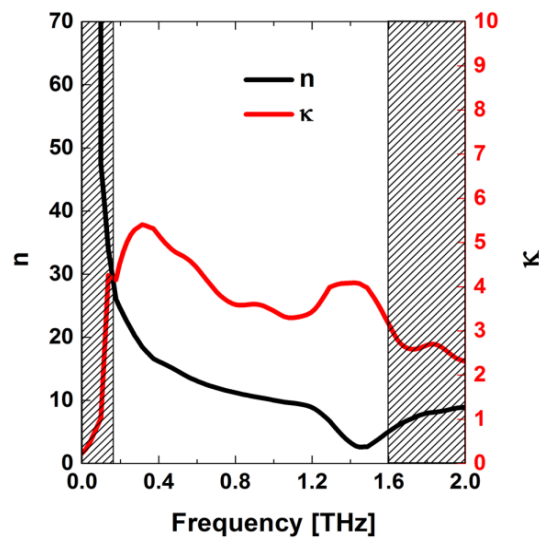


Figure 5.14 | Extracted real (n) and imaginary (k) parts of the complex index of refraction for a $30.3 \pm 2 \mu\text{m}$ -thick stoichiometric BST sample using THz-TDS in transmission geometry with CP-SDI technique in detection. The dashed area highlights the region with less accurate values.

Clearly, n exhibits a dispersion behavior as it decreases sharply from the higher value at lower frequencies to lower values at higher frequencies. The value of n is ~ 30 at 0.16 THz, reducing to ~ 10 at 1 THz and further decreasing to ~ 5.2 at 1.6 THz. Moreover, k increases at lower frequencies and then decreases at frequencies higher than 0.39 THz.

Comparison between the values of n (at 1 THz) obtained by conventional EOS (Fig. 5.7) and CP-SDI (Fig. 5.14) reveals that the latter registered a higher $n=10$ compared to $n=5.2$ in the former. This discrepancy in n values could be attributed to the enhanced SNR in the case of using CP-SDI to register the THz temporal waveforms of the reference and sample. The enhanced SNR resulted in enhancing the accuracy in determining the sample thickness that in turn resulted in accurate determination of n value ($=10$ at 1 THz) in this case.

5.6.1 Extraction of dielectric constants of stoichiometric BST sample using data obtained via CP-SDI THz detection technique

The higher SNR accompanied by the ultrahigh DR of CP-SDI THz detection technique enables extracting the dielectric parameters of our sample with an enhanced accuracy compared to those obtained with conventional EOS THz detection technique. One challenge in extracting the dielectric parameters is the accurate thickness determination. The ideal situation is that the sample thickness is uniform and its two surfaces are parallel. However, this is not the case in reality, as mentioned earlier, since thinning the sample is achieved mechanically with some errors in the thickness.

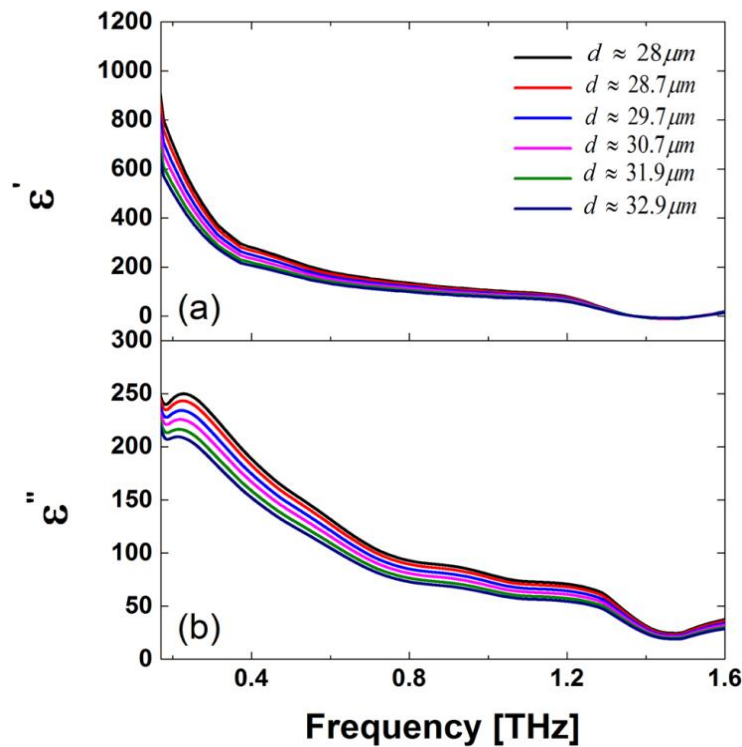


Figure 5.15 | Different measured values obtained by CP-SDI THz detection technique for (a) ϵ' and (b) ϵ'' spectra at different thicknesses of the stoichiometric BST sample from 0.16- 1.6 THz.

As already mentioned, the thickness is determined numerically using software [51], which evaluates the thickness based on THz temporal waveforms of the reference and sample [52-55]. Owing to the good SNR (~ 44.47 dB) and ultrahigh DR (10^7) of the measurement using CP-SDI detection technique, we believe the obtained thickness values are more accurate compared to that obtained in the case of conventional EOS detection technique.

Therefore, we could measure six thicknesses and average them to $30.3 \pm 2 \mu\text{m}$ and the error in estimating the thickness was considered as the standard deviation of the six thickness values. For each thickness, $\epsilon'(\omega)$ and $\epsilon''(\omega)$ are extracted, as depicted in Fig. 5.15. In order to further enhance the accuracy, we have averaged the six spectra to obtain $\epsilon'(\omega)$ and $\epsilon''(\omega)$ for stoichiometric BST sample at the averaged thickness of $30.3 \pm 2 \mu\text{m}$. The averaging process mitigates the error in thickness estimation, and moreover, it enhances the accuracy in extracting the BST sample dielectric constants $\epsilon'(\omega)$ and $\epsilon''(\omega)$.

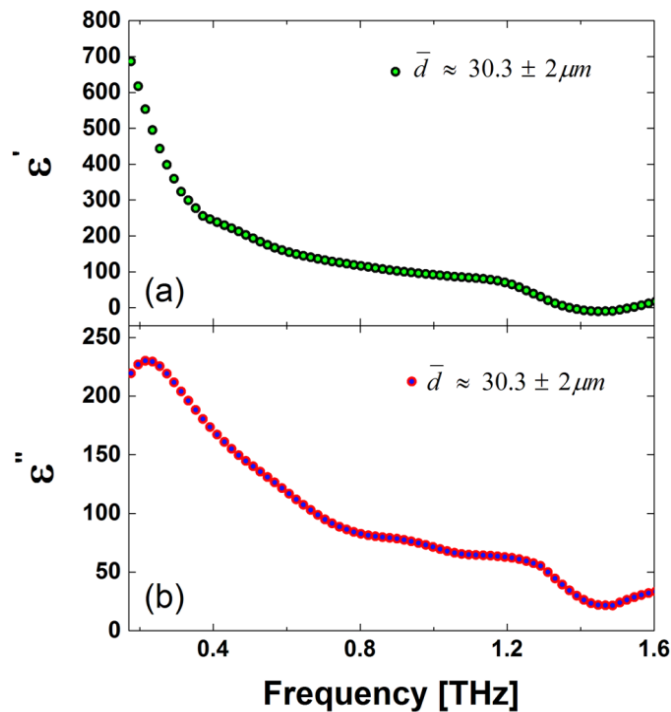


Figure 5.16 | CP-SDI technique measured spectra of (a) real part of permittivity ϵ' , and (b) imaginary part of permittivity ϵ'' at an average thickness of $30.3 \pm 2 \mu\text{m}$ of stoichiometric BST sample (A/B=1.00) from 0.16 – 1.6 THz.

Figure 5.16 shows the frequency dependence of (a) $\epsilon'(\omega)$ and (b) $\epsilon''(\omega)$ for a frequency range of 0.16 – 1.6 THz for the stoichiometric BST sample at an average thickness of $30.3 \pm 2 \mu\text{m}$. The

observed trend for both $\epsilon'(\omega)$ and (b) $\epsilon''(\omega)$ is that the value peaks at a low THz frequency and then decreases with increasing frequency.

For instance, the magnitude of the dielectric constant $\epsilon'(\omega)$ peaks at ~ 700 while $\epsilon''(\omega)$ peaks at 233, both decreasing as the frequency increases. The obtained values for $\epsilon'(\omega)$ and $\epsilon''(\omega)$ -when using the CP-SDI THz detection technique- are quite different from those obtained when using the conventional EOS THz detection technique for the same sample, however with increasing the THz signal. The difference in the obtained values for $\epsilon'(\omega)$ and $\epsilon''(\omega)$ by both detection techniques is attributed to better SNR in the CP-SDI THz detection technique compared to that via conventional EOS technique, which results in more accurate extracted values for the dielectric constants when using the CP-SDI technique.

Indeed, the dielectric response in the low THz frequency range of BST ceramic has been characterized by a few authors, for instance, Ostapchuk *et al.* [46] have shown that the dominant dielectric dispersion mechanism in the ceramic BST system in paraelectric phase is governed by soft-phonon mode. Moreover, they have shown that the soft-mode response in the vicinity of the ferroelectric transition comprises two coupled overdamped THz excitations, which show classical features of a coupled soft (SM) and central (CM) mode, known from many ferroelectric crystals with dynamics near the displacive and order–disorder crossover. Once more, the phonon feature for BST has been also confirmed by molecular dynamics simulations [44].

We have observed the dielectric dispersion and relaxation behavior of our stoichiometric BST sample, as can be seen in Fig. 5.16, where a large relaxation in $\epsilon'(\omega)$ spectrum with dielectric relaxation frequencies can be estimated as about 150-250 GHz. Moreover, $\epsilon''(\omega)$ spectrum exhibits a reasonable dispersion following Debye relaxation model, in agreement with published work on BST in THz frequency [44,46].

Indeed, the dominant dielectric dispersion mechanism in our sample can be assigned to soft phonon mode that comprises two coupled overlapped THz excitations that show the features of a coupled SM and CM, as Ostapchuk *et al.* have concluded [46]. The CM is attributed to dipole fluctuation, while the SM is attributed to optical phonon mode. Both modes are very close in frequency and are overlapped in our BST sample. The exhibited small peak in $\epsilon''(\omega)$ compared to the large dispersion in $\epsilon'(\omega)$ may indicate that the two modes, CM and SM, have significantly different relaxation frequencies and we are observing only the one with a higher frequency, which is SM.

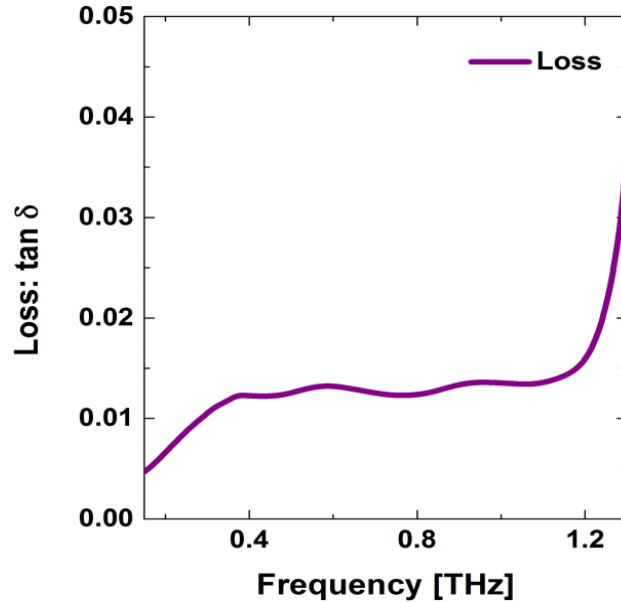


Figure 5.17 | Frequency dependence of the loss tangent of stoichiometric BST sample (A/B=1.00) from 0.15 – 1.3 THz at room temperature.

Figure 5.17 shows the THz tangent loss of stoichiometric BST sample in the frequency range between 0.15 -1.3 THz. The magnitude of the loss increases from 0.004 at 0.15 THz to 0.01 at 0.4 THz, after which it remains constant until 1.2 THz where it increases dramatically to 0.04. In general, the THz loss in the sample seems to be small, which indicates the suitability of BST ceramics for applications in MW and THz regions.

References

- [1] I. Vendik, O. Vendik, V. Pleskachev, M. Nikolski, *IEEE Trans. Appl. Supercond.* **13**, (2) 716-719 (2003).
- [2] W. -J. Kim, E. K. Kim, S.-E. Moon, S. Han, S. -J. Lee, K. Y. Kang, *Mater. Res. Soc. Symposium Proceedings* **720**, 191-196(2002).
- [3] J. C. Ustariz, R. A. R. Solis, S. Velez, S. R. Acosta, *Proc. of the SPIE-Inter. Soc. Optical Eng.* **4881**, 280-286(2003).
- [4] F. S. Galasso, *Perovskite and high- T_c superconductors*, (Gordon and Breach publishers 1990).
- [5] F. Jona and G. Shirane, *Ferroelectric Crystals*, (Dover Publications Inc., New York 1993).
- [6] O. Anciello, J. F. Scott, and R. Ramesh, *Phys. Today* **51**, 7 22 (1998).
- [7] O. G. Vendik, E. K. Hollmann, A. B. Kozyrev, and A. M. Prudan, *J. Supercon.*, **12**, 325 (1999).
- [8] M. J. Lancaster, J. Powell, and A. Porch, *Supercund. Sci. Techn.*, **11**, 1323 (1998).

- [9] F. A. Miranda, F. W. Van Keuls, R. R. Romanofsky, C. H. Mueller, S. Alterovitz, and G. Subramanyam, *Integr. Ferroelect.*, **42**, 131 (2001).
- [10] S. Gevorgian, E. Carlsson, E. Wikborg, and E. Kollberg, *Intergr. Ferroelect.*, **22**, 245 (1998).
- [11] S. A. Wolf and D. Treger, *Integr. Ferroelect.*, **42**, 39 (2001).
- [12] K. M. Rabe, C. H. Ahn, J.-M. Triscone, *Physics of Ferroelectrics: A Modern Perspective*, (Springer Science 2007).
- [13] A. K. Tagantsev, V. O. Sherman, K. F. Astafiev, J. Venkatesh, and N. Setter, *J. Electroceram.*, **11**, 5–66 (2003).
- [14] J. B. L. Rao, D. P. Patel, P. K. Park, T. K. Dougherty, J. A. Zelik, D. S. Prior, A. Moffat, L. C. Sengupta, *Mat. Res. Soc. Symposium Proceedings* **720**, 143-153 (2002).
- [15] N. Setter, *Electroceramic-Based MEEMS*, (Springer, New York 2005).
- [16] W. Chang and L. Sengupta, *J. Appl. Phys.* **92**, 3941 (2002).
- [17] Z. Yong, L. He, B. Li, M. Hu, C. H. Lam, and Y. Wang, *J. Amer. Ceram. Soc.* **97**, 6 1696-1699 (2014).
- [18] P. Kuzel and F. Kadlec, *C. R. Phys.* **9**, 197 (2008).
- [19] R. Piesiewicz, T. K. Ostmann, N. Krumbholz, D. Mittleman, M. Koch, J. Schoebel, and T. Kurner, *IEEE Antennas Propag. Mag.* **49**, 24 (2007).
- [20] P. Kuzel, C. Kadlec, F. Kadlec, J. Schubert, and G. Panaitov, *Appl. Phys. Lett.* **93**, 052910 (2008).
- [21] Q. Zhao, L. Kang, B. Du, H. Zhao, Q. Xie, X. Huang, B. Li, J. Zhou, and L. Li, *Phys. Rev. Lett.* **101**, 027402 (2008).
- [22] H. Nemeč, P. Kuzel, F. Kadlec, C. Kadlec, R. Yahiaoui, and P. Mounaix, *Phys. Rev. B* **79**, 241108 R (2009).
- [23] <http://its.fzu.cz/en/res-ferro.php>.
- [24] M. Zhang, H. Wang, H. Yang, X. Wu, W. Liu, X. Yao, *J. Alloy. Comp.* **509**, 344–347(2011).
- [25] V. V. Lemanov, E. P. Smirnova, P. P. Syrnikov and E. A. Tarakanov, *Phys. Rev. B* **54**, 3151 (1996).
- [26] C. Menoret, J.M. Kiat, B. Dkhil, M. Dunlop, H. Dammak and O. Hernandez, *Phys. Rev. B* **65**, 224104 (2002).
- [27] A. Chanthbouala, V. Garcia, R. O. Cherifi, K. Bouzehouane, S. Fusil, X. Moya, S. Xavier, H. Yamada, C. Deranlot, N.D. Mathur, M. Bibes, A. Barthelemy, J. Grollier, *Nat. Mater.* **11**, 860-864(2012).
- [28] S. Li, Y. Yao, Y. I. Yuzyuk, Y. Jia, X. Wang, S. Xie, Y. Jing, *Appl. Phys. Lett.* **105**, 092901(2014).
- [29] C. H. Mueller, R. R. Romanofsky, F. A. Miranda, *Potentials*, *IEEE* **20**, 36–39 (2001).
- [30] S. S. Gevorgian, E. L. Kollberg, *IEEE Trans. Micro. Theo. Tech.* **49**, 2117–2124 (2001).
- [31] D. S. Korn, H. D. Wu, *Integr. Ferroelectr.* **24**, 215–237 (1999).

- [32] G. A. Komandin, A. A. Volkov, I. E. Spektor, K. A. Vorotilov, V. M. Mukhortov, *Phys. Solid state* **51**, 1351-1355 (2009).
- [33] A. S. Seyit, L. Seungku, L. Victor, M. Amir, *Microw. Wirel. Compon. Lett. IEEE* **26**, 25 (2016).
- [34] M. Haghzadeh, H. M. Jaradat, C. Armiento, A. Akyurtlu, *Prog. Electromagn. Res. C* **62**, 167 (2016).
- [35] C. Kadlec, F. Kadlec, H. Nemeč, P. Kuzel, J. Schubert, and G. Panaitov, *J. Phys: Condens. Matter.* **21**, 11 (2009).
- [36] T. M. Shaw, Z. Suo, M. Huang, E. Liniger, R. B. Laibowitz, and J. D. Baniecki, *Appl. Phys. Lett.* **75**, 2129-2131 (1999).
- [37] H. M. Christen, J. Mannhart, E. J. Williams, and C. Gerber, *Phys. Rev. B* **49**, 12095–12104 (1994).
- [38] H. -C. Li, W. Si, A. D. West, and X. X. Xi, *Appl. Phys. Lett.* **73**, 464–466 (1998).
- [39] D. Fuchs, C. W. Schneider, R. Schneider, and H. Rietchel, *J. Appl. Phys.* **85**, 7362–7369 (1999).
- [40] T. Teranishi, T. Hoshina, H. Takeda, and T. Tsurumi, *J. Appl. Phys.* **105**, 054111 (2009).
- [41] T. Teranishi, R. Kanemoto, H. Hayashi and A. Kishimoto, *J. Am. Ceram. Soc.* **100**, 3 1037–1043 (2017).
- [42] J. Lia, H. Kakemoto, S. Wada, T. Tsurumi, and H. Kawaji, *J. Appl. Phys.* **100**, 024106 (2006).
- [43] V. K. Palukuru, J. Perantie, J. Jantti, H. Jantunen, *Int. J. Appl. Ceram. Technol.* **9**, 1 11-17 (2012).
- [44] T. Tsurumi, J. Li, T. Hoshina, H. Kakemoto, M. Nakada, and J. Akedo, *Appl. Phys. Lett.* **91**, 182905 (2007).
- [45] T. Ostapchuk, J. Petzelt, P. Kuzel, S. Veljko, A. Tkach, P. Vilarinho, I. Ponomareva, L. Bellaiche, E. Smirnova, V. Lemanov, A. Sotnikov and M. Weihnacht *Ferroelectrics* **367**, 139-148 (2008).
- [46] T. Ostapchuk, J. Petzelt, J. Hlinka, V. Bovtun, P. Kuzel, I. Ponomareva, S. Lisenkov, L. Bellaiche, A. Tkach, and P. Vilarinho, *J. Phys. Condens. Matt.* **21**, 474215 (2009).
- [47] J. Petzelt, P. Kuzel, I. Rychetsky, A. Pashkin and T. Ostapchuk, *Ferroelectrics* **288**, 169-185 (2003).
- [48] L. Wu, L. Jiang, Y. Xu, X. Ding, and J. Yao, *Appl. Phys. Lett.* **103**, 191111 (2013).
- [49] C. Luoa, J. Ji, F. Ling, D. Li, J. Yao, *J. Alloy. Comp.* **687**, 5 458–462 (2016).
- [50] C. Luoa, J. Ji, J. Yue, Y. Rao, G. Yao, D. Li, Y. Zeng, R. Li, L. Xiao, X. Liu, J. Yao, F. Ling, *Opt. Mat.* **60**, 383–386 (2016).
- [51] I. Pupeza, R. Wilk, and M. Koch, *Opt. Expr.* **15**, 7 4335-4350 (2007).
- [52] S. Krimi, J. Klier, J. Jonuscheit, G. von Freymann, R. Urbansky, and R. Beigang, *Appl. Phys. Lett.* **109**, 021105 (2016).
- [53] L. Duvillaret, F. Garet, and J.-L. Coutaz, *Appl. Opt.* **38**, 2 409-415 (1999).

- [54] J. C. Lagarias, J. A. Reeds, M. H. Wright, and P. E. Wright, *SIAM J. Optim.* **9**, 1 112-147 (1998).
- [55] M. Scheller, C. Jansen, and M. Koch, *Opt. Comm.* **282**, 7 1304–1306 (2009).
- [56] K. Berdel, J. G. Rivas, P. H. Bolívar, P. de Maagt, and H. Kurz, *IEEE Trans. Micro. Theo. Techni.* **53**, 4 (2005).
- [57] L. Razzari, F. H. Su, G. Sharma, F. Blanchard, A. Ayesheshim, H.-C. Bandulet, R. Morandotti, J.-C. Kieffer, T. Ozaki, M. Reid, and F. A. Hegmann, *Phys. Rev. B* **79**, 193204 (2009).

Chapter 6

Conclusions and perspectives

The objective of this thesis was to develop and experimentally demonstrate novel techniques for THz electric field measurement without over-rotation limitation. THz electric field measurement with excellent SNR and a higher DR is the cornerstone for successful and proper interpretation of the experimentally obtained data from such measurement, especially in THz nonlinear experiments where one needs to compare intense and weak THz signals. The current golden standard for measuring the THz waveform is the conventional electro-optic sampling (EOS) technique. However, conventional EOS technique has limited DR due to over-rotation. This limited DR poses a challenge to measure intense THz signals and weak signals at the same time with the EOS technique. Currently, researchers are forced to use THz filters to make sure that their measurements are within the DR of the EOS technique, and then calibrate them against reference data. However, this not only distorts the THz waveform but when the filters (such as silicon) are irradiated with intense THz radiation, there could be substantial changes in their transmission characteristics due to nonlinear THz effects. Therefore, a proper interpretation of the experimentally obtained data through conventional EOS technique in intense THz experiments could be complicated.

In the framework of this thesis project, we have proposed and experimentally demonstrated with success, three techniques for measuring intense THz electric field without over-rotation limitation. All of the proposed techniques exploit spectral-domain interferometry (SDI), but using different interferometers to interfere the optical probe beam (OPB). The first technique makes use of a glass plate in a Michelson-type interferometer arrangement (the standard SDI). The second technique makes use of Mach-Zehnder interferometer (MZI-SDI technique), while the third makes use of PM single-mode fiber (CP-SDI technique).

In the initial stage of this thesis, we have reproduced the THz electric field measurement with the standard SDI under same experimental conditions in order to enable comparison between the standard SDI, MZI-SDI, and CP-SDI techniques for THz electric field measurement. Furthermore, we have demonstrated successfully the self-referencing

method, which has significantly reduced the mechanical vibration in the setup thus offering six-fold enhancement in the SNR of the standard SDI.

In the second stage of the thesis, the MZI-SDI technique for coherent THz electric field measurement was successfully demonstrated, primarily to overcome the limited scan range in the standard SDI technique. Although the MZI-SDI technique offers high DR of ~ 56.02 dB, compared to ~ 26.02 dB for the conventional EOS technique, the SNR of the former was inferior ~ 31.21 dB, which is due to mechanical vibrations in the optical components that were used to interfere the two optical probe beam pulses in this version (those optical components are notably more in number compared to those used in the standard SDI technique). A comparison between the standard SDI and MZI-SDI techniques for THz electric field measurement was performed. Based on the outcome experimental findings, we concluded that the MZI-SDI technique for THz electric field measurement is better than the standard SDI technique for THz electric field measurement, because the former offers no limits in the temporal scan range, while the latter offers a limited temporal scan range (3 ps), once more both techniques offer comparable SNR.

In the third stage of the thesis, a novel technique (CP-SDI) for coherently detecting THz radiation was proposed and demonstrated successfully. Once more, this technique offers no limit in the temporal scan range, a tremendous DR $\sim 7 \times 10^6$, which represents 4 orders of magnitude higher than the DR of conventional EOS, and at the same time high SNR ~ 48.97 dB, which is comparable to the SNR of the conventional EOS technique. Comparing between MZI-SDI and CP-SDI techniques in THz electric field measurement reveals, based on the experimental findings, the merits (ultrahigh DR, and excellent SNR) of the latter and its suitability for THz spectroscopy.

The enhanced SNR offered by the CP-SDI technique is attributed to efficient noise mitigation in this version of the SDI technique, since both interfering signals are traveling through the same fiber, and any change in OPD is common to both signals. However, further enhancement in the SNR of the CP-SDI technique is limited, due to challenges in employing the common self-referencing method. This is because, in the common self-referencing method, the probe beam must sample at least two spatial points, one with finite THz field and the other with zero THz field. However, the use of the fiber in the SDI technique limits the spatial information to only one point in the THz beam, thus making common self-referencing a challenge. On the

other hand, the potential to enhance the SNR and consequently the DR in the MZI technique is high, by employing the common self-referencing method, which could be realized much easier compared with the CP-SDI technique. The potential enhancement in the SNR of the MZI-SDI technique when the common self-referencing method applied could be much larger compared with the standard SDI technique in THz electric field measurement, since in the MZI-SDI technique, there is more optics involved to interfere the two pulses, and thus measurements are much more sensitive to mechanical vibrations in the setup.

In the course of this thesis work, two attempts were carried out with the goal to increase the SNR in CP-SDI THz detection technique by (i) a new referencing method and (ii) using a compact CP-SDI module. The new referencing method has not contributed significantly to enhancing the SNR of the CP-SDI technique for THz electric field measurement due to the leakage of the OPB beam signal that is carrying both THz and noise information into the CCD camera reference signal frame that presumably contains solely pure noise signal. Thus when we apply our algorithm to obtain pure THz wave form with reduced noise, we were actually subtracting frames carrying (slightly leaked THz information+noise information signal) from frames carrying (THz information signal + noise information signal), leading to slightly reducing the THz signal itself. On the other hand the compact CP-SDI version offers better SNR, which is attributed to the fact that all optical components along with the PM fiber are firmly held together in one module. Such arrangement contributed significantly in mitigating the mechanical vibrational noise and establishing a vibration-insensitive system that offers better SNR.

In the final stage of the thesis work and in order to accomplish the second objective of the SDI project (the application part) we demonstrated the validation of the CP-SDI technique in THz spectroscopy application. We have chosen to perform THz-TDS measurements- *in transmission geometry*- on a material that encounters challenges in the THz frequency range, such as a high permittivity sample of Barium Strontium Titanate (BST) that exhibits significant absorption losses in THz frequencies region, thus affecting the SNR of the THz measurement. The experiment was carried out successfully using the compact CP-SDI module and it was an excellent testing opportunity to evaluate our new technique capabilities in determining BST dielectric response in the THz frequency region. Comparing the dielectric response results obtained with the CP-SDI THz detection technique with those obtained with the

conventional EOS THz detection technique for the same BST sample reveals that the former offers better results than the latter owing to its ultrahigh DR and good SNR.

In short, we have demonstrated novel SDI techniques for THz electric field measurements. Those techniques are promising and have the potential to significantly advance new areas of THz science and technology, such as nonlinear THz spectroscopy, thus opening new avenues in THz-TDS and imaging techniques that require large DR. The notorious long-standing problem of mechanical vibration noise in SDI techniques can be solved by several means. For example, more investigation is required in order to enhance the performance of the new referencing method in the CP-SDI technique. This could be achieved by eliminating the leakage of the OPB beam signal, which carries both the THz and noise information into the CCD camera reference signal frame, and is supposed to contain solely pure noise signal when the THz is momentarily blocked by the chopper blade. In other words, we should acquire the CCD camera frame that carries information on both the THz and noise signals, and after a very short time we should acquire the next frame that carries solely pure noise signal information. Moreover, the current home-made spectrometer attached to the CP-SDI technique setup could be replaced by a compact module of the spectrometer itself, where all optical components (the diffraction grating, the cylindrical lens, and the CCD camera) are held together firmly in one assembly, similar to the compact module of the PM fiber. With such approach, one can mitigate the mechanical vibration in the setup. As matter of fact, the current spectrometer attached to the CP-SDI technique setup was designed so that its different optical components are positioned separately and aligned on the optical table, which results in the SDI setup being highly susceptible to mechanical vibrations. Furthermore, both modules (the spectrometer and the PM fiber) could be mounted together firmly (for instance by a cage system that uses four rigid steel rods on which optical components can be mounted along a common optical axis) in order to reduce their sensitivity to any mechanical vibration that could introduce phase noise in the CP-SDI technique. Such measures could improve the overall SNR of the CP-SDI.

Résumé en français

1. Introduction

Le rayonnement TéraHertz (THz = 10^{12} Hz) est une région du spectre électromagnétique (EM) située entre les fréquences infrarouges (IR) et micro-ondes. Cette région, qualifiée d'infrarouge lointain, varie entre 0,1 à 10 THz, ce qui correspond à des nombres d'onde compris entre 3 et 300 cm^{-1} , des énergies de photons comprises entre 0,4 et 40 meV, et des longueurs d'onde entre 3 mm et $30\text{ }\mu\text{m}$. Cette partie du spectre EM n'a pas été bien explorée en raison du manque de sources efficaces pratiques et de détecteurs sensibles, ce qui donne à cette bande de fréquences le nom de « THz gap ». Dans le passé, les applications technologiques dans la région de THz ont été entravées par le fait que cette gamme de fréquences est située entre l'électronique et l'optique, c'est-à-dire qu'elle est dans la limite supérieure de ce qui est accessible par l'électronique et elle est dans la limite inférieure à ce qui est accessible par optique. La figure 1 représente la bande de THz dans le spectre électromagnétique [1-3].

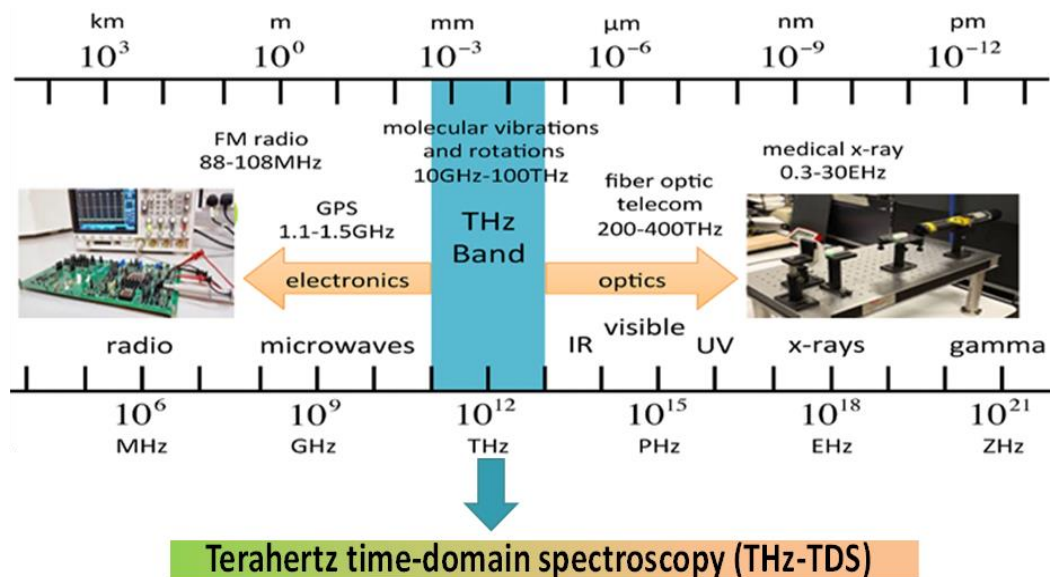


Figure 1 | Spectre électromagnétique avec des fréquences THz situées entre micro-ondes et infrarouges [3].

L'interaction du rayonnement électromagnétique avec la matière a été le centre d'intérêt pour les scientifiques et les chercheurs. L'un des jalons de l'étude du phénomène nouveau en physique et en chimie est la disponibilité de sources lumineuses et de détecteurs pouvant réaliser des techniques spectroscopiques dans les régimes linéaires et non linéaires. Les régions de micro-ondes et de fréquences optiques sont bien établies avec de nombreuses sources lumineuses et des détecteurs. Cependant, la région de THz reste bien inexplorée depuis longtemps. Plusieurs phénomènes importants se produisent dans ce domaine fréquentiel, ce qui fait de la région de THz une zone d'intérêt particulier pour la communauté scientifique. Par exemple, les vibrations intermoléculaires des matériaux solides sont observées aux fréquences THz. En biologie, des modes collectifs importants de protéines vibrent aux fréquences THz. Les niveaux d'énergie de

rotation des petites molécules entrent également dans la fréquence de THz. Les années récentes ont été témoins d'importants développements de techniques liées à la spectroscopie THz dans le domaine temporel (THz-TDS) et à l'imagerie. La polyvalence de ces techniques a été démontrée dans un large éventail d'applications et dans de nombreuses disciplines, telles que l'imagerie spectroscopique et la tomographie [4,5], le diagnostic et l'analyse génétiques sans étiquette [6], la spectroscopie biomoléculaire [7] et les applications biomédicales [8].

2. THz génération

Il existe diverses façons de générer du rayonnement THz à l'aide de lasers femtosecondes. L'une des méthodes les plus conventionnelles consiste à utiliser une antenne photoconductrice ultra-rapide (« photoconductive antenna » (PCA)) [9,10]. Lorsque les oscillateurs sont utilisés pour générer un rayonnement THz, la PCA est un bon choix. Dans le cas des systèmes laser amplifiés, les effets non linéaires dans les semi-conducteurs empêchent l'utilisation de PCA. La deuxième méthode couramment utilisée pour générer le rayonnement THz dans le cas des lasers amplifiés est la rectification électro-optique dans un cristal non linéaire. Normalement, les cristaux de ZnTe sont utilisés pour la génération de THz car ils satisfont la condition de l'accord de phase, mais le coefficient d'électro-optique est trop faible ce qui ne permet pas avoir une efficacité de génération supérieure à l'ordre de 10^{-5} . D'autres cristaux tels que LiNbO₃ ne pouvaient être utilisés auparavant en raison du désaccord de phase entre la vitesse de groupe des impulsions optique et la vitesse de phase de l'onde THz. Cependant, en 2002, Hebling *et al.* ont proposé la technique d'inclinaison du front d'onde pour faire correspondre la vitesse de groupe de l'impulsion optique à la vitesse de phase de l'impulsion THz dans le but de générer un rayonnement THz intense de LiNbO₃ [11]. La troisième méthode commune pour la génération de THz est par plasma [12]. La rectification électro-optique et les sources de plasma fournissent un rayonnement THz intense.

3. Techniques conventionnelles pour la détection cohérente de THz

En principe, les mécanismes d'émission THz décrits dans la section 2 peuvent être exploités pour la détection des impulsions THz. Par exemple, les mêmes structures PCA peuvent être utilisées comme détecteurs THz tandis que le mécanisme inverse pour OR est un échantillonnage électro-optique (« electro-optic sampling » (EOS)). Les deux techniques de détection sont habituellement utilisées pour mesurer la forme d'onde du champ électrique THz. Le mécanisme inversé pour la génération THz en plasma est connu sous le nom de la détection cohérente par polarisation électrique dans l'air (« THz-air-biased-coherent detection » (THz-ABCD)). Pour les techniques de détection de rayonnement THz intense, EOS et THz-ABCD sont les meilleurs candidats qui sont couramment exploités. Les détecteurs PCA ne sont pas couramment utilisés pour détecter des impulsions THz intenses, malgré leur qualité. Une des raisons est que le détecteur PCA est très sensible au bruit électromagnétique ambiant, qui pourrait être relativement élevé lors de l'utilisation de systèmes laser amplifiés à haute énergie. Cependant, le principal inconvénient de l'utilisation de PCA pour la détection d'impulsions intenses de THz est

la présence éventuelle d'effets non linéaires dans le substrat semi-conducteur induit par le champ THz intense, ce qui conduit à une interprétation incorrecte du signal THz détecté.

4. Technique EOS pour une détection intense de l'impulsion THz

La technique EOS apparaît comme le choix le plus populaire pour la mesure du champ électrique THz et cela est due à deux raisons : (i) les matériaux électro-optiques sont facilement disponibles, contrairement aux antennes temporisées, qui nécessitent généralement des techniques de microfabrication pour les fabriquer (ii) la détection électro-optique est adaptée aux signaux avec une grande bande passante, beaucoup plus grande que la bande passante offerte par le système PCA [13]. Dans la technique EOS, le champ électrique appliqué induit un changement d'indice de réfraction dans un matériau électro-optique (EO) à des fréquences visibles et proches IR qui sont proportionnelles au champ appliqué. La technique est basée sur l'effet Pockels dans un cristal EO où une impulsion optique femtoseconde est utilisée pour sonder le champ électrique de l'impulsion THz [14].

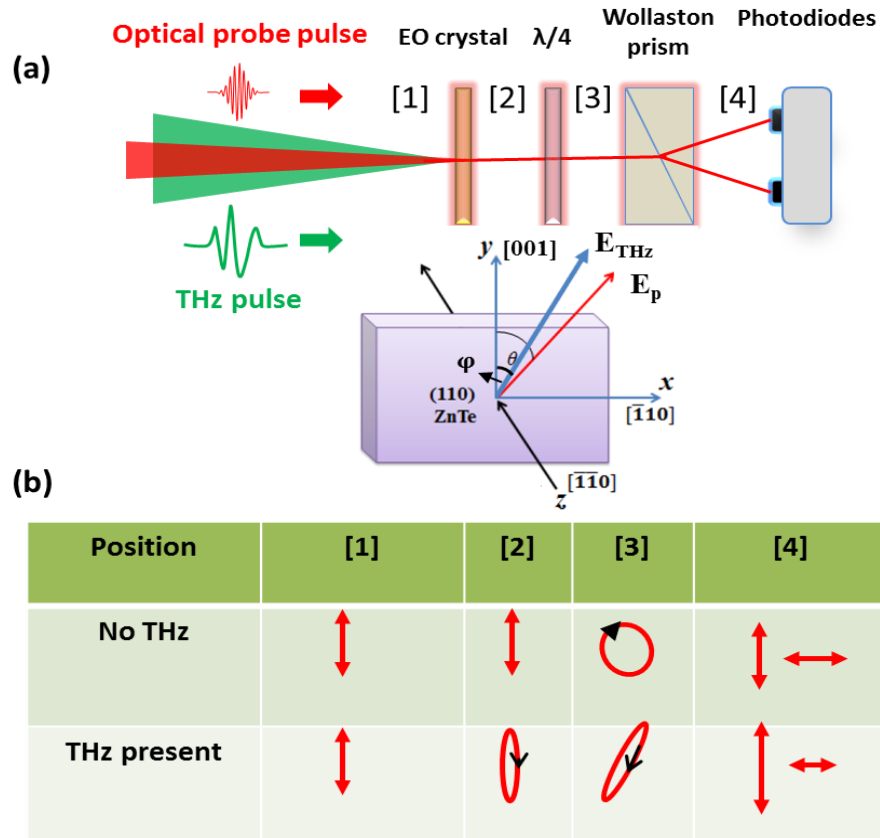


Figure 2 | Détection THz en utilisant la technique EOS avec une détection équilibrée (a). L'évolution des composants de polarisation du faisceau optique de sonde sans et avec présence de THz (b) [adapté de la réf. 15].

Le changement de l'indice de réfraction dans le cristal EO affecte l'ellipticité d'une impulsion laser ultra rapide polarisée circulairement quand l'impulsion THz traverse le même matériau. Cette modification de l'ellipticité est mesurée avec un diviseur de faisceau qui sépare les deux

composantes de polarisation orthogonale du faisceau de la sonde optique. En raison de l'effet de Pockels, la biréfringence induite dans le cristal EO non linéaire est directement proportionnelle à la force du champ électrique THz. Un photodétecteur équilibré mesure la différence d'intensité entre les deux composants et donne un signal directement proportionnel au champ électrique THz. En faisant varier le délai entre l'impulsion THz et l'impulsion laser sonde, on obtient le champ électrique dépendant du temps complet. Un diagramme schématique typique de la mesure équilibrée utilisant cette technique EOS est représenté sur la figure 2 (a) alors que la figure 2 (b) illustre l'évolution des composantes de polarisation du faisceau optique de sonde sans présence de THz. Sans l'impulsion THz, l'impulsion de sonde optique linéairement polarisée (position 1) traverse le cristal EO sans subir de biréfringence (position 2), qui passe ensuite par une plaque à lame d'onde et devient circulairement polarisée (position 3). Un analyseur d'état de polarisation, tel qu'un prisme Wollaston est utilisé pour séparer les composants de polarisation orthogonaux (position 4) et chacun est envoyé à l'une des photodiodes d'un détecteur équilibré.

Le détecteur connecté à un amplificateur à détection synchrone qui mesure la différence entre les deux signaux des photodiodes, ce qui donne une lecture nulle sans l'impulsion THz. Lorsque l'impulsion de la sonde optique et l'impulsion THz co-propagent à travers le cristal EO, le champ THz induit une biréfringence qui produit une polarisation elliptique de l'impulsion (position 3), introduisant ainsi un déséquilibre du signal entre et (position 4). Cette différence entre les deux signaux peut directement donner l'information d'amplitude du champ électrique de l'impulsion THz [14] en utilisant les équations suivantes :

$$I_s = I_y - I_x = I_0 \Delta\phi \propto E_{THZ} \quad (1)$$

Ici,

$$I_x = \frac{I_0}{2} (1 - \sin\Delta\phi) \approx \frac{I_0}{2} (1 - \Delta\phi) \quad (2)$$

$$I_y = \frac{I_0}{2} (1 + \sin\Delta\phi) \approx \frac{I_0}{2} (1 + \Delta\phi) \quad (3)$$

Où I_0 est l'intensité totale du faisceau de sonde optique et $\Delta\phi$ est le retard de phase entre les deux composants de polarisation. Il convient de noter que dans l'équation (2) et l'équation (3), on utilise une approximation, et ainsi une relation linéaire entre le champ électrique THz et le signal est observée dans l'équation. (1). Par conséquent, la plage dynamique («dynamic range» (DR)) de la technique EOS est limitée. La forme d'onde entière de THz peut être reconstituée dans le temps en employant un étage de retard optique pour analyser le délai entre l'impulsion de la sonde de femtoseconde et l'impulsion de THz.

5. Limitations et défis dans les méthodes classiques de détection de THz

La détection cohérente de champs électriques THz intenses est actuellement réalisée par diverses méthodes [16, 17]. Cependant, ces techniques conventionnelles pour la détection de THz ont plusieurs défis quand elles sont exploitées pour une mesure intense de champ électrique THz. Par exemple, avec la technique EOS, si le champ électrique THz est assez intense, une différence de phase de plus de $\pi/2$ sera introduite sur le faisceau optique de la sonde, ce qui

entraîne une inversion de la modulation d'intensité de l'impulsion de la sonde. Ceci, à son tour, entraînera des ambiguïtés dans le champ THz mesuré, ce qui posera une limitation dans la détection de champs électriques THz intenses en utilisant la technique conventionnelle EOS [18]. Cette limitation est connue sous le nom de sur-rotation qui pose certaines restrictions dans la mesure du champ électrique THz via la technique EOS, par exemple l'utilisation d'un cristal de détection plus épais (ce qui est nécessaire pour améliorer la résolution spectrale et le rapport signal sur bruit de la mesure de THz) est limitée en raison de la possibilité accrue de sur-rotation car la biréfringence introduite dans le cristal de détection est proportionnelle au champ électrique de THz et à l'épaisseur du cristal de détection EO. La technique EOS conventionnelle actuelle souffre encore une fois de la DR limitée atteinte en raison de la limitation de la rotation excessive dans la mesure du champ électrique THz intense. D'autre part, les détecteurs PCA ne sont pas couramment utilisés pour détecter des impulsions THz intenses, malgré leur qualité. Une des raisons est que le détecteur PCA est très sensible au bruit électromagnétique ambiant, mais l'inconvénient majeur d'utiliser la PCA pour la détection d'impulsions THz intenses est la présence possible d'effets non linéaires dans le substrat semiconducteur induit par le champ THz intense. Il convient de noter que la technique THz-ABCD n'a pas le problème de la rotation excessive, mais la nécessité d'une alimentation à haute tension rend plus compliqué à utiliser par rapport aux techniques EOS. Ainsi, l'EOS est la technique la plus pratique pour mesurer le champ électrique THz intense. Cependant, son DR limité rend très difficile la mesure de signaux THz intenses et de signaux faibles en même temps. Normalement, les filtres THz (tels que les goffres de silicium) sont utilisés pour s'assurer que les mesures se situent dans la DR de la technique EOS puis calibrées par rapport aux données de référence. Cependant, cela déforme non seulement la forme d'onde THz, mais lorsque ces filtres sont irradiés avec un rayonnement THz intense, il pourrait y avoir des changements substantiels dans leurs caractéristiques de transmission en raison des effets THz non linéaires. Dans le cadre de cette thèse, nous décrivons une nouvelle technique de mesure de la forme d'onde THz sans limitation de rotation excessive, possédant une énorme DR $\sim 7 \times 10^6$, tout en présentant un rapport signal sur bruit (« signal to noise ratio » (SNR)) élevé qui est comparable à celui des techniques EOS couramment utilisées. Dans cette nouvelle technique, nous utilisons la technique de l'interférométrie de domaine spectral (« spectral-domain interferometry » (SDI)) pour développer différents schémas de détection tels que la SDI basé sur le type d'interféromètre de Michelson (plus tard on le distingue comme SDI standard), la SDI basé sur l'interféromètre Mach-Zehnder (MZI-SDI) et la SDI à base de fibres (plus tard, nous les distinguons en tant que systèmes SDI (CP-SDI) à polarisation croisée pour mesurer des champs électriques THz intenses.

6. Configuration expérimentale SDI et résultats

6.1 Standard -SDI

Le schéma de la technique SDI standard pour la mesure du champ électrique THz est illustré à la Figure 3. Le laser Ti:saphir fournit une impulsion femtoseconde avec la durée de 40 fs, avec un taux de répétition de 2,5 kHz, une longueur d'onde de 800 nm, 4 mJ d'énergie par

impulsion, et un diamètre de faisceau de ~ 10 mm. Le faisceau laser entrant est divisé par le diviseur de faisceau (BS1) dans un bras de faisceau de sonde et un bras de faisceau de pompe. Le faisceau de pompe est utilisé pour générer l'impulsion THz à l'aide de la technique à impulsions inclinées à partir d'un cristal LiNbO_3 [19,20] pompé avec des impulsions optiques de 0,96 mJ. Des impulsions THz à cycle unique avec des énergies allant jusqu'à $0,3 \mu\text{J}$ sont générées avec une bande passante s'étendant de 0,1 à 3 THz. Le diviseur de faisceau (BS2) divise le faisceau de sonde optique (« optical probe beam » (OPB)) en deux parties égales : la partie transmise et la partie réfléchi. La partie réfléchi du faisceau est envoyée à une plaque de verre de 0,3 mm d'épaisseur. Les deux surfaces de la plaque de verre reflètent chacune $\sim 4\%$ du faisceau incident. La moitié du faisceau de sonde qui est réfléchi par la plaque de verre est transmise à travers le diviseur de faisceau à 50% (BS2).

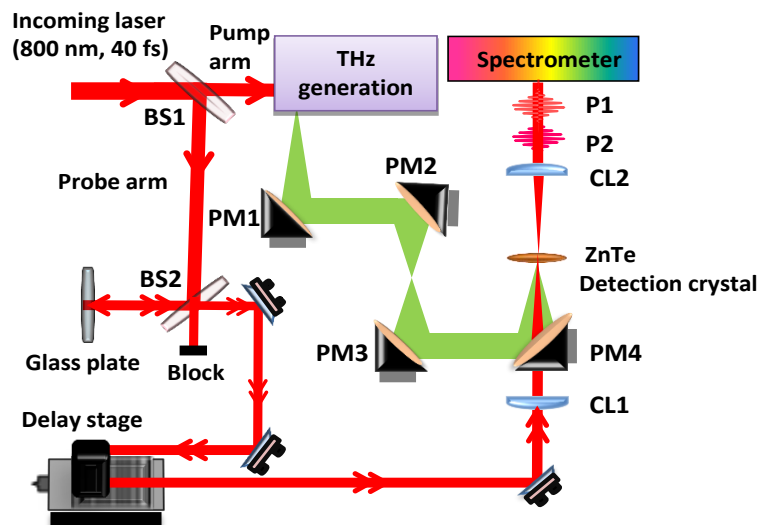


Figure 3 | Configuration expérimentale de la méthode SDI basée sur le type interféromètre de Michelson (SDI standard) pour la mesure du champ électrique THz, P1 et P2: impulsions optiques de référence et d'échantillon.

Le signal réfléchi de la plaque de verre comprend deux impulsions, une qui est réfléchi par la surface avant, et la seconde est réfléchi par la surface arrière de la plaque de verre. À l'aide d'une lentille cylindrique (CL1), ces deux impulsions sont focalisées sur le cristal détecteur ZnTe d'une épaisseur de 1 mm, se chevauchant avec le faisceau THz focalisé. Le faisceau THz est guidé et recentré sur le cristal de détection ZnTe par un ensemble de quatre miroirs paraboliques hors axe (PM1-PM4). Une lentille cylindrique (CL2) est utilisée pour collimater le faisceau de sonde, qui est ensuite envoyé à un spectromètre qui consiste en un réseau de diffraction (1200 rainures / mm), une lentille cylindrique (CL3, $f = 100$ mm) et une caméra CCD 2D (Dalsa Inc. CR-GM00-H6400, 480×640 pixels). La présence du champ électrique THz induit une biréfringence dans le cristal de détection ZnTe en raison de l'effet Pockels. La biréfringence est induite sur l'impulsion réfléchi par la surface arrière de la plaque de verre (P2), mais l'impulsion réfléchi par la surface avant de la plaque de verre (P1) traversera le cristal de détection ZnTe sans subir l'effet de biréfringence.

Immédiatement, la différence de chemin optique (« optical path difference » (OPD) (ou changement de phase) en raison de la différence de phase entre P1 et P2 peut être mesurée à partir des franges d'interférence obtenues, ce qui est à leur tour, proportionnel au champ électrique THz. On peut exprimer mathématiquement l'interférence entre les deux impulsions OPB P1 et P2 dans le schéma SDI standard, comme [21]

$$I(k) = I_R(k) + I_S(k) + 2\sqrt{I_R(k)I_S(k)}\cos[\varphi_o + kL] \quad (4)$$

Ici, $k = 2\pi / \lambda$ est le nombre d'onde, I_R est l'intensité de l'impulsion de référence, I_S est l'intensité de l'impulsion de l'échantillon, φ_o est la constante de phase, L est l'OPD introduit entre la référence et les impulsions de l'échantillon et la phase est introduite par le signal THz. En phase de mesure avec la SDI, l'information provenant de la différence de phase instantanée entre les deux impulsions P1 et P2 est extraite selon [22]

$$\varphi(L) = \tan^{-1} \left[\frac{\tilde{H}(I(L))}{I(L)} \right] \quad (5)$$

Ici, \tilde{H} et I sont la transformée de Hilbert et l'intensité du signal d'interférence de l'équation. (4) à une OPD de L qui correspond à l'OPD introduite entre P1 et P2 en raison de l'épaisseur de la plaque de verre. La modification de l'OPD au fil du temps peut être retracée en surveillant le changement de phase dans l'équation (5), qui est à son tour, comme mentionné précédemment, proportionnel à la force du champ électrique THz.

La figure 4 montre le champ électrique THz obtenu avec la technique SDI standard (a) et le spectre de puissance de la transformée de Fourier correspondant (b). On peut voir que la longueur de balayage temporel est limitée à 3 ps seulement, d'après le spectre de puissance de Fourier, nous avons évalué SNR ~38.12 dB.

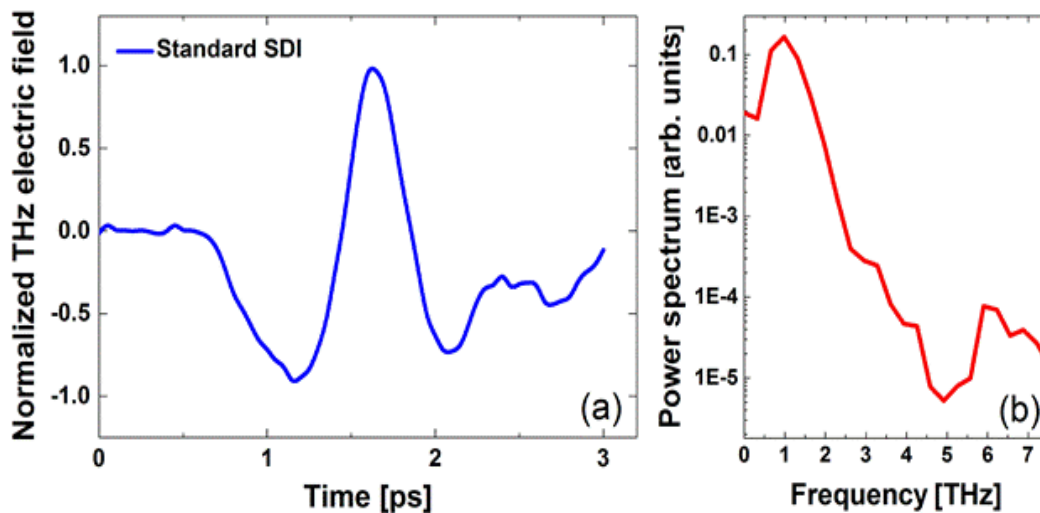


Figure 4 | Le champ électrique THz obtenu avec la technique SDI standard (a) et le spectre de puissance de la transformée de Fourier correspondant (b).

de l'impulsion THz à plusieurs cycles mesurés à l'aide du champ électromagnétique EOS classique au THz de $\sim 70 \text{ kV cm}^{-1}$. L'encadré illustre une courte fenêtre de numérisation (7 ps) pour mieux visualiser les limitations en raison de la rotation excessive. Comme on peut le voir, la sur-rotation est évidente dans certaines parties de l'impulsion principale de THz (à $\sim 5 \text{ ps}$) indiquée par des flèches, ce qui modifie sévèrement la forme de l'impulsion THz. À l'instant $\sim 26 \text{ ps}$ on peut voir la première réflexion THz à partir du cristal de détection ZnTe.

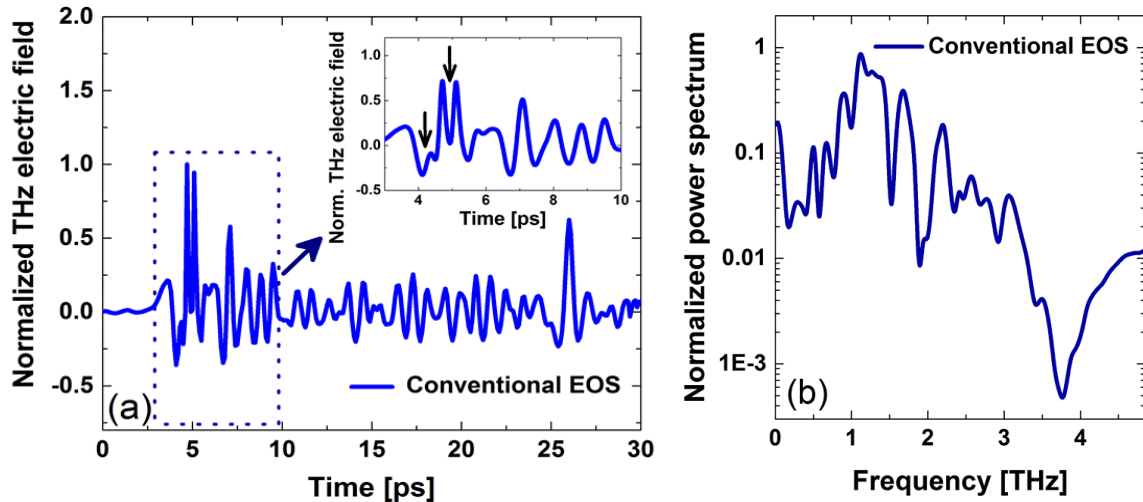


Figure 6 | La trajectoire de champ électrique THz obtenue avec la technique EOS conventionnelle avec sur rotation (a) et le spectre de puissance de Fourier du THz temporel (b) [22].

La figure 6(b) montre le spectre de puissance de Fourier correspondant de la trace de THz obtenue à la figure 6(a). Sur la figure 7 (a), nous montrons l'impulsion de THz à quelques cycles obtenus avec la technique SDI basée sur MZI à une OPD de $\sim 450 \mu\text{m}$ entre les impulsions de référence et d'échantillon du MZI.

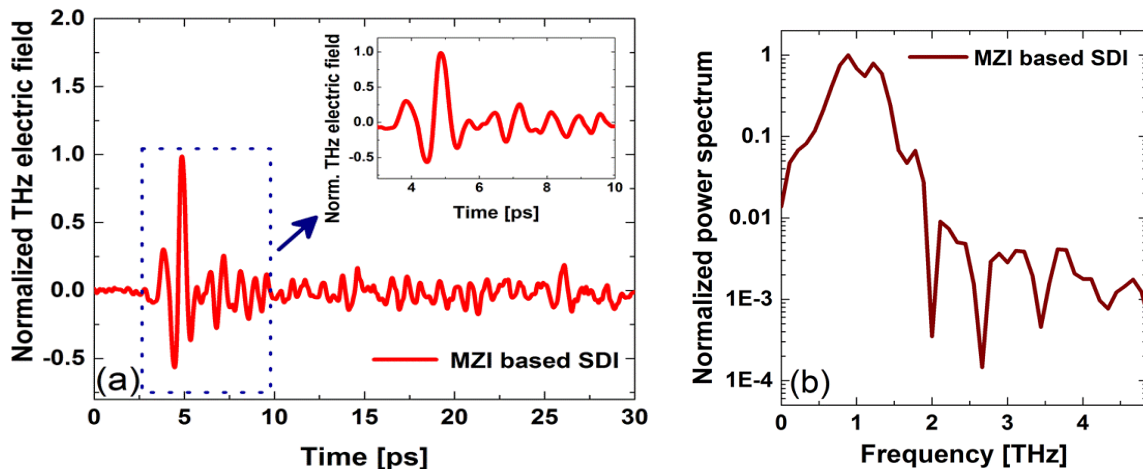


Figure 7 | THz trace de champ électrique obtenue avec la technique SDI basée sur MZI sans sur rotation (a) et spectre de puissance de Fourier de la trace temporelle THz (b) [22].

Nous notons qu'à l'instant $\sim 5 \text{ ps}$, le signal THz augmente avec une amplitude plus élevée indiquant ainsi l'impulsion THz principale, tandis qu'au moment $\sim 26 \text{ ps}$, le signal THz

correspond à la première réflexion du champ électrique THz dans le cristal de détection ZnTe. Nous avons évalué le SNR à partir du spectre de puissance de Fourier sur la figure 7 (b), à ~31,21 dB.

6.3 CP-SDI

Ici, nous utilisons la configuration expérimentale illustrée à la figure 8, où un faisceau laser femtoseconde de 800 nm est divisé par un diviseur de faisceau (BS) en deux bras : le bras de pompe et le bras de sonde. Le faisceau de pompe est utilisé pour générer l'impulsion THz à l'aide de la technique à impulsions inclinées à partir d'un cristal LiNbO₃ [19,20].

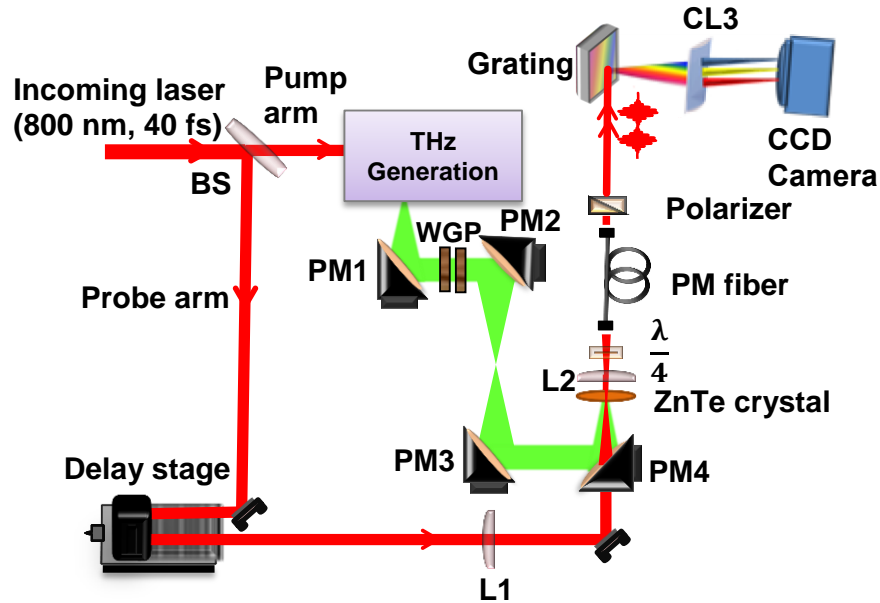


Figure 8 | Mise en place expérimentale de la technique CP-SDI pour la détection THz [23].

Le faisceau de la sonde est focalisé par une lentille plan-convexe sphérique (L1), puis se propage à travers un trou dans un miroir parabolique hors axe (PM4) et sur un cristal de détection ZnTe <110> de 1 mm d'épaisseur, où il chevauche avec l'impulsion THz focalisée. Une autre lentille plan-convexe sphérique (L2) est utilisée pour collimater le faisceau de sonde optique après le cristal de détection ZnTe. Une lame quart d'onde est utilisée avant une fibre optique PM à mode unique (Thorlabs, PM 780-HP) pour convertir l'état de polarisation linéaire de l'impulsion de la sonde en polarisation circulaire sans la présence de l'impulsion THz. Ensuite, l'impulsion de la sonde est couplée dans la fibre PM, avec ses composantes de polarisation (*s*- et *p*-) établis le long des deux axes biréfringents orthogonaux de la fibre PM en fonction de la biréfringence introduite dans le cristal ZnTe par le champ électrique THz. Les polariseurs de grille de fil (« wire grid polarizer » WGP) sont utilisés pour faire varier le champ électrique de pointe de THz.

Le spectromètre sur mesure (tel que décrit dans la section 3.2.1) se compose d'un réseau de diffraction (1200 rainures / mm), d'une lentille cylindrique plano-convexe CL3 ($f = 150$ mm) et d'une caméra CCD bidimensionnelle (2D) (Dalsa Inc., CR-GM00-H6400, 480640 pixels). Nous mesurons le changement de phase entre les composantes spectrales des deux signaux de

polarisation sortant de la fibre PM à mode unique à une longueur fixe, ce qui est proportionnel à la force du champ électrique THz uniquement.

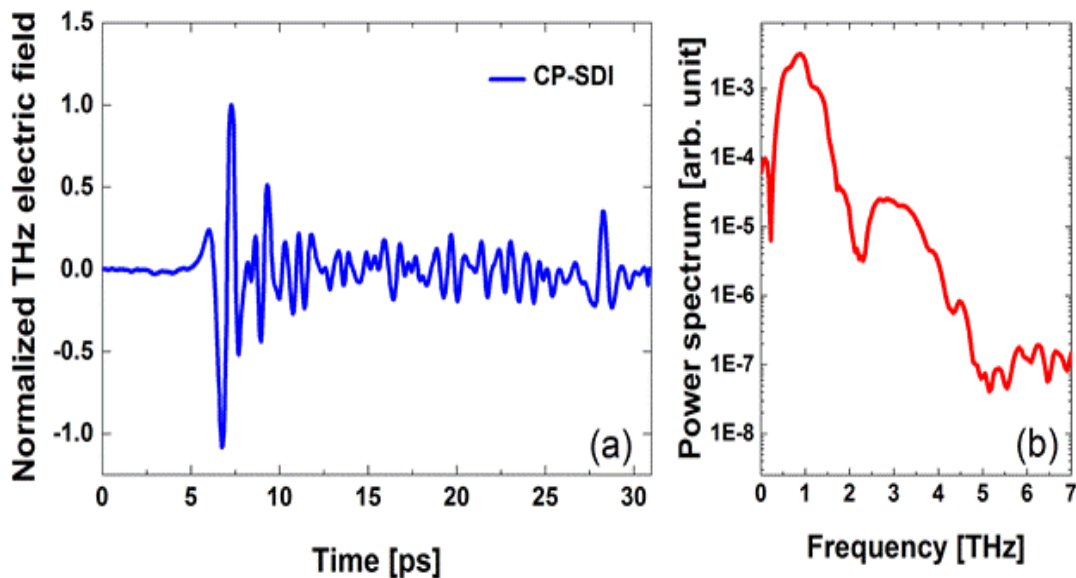


Figure 9 | La trace de champ électrique THz obtenue avec la technique CP-SDI (a) et le spectre de puissance de Fourier correspondant de la trace de THz obtenue avec la technique CP-SDI (b)[23].

En faisant varier le temps de retard entre l'impulsion de THz et l'impulsion de sonde optique en utilisant un étage de retard, la forme temporelle du champ électrique de THz peut être tracée. De plus, en employant la technique CP-SDI, nous avons obtenu un balayage temporel long (> 30 ps) pour la trace du champ électrique THz, comme il est représenté sur la figure 9 (a) avec le spectre de puissance de Fourier correspondant sur la figure 9 (b). Dans l'expérience pour acquérir la trace THz avec la technique CP-SDI, nous avons utilisé une longueur de fibre optique de 80 cm. Sur cette longueur, l'OPD entre les deux impulsions de sonde sera de $\sim 400 \mu\text{m}$ (une séparation temporelle de $\sim 1,33$ ps) à une longueur d'onde centrale $\lambda_0 = 790$ nm lorsqu'elles sortent de la fibre. Les traces THz obtenues avec les techniques CP-SDI (Fig. 9 (a)) montrent une impulsion THz à quelques cycles. En outre, pour les deux traces de THz à la fois $\sim 7,3$ ps, le signal de THz augmente avec une amplitude considérable, indiquant le pic principal de l'impulsion de THz, alors qu'à une heure $\sim 28,3$ ps, le signal augmente à nouveau avec une amplitude plus petite, correspondant à première réflexion du champ électrique THz dans le cristal de détection ZnTe. Nous avons évalué le SNR à partir du spectre de puissance de Fourier sur la figure 9 (b), à $\sim 48,97$ dB.

6.4 Comparaison entre la SDI standard, la SDI basées sur la MZI et la technique CP-SDI dans la mesure du champ électrique THz

Comme nous l'avons vu, la technique EOS conventionnelle pour la mesure intense du champ électrique de THz souffre d'effets de sur-rotation. Cependant, en utilisant notre nouvelle technologie CP-SDI pour la mesure du champ électrique THz, nous pourrions contourner cette

limitation tout en conservant un SNR comparable. En éliminant la sur-rotation, nous pourrions atteindre une gamme dynamique de 7×10^6 . D'autre part, la technique SDI standard dans la mesure du champ électrique THz présentée pour la première fois par Sharma *et al.* [18] ont obtenu le SNR et la DR inférieurs à ceux du SNR et de la DR offerts par la technique CP-SDI. Dans la technique standard SDI, l'une des principales sources de bruit de phase, est une vibration angulaire dans la plaque de verre en raison de la variation angulaire entre ses deux surfaces [18]. En outre, l'OPD entre les deux impulsions réfléchissant à partir des surfaces de la plaque de verre était relativement grande ($900 \mu\text{m}$), ce qui entraîne un fonctionnement relativement éloigné de l'OPD nul, ce qui entraîne une perte de signal d'interférence des deux impulsions et, par conséquent, diminue le SNR et la DR. Cependant, dans la technique CP-SDI, l'introduction de la fibre PM augmente le SNR dans la mesure THz principalement en raison du travail plus proche de zéro-OPD où la sensibilité de la technique est maximale. De plus, en utilisant la fibre PM, les bruits associés aux vibrations de la plaque de verre qui modifient l'OPD entre deux signaux parasites sont éliminés. Ce bruit est éliminé dans la technique CP-SDI, puisque les deux signaux parasites traversent la même fibre et toute modification de l'OPD est commune aux deux signaux. La fibre PM permet également une plage dynamique plus élevée, puisque les signaux parasites sont générés après le cristal de détection, tandis que dans la technique SDI standard, les signaux parasites sont générés avant le cristal de détection, limitant la longueur de balayage à l'épaisseur temporelle de la plaque de verre. Par conséquent, la technique CP-SDI a atteint un SNR et une DR plus élevés par rapport à la technique SDI standard. En outre, la nouvelle technique CP-SDI dans la mesure THz élimine la limite dans la longueur de balayage temporel qui est indispensable pour toute application spectroscopique THz. C'était un inconvénient de la version SDI standard de la technique [18] dans la détection de THz, en raison de la limite imposée par l'épaisseur de la plaque de verre. Cependant, dans la technique CP-SDI, la fibre PM n'impose aucune limite dans la longueur de balayage. Cependant, le SNR du CP-SDI est encore inférieur à celui de la technique EOS conventionnelle, et l'amélioration supplémentaire dans le SNR est limitée, en raison des défis liés à l'utilisation de la méthode d'auto-référencement commune [24]. C'est parce que, dans la méthode d'auto-référencement commune, le faisceau de la sonde doit échantillonner au moins deux points spatiaux, l'un avec le champ THz fini et l'autre avec un champ zéro THz. L'information provenant du faisceau de sonde à un point de champ nul THz pourrait être utilisée comme référence. Cependant, l'utilisation de la fibre dans la technique SDI (CP-SDI) limite l'information spatiale à un seul point du faisceau THz, ce qui rend l'auto-référencement commun un défi. D'autre part, le potentiel d'amélioration du SNR et, par conséquent, la DR dans la technique SDI basée sur MZI pour la mesure du champ électrique THz est élevé, en utilisant la méthode d'auto-référencement commune, qui pourrait être beaucoup mieux améliorée par rapport au CP-SDI technique. Ainsi, pour une amélioration potentielle et profonde du SNR et la DR, la SDI basée sur MZI a l'avantage par rapport à la technique CP-SDI, qui nécessite encore une méthode compliquée pour effectuer le référencement.

7. Nouveau référencement et module compact de CP-SDI

Ainsi, pour améliorer encore le SNR de la technique CP-SDI pour la mesure du champ électrique THz, nous avons tenté une nouvelle méthode de référencement, comme représenté sur la figure 10. Ici, un hacheur optique est placé dans le chemin du faisceau THz, alternativement bloquant et débloquant le faisceau THz par la lame de coupe, tandis que la caméra CCD (SK1024VPD, 1024 pixels, $10 \times 10 \mu\text{m}$, Schäfter + Kirchhoff Inc.) enregistre alternativement des cadres de frange sans et avec l'effet de la THz sur eux. La forme d'onde THz est reconstruite par échantillonnage en temps équivalent tandis que le délai entre l'impulsion de THz et l'impulsion laser de sonde optique varie en utilisant une ligne à retard. À chaque position de la ligne à retard, deux trames d'image consécutives (Frame 1 et Frame 2 telles que représentées sur la figure 10) sont acquises dans un court laps de temps, de sorte que le bruit contenu dans les deux images comporte approximativement la même valeur. Nous désignons les informations de signal obtenues à partir du cadre 1 comme le signal de référence qui contient uniquement les informations de bruit, tandis que celui obtenu à partir du cadre 2 en tant que signal THz plus l'information du signal de bruit. En soustrayant l'ancien de ce dernier, on obtient l'information de forme d'onde THz pure résultante sans bruit vibratoire pour un point temporel dans la longueur de balayage. L'acquisition et le traitement des données sont réalisés à l'aide d'un code LabVIEW développé dans notre groupe THz. Ainsi, en suivant une telle approche, nous pourrions éliminer le bruit présent dans la mesure THz. En exploitant la technique CP-SDI standard (c'est-à-dire la technique CP-SDI sans mettre en œuvre la nouvelle méthode de référence), une trace temporelle THz a été obtenue, comme montré dans la figure 11 (a).

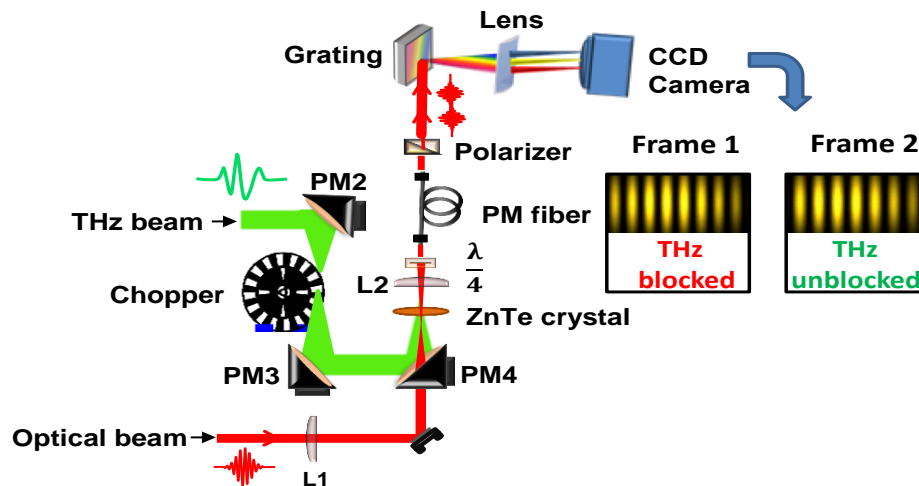


Figure 10 | Schéma partiel de la configuration expérimentale de THz où la technique CP-SDI pour la détection de THz incorporée avec le hacheur a été utilisée pour réaliser la nouvelle méthode de référencement dans la technique CP-SDI. L'hacheur bloque de manière synchrone et débloque le faisceau THz. Les interférogrammes dans les cadres de caméra CCD 1 et 2 représentent respectivement des états bloqués et débloqués.

En raison du niveau de bruit vibratoire important dans la configuration, nous n'avons pas pu distinguer le premier signal de réflexion THz du niveau du signal de bruit dans la mesure. L'encart montre une région agrandie de la ligne de base THz (1-4 ps) où nous pourrions mesurer

le SNR temporel comme le rapport entre la valeur de pic THz et l'écart-type de la ligne de base. Maintenant, en mettant en œuvre la nouvelle méthode de référencement dans la technique CP-SDI, une trace temporelle THz a été obtenue à $E_{\text{THz}} = 54 \text{ kV cm}^{-1}$, comme le montre la figure 11 (b). Nous notons que la forme d'onde dans ce cas est lisse, avec le pic principal de l'impulsion THz à $\sim 5,5 \text{ ps}$ accompagné cette fois par un premier pic de réflexion THz clair à $\sim 48,3 \text{ ps}$. L'apparition du premier pic de réflexion est une indication de l'efficacité de notre nouvelle méthode de référence pour éliminer une quantité considérable de niveau de bruit vibratoire dans la configuration. L'insertion montre une région agrandie de la ligne de base de THz (1-4 ps) où nous pourrions mesurer le SNR temporel. Sur la figure 11 (c), nous montrons que la quantité de bruit de phase de la nouvelle méthode de référence a été éliminée avec succès. De plus, nous montrons à la figure 11 (d) une comparaison entre les spectres de Fourier des traces de THz obtenues avec et sans utiliser la nouvelle méthode de référencement. Comme on l'a vu à des fréquences THz inférieures, certaines composantes de bruit ont été atténuées avec succès.

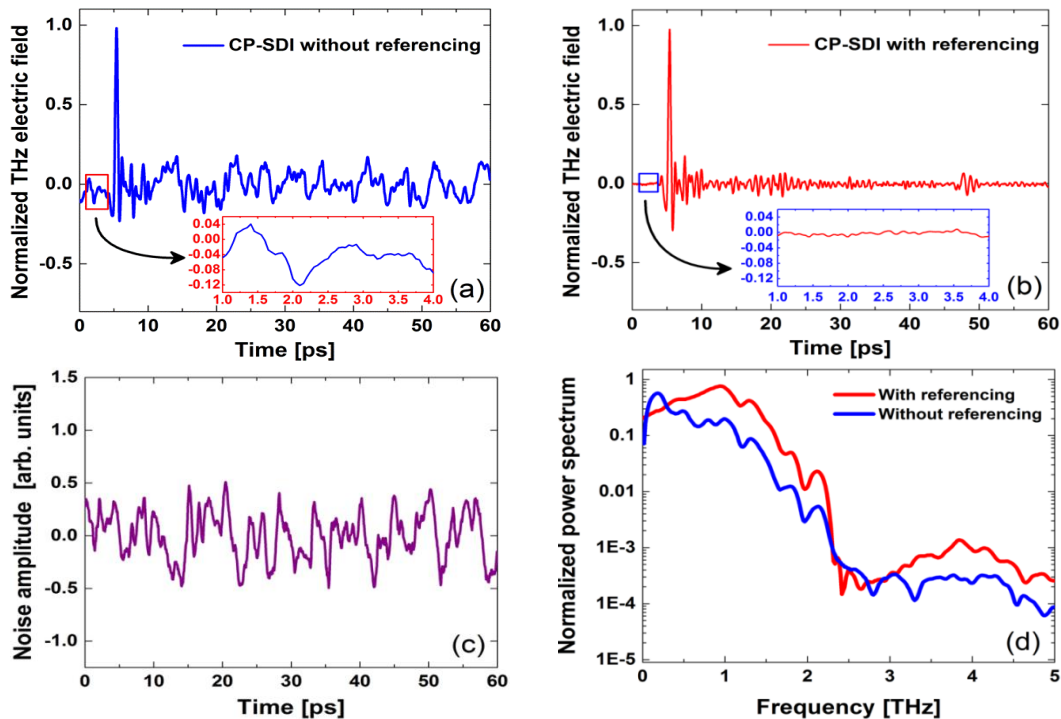


Figure 11 | La trace de champ électrique de THz obtenue avec CP-SDI sans référence (a), l'insertion dans (a) montre un bruit temporel agrandi, la trace de champ électrique de THz obtenue avec CP-SDI avec la méthode de référence (b), l'encart en (b) montre un bruit temporel agrandi, l'amplitude de bruit soustraite à l'aide de la méthode de référence (c) et les spectres de puissance de Fourier correspondants de la trace de THz obtenue avec (ligne rouge) et sans (ligne bleue) la nouvelle méthode de référencement (d).

À partir des spectres de puissance de Fourier, nous avons mesuré le SNR à $\sim 41.14 \text{ dB}$ sans utiliser la nouvelle méthode de référencement alors qu'il est calculé à $\sim 43.13 \text{ dB}$ lors de l'application de la méthode de référencement. Nous notons que lorsque nous avons suivi l'approche de la mesure du SNR temporel, le SNR mesuré est de ~ 25 pour la mesure de THz sans référence et ~ 250 lors de l'application de la nouvelle méthode de référencement, ce qui

représente une augmentation de dix fois dans SNR temporel. À partir de nos résultats expérimentaux, nous avons conclu que la nouvelle méthode de référence est efficace pour éliminer le bruit à basse fréquence et a amélioré avec succès la forme temporelle de la pulsation THz. Un autre effort a été fait afin de réduire le bruit résultant des vibrations dans la configuration. Cela a été réalisé en utilisant un petit module compact CP-SDI tel que représenté schématiquement dans la figure 12. Le module compact consiste en une lentille asymétrique collimatante (L1) avec une longueur focale courte ($f = 30$ mm). Après collimation, l'OPB passe à travers une lame quart d'onde placée avec son axe de transmission à 45° par rapport à l'axe rapide et lent de la fibre PM (780HP, MDF = $5\mu\text{m}$, 80 cm de longueur, connecteurs FC / APC les deux extrémités, axe lent orienté). Une lame demi-onde a été utilisée pour ajuster une petite erreur dans l'alignement de polarisation dans les axes de la fibre PM. La lentille asphérique focalisée (L2) ($f = 20$ mm) a été utilisée pour coupler le laser à la fibre PM. La fibre PM est connectée au module avec un connecteur FC / APC. À l'extrémité de sortie de la fibre PM, une lentille asymétrique collimatante (L3) ($f = 13,8$ mm) a été utilisée pour envoyer le faisceau collimaté au spectromètre. En exploitant le module compact CP-SDI, nous pourrions mesurer la forme d'onde temporelle du champ électrique de THz, comme représenté sur la figure 13 (a). Nous notons que la forme d'onde est lisse avec le pic de THz principal à $\sim 4,2$ ps, tandis que le premier pic de réflexion THz est de $\sim 46,7$ ps. Une fois de plus, l'apparition du premier pic de réflexion est révélatrice de l'efficacité du module dans l'atténuation du niveau de bruit vibratoire dans la configuration. L'insertion montre une région agrandie de la ligne de base de THz (0 - 2 ps) où nous pourrions mesurer le SNR temporel. La figure 13 (b) représente le spectre de puissance de Fourier des traces THz obtenues avec le module compact.

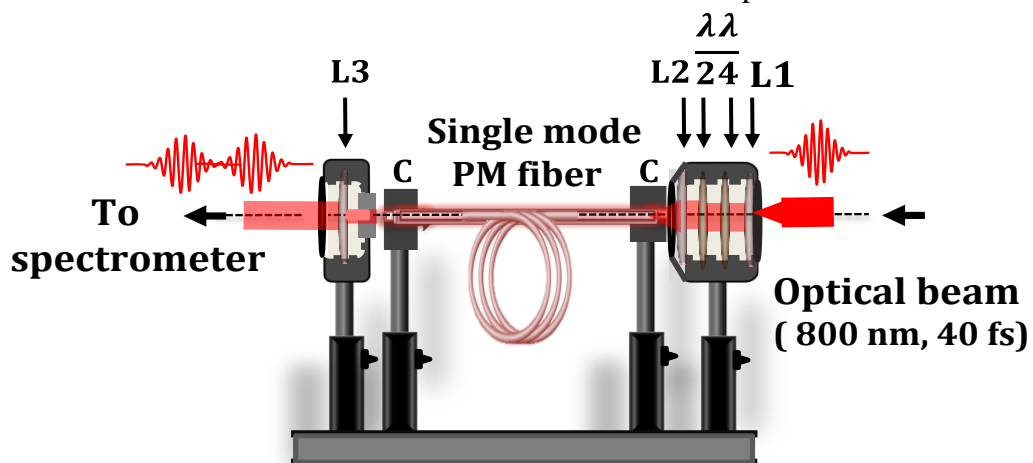


Figure 12 | Illustration schématique de la configuration expérimentale du module compact CP-SDI pour la mesure du champ électrique THz.

Le SNR mesuré du spectre de puissance est supérieur à ~ 45.44 dB alors que le SNR temporel évalué à partir de la trace temporelle est supérieur à 370.

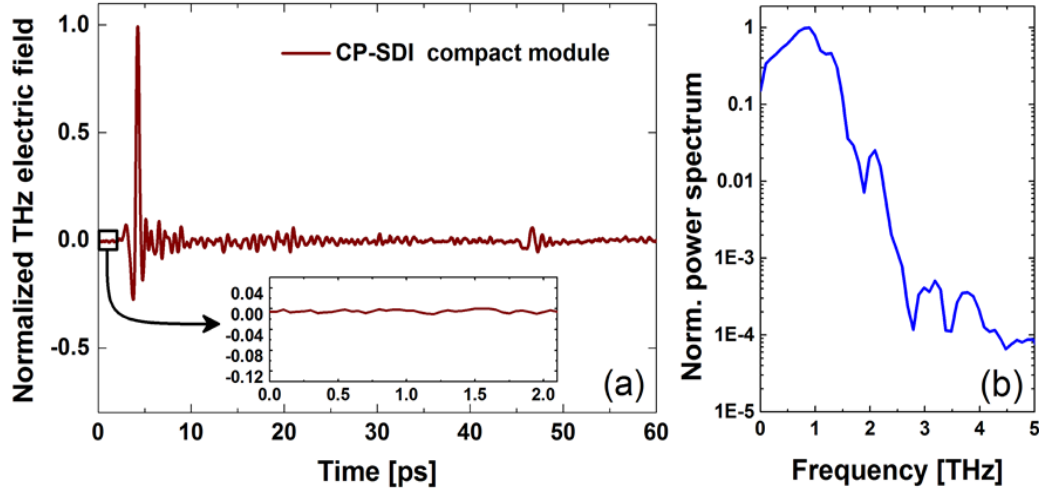


Figure 13 | La trace de champ électrique THz obtenue avec le module compact CP-SDI (a) l'insertion dans (a) montre un bruit temporel agrandi. Le spectre de puissance de Fourier correspondant de la trace de THz obtenue avec le module compact CP-SDI (b).

La performance du module compact est efficace pour éliminer un signal de bruit vibratoire à basse fréquence considérable qui est dû au fait que tous les composants optiques du module sont tous maintenus fixés ensemble et avec une plus grande stabilité, et donc ils vibrent avec une fréquence similaire conduisant à beaucoup moins d'impact sur le système par rapport à la technique CP-SDI standard (nous avons utilisé la CP-SDI standard pour le distinguer de CP-SDI avec le référencement et le module compact CP-SDI) où les composants optiques étaient montés séparément (non tenu ensemble) et donc chaque composant optique vibre séparément, ce qui conduit à de mauvaises performances (SNR pauvres). De plus, dans la norme CP-SDI, les deux extrémités de fibres sont fixées dans des étages micro-blocs XYZ avec leurs pointes libres dans l'air, sous réserve de vibrations mécaniques lors de la mise en place, ce qui conduit à influencer la qualité du couplage et le mouvement sur le motif de frange. Cela affecte à son tour le SNR de la mesure du champ électrique THz réalisée avec la technique CP-SDI standard. Nous avons conclu que le module compact réduit considérablement la sensibilité CP-SDI aux vibrations mécaniques dans la configuration et améliore ainsi le SNR.

8. Applications de la technique de détection CP-SDI dans la spectroscopie THz de matériaux à haute perméabilité

Les avantages offerts par la technique de détection de CP-SDI THz dans la détection de signaux THz intenses, par exemple, éviter la rotation excessive et le DR ultra-élevé inhérent, permettent de mesurer les signaux THz qui ont été difficiles à mesurer lors de l'utilisation de la technique de détection EOS THz classique. La démonstration de CP-SDI dans THz-TDS sert simultanément deux objectifs principaux : i) valider notre nouvelle technique de détection de THz CP-SDI et tester ses capacités dans la THz-TDS, ainsi que ii) effectuer des mesures THz-TDS en géométrie de transmission sur le matériau qui rencontre des défis dans la gamme de fréquences THz. Afin d'atteindre les objectifs susmentionnés, nous avons choisi un échantillon de haute permittivité titanate de strontium de baryum (« barium strontium titanate » BST)

comme matériau de test pour évaluer sa réponse diélectrique dans la région de fréquence de THz. En outre, nous avons comparé les résultats de réponse diélectrique obtenus via la technique de détection CP-SDI THz avec ceux obtenus grâce à la technique de détection EOS THz classique pour le même échantillon BST. Nous montrons que les résultats obtenus via le premier sont plus précis que ceux obtenus par le second et qu'ils sont comparables aux résultats publiés dans la littérature. Les formes d'ondes temporelles de térahertz nécessaires à déterminer la réponse diélectrique de l'échantillon stœchiométrique BST sont obtenues par la technique de détection EOS THz classique sont représentées sur la figure 14 (a). Ici, la ligne rouge solide représente la forme d'onde transitoire (air) térahertz de référence et la ligne solide bleue est la forme d'onde THz transmise par un échantillon stœchiométrique BST à température ambiante. Les deux formes d'onde sont mesurées à l'aide d'un cristal de détection ZnTe de 2 mm d'épaisseur. Effectuer l'analyse complexe complète, d'abord en prenant la transformée de Fourier de la référence et transmis (échantillon) des formes d'onde THz sur la figure 14 (a). À partir du spectre de puissance, le SNR mesuré de l'impulsion de référence THz est de ~ 34.77 dB tandis que le SNR de la forme d'onde transmise à travers l'échantillon BST était de ~ 26.99 dB. En effet, nous ne pouvions pas exploiter la pleine valeur du champ électrique de pointe de THz (E_{THz}) lors de la mesure des formes d'ondes temporelles en utilisant une technique de détection EOS classique avant que les effets de sur-rotation ne commencent à apparaître dans la forme d'onde de référence. Par conséquent, cela impose une limitation de la valeur de E_{THz} utilisée dans une telle mesure. Nous avons utilisé la technique de détection CP-SDI THz pour mesurer les formes d'ondes temporelles du champ électrique THz, comme le montre la figure 14 (b) pour la référence (air) et pour la forme d'onde THz transmise à travers le même échantillon stœchiométrique BST.

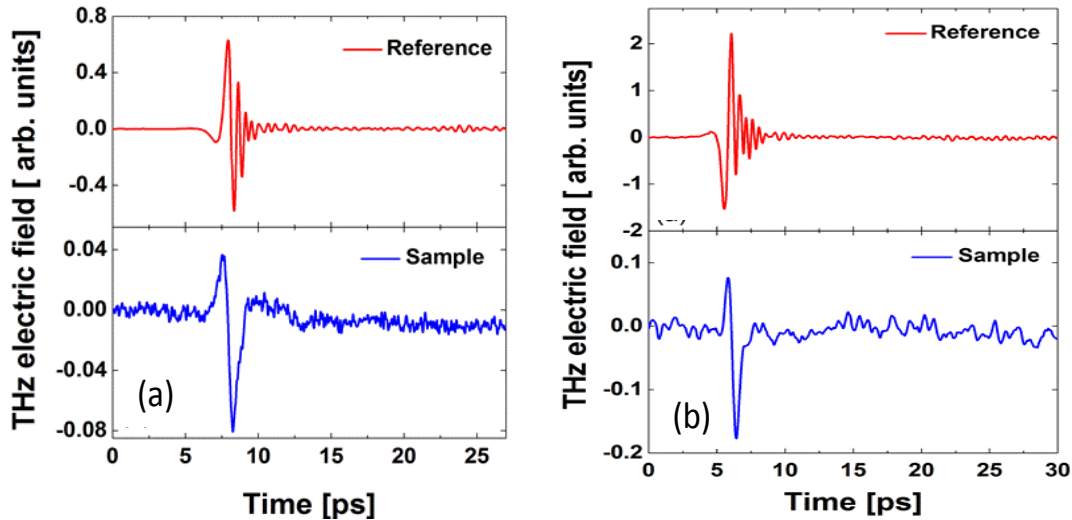


Figure 14 | Mesure de la forme d'onde temporelle THz (a) référence (air) et transmise à travers l'échantillon stœchiométrique BST $A / B = 1,00$, tous deux mesurés par EOS conventionnel à faible $E_{\text{THz}} \approx 28 \text{ kVcm}^{-1}$ et (b) référence et transmis par l'échantillon stœchiométrique BST mesuré via la technique de détection CP-SDI THz à haute $E_{\text{THz}} \approx 439 \text{ kVcm}^{-1}$.

À partir des spectres de puissance, le SNR mesuré de la forme d'onde transmise à travers l'échantillon a été mesuré à ~ 36.23 dB, tandis que le SNR de la référence a été mesuré à ~ 44.47 dB. Immédiatement, on peut remarquer de l'amélioration de SNR des formes d'onde THz mesurées à l'aide de la technique CP-SDI par rapport au SNR des formes d'onde THz mesurées à l'aide de la technique EOS pour le même échantillon, mais mesurées à plus faible E_{THz} . L'amélioration de SNR est attribuée au fait que la technique CP-SDI nous permet d'exploiter la valeur maximale totale de E_{THz} offerte par notre THz mis en place à ≈ 439 kV cm $^{-1}$ sans avoir d'effet de sur-rotation dans l'impulsion de référence THz obtenue, contrairement à la technique de détection classique EOS THz où nous avons été forcés de réduire la valeur de E_{THz} pour éviter les effets de sur-rotation. Ainsi, l'augmentation de l' E_{THz} entraînera une amélioration supplémentaire du SNR des mesures THz. Dans la figure 15 (a), nous montrons les spectres de THz mesurés de la partie réelle de la permittivité ϵ' et de la partie imaginaire de la permittivité ϵ'' à une épaisseur moyenne de $31,2 \pm 4$ μm de l'échantillon de BST en utilisant la technique EOS à la figure 15 (b), nous montrons la partie réelle mesurée de la permittivité ϵ' , et une partie imaginaire de la permittivité ϵ'' à une épaisseur moyenne de $30,3 \pm 2$ μm du même échantillon BST de 0,16 à 1,6THz obtenu par la technique CP-SDI.

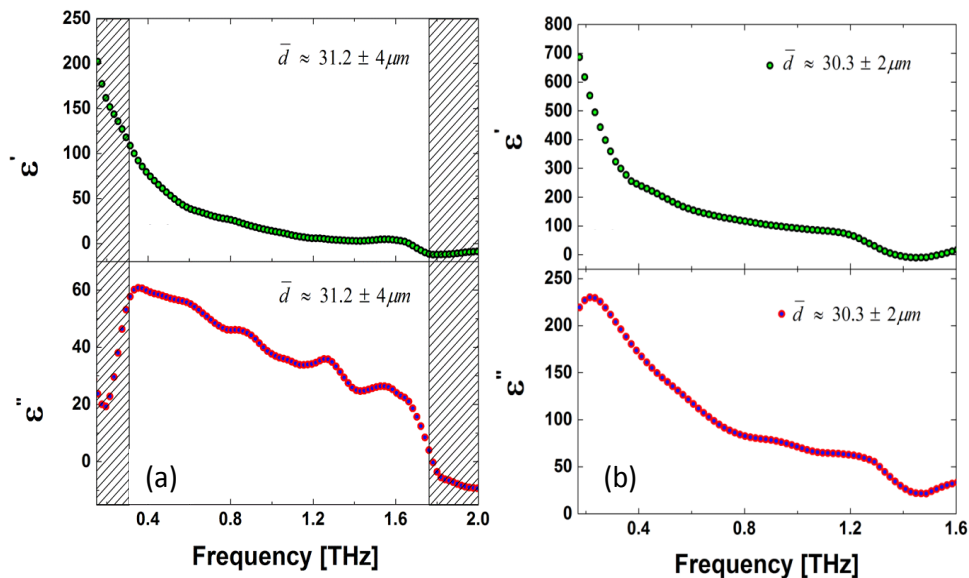


Figure 15 | L'EOS conventionnel a mesuré les spectres de THz de (a) une partie réelle de permittivité ϵ' et une partie imaginaire de permittivité ϵ'' à une épaisseur moyenne de $31,2 \pm 4$ μm d'échantillon de BST. Les zones pointillées mettent en évidence la bordure de la région spectrale la plus fiable et (b) la partie réelle mesurée CP-SDI de la permittivité ϵ' et la partie imaginaire de la permittivité ϵ'' à une épaisseur moyenne de $30,3 \pm 2$ μm du même échantillon BST de 0,16 - 1,6THz.

En effet, le mécanisme de dispersion diélectrique dominante dans notre échantillon peut être affecté par un mode de phonon d'où qui comprend deux excitations THz superposées couples et qui montrent les caractéristiques d'un mode du couplé (« soft mode » SM) et du mode central (« central mode » CM), comme Ostapchuk *et al.* ont conclu [25]. Le CM est attribué à la

fluctuation du dipôle, tandis que le SM est attribué au mode phonon optique. Les deux modes sont très proches de la fréquence et se chevauchent dans notre échantillon BST. Le petit pic exposé dans $\varepsilon''(\omega)$ par rapport à la grande dispersion dans $\varepsilon'(\omega)$ peut indiquer que les deux modes, CM et SM ont des fréquences de relaxation significativement différentes et nous observons seulement celui avec une fréquence plus élevée, ce qui est SM.

9. Conclusions

En conclusion, nous avons développé une technique de détection THz intense basée sur la technique SDI afin de pouvoir surmonter les limites de la sur-rotation. La nouvelle technique a une énorme DR ($\sim 7 \times 10^6$) et avec le SNR (~ 48.97 dB) ce qui est comparable à l'EOS conventionnel. Nous avons démontré la validation des techniques THz-TDS de la technologie CP-SDI dans la géométrie de transmission sur des matériaux qui rencontrent des défis dans la gamme de fréquences THz, comme un échantillon de haute permittivité de BST qui présente des pertes importantes dans la région des fréquences de THz. La comparaison des résultats de réponse diélectrique obtenus avec la technique de détection de CP-SDI THz avec celles obtenues avec la technique de détection EOS THz classique pour le même échantillon de BST révèle que l'ancien offre de meilleurs résultats que ce dernier en raison de son DR ultra-élevé et de son bon SNR.

Références

- [1] Handi, *Int. J. Infrared Millim. Waves* **24**, 91-118 (2003).
- [2] M. F. Kimmitt, *J. Biol. Phys.* **29**, 77-85 (2003).
- [3] <http://pratt.duke.edu/about/news/willie-padilla-exploring-technologies-terahertz-gap>.
- [4] Y. Watanabe, K. Kawase, T. Ikari, H. Ito, Y. Ishikawa and H. Minamide, *Appl. Phys. Lett.* **83**, 800-802 (2003).
- [5] S. Wang, B. Ferguson, D. Abbott, and X. C. Zhang, *J. Biol. Phys.* **29**, 247-256 (2003).
- [6] M. Nagel, P. H. Bolivar, M. Brucherseifer, H. Kurz, A. Bosserhoff and R. Buttner, *Appl. Phys. Lett.* **80**, 154-156 (2002).
- [7] A. Markelz, S. Whitmire, J. Hillebrecht, and R. Birge, *Phys. Med. Biol.* **47**, 3797-3805 (2002).
- [8] S. P. Mickan, A. Menikh, H. Liu, C. A. Mannella, R. MacColl, D. Abbott, J. Munch and X.-C. Zhang, *Phys. Med. Biol.* **47**, 3789-3795 (2002).
- [9] D. H. Auston, K. P. Cheung and P. R. Smith, *Appl. Phys. Lett.* **45**, 284-6 (1984).
- [10] D. H. Auston, *Appl. Phys. Lett.* **26**, 101 3 (1975).
- [11] J. R. Morris and Y. R. Shen, *Opt. Commun.* **3**, 81-4 (1971).
- [12] X. Xie, J. Dai and X.-C. Zhang, *Phys. Rev. Lett.* **96**, 075005 (2006).
- [13] A. Leitensdorfer, S. Hunsche, J. Shah, M. C. Nuss, and W. Knox, *Phys. Rev. Lett.* **82**, 5140-5143 (1999).
- [14] Y. -S. Lee, *Principles of Terahertz Science and Technology* (Berlin: Springer 2009).
- [15] H. A. Hafez, X. Chai, A. Ibrahim, S. Mondal, D. Férachou, X. Ropagnol and T. Ozaki, *J. Opt.* **18**, 093004 (2016).
- [16] Q. Wu and X.-C. Zhang, *Appl. Phys. Lett.* **67**, 3523-5 (1995).

- [17] J. R. Fletcher, *Opt. Express* **10**, 1425 (2002).
- [18] G. Sharma, K. Singh, I. Al-Naib, R. Morandotti and T. Ozaki, *Opt. Lett.* **37**, 4338–40 (2012).
- [19] J. Hebling, A. G. Stepanov, G. Almási, B. Bartal, and J. Kuhl, *Appl. Phys.* **B** 78, 593-599 (2004).
- [20] J. A. Fulop, L. Palfalvi, S. Klingebiel, G. Almasi, F. Krausz, S. Karsch, and J. Hebling, *Opt. Lett.* **37**, 557-559 (2012).
- [21] K. Singh, C. Dion, M. R. Lesk, T. Ozaki, and S. Costantino, *Rev. Sci. Instrum.* **82**, 023706 (2011).
- [22] A. Ibrahim, G. Sharma, K. Singh, T. Ozaki, *J. Infrared. Milli. Terahz. Waves* **37**, 837 (2016).
- [23] A. Ibrahim, D. Férachou, G. Sharma, K. Singh, M. K.-Turmel, and T. Ozaki, *Sci. Rep.* **6**, 23107 (2016).
- [24] G. Sharma, K. Singh, A. Ibrahim, I. Al-Naib, R. Morandotti, F. Vidal and T. Ozaki, *Opt. Lett.* **38**, 15 2705 (2013).
- [25] T. Ostapchuk, J. Petzelt, J. Hlinka, V. Bovtun, P. Kuzel, I. Ponomareva, S. Lisenkov, L. Bellaiche, A. Tkach, and P. Vilarinho, *J. Phys. Condens. Matt.* **21**, 474215 (2009).